

Chemical Processes in the Space Environment

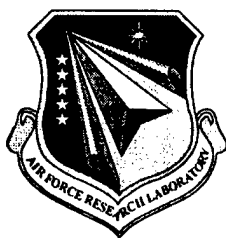
**Skip Williams
Dale Levandier**

**Orion International Technologies, Inc.
2201 Buena Vista Drive, SE
Albuquerque, NM 87106**

29 July 1999

Final Report

APPROVED FOR PUBLIC RELEASE; DISTRIBUTION UNLIMITED.



**AIR FORCE RESEARCH LABORATORY
Space Vehicles Directorate
29 Randolph Rd
AIR FORCE MATERIEL COMMAND
Hanscom AFB, MA 01731-3010**

20000127 125

REPORT DOCUMENTATION PAGE			Form Approved OMB No. 0704-0188	
<small>Public reporting burden for this collection of information is estimated to average 1 hour per response, including the time for reviewing instructions, searching existing data sources, gathering and maintaining the data needed, and completing and reviewing the collection of information. Send comments regarding this burden estimate or any other aspect of this collection of information, including suggestions for reducing this burden, to Washington Headquarters Services, Directorate for Information Operations and Reports, 1215 Jefferson Davis Highway, Suite 1204, Arlington, VA 22202-4302, and to the Office of Management and Budget, Paperwork Reduction Project (0704-0188), Washington, DC 20503.</small>				
1. AGENCY USE ONLY (Leave blank)		2. REPORT DATE June 1999		3. REPORT TYPE AND DATES COVERED Scientific, Final;
4. TITLE AND SUBTITLE Chemical Processes in the Space Environment			5. FUNDING NUMBERS Contract F19628-94-C-0072 PR 2303 TA G2 WU OR	
6. AUTHOR(S) Skip Williams Dale J. Levandier				
7. PERFORMING ORGANIZATION NAME(S) AND ADDRESS(ES) Orion International Technologies 2201 Buena Vista Drive SE Albuquerque, NM 87106			8. PERFORMING ORGANIZATION REPORT NUMBER	
9. SPONSORING/MONITORING AGENCY NAME(S) AND ADDRESS(ES) AFRL/VSBS (Rainer Dressler) 29 Randolph Rd. Hanscom AFB, MA			10. SPONSORING/MONITORING AGENCY REPORT NUMBER AFRL-VS-TR-1999-1523	
11. SUPPLEMENTARY NOTES				
12a. DISTRIBUTION AVAILABILITY STATEMENT Approved for Public Release; Distribution Unlimited			12b. DISTRIBUTION CODE	
13. ABSTRACT (Maximum 200 words) The present report discusses a series of ion-neutral collision experiments conducted in direct collaboration between Orion researchers and USAF customer affiliated sequentially with: PL/WSSI, PL/GPID, PL/GPOS, AFRL/VSBM, AFRL/VSBS. The work addresses hyperthermal chemical processes of importance in the space environment. The reaction between ionospheric ions and water were studied in detail as to the potential source of infrared radiation and ionospheric holes. New experiments were developed to study the reactions of atmospheric ions with metal vapors and to investigate metastable formation in the nonequilibrium environments of supersonic jets. The energy dependence of atmospheric ion + Na charge-transfer reactions were measured using a novel high-temperature octopole for which a US patent was granted. The results were transitioned to a model of atmospheric, meteoric metal layers. The methodology was developed to elucidate molecular ion excited state surface topography using photofragment recoil velocity analysis in an octopole ion guide.				
14. SUBJECT TERMS Space environment, Charge exchange, metals, meteors, cluster ions, photodissociation, metastables			15. NUMBER OF PAGES	
			16. PRICE CODE	
17. SECURITY CLASSIFICATION OF REPORT Unclassified	18. SECURITY CLASSIFICATION OF THIS PAGE Unclassified	19. SECURITY CLASSIFICATION OF ABSTRACT Unclassified	20. LIMITATION OF ABSTRACT SAR	

Foreword

This "Final Report" document has been compiled by ORION International Technologies, Inc., 2201 Buena Vista Drive, SE, Albuquerque, NM 87106, for Contract F19628-94-C-0072, in accordance with Modification P00012, dated 01 March 99, which states "the contractor will provide a compilation of the published work under this effort."

Summary

This contract involved the direct collaboration between ORION researchers, Drs. Skip Williams and Dale Levandier, and the laboratory personnel of the USAF Customer. The 11 attached publications fully describe the research to which the work completed under this contract has contributed. These publications are listed below. The body of work detailed here is in full compliance with the changes in Customer requirements, due to amendments in Customer priorities over the duration of the contract. These revisions in Customer priorities are directly related to the changes of Customer affiliation during the contract period of performance, through the following organizations: PL/WSSI (Spacecraft Interactions), PL/GPID (Ionospheric Effects), PL/GPOS(C) (Clutter Mitigation), AFRL/VSBM (Background Clutter Mitigation), and AFRL/VSBS (Space Hazards).

The principal elements of the original contract proposal comprised the studies of a) hyperthermal ion-molecule reactions, b) plasma dynamics, c) hyperthermal neutral-neutral reactions, d) neutral and ionic water clusters. While the specifics in each category have been affected by the changes in Customer priorities, each category has been addressed by the work performed under this contract.

Hyperthermal ion-molecule reactions

Publication [1] is a study on the most important ion-molecule reaction occurring in the contaminant cloud surrounding the space shuttle and, in general, newly launched space vehicles. This paper contributed to an ongoing study that culminated in the development of a model describing charge transfer reactions with water, as described in publication [2]. Some of the principles elucidated in this work, on exothermic charge transfer reactions, are generalized in publication [6].

Publications [8] and [10] also relate to reactions between ionospheric ions and molecules released by space-based systems.

Publications [3] and [5] involve ion-atom reactions in the ionosphere due to meteor activity. This work relates to ionospheric effects, clutter mitigation and space hazards.

Publication [11] describes new information on one of the principal ion-molecule reactions in the ionosphere provided by the state-of-the-art experiments used in this contract.

Plasma dynamics

Publications [3], [5], [8], [10] and [11] all relate to observable plasma dynamic effects in the ionosphere, including the occurrence of ionospheric 'holes' due to human activity, [8] and [10], and sporadic metal layer activity, [3] and [5].

One of the original aspects of the contract proposal involved the Critical Ionization Velocity theory. Publication [3] describes the instrument developed for the determination of the $O^+ + Ba$ charge transfer cross section. Preliminary work on this reaction was not followed up due to Customer priority revisions, however this instrument will enable a return to this reaction in the future. The instrument described in Publication [3] was the basis for a U.S. Patent awarded to the USAF:

High Temperature Octopole Ion Guide with Coaxially Heated Rods. R. A. Dressler and D. J. Levandier. U.S. Patent # 5767513, 1998.

Hyperthermal neutral-neutral reactions

The USAF equipment originally intended for use in these studies was determined to be inadequate. The equipment in question, a high temperature mass spectrometer, was used in support of the work described in Publications [3] and [5].

Neutral and ionic water clusters

The initial Customer interest in ionic water clusters evolved to interest in ionic clusters of water with other molecules and other ionic clusters relating to spacecraft interactions and other phenomena outlined in the relevant publications. Publications [4], [7] and [9] describe a series of studies on the $(N_2O \cdot H_2O)^+$ cluster ion. This joint USAF-ORION effort also resulted in the development of a new application of the USAF guided-ion beam facility, as described in Publication [9]. This application comprises the detailed analysis of the dynamics of the photodissociation of ionic clusters using a combination of the guided-ion beam time-of-flight experiment with a variable field octopole ion guide.

After a brief examination of the feasibility of studying neutral water clusters in the existing USAF facilities, this program of work was discontinued.

List of Attached Publications:

- [1] A study of isotope effects in the reaction $O^+ + H_2O/D_2O \rightarrow OH^+/OD^+ + OH/OD$ using guided-ion beams. D. J. Levandier, R. A. Dressler and E. Murad, *Chemical Physics Letters* 251 (1996) 174.
- [2] Empirical model of the state-to-state dynamics in near-resonant hyperthermal $X^+ + H_2O$ charge-transfer reactions. R. A. Dressler, M. J. Bastian, D. J. Levandier and E. Murad, *International Journal of Mass Spectrometry and Ion Processes* 159 (1996) 245.
- [3] A high-temperature octopole ion guide for measuring absolute cross sections of ion-metal atom reactions. D. J. Levandier, R. A. Dressler and E. Murad, *Review of Scientific Instruments* 68 (1997) 64.
- [4] Low energy collision-induced dissociation and photodissociation studies of the $(N_2O \cdot H_2O)^+$ cluster ion. M. J. Bastian, R. A. Dressler, D. J. Levandier, E. Murad, F. Muntean and P. B. Armentrout, *Journal of Chemical Physics* 106 (1997) 9570.
- [5] A high-temperature guided-ion beam study of $Na + X^+$ ($X = O_2, NO, N_2$) charge transfer reactions. D. J. Levandier, R. A. Dressler, S. Williams and E. Murad, *Special Issue on Atmospheric Chemistry, Journal of the Chemical Society Faraday Transactions* 93 (1997) 2611.
- [6] Comments relating to energy resonance, Franck-Condon and Langevin criteria in low-energy charge-transfer collisions. R. A. Dressler, D. J. Levandier, S. Williams and E. Murad, *Comments on Atomic and Molecular Physics. Comments on Modern Physics: Part D* 34 (1998) 43.
- [7] Deuterium isotope effects in the collision-induced dissociation and photodissociation of the $(N_2O, H_2O)^+$ cluster ion. S. Williams, Y.-H. Chiu, R. A. Dressler, D. J. Levandier and E. Murad, *Journal of Chemical Physics* 108 (1998) 9383.
- [8] Collision energy dependence and product recoil velocity analysis of $O^+(^1S) + C_2H_2$ charge-transfer and chemical reaction channels. Y.-H. Chiu, R. A. Dressler, D. J. Levandier, S. Williams and E. Murad, *Journal of Chemical Physics* 109 (1998) 5300.
- [9] Determination of photofragment ion translational energy and angular distributions in an octopole ion guide: A case study of the Ar_2^+ and $(N_2O \cdot H_2O)^+$ cluster ions. S. Williams, Y.-H. Chiu, D. J. Levandier and R. A. Dressler, *Journal of Chemical Physics* 109 (1998) 7450.
- [10] Guided-ion beam study of the $O_2^+ + C_2H_2$ charge-transfer and chemical reaction channels. Y.-H. Chiu, R. A. Dressler, D. J. Levandier, S. Williams and E. Murad, *Journal of Chemical Physics* 110 (1999) 4291.
- [11] The reaction of $O^+(^1S)$ and $N_2(X^1\Sigma_g^+)$ revisited: Recoil velocity analysis of the NO^+ product, D. J. Levandier, R. A. Dressler, Y.-H. Chiu and E. Murad, *Journal of Chemical Physics*, *submitted April, 1999*.

Reprinted from

CHEMICAL PHYSICS LETTERS

Chemical Physics Letters 251 (1996) 174–181

A study of isotope effects in the reaction
 $O^+ + H_2O/D_2O \rightarrow OH^+/OD^+ + OH/OD$ using guided-ion
beams

Dale J. Levandier ^a, Rainer A. Dressler ^b, Edmond Murad ^b

^a *ORION International Technologies, Inc., Albuquerque, NM 87110, USA*

^b *Phillips Laboratory, PL/WSSI, Hanscom AFB, MA 01731-3010, USA*

Received 1 October 1995; revised 18 December 1995



ELSEVIER

EDITORS: A.D. BUCKINGHAM, D.A. KING, A.H. ZEWAİL
Assistant Editor: Dr. R. Kobayashi, Cambridge, UK

FOUNDING EDITORS: G.J. HOYTINK, L. JANSEN
FORMER EDITORS: R.B. BERNSTEIN, D.A. SHIRLEY, R.N. ZARE

ADVISORY EDITORIAL BOARD

Australia
B.J. ORR, Sydney

Canada
P.A. HACKETT, Ottawa
J.W. HEPBURN, Waterloo
C.A. McDOWELL, Vancouver

Czech Republic
Z. HERMAN, Prague

Denmark
F. BESENBACHER, Aarhus
J.K. NØRSKOV, Lyngby

France
E. CLEMENTI, Strasbourg
J. DURUP, Toulouse
J.-M. LEHN, Strasbourg
J.-L. MARTIN, Palaiseau
B. SOEP, Orsay

Germany
R. AHLRICHS, Karlsruhe
V.E. BONDYBEY, Garching
L.S. CEDERBAUM, Heidelberg
G. ERTL, Berlin
G. GERBER, Würzburg
G.L. HOFACKER, Garching
D.M. KOLB, Ulm
J. MANZ, Berlin
M. PARRINELLO, Stuttgart
S.D. PEYERIMHOFF, Bonn
R. SCHINKE, Göttingen
E.W. SCHLAG, Garching
J. TROE, Göttingen
H. WALTHER, Garching
H.C. WOLF, Stuttgart

India
C.N.R. RAO, Bangalore

Israel
J. JORTNER, Tel Aviv
R.D. LEVINE, Jerusalem

Italy
V. AQUILANTI, Perugia

Japan
H. HAMAGUCHI, Tokyo
M. ITO, Okazaki
T. KOBAYASHI, Tokyo
K. KUCHITSU, Sakado
H. NAKATSUJI, Kyoto
K. TANAKA, Tokyo
K. YOSHIHARA, Okazaki

People's Republic of China
C.-H. ZHANG, Beijing

Poland
Z.R. GRABOWSKI, Warsaw

Russian Federation
A.L. BUCHACHENKO, Moscow
V.S. LETOKHOV, Troitzk
Yu.N. MOLIN, Novosibirsk

Spain
A. GONZÁLEZ UREÑA, Madrid

Sweden
P.E.M. SIEGBÄHN, Stockholm
V. SUNDSTRÖM, Lund

Switzerland
M. CHERGUI, Lausanne-Dorigny
R.R. ERNST, Zurich
M. QUACK, Zurich

Taiwan, ROC
Y.T. LEE, Taipei

The Netherlands
A.J. HOFF, Leiden
A.W. KLEYN, Amsterdam
D.A. WIERSMA, Groningen

United Kingdom
M.N.R. ASHFOLD, Bristol
G.S. BEDDARD, Manchester
M.S. CHILD, Oxford
D.C. CLARY, Cambridge

R. FREEMAN, Cambridge
R.H. FRIEND, Cambridge
N.C. HANDY, Cambridge
A.C. LEGON, Exeter
R.M. LYNDEN-BELL, Belfast
J.P. SIMONS, Oxford
I.W.M. SMITH, Birmingham

USA
P. AVOURIS, Yorktown Heights, NY
A.J. BARD, Austin, TX
A.W. CASTLEMAN Jr., University Park, PA
Y. CHABAL, Murray Hill, NJ
D. CHANDLER, Berkeley, CA
F.F. CRIM, Madison, WI
A. DALGARNO, Cambridge, MA
P.M. DEHMER, Argonne, IL
C.E. DYKSTRA, Indianapolis, IN
K.B. EISENTHAL, New York, NY
M.A. EL-SAYED, Atlanta, GA
M.D. FAYER, Stanford, CA
G.R. FLEMING, Chicago, IL
D.W. GOODMAN, College Station, NY
R.M. HOCHSTRASSER, Philadelphia, PA
J.L. KINSEY, Houston, TX
S.R. LEONE, Boulder, CO
C.M. LIEBER, Cambridge, MA
W.C. LINEBERGER, Boulder, CO
B.V. McKOY, Pasadena, CA
W.H. MILLER, Berkeley, CA
K. MOROKUMA, Atlanta, GA
S. MUKAMEL, Rochester, NY
A. PINES, Berkeley, CA
A.R. RAVISHANKARA, Boulder, CO
S.A. RICE, Chicago, IL
P.J. ROSSKY, Austin, TX
R.J. SAYKALLY, Berkeley, CA
H.F. SCHAEFER III, Athens, GA
G.C. SCHATZ, Evanston, IL
R.E. SMALLEY, Houston, TX
W.C. STWALLEY, Storrs, CT
D.G. TRUHLAR, Minneapolis, MN
J.J. VALENTINI, New York, NY
C. WITTIG, Los Angeles, CA
P.G. WOLYNES, Urbana, IL
R.N. ZARE, Stanford, CA

Contributions should, preferably, be sent to a member of the Advisory Editorial Board (addresses are given in the first issue of each volume) who is familiar with the research reported, or to one of the Editors:

A.D. BUCKINGHAM
D.A. KING
Editor of Chemical Physics Letters
University Chemical Laboratory
Lensfield Road
Cambridge CB2 1EW, UK
FAX 44-1223-336362

A.H. ZEWAİL
Editor of Chemical Physics Letters
A.A. Noyes Laboratory of Chemical Physics
California Institute of Technology
Mail Code 127-72
Pasadena, CA 91125, USA
FAX 1-818-4050454

After acceptance of the paper for publication, all further correspondence should be sent to the publishers (Ms. S.A. Hallink, Editorial Department, Chemistry & Chemical Engineering Department, P.O. Box 330, 1000 AH Amsterdam, The Netherlands; telephone 31-20-4852664, FAX 31-20-4852459, telex 10704 espom nl; electronic mail X400: C=NL; A=400NET; P=SURF; O=ELSEVIER; S=HALLINK, I=S or RFC822: S.HALLINK@ELSEVIER.NL).

Chemical Physics Letters (ISSN 0009-2614). For 1996, volumes 246–263 are scheduled for publication. Subscription prices are available upon request from the publisher. Subscriptions are accepted on a prepaid basis only and are entered on a calendar year basis. Issues are sent by surface mail except to the following countries where air delivery via SAL is ensured: Argentina, Australia, Brazil, Canada, Hong Kong, India, Israel, Japan, Malaysia, Mexico, New Zealand, Pakistan, PR China, Singapore, South Africa, South Korea, Taiwan, Thailand, USA. For all other countries airmail rates are available upon request. Claims for missing issues must be made within six months of our publication (mailing) date. Please address all your requests regarding orders and subscription queries to: Elsevier Science B.V., Journal Department, P.O. Box 211, 1000 AE Amsterdam, The Netherlands. Tel.: 31-20-4853642, fax: 31-20-4853598.

US mailing notice – Chemical Physics Letters (ISSN 0009-2614) is published weekly by Elsevier Science B.V., Molenwerf 1, P.O. Box 211, 1000 AE Amsterdam. Annual subscription price in the USA US\$ 6915.00, including air speed delivery, valid in North, Central and South America only. Second class postage paid at Jamaica, NY 11431. USA POSTMASTERS: Send address changes to Chemical Physics Letters, Publications Expediting, Inc., 200 Meacham Avenue, Elmont, NY 11003. Airfreight and mailing in the USA by Publication Expediting.

A study of isotope effects in the reaction $O^+ + H_2O/D_2O \rightarrow OH^+/OD^+ + OH/OD$ using guided-ion beams

Dale J. Levandier^a, Rainer A. Dressler^b, Edmond Murad^b

^a ORION International Technologies, Inc., Albuquerque, NM 87110, USA

^b Phillips Laboratory, PL/WSSI, Hanscom AFB, MA 01731-3010, USA

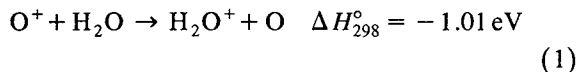
Received 1 October 1995; revised 18 December 1995

Abstract

Guided-ion beam methods were used to measure the absolute cross sections for OH^+/OD^+ derived from O^+ and H_2O/D_2O collisions over the range of 0.25–20 eV relative energy. The cross sections for the isotopic homologues have the same form, a bimodal behavior that appears to be related to the thermochemical thresholds for two reaction channels that give rise to OH^+/OD^+ . The analysis of time-of-flight (TOF) measurements, based on the osculating complex model, is compared to phase-space theory calculations. The results indicate that the low-energy channel involves atom transfer via an orbiting complex. The high-energy feature appears to be associated with the opening of the $OH^+/OD^+ + OH/OD$ $A^2\Sigma^+$ channel.

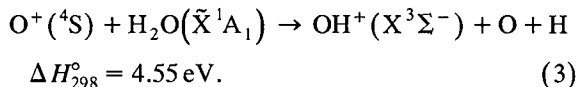
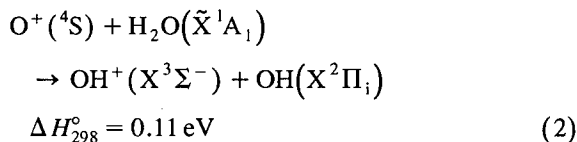
1. Introduction

As the primary ion–molecule reaction involved in the interaction between the ambient low-earth orbit atmosphere and the so-called spacecraft contaminant cloud [1–3], the charge transfer process



has been the subject of renewed interest [4–9]. In a recent study, Li et al. [9] observed for the first time a hydrogen atom abstraction channel for the $O^+ + H_2O$ collision system, which constitutes ca. 1% of the total cross section. The energy dependence of the absolute cross section for OH^+ production revealed

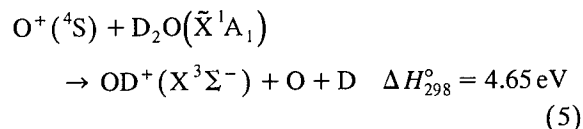
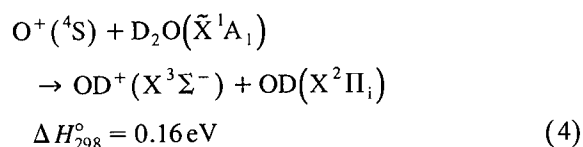
two features, which were interpreted on the basis of thermochemical thresholds to involve the reactions



The low-energy feature, reaction (2), is attributed to a collision complex mechanism, due to the rise from the threshold to a maximum at ca. 0.5 eV, followed by a decrease in cross section with energy. The high-energy feature in the OH^+ cross section is associated with the 4.55 eV threshold for reaction (3)

and is suggested by Li et al. to derive from a stepwise process involving endothermic charge transfer to the $\text{H}_2\text{O}^+ \tilde{\text{B}}^2\text{B}_2$ state, which has been observed to predissociate to OH^+ [10]. Similar observations have been seen for $\text{O}^+(\text{}^4\text{S}) + \text{CO}_2$ and $\text{O}^+(\text{}^2\text{D}, \text{}^2\text{P}) + \text{N}_2$, where the cross sections for CO^+ and C^+ , and for N^+ have onsets consistent with dissociation from a charge transfer intermediate [11,12].

The aim of the present work is to gain more insight into the hydrogen atom abstraction by studying the effects of isotope substitution on the absolute cross section for the reactions



Product ion time-of-flight (TOF) measurements are presented, which provide information on energy partitioning and the scattering dynamics.

2. Experimental

The guided-ion beam instrument used in these studies has been described elsewhere [13], and features a two-segment octopole ion guide–collision cell arrangement imbedded in a tandem mass spectrometer. The primary O^+ ion beam is injected into the first 7.4 cm long octopole after being produced by electron impact dissociative ionization of CO_2 , and mass selected in a Wien filter. The O^+ ions are almost exclusively formed (ca. 98%) in the ground state by keeping the electron energy less than 2 eV above the appearance potential for O^+ from CO_2 (19.1 eV) [14]. The first octopole passes through the 3.5 cm long collision cell, in which the target gas is maintained at pressures ≤ 0.200 mTorr for the absolute cross section measurements, and ≤ 0.260 mTorr for the TOF experiments. Transmitted primary and product ions pass into the second 16.7 cm long octopole segment at the exit of the collision cell and

are transported to the quadrupole mass filter, which employs a channel electron multiplier for ion detection. Data acquisition is achieved by passing the amplified detector output to a PC-based multichannel scaler. For the work discussed here, an octopole RF amplitude of ca. 100 V (at 10 MHz) was used, which should ensure nearly 100% collection of all reaction products without affecting the velocity distribution [15].

Absolute integral cross sections are obtained by integrating the mass spectrometer signal intensities of product ions I_{sec} and transmitted primary ions I_{prim} , and using the equation:

$$\sigma = \frac{I_{\text{sec}}}{(I_{\text{sec}} + I_{\text{prim}})nl}, \quad (6)$$

where n is the target gas density, measured with a capacitance manometer, and l is the effective interaction length, determined as described elsewhere [13].

Product ion TOF spectra are obtained by pulsing the primary ion beam with a deflector electrode just in front of the octopole injection optics, and measuring the ion flight times using a time-to-digital converter. Very slow ions, which would otherwise result in background in subsequent timing cycles, are eliminated by operating the octopole in an RF burst mode, in which the trapping potential is turned off briefly prior to the next cycle.

For these experiments ion beam energies are known to within ± 0.1 eV, with energy spreads of 0.30–0.35 eV fwhm.

3. Results and discussion

The collision energy dependence of the absolute cross sections for OH^+ and OD^+ production from collisions of O^+ with H_2O and D_2O over the energy range of 0.25–20 eV is shown in Fig. 1. Also plotted is the OH^+ cross section measured by Li et al. [9]. Considering the $\leq 30\%$ absolute error we estimate for the cross section measurements and the $\geq 25\%$ error indicated in the other work, the OH^+ cross sections are in good agreement. A dramatic isotope effect is observed that exceeds the $\leq 10\%$ uncertainties we estimate for the isotopic comparison from

reproducibility tests. The OH^+ and OD^+ cross sections exhibit the same bimodal behavior; however, in the low-energy region the ratio of OH^+ to OD^+ cross section is ca. 3, whereas in the higher-energy region the ratio is ca. 2. The difference in onsets for the high-energy OH^+ and OD^+ features is greater than would be expected from the 0.1 eV difference in the heats of reaction for the normal and heavy water systems. The threshold for reaction (3) is indicated in Fig. 1 with an arrow.

The results of OH^+ and OD^+ TOF experiments at collision energies near those at the maximum of the low-energy feature are presented in Fig. 2. The data are plotted with respect to the laboratory velocity component parallel to the ion beam axis, v'_p , after having been transformed from the raw TOF data, as described previously [16]. Also indicated on each plot are the velocities of the system center of mass, v_{CM} , and of the thermochemical limit for forward scattered product ions, $v'_{p,\text{max}}$. The present convention defines the direction of the ion beam as the forward direction, in both laboratory and CM frames.

For both systems, the product ion laboratory velocity distributions seen at the low collision energy show scattering peaked in the forward direction, however there are substantial backward scattering

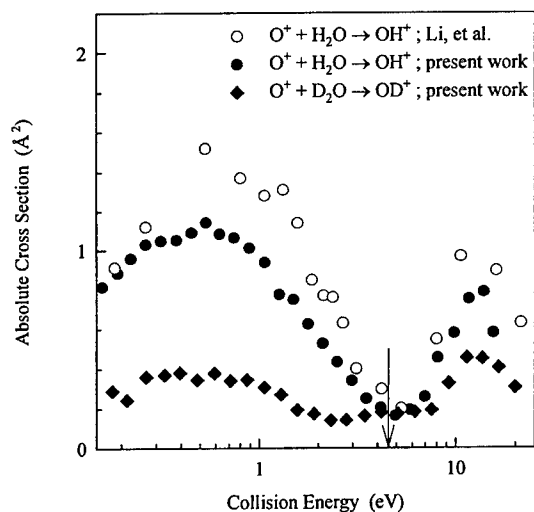


Fig. 1. Relative collision energy dependence of the cross section for OH^+/OD^+ from reactions of O^+ and $\text{H}_2\text{O}/\text{D}_2\text{O}$. The present OH^+ measurement is compared to results by Li et al. [9]. The arrow indicates the threshold for reaction (3).

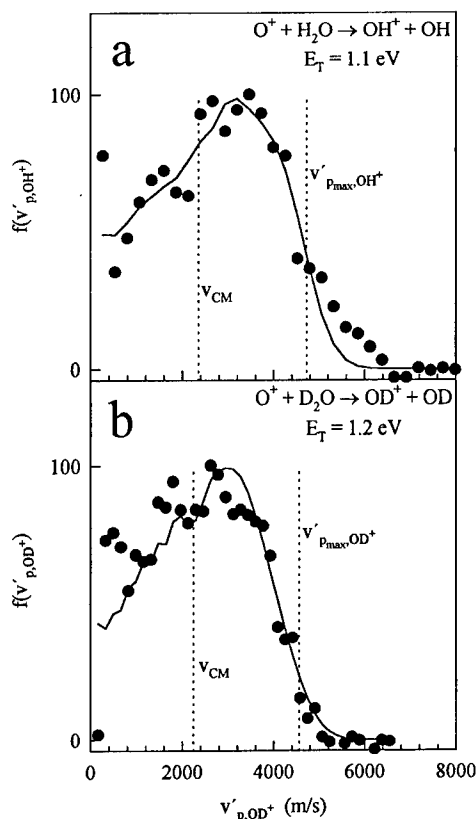


Fig. 2. Laboratory velocity distributions $f(v'_p)$ of (a) OH^+ and (b) OD^+ from reactive collisions of O^+ with H_2O and D_2O , respectively, at the relative energies shown. v'_p is the OH^+/OD^+ velocity component parallel to the octopole axis. The vertical dotted lines are at the positions of the velocity of the center of mass (v_{CM}) and the thermochemical limit of product ion laboratory velocity ($v'_{p,\text{max}}$), as indicated. The solid curves are simulations based on the oscillating complex model with $\tau_r/\tau_c = 2$. The product velocity distributions derived from the fits are shown in Fig. 3.

intensities. The velocity distributions also indicate a significant amount of translational to internal energy conversion, as evidenced by the considerable product intensity in the vicinity of the CM velocity. Such velocity distributions are consistent with products evolving from a collision complex with an average lifetime that is comparable to the complex rotational period, and supports the interpretation by Li et al. that the low-energy peak in the cross section involves a long-lived orbiting complex.

To derive quantitative information on energy partitioning in the present systems, knowledge is needed

of the angular scattering distributions. The angular distributions are modeled using the osculating complex model [17,18], which treats the angular distribution of fragments from an orbiting complex by expressing the scattering intensity as a convolution of an angular distribution function for long-lived complexes with a fall-off function that accounts for the random lifetimes of the decaying species. The adjustable parameters are the translational energy exoergicity, ΔE_T , and the ratio of complex rotational period and complex lifetime, τ_r/τ_c . By varying these parameters and averaging over the reactant velocities and over collision and scattering angles the experimental velocity distributions can be simulated [16,19], thus yielding energy transfer distributions. The solid curves in Fig. 2a and b are the fits of the velocity distributions. The poorer fit for the OH^+ spectrum, noticeable at high velocity, can be related to the inability to resolve completely the primary and product ion masses. The required subtraction of poorly discriminated primary ion signal from the product TOF spectrum results in greater uncertainty in the data in the high-velocity region.

The product translational energy distributions resulting from the osculating complex model fits are shown as bar plots in Fig. 3a and b. For both the water and heavy water cases, the simulations indicate that the translational energy distributions are broad, with reactive scattering resulting from events for which $\tau_r/\tau_c \approx 2$, corresponding to complexes that survive for an average of half a rotational period.

The involvement of a collision complex in the low-energy atom abstraction implies that statistical product energy partitioning is possible. To test this suggestion, we have performed phase-space theory (PST) calculations [20,21] of the relative kinetic energy distribution of OD^+/OH^+ and OD/OH fragments recoiling from the collision complex. In these calculations, the exit centrifugal barrier is assumed to determine the partitioning of the total angular momentum between product rotational excitation, J' , and exit channel orbital angular momentum, L' , the maximum of which is obtained as follows, for a given recoil energy:

$$L'_{\max} = [E'_T \alpha' e^2 (\mu')^2 / 2]^{1/4} \hbar^{-1}, \quad (7)$$

where α' is the polarizability of the neutral fragment, and μ' is the product reduced mass. The

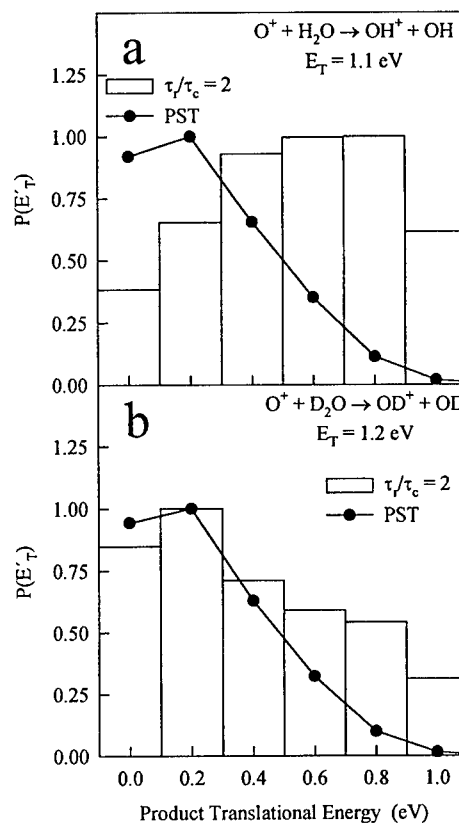


Fig. 3. Product translational energy distributions $P(E'_T)$ derived from the osculating complex model simulations of the laboratory velocity distributions, shown in Fig. 2, for (a) OH^+ and (b) OD^+ produced in 1.1 and 1.2 eV collisions, respectively. Also shown are the product translational energy distributions derived from the phase space theory calculations. The plots are normalized to unit maximum probability. The widths of the bars and the spacing of the PST points represent the energy resolution of the calculations.

maximum total angular momentum of the complex, J_{\max} , is estimated as the sum of the rotational angular momentum, J , of the room temperature target gas and the maximum orbital angular momentum, L_{\max} , implied by the cross section for complex formation, σ_{complex} . The latter is taken as the sum of the reactive cross sections measured in this work and the cross section for complex-mediated $\text{O}^+ + \text{H}_2\text{O}$ charge transfer, estimated to be equal to the CM frame forward-scattered charge transfer cross section determined in TOF studies [7]. Then,

$$\sigma_{\text{complex}} = (\pi/2 E_T \mu) (L_{\max} + 1)^2 \hbar^2, \quad (8)$$

where E_T is the collision energy and μ is the reactant reduced mass. The input parameters for the PST calculations are listed in Table 1. The largest contribution to \mathcal{J}_{\max} is derived from the complex-mediated charge transfer cross section, which is extracted as a very minor component of the charge transfer cross section and which is assumed to behave similarly with respect to collision energy for the two isotopes. This difficulty in assessing \mathcal{J}_{\max} , and the uncertainty in the osculating complex model simulations limit the usefulness of the PST calculations to a qualitative level, however, some insight into the collision dynamics can be derived.

The results of the PST calculations, for the respective reactions at collision energies of 1.1 and 1.2 eV, are also presented in Fig. 3. Comparison of the PST results with the osculating complex model simulations shows that for $\text{OD}^+ + \text{OD}$ products the statistical model recovers the most probable product translation energy quite well, however the translational energy distribution derived from the experiment clearly has a broader high-energy tail. The observed product translational energy distributions are thus consistent with a complex-mediated reaction in which the complex lifetime is just short of that required for complete energy randomization in the products. This system can therefore be interpreted as representing an intermediate case between a mechanism involving

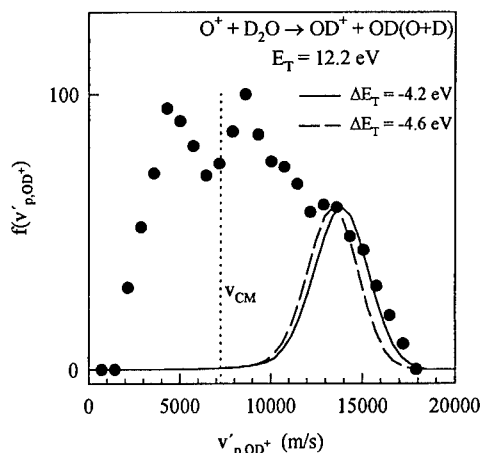


Fig. 4. Laboratory velocity distributions of OD^+ from reactive collisions of O^+ with D_2O at the 12.2 eV relative energy. v'_p is the OD^+ velocity component parallel to the octopole axis. The vertical dotted line indicates the velocity of the center of mass (v_{CM}). The curves are simulations of direct, forward scattering atom abstraction events with $\Delta E_T = -4.2$ eV (solid line) and $\Delta E_T = -4.6$ eV (dashed line), and are scaled arbitrarily to the data.

a long-lived orbiting complex and a direct spectator-stripping process, the latter being normally observed for exothermic hydrogen atom transfer reactions [13,22,23].

Although the osculating model simulations for $\text{OH}^+ + \text{OH}$ products indicate a substantial degree of translational energy conversion, the PST results are in poorer agreement for this isotopic system, possibly owing to the lower density of states or the shorter complex lifetime. The lighter complex is expected to have a smaller rotational period, so for the same τ_r/τ_c ratio the lighter species would be shorter lived, with less time for energy randomization.

Fig. 4 is the velocity-transformed TOF spectrum of OD^+ derived from $\text{O}^+ + \text{D}_2\text{O}$ collisions at 12.2 eV, corresponding to the region of the high-energy feature in the OD^+ cross section. The velocity distribution at higher collision energy also exhibits forward and backward scattering, however, there is a marked asymmetry in translational energy transfer with respect to the CM velocity. This distribution could arise from pure, low-impact parameter direct scattering, where energy transfer is more efficient in

Table 1
Quantities used for phase-space theory calculations for reactions (2) and (4) at collision energies of 1.1 and 1.2 eV, respectively

	$\text{OH}^+ + \text{OH}$	$\text{OD}^+ + \text{OD}$
$B_{\text{ion}} (\text{cm}^{-1})^a$	16.42	8.77
$B_{\text{neutral}} (\text{cm}^{-1})^a$	18.55	9.88
$\nu_{\text{ion}} (\text{cm}^{-1})^a$	3034.9	2227.6
$\nu_{\text{neutral}} (\text{cm}^{-1})^a$	3652.9	2676.2
$\alpha_{\text{neutral}} (\text{\AA}^2)^{b,c}$	1.16	1.16
$E_{\text{avail}} (\text{eV})^d$	1.0	1.0
$\mathcal{J}_{\max} (\hbar)^e$	95	100

^a Obtained from [29].

^b Obtained from [30].

^c Assumed the same for OH and OD.

^d E_{avail} represented as a Gaussian distribution of FWHM 0.3 eV centered at these values.

^e \mathcal{J}_{\max} represents as an arbitrary triangular distribution of FWHM 30 \hbar centered at these values.

the hard-sphere rebounding, which results in backward scattering. Alternatively, a combination of complex formation and direct forward scattering with less efficient energy transfer may account for the velocity distribution observed.

If three fragments are formed in a charge-transfer–predissociation channel, as invoked by Li et al. [9], the simulation of the product velocity spectrum is not straightforward. On the other hand, it is interesting to consider an atom transfer process that accesses the OH/OD $A^2\Sigma^+$ state, which has a slightly lower threshold of 4.2 eV. Fig. 4 includes two curves derived from simulations of a direct, forward-scattered reaction channel ($\tau_r/\tau_c = 20$) at translational exoergicities of -4.2 and -4.6 eV, the latter representing the three-fragment threshold. The $\Delta E_T = -4.2$ eV curve reproduces the high-velocity edge of the 12.2 eV TOF spectrum, which indicates that some of the scattering at the higher collision energies is associated with a channel that has a threshold at ca. 4.2 eV, presumably the OH⁺/OD⁺ $X^3\Sigma^- + OH/OD A^2\Sigma^+$ channel. A similar comparison to a high-energy OH⁺ TOF spectrum, obtained with poorer *S/N*, supports this suggestion. It should be pointed out that at 3.6 eV the OH⁺/OD⁺ $A^3\Pi_i$ state becomes energetically accessible, but does not appear to play a role here near the threshold. Although the threshold is consistent with OD⁺/OH⁺ $X + OD/OH A$ products, the occurrence of the endothermic charge-transfer–predissociation mechanism cannot be ruled out at 12.2 eV. Further, it cannot be distinguished whether the atom transfer channel involves an initial charge transfer followed by a proton transfer, which has been observed to be more efficient than hydrogen atom abstraction [24]. In an additional effort to elucidate the high-energy reaction mechanism, an $^{18}\text{O}^+ + \text{H}_2\text{O}$ experiment was carried out at 12.2 eV collision energy; however, it was not possible to discern $^{18}\text{OH}^+$, due to interference from the very efficient secondary reactions of charge transfer product (to give $\text{H}_3^{16}\text{O}^+$), nor was $^{16}\text{OH}^+$ clearly distinguished, due to the small cross section and the large low-mass tail of the primary ion peak in the mass spectrometer.

The difference in efficiency for production of OH⁺ and OD⁺ in collisions of O⁺ with H₂O and D₂O is remarkable, particularly in view of the expectation that the product density of states should dictate

that D₂O reacts more readily. Isotope effects in ion–molecule reactions have been observed in a number of hydrogen atom transfer systems [13,22,25–28]; however, the explanation of the apparently anomalous preference for H abstraction, compared to D transfer, has met with limited success. In studies of Ar⁺ and N₂⁺ reactions with H₂O and D₂O [13], the difference in magnitude of the exothermic isotopic hydrogen transfer cross sections was attributed to spectator stripping, or pairwise interaction, the isotope effect disappearing when the cross sections were plotted against the relative collision energy of the ion and abstracted atom.

In reactions of Kr⁺ $^2P_{3/2}$ with H₂, D₂ and HD, the thresholds of a high-energy atom transfer channel for the different isotopomers were accounted for by spectator stripping, although the more efficient abstraction from H₂, compared to D₂, could not be explained [28]. Similarly, in angle-resolved studies of reactions of O⁺ with H₂, D₂ and HD [26], spectator stripping was observed, although the greater efficiency for abstraction by O⁺ from H₂, versus D₂, remains unexplained.

In the present endothermic reactions, the reaction energy in a stripping mechanism must be supplied by the pairwise interaction. For O⁺ + H₂O/D₂O, the pairwise energies are equal to the thresholds at collision energies of 1.0 and 0.8 eV, respectively. The isotope effect is thus not consistent with a spectator stripping process, in accordance with the experimental observation that complex formation plays a major role in the dynamics.

The substantial difference in isotopic thresholds for reactions (2) and (4) could be a key contributor to the observed isotope effects. An additional factor may be provided by the present hyperthermal energy conditions, in which the relevant interaction times are comparable to the molecular vibrational periods. In such circumstances, the phases of the vibrational modes are not averaged over many vibrational periods. If the reaction probability depends strongly on the phase of the relevant vibrational motion, in the present case presumably the H₂O asymmetric stretch coordinate, the higher vibrational frequency associated with the lighter isotope would result in a greater probability of the appropriate phase during the collision event. Moreover, it is conceivable that the reaction probability increases dramatically with stretch-

ing coordinate amplitude. The substantial difference in isotopic zero point energies, signifying different turning point amplitudes, would then further favor the lighter isotope.

4. Conclusion

The cross section for OD^+ production in collisions of O^+ and D_2O exhibits the same bimodal behavior seen in the normal water homologue. The participation of an orbiting complex in the low-energy reaction was confirmed for both water and heavy water. Osculating complex model simulations of product velocity distributions for collisions in the low-energy regime indicate that the complexes giving rise to OH^+ and OD^+ have average lifetimes about half their rotational periods. The substantial translational energy transfer evidenced by the modeling verifies that the collision complexes are sufficiently long-lived for a large degree of energy redistribution. However, results of phase-space theory calculations suggest that the energy transfer is not wholly statistical, particularly for the H_2O system.

TOF measurements for OD^+ derived from the high-energy channel do not rule out the predissociation of a $\text{D}_2\text{O}^+ \tilde{\text{B}}^2\text{B}_2$ state charge transfer intermediate suggested by Li et al. [9], but indicate a contribution from an atom transfer mechanism which involves production of $\text{OD A}^2\Sigma^+$.

To explain the larger OH^+ versus OD^+ cross section, it is suggested that the reaction efficiency depends strongly on the phase and/or amplitude of the asymmetric stretch mode in the target species during the collision event. The lighter isotope reacts more readily by virtue of the higher zero point vibrational frequency and turning point amplitudes.

Acknowledgements

The authors are grateful to Professor C.Y. Ng and coworkers for communicating the results of their $\text{O}^+(\text{}^4\text{S}) + \text{H}_2\text{O}$ work prior to publication, and to Professor J.M. Farrar for the copy of his PST program. This work was supported by AFOSR under Task 2303EP2.

References

- [1] R.S. Narcisi, E. Trzcinski, G. Federico, L. Wlodyka and D. Delorey, Proc. AIAA, AIAA 83-2659, Washington, DC, October 1983.
- [2] J.M. Grebowsky, H.A. Taylor Jr., M.W. Pharo III and N. Reese, Planetary Space Sci. 35 (1987) 501.
- [3] J.M. Grebowsky, H.A. Taylor Jr., M.W. Pharo III and N. Reese, Planetary Space Sci. 35 (1987) 1463.
- [4] G.E. Caledonia, J.C. Person and D.E. Hastings, J. Geophys. Res. A92 (1987) 273.
- [5] J.M. Grebowsky and A. Schaefer, Indian J. Radio Space Phys. 19 (1990) 49.
- [6] R.A. Dressler, J.A. Gardner, D.L. Cooke and E. Murad, J. Geophys. Res. 96 (1991) 13,795.
- [7] R.A. Dressler, R.H. Salter and E. Murad, Planetary Space Sci. 40 (1992) 1695.
- [8] R.A. Dressler, R.H. Salter and E. Murad, Chem. Phys. Letters 204 (1993) 111.
- [9] X. Li, Y.L. Huang, G.D. Flesch and C.Y. Ng, J. Chem. Phys. 102 (1995) 5100.
- [10] D. Norwood, A. Ali and C.Y. Ng, J. Chem. Phys. 95 (1991) 8029.
- [11] G.D. Flesch and C.Y. Ng, J. Geophys. Res. 96-A12 (1991) 21 403.
- [12] G.D. Flesch and C.Y. Ng, J. Geophys. Res. 96-A12 (1991) 21 407.
- [13] R.A. Dressler, R.H. Salter and E. Murad, J. Chem. Phys. 99 (1993) 1159.
- [14] M.J. Bastian, R.A. Dressler and E. Murad, J. Chem. Phys. 103 (1995) 144.
- [15] D. Gerlich, in: State-selected and state-to-state ion-molecule reaction dynamics, Part I, eds. M. Baer and C.Y. Ng, Advances in Chemical Physics, Vol. 82 (Wiley, New York, 1992) p. 1.
- [16] R.A. Dressler and E. Murad, in: Unimolecular and bimolecular ion-molecule reaction dynamics, eds. C.Y. Ng, T. Baer and I. Powis, Wiley Series in Ion Chemistry and Physics (Wiley, New York, 1994) p. 87.
- [17] G.A. Fisk, J.D. McDonald and D.R. Herschbach, Discussions Faraday Soc. 44 (1967) 228.
- [18] M.K. Bullit, C.H. Fisher and J.L. Kinsey, J. Chem. Phys. 60 (1974) 478.
- [19] D. Gerlich, J. Chem. Phys. 90 (1989) 127.
- [20] P. Pechukas, J.C. Light and C. Rankin, J. Chem. Phys. 44 (1966) 794.
- [21] W.J. Chesnavich and M.T. Bowers, J. Chem. Phys. 66 (1977) 2306.
- [22] K.M. Ervin and P.B. Armentrout, J. Chem. Phys. 83 (1985) 166.
- [23] R.H. Schultz and P.B. Armentrout, J. Chem. Phys. 96 (1992) 1036.
- [24] M. Baer, Mol. Phys. 35 (1978) 1637.
- [25] A. Henglein, in: Ion-molecule reactions in the gas phase, ed. R.F. Gould, Advances in Chemistry Series, Vol. 58 (Ameri-

- can Chemical Society, Washington, DC, 1966) p. 63; and references therein.
- [26] K.T. Gillen, B.H. Mahan and J.S. Winn, *J. Chem. Phys.* 58 (1973) 5373 and references therein.
- [27] J.L. Elkind and P.B. Armentrout, *J. Chem. Phys.* 84 (1986) 4862.
- [28] K.M. Ervin and P.B. Armentrout, *J. Chem. Phys.* 85 (1986) 6380.
- [29] K.P. Huber and G. Herzberg, *Molecular spectra and molecular structure*, Vol. IV, Constants of diatomic molecules (Van Nostrand Reinhold, New York, 1979).
- [30] A.D. Esposti and H. Werner, *J. Chem. Phys.* 93 (1990) 3351.

Reprinted from

International Journal of

Mass Spectrometry and Ion Processes

International Journal of Mass Spectrometry and Ion Processes 159 (1996) 245–256

Empirical model of the state-to-state dynamics in near-resonant hyperthermal $X^+ + H_2O$ charge-transfer reactions

Rainer A. Dressler*, Michael J. Bastian¹, Dale J. Levandier², Edmond Murad

Phillips Laboratory, Spacecraft Interactions Branch, PL/WSCI Hanscom AFB, MA 01731-3010 USA

Received 28 November 1995; accepted 3 June 1996



INTERNATIONAL JOURNAL OF MASS SPECTROMETRY AND ION PROCESSES

GENERAL INFORMATION

EDITORS

M.T. Bowers (Santa Barbara, CA)
H. Schwarz (Berlin)
J.F.J. Todd (Canterbury)

EDITORIAL BOARD:

P.B. Armentrout (Salt Lake City, UT)
T. Baer (Chapel Hill, NC)
B. Bentz (Princeton, NJ)
J.H. Beynon (Swansea)
D. K. Bohme (North York, Ont.)
R.G. Cooks (West Lafayette, IN)
M.A. Duncan (Athens, GA)
D. Gerlich (Chemnitz)
M.L. Gross (St. Louis, MO)
Z. Herman (Prague)
F. Hillenkamp (Münster)
K.R. Jennings (Coventry)
Y. LeBeyec (Orsay)
C. Lifshitz (Jerusalem)

J.C. Lorquet (Liège)
T.D. Märk (Innsbruck)
A.G. Marshall (Columbus, OH)
S.A. McLuckey (Oak Ridge, TN)
T.B. McMahon (Waterloo, Ont.)
H.J. Neusser (Garching)
N.M.M. Nibbering (Amsterdam)
D. Price (Salford)
L. Radom (Canberra, ACT)
F. Röhlgen (Bonn)
D. Smith (Keele)
M. Tsuchiya (Tokyo)
H. Wollnik (Giessen)
R.A. Yost (Gainesville, FL)

Scope of the journal

The journal contains papers which consider fundamental aspects of mass spectrometry and ion processes, and the application of mass spectrometric techniques to specific problems in chemistry and physics. The following topics, amongst others, can be found in the journal: theoretical and experimental studies of ion formation (i.e. by electrons, laser or other forms of radiation, heavy ions, high-energy particles, etc.), ion separation and ion detection processes; the design and performance of instruments (or their parts) and accessories; measurements of natural isotopic abundances, precise isotopic masses, ionization, appearance and excitation energies, ionization cross-sections; development of techniques related to determining molecular structures, geological age determination, studies of thermodynamic properties, chemical kinetics, surface phenomena, radiation chemistry, and chemical analyses; theory of mass spectra, application of computer techniques to mass spectral data; chemistry and physics of cluster ions; spectroscopy of gaseous ions including studies related to interstellar chemistry; mechanistic studies of unimolecular processes and ion/molecule reactions in the gas phase including computational aspects (ion trajectory calculations, quantum mechanical studies of potential energy surfaces); physical organic chemistry of isolated ions; biological applications of mass spectrometry.

The journal is of interest to all mass spectrometrists and other scientists interested in the chemistry and physics of charged particles.

Categories of manuscripts

The journal welcomes the following types of papers.

Full-length articles: Comprehensive description and discussion of original research investigations; the experimental techniques must be described in detail.

Letters: Brief reports (no longer than 4 printed pages or 2000 words) of significant, original and timely research. In considering the suitability of a letter for publication, the editors pay particular attention to the originality of the research and the desirability of rapid publication. **Letters will be published within 6–8 weeks** after acceptance of the article by the editor concerned. No proofs will be sent to the authors.

Reviews: Timely, critical reviews will focus on recent developments while keeping historical documentation to a minimum. Reviews will often be solicited, but prospective authors are also encouraged to contact the editors or editorial board members regarding the appropriateness of the subject matter. In general the length should not exceed 30–40 printed pages. The publisher provides authors of Reviews with a modest honorarium.

Book Reviews: Normally invited by the editors, the style should conform to that of previously published Book Reviews.

Copyright © 1996 Elsevier Science B.V. All rights reserved

0168-1176/96/\$15.00

This journal and the individual contributions contained in it are protected by the copyright of Elsevier Science B.V., and the following terms and conditions apply to their use:

Photocopying

Single photocopies of single articles may be made for personal use as allowed by national copyright laws. Permission of the publisher and payment of a fee is required for all other photocopying; including multiple or systematic copying, copying for advertising or promotional purposes, resale, and all forms of document delivery. Special rates are available for educational institutions that wish to make photocopies for non-profit educational classroom use.

In the USA, users may clear permissions and make payment through the Copyright Clearance Center, Inc., 222 Rosewood Drive, Danvers, MA 01923, USA. In the UK, users may clear permissions and make payment through the Copyright Licensing Agency Rapid Clearance Service (CLARCS), 90 Tottenham Court Road, London W1P 0LP, UK. In other countries where a local copyright clearance centre exists, please contact it for information on required permissions and payments.

Derivative Works

Subscribers may reproduce tables of contents or prepare lists of articles including abstracts for internal circulation within their institutions. Permission of the publisher is required for resale or distribution outside the institution.

Permission of the publisher is required for all other derivative works, including compilations and translations.

Electronic Storage

Permission of the publisher is required to store electronically any material contained in this journal, including any article or part of an article. Contact the publisher at the address indicated.

Except as outlined above, no part of this publication may be reproduced, stored in a retrieval system or transmitted in any form or by any means, electronic, mechanical, photocopying, recording or otherwise, without prior written permission of the publisher.

Disclaimers

No responsibility is assumed by the publisher for any injury and/or damage to persons or property as a matter of products liability, negligence or otherwise, or from any use or operation of any methods, products, instructions or ideas contained in the material herein.

Although all advertising material is expected to conform to ethical (medical) standards, inclusion in this publication does not constitute a guarantee or endorsement of the quality or value of such product or of the claims of it by its manufacturer.

⊗ The paper used in this publication meets the requirements of ANSI/NISO Z39.48-1992 (Permanence of Paper).

Printed in The Netherlands

Empirical model of the state-to-state dynamics in near-resonant hyperthermal $X^+ + H_2O$ charge-transfer reactions

Rainer A. Dressler*, Michael J. Bastian¹, Dale J. Levandier², Edmond Murad

Phillips Laboratory, Spacecraft Interactions Branch, PL/WSCI Hanscom AFB, MA 01731-3010 USA

Received 28 November 1995; accepted 3 June 1996

Abstract

$H_2O^+ \tilde{A} - \tilde{X}$ luminescence studies involving $X^+ + H_2O$ ($X = Ar, N, Kr, N_2$) charge-transfer systems are consolidated into an empirical model for the charge-transfer product state distributions associated with hyperthermal collisions of ground-state reactants. The model predicts that Franck–Condon active states are populated with a Gaussian vibrational energy distribution that is shifted by approximately -0.18 eV with respect to energy resonance. The model is applied to hyperthermal $O^+(^4S) + H_2O$ charge-transfer collisions for which luminescence experiments are too insensitive because weakly emitting vibrationally excited states of the $H_2O^+ \tilde{X}^2B_1$ state are populated. Isotope effects in the $O^+(^4S) + H_2O/D_2O$ charge-transfer cross sections are measured using guided-ion beams to test the model. The model correctly predicts the observed isotope effect within the hyperthermal collision energy range of 2 and 8 eV.

Keywords: Luminescence studies; Hyperthermal collisions

1. Introduction

Charge-transfer reactions play a prominent role in the environment of low-Earth orbiting spacecraft [1–3]. Due to its high recombination energy of 13.6 eV, O^+ , the main ion at low-Earth orbit altitudes, will efficiently undergo charge-transfer with most molecular species released by spacecraft. H_2O is the principal constituent of a contaminant cloud surrounding low-Earth orbiting spacecraft, and interacts with O^+ at the high orbiting relative velocity of 7.8 km s^{-1} , corresponding to a center-of-mass collision energy

of 2.65 eV. At these hyperthermal collision energies, exothermic charge-transfer reactions are predominantly governed by long-range dynamics accompanied by little translational energy transfer. The exothermicity of the reaction is thus almost entirely channelled into internal energy of the products. Consequently, the hyperthermal molecular charge-transfer collisions result in highly excited molecular species that produce background optical emissions seen by spaceborne sensors. Because of the advent of spaceborne astronomy in the visible and infrared spectral regions [4,5], it is important to identify the source and spectral distribution of the induced backgrounds.

A correlation between the diurnal variations of infrared background and the O^+ density in the

* Corresponding author.

¹ NRC Postdoctoral Fellow

² Orion International, Albuquerque, NM, USA

measurements of Spacelab 2 has been associated with $O^+ + H_2O$ charge-transfer luminescence [6]. Currently, well-characterized ion beam luminescence experiments do not have adequate sensitivity to resolve infrared emissions from hyperthermal ion–molecule collisions, and H_2O^+ laser probing schemes have not been developed. Therefore, in order to verify the assertion that charge-transfer luminescence contributes to observable infrared background of low-Earth orbiting spacecraft, the state-to-state dynamics of the $O^+ + H_2O$ charge-transfer systems needs to be understood to establish the spectral regions of H_2O^+ emissions.

We have obtained in previous work valuable insight into the detailed dynamics of hyperthermal ion– H_2O charge-transfer reactions from luminescence and guided-ion beam studies of the $X^+ + H_2O$ ($X = Ar, N, Kr, N_2$) collision systems [7–11]. These collision systems populate vibrational levels of the $H_2O^+ \tilde{A}$ state in near-resonant charge-transfer, producing $H_2O^+ \tilde{A} - \tilde{X}$ visible emissions that are readily observed. The analysis of the luminescence spectra in conjunction with guided-ion beam cross section and time-of-flight measurements, and high-level ab initio calculations of the $H_2O^+ \tilde{A}$ and \tilde{X} potential energy surfaces [12], have contributed substantially to the understanding of the state-to-state dynamics of near-resonant ion–polyatomic charge-transfer systems.

In this work an attempt is made to consolidate the ion– H_2O charge-transfer studies into an empirical model that predicts the product ion vibrational distribution. The model is applied to the $O^+(^4S) + H_2O$ charge-transfer system, which has an exothermicity of only 1.0 eV and thus does not produce observable visible luminescence in near-resonant charge-transfer. New guided-ion beam measurements of the $O^+(^4S) + H_2O/D_2O$ isotopic charge-transfer cross sections are presented which are used to validate the model by comparing predicted and observed isotope effects.

2. Experimental

The luminescence and guided-ion beam experiments discussed in this work have been conducted in experiments described in detail previously [7,8]. In the luminescence studies, an intense ion beam is generated using a dc discharge plasma source (Colutron). The ion beam is mass selected using a Wien velocity filter, following which the ions are decelerated to the desired energy before entering a collision cell containing water vapor at an approximate pressure of 1 mTorr. The collision cell is fiber-optically coupled to an optical multichannel analyser consisting of a 0.18 m Czerny–Turner spectrograph and an intensified photodiode array or liquid nitrogen cooled CCD array detector. After passage through the collision cell, the ion beam is monitored with a quadrupole mass analyzer.

In the guided-ion beam studies, an ion beam is generated using electron impact ionization. In the $O^+ + H_2O$ studies, a beam of >98% pure ground-state $O^+(^4S)$ is produced from CO_2 by electron impact at an electron energy within 2 eV of the appearance potential (19.1 eV). Following mass selection in a Wien velocity filter, the ion beam is decelerated and injected into a system of two octopoles in series. An rf voltage applied to the octopole generates a cylindrical ion trap. The first octopole guides the ions through a 3.5 cm long collision cell containing water vapor at an approximate pressure of 0.2 mTorr. The trapping potential ensures that all product ions are collected irrespective of their scattering trajectories. Following transmission through the longer second octopole, primary and secondary ions are extracted into a quadrupole mass filter for mass analysis. Low-resolution energy partitioning and scattering dynamics information is derived from time-of-flight studies, in which the experiment is operated in a pulsed mode and secondary ion times-of-flight through the second octopole are determined.

Table 1
Exothermicities, ΔH , of experimentally investigated $X^+ + H_2O$ charge-transfer systems.

$X^+ + H_2O/D_2O$	ΔH (eV)
$O^+(^4S) + H_2O/D_2O$	1.01/0.98
$N^+(^3P) + H_2O$	1.91
$Kr^+(^2P_{1/2}) + H_2O$	2.04
$N_2^+ + H_2O$	2.96
$Ar^+(^2P_{3/2}) + H_2O$	3.14

3. Results

3.1. Charge-transfer luminescence measurements

Guided-ion beam cross section and time-of-flight measurements of the ion– H_2O collision systems of interest in this work have shown that charge-transfer is efficient at hyperthermal energies and that little translational energy transfer occurs, signifying a predominantly long-range mechanism [13,8–10]. The systems thus undergo near-resonant charge-transfer, where the charge-transfer exothermicity is almost

entirely partitioned into internal excitation of the products. The exothermicities of the investigated systems, given by the difference between reactant ion and product ion recombination energies, are listed in Table 1. The $O^+(^4S) + H_2O/D_2O$ systems have the lowest exothermicities resulting in the least product internal excitation of the investigated systems. In the other systems, the excitation energy available in near-resonant charge-transfer suffices to promote the product water ions to vibrational levels of the first electronically excited $\tilde{A} \ ^2A_1$ state that are readily observed optically. The excitation energy of the ground vibrational level of the \tilde{A} state is approximately 1.04 eV, and thus potentially accessible by $O^+(^4S) + H_2O$ reactants. As will become clearer in the following sections of this paper, dynamical constraints in the $O^+(^4S) + H_2O$ system prevent significant population of the lowest vibrational levels of the \tilde{A} state, which have weak infrared transitions to the \tilde{X} state.

In first optical experiments of this laboratory, $\tilde{A} - \tilde{X}$ emissions were observed in the Ar^+ and $N_2^+ + H_2O$ collision systems [7]. The resolution of the

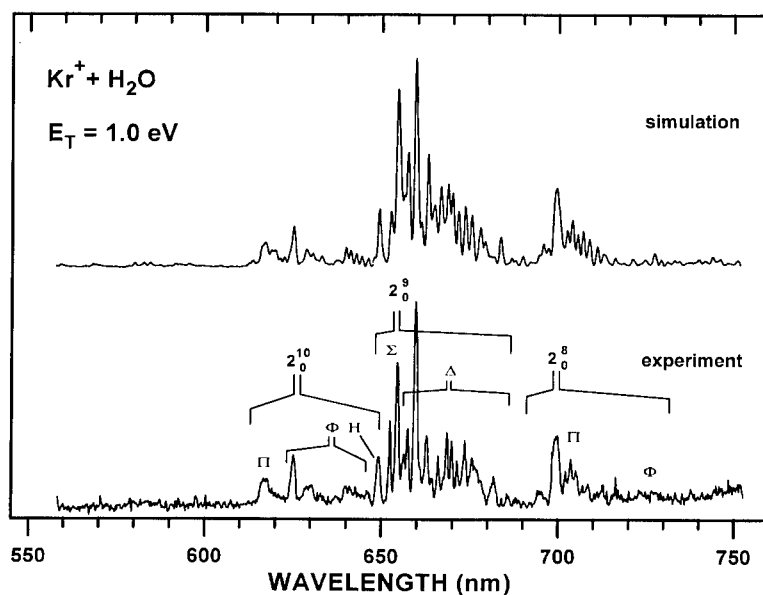


Fig. 1. $Kr^+ + H_2O$ luminescence spectrum (bottom curve) is compared to a spectrum calculated for $H_2O^+ \tilde{A} - \tilde{X}$ transitions (top curve). Various bending vibrational transitions and respective Renner–Teller subbands are identified. In the simulation, vibrational state populations, $n_i(\nu_2', K')$, and rotational temperatures are chosen to provide a best fit with respect to the experimental observation.

luminescence spectra was adequate to determine nascent H_2O^+ vibrational populations through the spectral analysis. The sensitivity, however, was insufficient to perform an analysis at collision energies below 10 eV. More recently, the use of a highly red sensitive liquid nitrogen cooled CCD detector permitted the recording of Kr^+ and $\text{N}^+(\text{}^3\text{P}) + \text{H}_2\text{O}$ luminescence spectra over a large range of collision energies [10,11]. An example of a $\text{Kr}^+ + \text{H}_2\text{O}$ luminescence spectrum is shown in Fig. 1. The spectrum (bottom curve) has been recorded for a collision energy of 1 eV at a spectral resolution of 0.8 nm FWHM. The top curve is a synthetic spectrum calculated using the asymmetric rotor program of Birss and Ramsay and the methodology described previously [7,11]. The figure identifies the vibronic subbands attributable to Renner–Teller K structure of bending vibrational transitions of the $\text{H}_2\text{O}^+ \tilde{A} - \tilde{X}$ system. $\Sigma, \Pi, \Delta, \Phi, \Gamma, H \dots$ bands signify emissions from $K_a' = 0, 1, 2, 3, 4, 5 \dots$ rotational levels. As in all of the ion– H_2O luminescence studies, only bending vibrational transitions are identified. The emissions in Fig. 1 stem from $\text{H}_2\text{O}^+ \tilde{A}$ state $v_2' = 8, 9$ and 10 vibrational

states. The bending vibrational quantum numbers are those of the linear notation. $\text{Kr} + \text{H}_2\text{O}^+ (\tilde{A}, v_2' = 10)$ products are near-resonant with $\text{Kr}^+(\text{}^2\text{P}_{1/2}) + \text{H}_2\text{O}$ reactants, and the bands can thus be identified as near resonant charge-transfer luminescence of spin-orbit excited reactants. $\text{Kr}^+(\text{}^2\text{P}_{1/2})$ ions constitute approximately 30% of the ion beam in this particular experiment. The sensitivity of the experiment is insufficient to identify positively luminescence from near-resonant charge-transfer of $\text{Kr}^+(\text{}^2\text{P}_{3/2}) + \text{H}_2\text{O}$ reactants. These emissions are expected above 900 nm from transitions with weak transition moments into the ground vibrational level of the \tilde{X} state.

Product-state distributions are obtained from the spectral simulations of the observed $\text{H}_2\text{O}^+ \tilde{A} - \tilde{X}$ bands. Examples of product \tilde{A} state bending vibrational distributions determined for the four investigated systems are shown in Fig. 2. The product rotational excitation is generally found not to exceed a rotational temperature of 600 K, which is consistent with the predominantly long-range nature of the charge-transfer dynamics. The nearest resonant state is gray-shaded for each

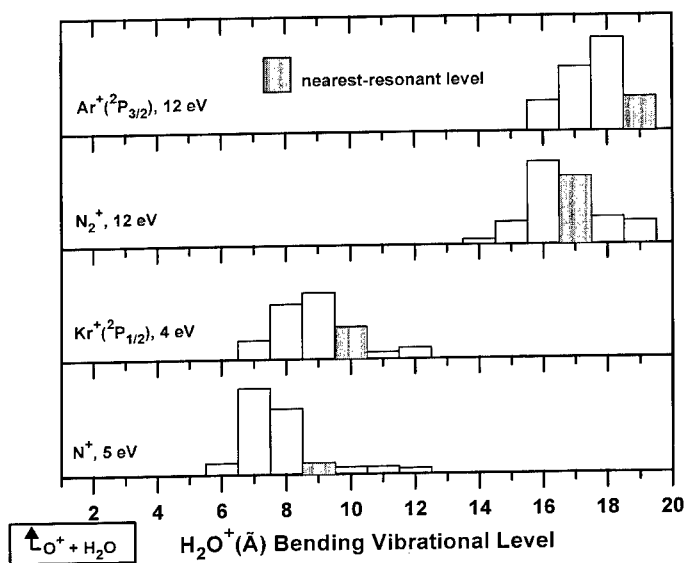


Fig. 2. $\text{H}_2\text{O}^+ \tilde{A}$ state bending vibrational populations produced in ion– H_2O charge-transfer collisions with various ions at respective hyperthermal center-of-mass collision energies. The populations of nearest-resonant vibrational states are shaded gray. The approximate $\text{O}^+(\text{}^4\text{S}) + \text{H}_2\text{O}$ resonance position on the bending vibrational scale is also indicated.

system. The location of the $O^+(^4S)+H_2O$ resonance on the respective bending vibrational level scale is also shown.

A preference for exothermic states is clearly visible in Fig. 2. The reasons for this discrepancy with respect to energy resonance criteria are rationalized in the following section. The energy dependence of state-to-state cross sections observed for the $N^+(^3P)$ and $Kr^+(^2P_{1/2})+H_2O$ systems reveal two distinctly different types of behavior. While the low energy state-to-state cross sections of exothermic product states exhibit an approximate $E_T^{-0.5}$ dependence, the fluxes into near-resonant and endothermic states increase with collision energy [10,11], similar to observations made for singly-charged exo- or endothermic atomic charge-transfer systems [14,15]. Relative populations of the relevant exothermic states are found not to vary with collision energy within the errors of the analysis at collision energies below 15 eV [10,11].

3.2. $O^+ + H_2O/D_2O$ measurements

Examples of previously unpublished guided-ion beam $O^+(^4S)+H_2O/D_2O$ charge-transfer cross

section measurements recorded in this laboratory are shown in Fig. 3. The cross sections are plotted on a logarithmic scale with respect to the center-of-mass collision energy. The results are compared to measurements of Li et al. [16], who generated a state-selected $O^+(^4S)$ beam using photoionization techniques. Given the absolute errors of $\pm 30\%$ reported for both experiments, it can be stated that good agreement exists between the two experiments. The present measurements are approximately 30% higher than previously reported measurements of this laboratory [13]. Since then, we have improved our octopole extraction optics.

An exponential drop in cross section with collision energy is observed below 1 eV (c.m.), and no significant difference is observed between the isotopic charge-transfer systems. At energies above 1 eV, the cross section is less energy dependent and an isotope effect in favor of H_2O is apparent. Since the isotopic comparison stems from measurements recorded with the same instrument on successive days, the relative error between the two measurements is considerably smaller than the absolute error stated above. We estimate the relative error to be smaller than 10% below 10 eV, thus establishing the existence of an isotope effect. At energies above 10 eV, discrimination effects associated with the large difference between primary and secondary ion LAB frame kinetic energies result in slightly larger experimental uncertainties.

The large hyperthermal cross sections signify long-range dynamics accompanied by little energy transfer. This is confirmed by time-of-flight measurements [13], which exhibit primarily near-thermal velocity product ions (LAB frame). Fast product ions are also observed that are attributed to collision complex orbiting. The features of the $O^+ + H_2O$ guided-ion beam measurements are very similar to those observed in the N^+ , Kr^+ , Ar^+ , and $N_2^+ + H_2O$ charge-transfer systems [8–10]. All of the systems have large hyperthermal charge-transfer cross sections and similar orbiting propensities, as identified by the

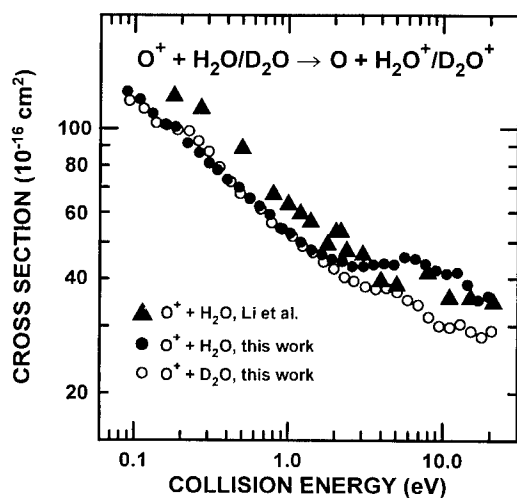


Fig. 3. Center-of-mass collision energy dependence of the $O^+(^4S)+H_2O/D_2O$ charge-transfer cross sections. The present measurements are compared to state-selected ion measurements by Li et al. [22]

low-energy cross sections and time-of-flight measurements.

3.3. Empirical state-to-state model

A unified theory for molecular charge-transfer collisions does not exist. Full quantal treatments have only successfully reproduced experimental data in the case of small ion–diatomic systems. An empirical approach is thus necessary to predict the state-to-state dynamics of ion–H₂O charge-transfer systems for which experiments have not provided product state-resolved information. In this section, the information gained from the laboratory ion–H₂O studies is consolidated into a simple model for the ion–H₂O charge-transfer product state distributions.

As discussed in semiclassical theoretical work, the two most important criteria governing molecular charge-transfer probabilities in exothermic systems are energy resonance and Franck–Condon overlap [17,18]. The conditions postulated for large vibrational state-to-state cross sections at hyperthermal energies are small energy gaps, ΔE , between reactant and product vibronic levels and significant overlap between reactant and product vibrational wave functions. The luminescence measurements discussed above fully corroborate the importance of Franck–Condon overlap. As seen in the photoelectron spectrum of H₂O [19–21], only bending vibrational levels have significant Franck–Condon overlap in H₂O \tilde{X}^1A_1 –H₂O⁺ \tilde{A}^2A_1 transitions. In agreement with Franck–Condon predictions, only bending vibrational excitation is observed in the H₂O⁺ \tilde{A}^2A_1 – \tilde{X}^2B_1 charge-transfer luminescence studies. Interestingly, the Franck–Condon overlap is near-zero at resonance in the O⁺(⁴S)+H₂O system, suggesting inefficient charge-transfer. Contrary to energy resonance and Franck–Condon arguments, the O⁺(⁴S)+H₂O charge-transfer cross sections are among the largest observed for ion–H₂O systems [16,13]. This is a first indication that the product state distribution of this system is also shifted in

favor of exothermic states, as observed for the systems of our optical studies. It is shown below that this implies that exothermic vibrational levels of the \tilde{X} state with significant Franck–Condon overlap are populated.

Different empirical analytical expressions for vibrational state-to-state cross sections have been proposed for long-range charge-transfer [22–26], many of which take the form

$$\sigma_{v' \rightarrow v''} = \sigma_0(\Delta E, E_T) \langle v' | v'' \rangle^2, \quad (1)$$

where $\langle v' | v'' \rangle^2$ is the Franck–Condon factor between vibrational wave functions v' and v'' and $\sigma_0(\Delta E, E_T)$ is the pure electronic charge-transfer cross section expressed as a function of the energy gap, ΔE , and the translational energy, E_T , at infinite intermolecular distances. The electronic charge-transfer cross section is usually taken from atomic charge-transfer models, such as the Rapp and Francis [27], Demkov [28], or Rosen–Zener type [29,30] models. In most cases, models based on expressions of the form (1) have not provided satisfactory interpretation of experimental observations in molecular systems at near-thermal and hyperthermal collision energies.

The experimentally determined product state populations shown in Fig. 2 reflect both the importance of energy gap and Franck–Condon overlap in those ion–H₂O charge-transfer systems that populate vibrational levels of the H₂O⁺ \tilde{A} state. In order to derive a model similar to Eq. (1) specific for the present ion–H₂O systems, the normalized product populations of the four distributions in Fig. 2 are plotted with respect to the asymptotic energy gap, ΔE , in Fig. 4. Despite the fact that the data stem from different charge-transfer systems involving different electronic interactions, a bell-shaped distribution with a maximum near ~ -0.2 eV is clearly visible. The solid line is a nonlinear least-squares fit of a shifted Gaussian distribution:

$$p(\Delta E) = A \exp \left(- \left(\frac{1.66(\Delta E - \delta)}{\gamma} \right)^2 \right) \quad (2)$$

where δ is the energy shift with respect to resonance, γ represents the half width (FWHM) of the distribution, and A is a constant. As seen in Fig. 4, the fit is very good except at positive energy gaps, where endothermic state population is evident. Endothermic level population is only significant at collision energies above 10 eV. The fit yields $A = 0.38 \pm 0.02$, $\delta = -0.18 \pm 0.02$ eV and $\gamma = 0.28 \pm 0.09$ eV. It is worth noting that the determined $\text{Kr}^+(\text{}^2\text{P}_{1/2}) + \text{H}_2\text{O}$ product state distributions have the smallest errors, and are, apart from the endothermic levels, in superb agreement with the fit.

The luminescence measurements demonstrate that the relative populations of the relevant exothermic levels of the investigated systems only weakly depend on collision energy below 15 eV [7,10,11]. Given the errors in determining the product state distributions, the present approach involving measurements at collision energies ranging between 4 and 12 eV is justified for the collision energies of interest in this work.

In comparison to Eq. (1), Eq. (2) neglects a dependence of the probabilities on the respective Franck–Condon factors. In an effort to incorporate a Franck–Condon dependence, we have

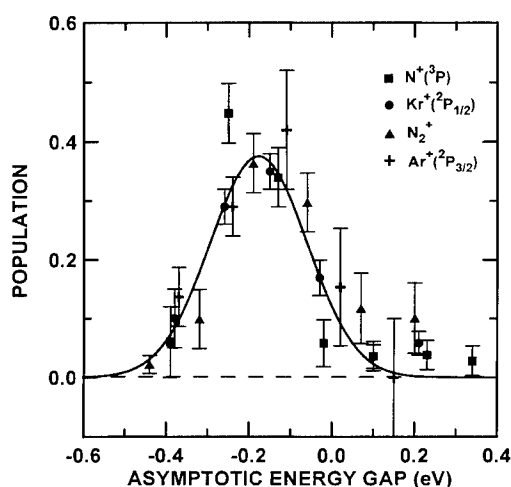


Fig. 4. Normalized H_2O^+ charge-transfer product populations shown in Fig. 2 are plotted on an asymptotic energy gap scale. The solid line is a nonlinear least squares fit of Eq. (2) yielding $A = 0.38 \pm 0.02$, $\delta = -0.18 \pm 0.02$ eV, and $\gamma = 0.28 \pm 0.09$ eV.

also examined plots in which the experimentally determined populations have been normalized by the corresponding Franck–Condon factors, thus plotting $n(v_2')/\text{FC}(v_2')$, where $\text{FC}(v_2')$ is the respective ionization Franck–Condon factor. The inclusion of Franck–Condon factors, however, greatly enhances the scatter of the data, thus precluding reasonable modeling. We, therefore, conclude that the state-to-state charge-transfer probabilities do not depend strongly on the absolute magnitude of the respective Franck–Condon factors, but that only Franck–Condon active states are subject to Eq. (2). Lee and DePristo [31] have also observed poor correlations between state-to-state cross sections and Franck–Condon factors at low collision energies in semiclassical energy conserving trajectory (SCECT) calculations of isotopic variations of the $\text{H}_2^+ + \text{H}_2$ charge-transfer system.

In the following, the dynamical origin of the observed product state distributions is discussed in order to justify the application of this empirical model to an ion– H_2O system that is more strongly coupled to the $\text{H}_2\text{O}^+ \tilde{X}$ state due to a substantially smaller exothermicity. Charge-transfer transitions are induced by nuclear motion in regions of strong nonadiabatic interaction. In cases where an energy hop occurs, the probability for a nonadiabatic transition is high when the energy uncertainty, $\hbar/\Delta t$, governed by the characteristic interaction time, Δt , is similar or larger than the energy gap. This amounts to the frequently cited Massey adiabaticity criterion [32]. In atomic systems, the only available nuclear motion that can increase the uncertainty of energy levels is translational, and one therefore normally observes a rapidly increasing charge-transfer cross section from near-thermal to hyperthermal collision energies in singly-charged systems, both for exothermic and endothermic transitions [15].

In molecular systems, additional nuclear coordinates are present, most importantly vibrational and angular coordinates. Since the vibrational motion is comparable or faster than

the translational motion at near-thermal energies, the vibrational motion is found to be crucial in inducing charge-transfer transitions in many molecular systems at low collision energies [22]. Nonadiabatic transitions induced by vibrational motion are in part responsible for the fact that exothermic molecular charge-transfer systems normally exhibit a rapidly declining cross section with collision energy at near-thermal energies, opposite to observations of atomic systems. This behavior has also been observed in the present ion–H₂O systems [8–10,13,16].

For the N⁺ and Kr⁺(²P_{1/2})+H₂O systems, Dressler et al. [11] have shown that the reactant zero-point bending vibrational motion negotiates a potential surface crossing with the H₂O⁺(\tilde{A}) product surface, resulting in large charge-transfer probabilities in regions of significant electronic interaction. Due to the strong ion–dipole interaction, the reactant interaction potential is substantially more attractive at long range than the product potential, which is primarily an ion-induced dipole interaction. The energy gap, ΔE , is thus not independent of the interfragment coordinate, as assumed in most energy resonance models. The stronger entrance channel interaction causes the reactant energy levels to decrease with respect to the product levels as the projectiles approach, creating resonances with exothermic product states. The exothermic states can then be efficiently accessed via a curve-crossing mechanism through the bending vibrational motion. The low populations of near-est-resonant states seen in Fig. 2 can be attributed to the fact that resonances with these states occur at very large interfragment distances, where the exchange energy is still very weak.

The observed shift, δ , of the product state distribution with respect to resonance can thus be explained by the strong long-range interaction of the entrance channel in those regions where the nonadiabatic transition probabilities are high. The fact that the optically investigated ion–H₂O systems exhibit similar product state distributions with respect to energy resonance is

consistent with the above interpretation, because the average long-range interaction of the entrance channel is the same for all of these systems. It is thus likely that all of the optically investigated systems are primarily vibrationally coupled at low energies.

Endothermic and quasi-resonant states are not interpreted to be populated through such a mechanism. The energy dependence of endothermic state-to-state cross sections resembles those observed in atomic systems. We thus conclude that these product states are primarily accessed through a translationally induced mechanism, such as that described by Demkov [28]. At collision energies above 100 eV, a translationally coupled mechanism becomes dominant for all product states, and the product state distributions become substantially broader. As the collision energy is further raised, the energy uncertainty associated with the characteristic interaction time becomes comparable to the width of the Franck–Condon envelope, and a Franck–Condon product distribution is then expected [17]. H₂O⁺ \tilde{A} Franck–Condon distributions have been observed in the N₂⁺ and Ar⁺ systems at near keV energies [7]. The transition probabilities associated with translational energy induced charge-transfer thus depend on the absolute magnitude of the respective Franck–Condon factor at high energies, unlike the vibrationally coupled transitions of the presently investigated charge-transfer systems.

Translationally coupled charge-transfer probabilities are not significant at the low collision energies of interest in this work, as evidenced by the weak near-resonant and endothermic product state populations. It is therefore safe to state that the present empirical product state distribution primarily applies to vibrationally coupled product states at energies where collision energy induced broadening is negligible.

The guided-ion beam measurements of the five ion–H₂O systems in Table 1 have similar energy dependences of the integral charge-transfer cross section and almost identical orbiting propensities

[8–10,13]. The latter is determined from the center-of-mass forward scattered signal observed in time-of-flight measurements. The resemblance indicates that the long-range interactions promoting charge-transfer in the $O^+(^4S)+H_2O/D_2O$ systems are comparable to those of the optically investigated ion– H_2O systems and that predominantly vibrationally coupled transitions occur at low energies. This is a reasonable assessment when considering that the formation of both $H_2O^+ \tilde{X}$ and \tilde{A} states involves the ejection of an electron from a H_2O lone-pair orbital, thus implying a strong exchange interaction in an attractive ion–dipole orientation.

Unlike the other ion– H_2O systems, the bending vibrational motion may be assumed inactive in the $O^+(^4S)+H_2O/D_2O$ systems. This is seen in the photoelectron spectrum of H_2O [19–21], where the states observed closest to a resonance shift of $\delta = -0.18$ eV are symmetric stretch and symmetric stretch–bend combination bands of the ground \tilde{X}^2B_1 state. It may thus be assumed that the nuclear motion with respect to the symmetric stretch coordinate induces charge-transfer.

The importance of the symmetric stretch coordinate is verified in Fig. 5, where the asymptotic H_2O/H_2O^+ symmetric stretch and bending potentials are shown for infinitely separated reagents on the absolute energy scales of the $O^+(^4S)+H_2O$ charge-transfer system. The bending curves are calculated for the equilibrium OH bond length of 1.84 a.u. and the symmetric stretch curves are determined for the H_2O equilibrium angle of 105° . The H_2O bending potential is obtained from Bunker and Landsberg [33], while the symmetric stretch curve is from ab initio calculations of Theodorakopoulos et al. [34]. The Renner–Teller H_2O^+ potentials are those of high-level ab initio calculations of Brommer et al. [12]. Pure bending and symmetric stretch vibrational levels of H_2O are indicated for the bending and stretch potentials, respectively. The stretch potentials also include symmetric stretch levels of D_2O , indicated with broken lines. It is readily seen that \tilde{A} state products are not accessible to this system along either coordinate, and that the strongest interaction is in the region where the reactant and product \tilde{X} state

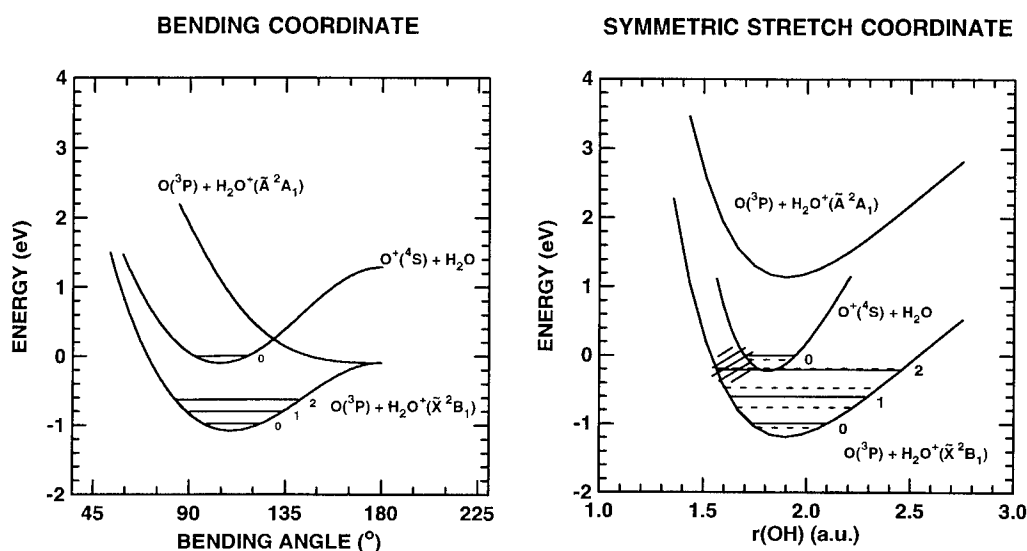


Fig. 5. Asymptotic Born–Oppenheimer potential curves of the $O^+(^4S)+H_2O$ charge-transfer system along the bending and symmetric stretch vibrational coordinates. The potentials are taken from ab initio calculations of Brommer et al. [12], Bunker and Landsberg [33], and Theodorakopoulos et al. [34]. The solid and dashed horizontal lines indicate vibrational levels of H_2O/H_2O^+ and D_2O/D_2O^+ , respectively. The shaded area points out the region of significant charge-transfer interaction.

curves approach to within 0.2 a.u. in the repulsive part of the symmetric stretch potential (cross-hatched area in Fig. 5). In contrast to the curve-crossing situation documented in those ion–H₂O systems that are governed by the bending vibrational motion, this system must undergo a non-adiabatic transition to a classically forbidden region through uncertainty in position, Δr , or momentum, Δp . That such transitions have significant probabilities is indicated by the substantial Franck–Condon factors in this energy regime. We therefore conclude that a vibrationally coupled mechanism is also plausible for the $O^+(^4S) + H_2O$ charge-transfer system and that it is reasonable to apply the same shifted Gaussian to the Franck–Condon active states of this system. This hypothesis is further tested with respect to the $O^+ + H_2O/D_2O$ isotopic differences in the following section.

3.4. Nascent $O^+(^4S) + H_2O/D_2O$ charge-transfer product distributions

The Gaussian distribution derived in the previous section is applied to the $O^+(^4S) + H_2O/D_2O$

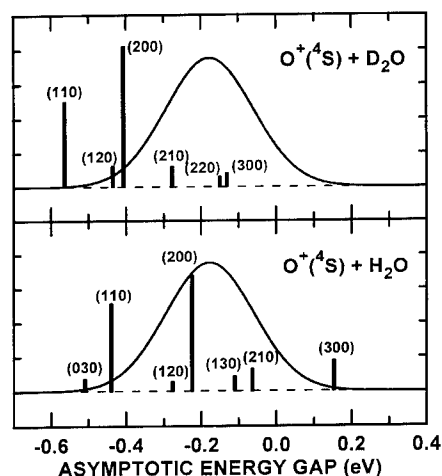


Fig. 6. $O^+(^4S) + H_2O/D_2O$ vibrational energy levels are plotted with respect to the asymptotic energy gap scale. The height of the bars indicates the respective Franck–Condon overlap. States with the observable photoelectron intensity are plotted. The Franck–Condon active states are compared to the Gaussian distribution of Fig. 4.

systems in Fig. 6. The various H_2O^+ and D_2O^+ \tilde{X} state vibrational levels observed either in photoelectron spectroscopic work [21] or in emission studies [35,36] are shown on an asymptotic energy gap scale. The height of the vibrational state bars represent the respective ionization Franck–Condon factors. Energy gaps, Franck–Condon factors and the respective predicted relative nascent H_2O^+ vibrational populations given by the Gaussian distribution are listed in Table 2 for the relevant levels. The table also lists the unnormalized total probabilities obtained from the sum of all probabilities for the two isotopic charge-transfer systems. Comparison of the unnormalized total probabilities yields a predicted H_2O/D_2O charge-transfer cross section ratio of 1.14.

The model predictions are in reasonable agreement with the observed isotope effect (Fig. 3) between 2 and 8 eV. The isotope effect at these hyperthermal energies is thus consistent with the present model. The lack of an isotope effect at collision energies below 1 eV, where

Table 2

H_2O^+/D_2O^+ charge-transfer product vibrational state probabilities, p , given by the Gaussian distribution shown in Figs. 4 and 6. Unnormalized total probabilities obtained from the sum of all probabilities for the two isotopic charge-transfer systems are also shown.

	$\nu_1\nu_2\nu_3$	ΔE (eV) ^a	I_{FC}^b	p
H ₂ O	030	−0.510	0.36	0.007
	110	−0.440	2.57	0.031
	120	−0.277	0.29	0.262
	200	−0.225	3.39	0.346
	130	−0.110	0.43	0.320
	210	−0.064	0.64	0.237
	300	0.153	0.89	0.007
	Total:			1.209
D ₂ O	110	−0.564	2.5	0.002
	120	−0.435	0.61	0.034
	200	−0.407	4.1	0.055
	210	−0.278	0.6	0.260
	220	−0.150	0.3	0.366
	300	−0.131	0.4	0.348
	Total:			1.065

^a Energy gap.

^b Franck–Condon intensities taken from photoelectron spectra [19–21].

longer-lived intermediates are important, may be attributed to the long interaction times associated with orbiting collisions. Several passages through the strong interaction region along the stretch coordinate are then possible during a collision, allowing for multiple nonadiabatic transitions. Charge-transfer probabilities from excited vibrational levels of the reactants as well as vibrational-to-rotational energy transfer then play an important role, and substantial averaging of the predicted differences in state-to-state transitions can thus be expected.

As the collision energy is increased, the isotope effect becomes more pronounced. This may be attributed to an increasing importance of translationally coupled transitions into near-resonant states with substantial Franck–Condon factors in the $O^+(^4S) + H_2O$ system, such as the $H_2O^+ \tilde{X} (200)$ product level. As can be seen in Fig. 6, D_2O^+ levels with large Franck–Condon factors have considerably higher energy gaps and are distant from the maximum of the model distribution. Indeed, if the total probabilities based on the Gaussian distribution are determined with the inclusion of Franck–Condon factors, as would be prescribed by models based on Eq. (1), a substantially higher H_2O/D_2O ratio of 2.5 would be predicted.

The total probabilities have also been determined for the case where all vibrational levels, as calculated by Weis et al. [37], are subject to the determined Gaussian probability distribution of Fig. 4. As a result of the higher density of states in the D_2O system, a H_2O/D_2O ratio of approximately 0.6 would be expected at hyperthermal collision energies, in stark contrast to the experimental observations.

4. Conclusions

The product vibrational state distributions determined for four hyperthermal ion– H_2O charge-transfer systems that produce $H_2O^+ \tilde{A}$ state products can be described by a Gaussian

energy distribution of Franck–Condon active states that is shifted with respect to the ground rovibrational level of the reactants. The distribution has a maximum of -0.18 ± 0.02 eV and a width (FWHM) of 0.28 ± 0.09 eV, signifying a preference of exothermic states. The similarity of all of the distributions with respect to energy resonance is attributed to the long-range dynamics that is primarily governed by the strong long-range interaction of the entrance channel, which is essentially the same for all of the systems. It is concluded that the observed distribution can be applied to primarily vibrationally coupled product states of ion– H_2O systems that charge-transfer efficiently at long range and exhibit large enhancements due to orbiting.

The model distribution is applied to Franck–Condon active vibrational levels of the $O^+(^4S) + H_2O/D_2O$ systems, where population of vibrationally excited levels of the $H_2O^+ \tilde{X}$ state is predicted. The model correctly predicts the measured charge-transfer cross section isotope effect in the hyperthermal collision energy range of 2 and 8 eV. This is the energy range of importance in the environment of low-Earth orbiting spacecraft. The determined $O^+(^4S) + H_2O$ product state distributions can thus be used to calculate infrared luminescence spectra that contribute to spacecraft backgrounds. Examples of such spectra have recently been reported [38].

Acknowledgements

This work is supported by the Air Force Office of Scientific Research under Task 2303EP2.

References

- [1] R.S. Narcisi, E. Trzcinski, G. Federic, L. Wlodyka and D. Delorey, AIAA Pap., 83 (1983) 2659.
- [2] E. Wulf and U. von Zahn, J. Geophys. Res., 91 (1986) 3270.
- [3] R.A. Dressler and E. Murad, In: C.-Y. Ng, T. Baer and I. Powis (Editors), Unimolecular and Bimolecular Ion–Molecule Reaction Dynamics, Wiley Series in Ion Chemistry and Physics, Wiley, New York, Chichester, 1994.

- [4] C.A. Beichman, *Ann. Rec. Astron. Astrophys.*, 25 (1987) 521.
- [5] B.T. Soifer, J.R. Houck and G. Neugebauer, The IRAS view of the extragalactic sky, *Ann. Rev. Astron. Astrophys.*, 25 (1987) 187.
- [6] R.E. Meyerott, G.R. Swenson, E.L. Schweitzer, and D.G. Koch, *J. Geophys. Res.*, 99 (1994) 17 559.
- [7] R.A. Dressler, J.A. Gardner, R.H. Salter and E. Murad, *J. Chem. Phys.*, 96 (1992) 1062.
- [8] R.A. Dressler, R.H. Salter and E. Murad, *J. Chem. Phys.*, 99 (1993) 1159.
- [9] R.A. Dressler and E. Murad, *J. Chem. Phys.*, 100 (1994) 5656.
- [10] S.T. Arnold, R.A. Dressler, M.J. Bastian, J.A. Gardner, and E. Murad, *J. Chem. Phys.*, 102 (1995) 6110.
- [11] R.A. Dressler, S.T. Arnold and E. Murad, *J. Chem. Phys.*, 103 (1995) 9989.
- [12] M. Brommer, B. Weiss, B. Folmeg, P. Rosmus, S. Carter, N.C. Handy, H.J. Werner and P.J. Knowles, *J. Chem. Phys.*, 98 (1993) 5222.
- [13] R.A. Dressler, R.H. Salter and E. Murad, *Planet. Space Sci.*, 40 (1992) 1695.
- [14] J.B. Delos, *Rev. Mod. Phys.*, 53 (1981) 287.
- [15] M.J. Bastian, R.A. Dressler and E. Murad, *J. Chem. Phys.*, 103 (1995) 144.
- [16] X. Li, Y.-L. Huang, G.D. Flesch and C.Y. Ng, *J. Chem. Phys.*, 102 (1995) 5100.
- [17] E.A. Gislason and G. Parlant, *Comments At. Mol. Phys.*, 19 (1987) 157.
- [18] E.A. Gislason, G. Parlant and M. Sizun, *Adv. Chem. Phys.*, 82 (1992) 321 (Part 2), edited by M. Baer and C.Y. Ng, Wiley, New York, 1992.
- [19] R.N. Dixon, G. Duxbury, J.W. Rabalais and L. Åsbrink, *Mol. Phys.*, 31 (1976) 423.
- [20] L. Karlsson, L. Mattsson, R. Jadrny, R.G. Albridge, S. Pinchas, T. Bergmark and K. Siegbahn, *J. Chem. Phys.*, 62 (1975) 4745.
- [21] J.E. Reutt, L.S. Wang, Y.T. Lee and D.A. Shirley, *J. Chem. Phys.*, 85 (1986) 6928.
- [22] S.L. Anderson, T. Turner, B.H. Mahan and Y.T. Lee, *J. Chem. Phys.*, 77 (1982) 1842.
- [23] T. Kato, K. Tanaka and I. Koyano, *J. Chem. Phys.*, 77 (1982) 834.
- [24] Y. Shiraishi and I. Kusunoki, *J. Chem. Phys.*, 87 (1987) 6530.
- [25] I. Kusunoki and T. Ishikawa, *J. Chem. Phys.*, 82 (1985) 4991.
- [26] M.R. Spalburg, J. Los and E.A. Gislason, *Chem. Phys.*, 94 (1985) 327.
- [27] D. Rapp and W.E. Francis, *J. Chem. Phys.*, 37 (1962) 2631.
- [28] Y.U. Demkov, *Sov. Phys. JETP*, 18 (1964) 138.
- [29] N. Rosen and C. Zener, *Phys. Rev.*, 40 (1932) 502.
- [30] T.R. Dinerman and J.B. Delos, *Phys. Rev.*, A15 (1977) 463.
- [31] C.Y. Lee and A.E. DePristo, *J. Chem. Phys.*, 81 (1984) 3512.
- [32] N.F. Mott and H.S.W. Massey, *The Theory of Atomic Collisions*, 3rd ed., Oxford, London, 1965.
- [33] P.R. Bunker and B.M. Landsberg, *J. Mol. Spect.*, 67 (1977) 374.
- [34] G. Theodorakopoulos, I.D. Petsalakis, R.J. Buenker and S.D. Peyerimhoff, *Chem. Phys. Lett.*, 105 (1984) 253.
- [35] H. Lew, *Can. J. Phys.*, 54 (1976) 2028.
- [36] H. Lew and R. Groleau, *Can. J. Phys.*, 65 (1987) 739.
- [37] B. Weis, S. Carter, P. Rosmus, H.-J. Werner and P.J. Knowles, *J. Chem. Phys.*, 91 (1989) 2818.
- [38] R.A. Dressler and E. Murad, *Geophys. Res. Lett.*, 22 (1995) 3457.

Submission of papers (in English, French or German (English is preferred))

Papers should be sent to:

M.T. BOWERS, Department of Chemistry, University of California, Santa Barbara, CA 93106, USA (Fax: +1 805 893 8703)
or to: H. SCHWARZ, Department of Chemistry, Technical University, Strasse des 17. Juni 135, +1 D-10623 Berlin, Germany (Fax: +49 30 3142 1102)
or to: J.F.J. TODD, University Chemical Laboratory, University of Kent, Canterbury, Kent CT2 7NH, UK (Fax: +44 (0) 1227 475475)

Submission of an article is understood to imply that the article is original and unpublished and is not being considered for publication elsewhere.

Upon acceptance of an article by the journal, author(s) will be asked to transfer the copyright of the article to the publisher. This transfer will ensure the widest possible dissemination of information.

Publication

International Journal of Mass Spectrometry and Ion Processes (ISSN 0168-1176). For 1996 volumes 152–162 are scheduled for publication.

Subscription prices are available on request from the publisher.

Subscriptions are accepted on a prepaid basis only and are entered on a calendar year basis. Issues are sent by surface mail except to the following countries where air delivery via SAL (Surface Air Lift) mail is ensured: Argentina, Australia, Brazil, Canada, Hong Kong, India, Israel, Japan, Malaysia, Mexico, New Zealand, Pakistan, PR China, Singapore, South Africa, South Korea, Taiwan, Thailand, USA. For all other countries airmail rates are available upon request. Claims for missing issues must be made within six months of our publication (mailing) date.

Please address all your requests regarding orders and subscription queries to: Elsevier Science B.V., Journal Department, P.O. Box 211, 1000 AE Amsterdam, The Netherlands (Tel: +31 20 5843 642; Fax: +31 20 5803 598).

Reprints

Fifty reprints will be supplied free of charge. Additional reprints (minimum 100) can be ordered at quoted prices. They must be ordered on order forms which are sent together with the proofs.

Advertisements

For rates apply to the publisher.

Subscriptions should be sent to: ELSEVIER SCIENCE B.V., Journals Department, P.O. Box 211, 1000 AE Amsterdam, The Netherlands (Tel: +31 20 5803 911; Telex: 18582).

US mailing notice—International Journal of Mass Spectrometry and Ion Processes (ISSN 0168-1176) is published semi-monthly (except in January when it will appear monthly) by Elsevier Science B.V., Molenwerf 1, Postbus 211, 1000 AE Amsterdam. Annual subscription price in the USA US\$2985.00 (valid in North, Central and South America only), including air speed delivery. Second class postage is paid at Jamaica, NY 11431.

USA POSTMASTERS: Send address changes to International Journal of Mass Spectrometry and Ion Processes, Publications Expediting, Inc., 200 Meacham Avenue, Elmont, NY 11003. Airfreight and mailing in the USA by Publication Expediting.

INSTRUCTIONS TO AUTHORS

Manuscripts

Authors should submit the original and two copies in double-spaced type with adequate margins on pages of uniform size. Manuscripts should be written in English. Instructions for the preparation of compuscripts are available from the publisher.

Acknowledgements and references should be placed at the end of the paper. It is recommended that authors use the nomenclature and symbols adopted by IUPAC (Quantities, Units and Symbols in Physical Chemistry, Blackwell Scientific, Oxford, 1993). See also the IUPAC Recommendations for Symbolism and Nomenclature for Mass Spectrometry, Pure Appl. Chem., 63 (1991) 1541–1566, and reprinted in Int. J. Mass Spectrom. Ion Processes, 142 (1995) 211–240.

Tables should be typed on separate pages and numbered with Arabic numerals in the order in which they are mentioned in the text. All tables should have descriptive titles. The use of chemical formulae and conventional abbreviations is encouraged in tables and figures but chemical formulae should not be used in the text unless they are necessary for clarity. Units of weight, volume, etc., when used with numerals should be abbreviated and unpunctuated (e.g. 2%, 2 ml, 2 g, 2 μ l, 2 μ g, 2 ng, 2 cm, 200 nm).

Figures should be drawn in black, waterproof drawing ink on drawing or tracing paper. Standard symbols should be used in line drawings; the following are available to the typesetter:

○ ⊕ ● × + △ ▲ ◆ ◇ □ ■ ☆ ★ —

Photographs should be submitted as clear black-and-white glossy prints. Figures and photographs should be of the same size as the typed pages. Legends for figures should be typed on a separate page. Figures should be numbered with Arabic numerals in the order in which they are mentioned in the text.

References in text should be numbered (on the line and in square brackets) in the order of their appearance. The reference list at the end of the article should be in numerical order of appearance in the text. Abbreviations of journal titles should conform to those adopted by the Chemical Abstract Service (Bibliographic Guide for Editors and Authors, The American Chemical Society, Washington, DC, 1974). The recommended form for references to journal papers and books is as follows: 1 J.J. Lingane and A.M. Hartley, Anal. Chim. Acta, 11 (1954) 475. 2 F. Feigl, Spot Tests in Organic Analysis, 7th edn., Elsevier, Amsterdam, 1966, p. 516. For multi-author references, all authors must be named, and initials given, in the reference list, although the use of, for example, Smith et al., is desirable in the text. An abstract of not more than 500 words should be provided. It should be a concise and factual description of the contents and conclusions as well as an indication of any new findings. References should be avoided in the abstract if at all possible. If they are necessary, they should be given in full and not included as part of the numbered list. Illustrations (e.g. formulae and schemes which cannot be typeset) should be avoided in the abstract if at all possible.

Detailed suggestions and instructions to authors are published in Int. J. Mass Spectrom. Ion Processes, 154 (1996) 229–234. A free copy of these instructions is available from the publisher on request.

A high-temperature octopole ion guide for measuring absolute cross sections of ion-metal atom reactions

Dale J. Levandier,^{a)} Rainer A. Dressler, and Edmond Murad
Phillips Laboratory, Geophysics Directorate, Ionospheric Effects Division, Hanscom AFB,
Massachusetts 01731-3010

(Received 9 September 1996; accepted for publication 14 October 1996)

We describe in detail a high-temperature octopole/collision cell apparatus for studying ion-molecule reactions involving nonvolatile target species, including metals. The system can be operated at temperatures up to ~ 1200 K and features coaxially heated octopole rods and a heated collision cell in which the vapor of a nonvolatile target material is generated by evaporation from a bulk sample contained therein. The poles are heated independently of the cell and are maintained at a higher temperature to prevent condensation of the sample on the poles. This ensures a well characterized operating temperature that is necessary for absolute cross-section measurements. The apparatus design permits two independent methods for the determination of the target vapor density. The absolute $\text{Na} + \text{N}_2^+$ charge transfer cross section has been measured for collision energies in the range 0.1–2.25 eV. These results represent the first guided-ion beam measurement of an absolute ion-metal atom reaction cross section, and are compared to earlier studies conducted with other methods. © 1997 American Institute of Physics. [S0034-6748(97)02701-9]

I. INTRODUCTION

The importance of gas phase ion-metal atom reactions in accounting for the transport of metal species in the atmosphere and ionosphere has been recognized for many years.¹ The lack of accurate absolute cross sections for such reactions at thermal and hyperthermal collision energies has limited the utility of the models needed for a thorough understanding of these multicomponent environments. Typically, thermal ion-metal atom rate constants are either estimated, extrapolated from higher energy data, or excluded altogether.^{2–5}

The difficulty in obtaining absolute ion-metal atom cross sections is evidenced by the few studies to date. Flowing afterglow experiments⁶ and metal atom beam-ion trap experiments⁷ have provided rate constants at single values of collision energy. Crossed beam studies have yielded the translational energy dependence of charge transfer reactions with Mg and Na.^{8,9} These experiments, however, have inherent difficulties in product ion collection and in neutral beam density determination that are critical for obtaining absolute cross sections. Moreover, for the test system discussed below, extrapolation of the crossed beam data to lower energy resulted in a much larger thermal rate constant than provided by the flowing afterglow work. This lack of agreement indicates that the models for describing charge transfer at collision energies from thermal to a few eV are not satisfactory and points to the need for better measurements in this region.

We describe here a new¹⁰ high-temperature octopole ion guide-collision cell assembly that enables the measurement of absolute integral cross sections for ion-metal atom reactions. The guided-ion beam technique generally has been accepted as the method of choice for obtaining absolute ion-molecule/atom reaction cross sections at hyperthermal

energies. In a guided-ion beam experiment, first implemented by Teloy and Gerlich,¹¹ ion-neutral collisions occur within the confining fields of a radiofrequency (rf) multipole, typically an octopole consisting of eight parallel rods in a circular array on which opposite phases of a rf voltage are applied to adjacent poles. Ions are collected irrespective of scattering angle, thus overcoming the collection efficiency problems of the crossed beam and ion beam-cell experiments.^{12,13} This technique has proven to yield accurate cross sections from near-thermal collision energies to hyperthermal energies exceeding 20 eV.

The guided-ion beam technique relies on introducing the vapor of a target material into a collision cell through which the multipole guides the ions. The currents due to product ions I_{prod} and transmitted reactant ions I_{reac} are monitored and used to derive the reaction cross section via Beer's Law, assuming single collision conditions,

$$\sigma = \frac{I_{\text{prod}}}{(I_{\text{prod}} + I_{\text{reac}})nl}. \quad (1)$$

The target vapor density n and effective interaction length l must be measured in order to determine absolute reaction cross sections. For volatile samples, the target gas density is typically measured using a capacitance manometer. Most experiments to date have, therefore, involved target materials with sufficient vapor pressures at room temperature. Anderson and co-workers¹⁴ have constructed a guided-ion beam experiment in which a nonvolatile sample is heated in an oven collision cell. Absolute cross sections, however, were not obtained since the temperature of the octopole rods was not measured and was lower than that of the cell, thus, precluding the exact determination of the target density from the collision cell temperature. Since a capacitance manometer cannot be used, an absolute measurement relies on deducing the target density from an accurate measurement of the coldest temperature to which the target vapor is exposed in the cell. This requires knowledge of the temperature dependence

^{a)}Also at Orion International Technologies, Inc., Albuquerque, NM 87110;
Electronic mail: levandier@plh.af.mil

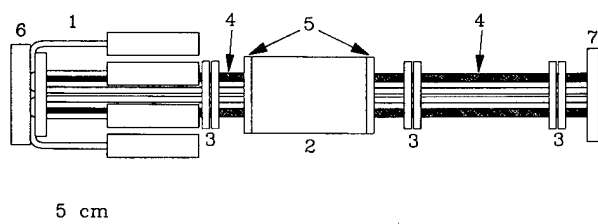


FIG. 1. Scaled diagram of the high-temperature octopole and collision cell assembly. The numbered objects are described in the text.

of the target species vapor pressure. Alternatively, as described below, the vapor density may be measured directly using optical methods.

Sunderlin and Armentrout¹⁵ have developed a system in which both collision cell and rod supports are either heated or cooled with a circulated fluid. That experiment, which relies on temperature equilibrium of the collision cell, rod supports, and poles, was designed primarily to obtain absolute integral cross sections at temperatures below 300 K. Due to the lack of high-temperature, nonconducting fluids, the experiment was limited in the high-temperature range. No measurements have been reported in which nonvolatile samples were investigated.

The device described here represents a novel approach to measuring ion-molecule/atom reaction cross sections at high temperatures in which the nominal temperature of the experiment is well characterized. The design addresses the difficulty in handling metal vapors, *per se*, and deals particularly with the issue of accurate vapor density measurement. The apparatus also permits the investigation of nonvolatile non-metallic targets. The following sections include the description of the new high-temperature octopole ion guide/collision cell apparatus, an account of the operation and characterization of the device, and the discussion of the first ion-metal reaction cross section obtained.

II. DESCRIPTION OF THE HIGH-TEMPERATURE OCTOPOLE/COLLISION CELL APPARATUS

The high-temperature guided-ion beam assembly has been incorporated into an existing tandem mass spectrometer, which is described elsewhere.^{16,17} Briefly, an ion beam is generated by electron impact on a precursor gas emanating from either a continuous effusive source or a pulsed supersonic jet. After passing into a second differentially pumped chamber via a skimmer/lens assembly, the ion beam is turned 90° using a dc quadrupole bender. The beam is accelerated into a Wien velocity filter (Colutron Research Corp.), and the mass-selected ions are then decelerated to the desired energy and injected into the 22.8 cm long high-temperature octopole assembly. While within the ion guide, the ions pass through the target vapor in the heated, 5.4 cm long, tantalum oven collision cell, and the resulting secondary ions as well as the transmitted primary ions are passed into a quadrupole mass filter by an extraction lens assembly. Ions are detected with an off-axis twin-microchannel plate detector (Galileo Electro-optics).

Figure 1 shows a scaled drawing of the high-temperature

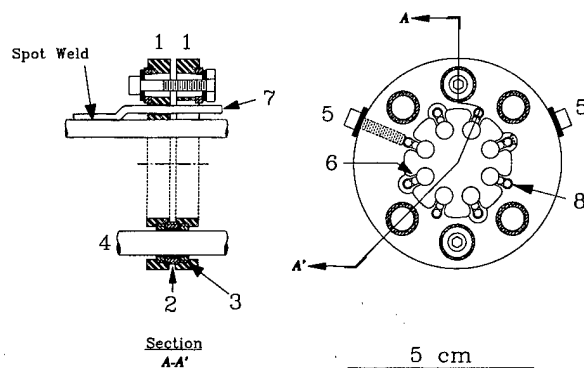


FIG. 2. Scaled diagram of the pole holder assembly. The numbered objects are described in the text. The cut away at the left corresponds to the A-A' line at right.

octopole assembly. The octopole/cell arrangement is designed to allow easy installation and removal from the vacuum chamber and is supported by a stainless steel (SS) injector and a SS and ceramic shield for the extraction lens assembly. The ease of removal and insertion is an important feature for facilitating the replenishment of target material in the oven-cell cavity. Each of the eight poles (1) consists of a 2.4 mm (3/32 in.) diam "biax" heater (ARi Industries, Aerorod BXX Heater), and is arranged in a circular array on a 7.1 mm (0.279 in.) diam included circle. This configuration satisfies the criterion¹² that the optimal confinement field for a circular rod multipole ion guide is obtained when the radius of the circle included by the poles, r_0 , and the pole radius, r_p , are related by

$$r_0 = (n-1)r_p, \quad (2)$$

where n is the number of pairs of poles. Further, the overall dimensions of the circular pole array must be kept as small as possible to minimize target vapor leakage from the oven cell. The "biax" heater design features a pair of nickel-chrome-iron heater wires packed in MgO and encased in an Inconel 600 sheath from which the heater wire is electrically isolated. The twin conductors minimize the magnetic field generated by the heater current, while the heater wire-sheath isolation allows rf voltage to be applied to the heater sheath without interference from the power applied to the heater wires.

Structural support for the tantalum collision cell (2) and for the pole holders (3) is provided by four tantalum support rods (4) attached to either cell end plate (5) and to the injector (6) and extractor (7) end elements. The SS octopole extraction end element, which inserts into the existing extraction lens shield assembly, is cooled with chilled kerosene to avoid exposing the extraction lens to excessive heat. The pole heaters have diameter tolerances of ± 0.13 mm (± 0.005 in.) and comparable tolerances for straightness, however, this should not affect ion confinement significantly.¹²

Figure 2 is a drawing of the pole holder assembly, three of which were included in the design to minimize sagging of the poles at very high temperatures. The heaters are also supported by a MACOR clamp, which holds the heaters against the MACOR injection end element (see Fig. 1). Each

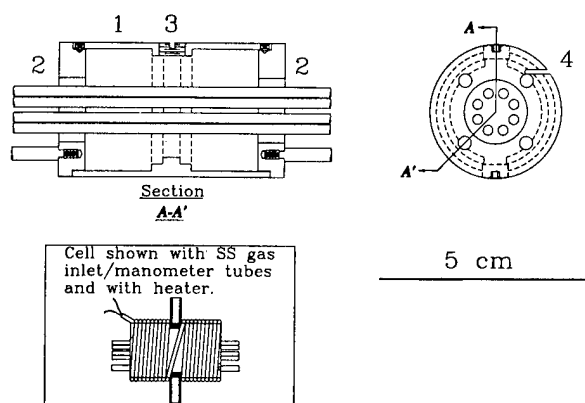


FIG. 3. Scaled diagram of the collision cell assembly. The numbered objects are described in the text. The cut away at left corresponds to the A-A' line at right. The inset shows the cell configured with the gas inlet tubes used for the calibration experiment and with the "biax" cell heater in place.

holder assembly features a pair of identical SS plates (1) arranged so that either plate is in contact with the four poles to which one phase of the rf voltage is applied. The plates are insulated from each other (2) and the support structure (3) with alumina spacers. The alumina spacers serve primarily as electrical insulation, however, the good thermal insulating properties of alumina allow the use of SS plates, as opposed to tantalum ones, since the holder assembly is not directly heated. The holder assemblies can slide freely along the support rods (4), which allows the poles to expand when heated without distorting the octopole. The rf potential is applied to the poles by leads (5) attached to one holder assembly. To avoid affecting the rf potential on the inside of the octopole, the poles are seated on narrow supports (6). The poles are held in place with small 1 mm diam SS hangers (7), which are spot welded to the poles and which penetrate an aperture (8) in each holder. The poles/heaters have two 90° bends at the injection end so that heater leads can be connected. The injector lens extends past the bends in the poles to minimize the effects of fringe fields near the bends.

Figure 3 shows details of the oven cell assembly. The oven cell main body (1), end plates (2) and heat shield (not shown) are made of tantalum, chosen for strength at high temperature, chemical inertness, and ease of machining. The main oven body has two 1/4–20 tapped inlets (3), which are ordinarily plugged by the threaded sample crucibles. As shown in the inset, the cell is wrapped with 2.4 mm "biax" heaters (ARi Industries, Aerobias Cable). The inset also shows the cell configured with 6.4 mm (1/4 in.) SS tubes threaded into the inlets for cell-length calibration using a volatile sample. One tube serves as a sample inlet and the other leads to a capacitance manometer for pressure determination. Tantalum, molybdenum, or tungsten sample crucibles may be used depending on the thermochemical compatibility of the investigated target material. A sample is introduced by placing it in the crucible and screwing the plug into the oven-cell body. The heat shield has a sliding shutter that allows sample introduction without removal of the shield.

Thermocouples for temperature measurement are attached to one cell end plate and to the cell body at a point

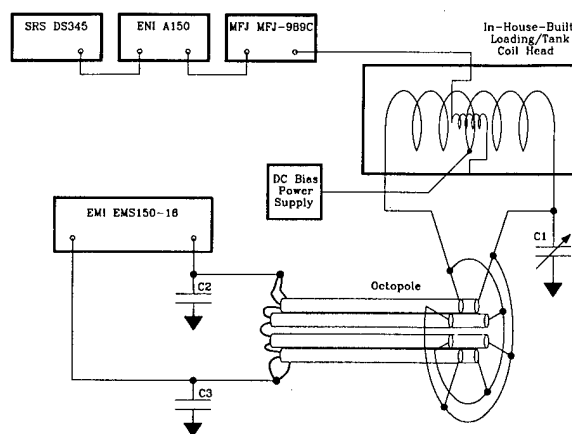


FIG. 4. Schematic of the octopole radiofrequency and heater circuitry. The heaters are connected as two parallel bands of four heaters in series.

near the plug/sample crucible. The main body also has a small blackbody hole (4) for pyrometric temperature determination. The region of the smaller cell bore about the middle of the cell provides the depth required for the sample plug thread and for the blackbody hole.

Standard radioelectronic transmission circuitry is used to generate a rf potential on the poles, a schematic of which is shown in Fig. 4. A function generator (Stanford Research Systems DS345) is used as the rf source. A linear power amplifier (ENI A150) drives a loading coil (in-house design) via an impedance matching network (MFJ Versa Tuner V MFJ-989C). The inductance of the main coil of the antiresonant tank circuit in the test experiments is approximately 0.4 μH , yielding a resonant frequency of 6.4 MHz. A variable capacitor C1 is used to balance the amplitudes of the rf phases. The octopole bias potential is applied to the center of the main coil. The difference between this bias potential and the potential of the ionization region of the ion source determines the ion energy within the ion guide.

The oven-cell heater and poles are heated with two 2500 W power supplies (Electronic Measurements, Inc., EMS300-8 and EMS150-16). Capacitors to ground (C2, C3) protect the pole heater power supply from capacitively coupled rf power, as indicated in Fig. 4. All other potentials are generated with standard dc power supplies and applied to the electrodes via tech-alloy wires insulated with ceramic tubes.

III. HIGH-TEMPERATURE OCTOPOLE OPERATION AND CHARACTERIZATION

The operating characteristics of the high-temperature ion guide have been verified at thermal and elevated temperatures. Proper operating conditions at near-thermal ion energies, as well as the ion beam energy resolution, can be examined by conducting octopole dc potential retardation scans. Figure 5 shows an example of transmitted Ar^+ ion current as a function of octopole dc potential. The collision cell temperature was 619 K and the poles were hotter. A sharp cutoff is observed in the retardation scan at 87.075 V, corresponding to the ion formation potential. At this potential, ions in the octopole have near-zero kinetic energy. The

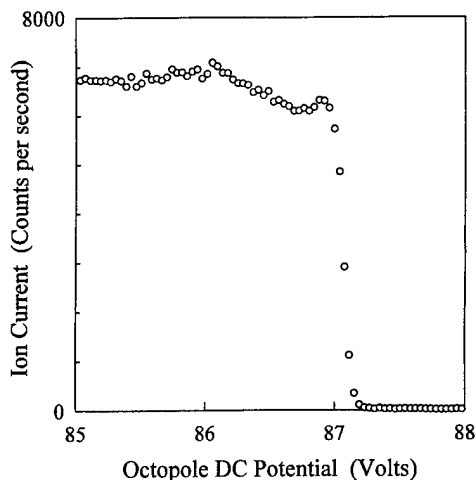


FIG. 5. Primary Ar^+ ion beam current as a function of octopole dc bias potential. The middle of the sharp cutoff corresponds to zero ion kinetic energy, and the steepness, as defined by the 0.0393 V step size, indicates the ion beam energy resolution. The sharp cutoff, and zero current at higher bias voltages indicates that the ions are not being heated by the rf trapping potential.

steepness of the sharp fall-off region represents the energy resolution, which in this case is approximately 120 meV, full width at half-maximum. The good resolution is an indication that the rf potential is not affecting the translational energy distribution of the ions, and that an appropriate trapping frequency for this particular mass has been chosen. To ensure proper operation at hyperthermal energies, the ion beam energy and energy distribution are also determined using time-of-flight (TOF) measurements. TOF measurements are useful for detecting potential barriers in the octopole that cause the cut-off potential in the retardation scan to shift to lower voltages, resulting in an error in the ion beam energy calibration. The barriers are caused by the accumulation of charge on nonconducting material that may derive from reactions with sodium deposits.

The rf frequency must be selected to ensure ion guide operation in the adiabatic regime, in which rf coupling to the oscillatory motions of the ions is minimal. A suitable rf frequency, Ω , is confirmed by considering the adiabaticity parameter¹²

$$\eta = \left(\frac{n-1}{n} \right) \frac{q V_0}{\epsilon} \hat{r}^{n-2}, \quad (3)$$

where

$$\epsilon = \frac{m \Omega^2 r_0^2}{2 n^2}, \quad (4)$$

q is the ion charge, V_0 is the rf voltage amplitude, \hat{r} is the ratio of the radial position r to r_0 , and m is the ion mass. Figure 6 shows that with the current design operating at 6.4 MHz, and $V_0 = 60$ V, Ar^+ ions ($m/q = 40$) satisfy the empirical condition $\eta < 0.3$ typically required for stable behavior.¹²

The effective path length of the high-temperature octopole collision cell is calibrated by measuring the product ion yields from the well-known ion-molecule reaction,

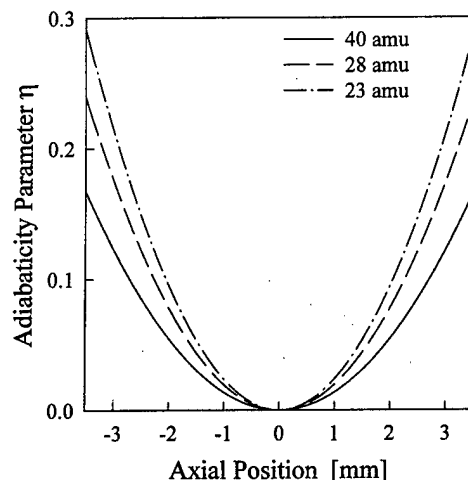
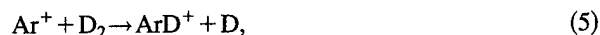


FIG. 6. Plot of the adiabaticity parameter vs position relative to the axis of the octopole operating with 60 V at 6.4 MHz. The extremes in position represent the circle inscribed by the poles, and $\eta \leq 0.3$ corresponds to stable behavior. The curves are shown for Ar^+ (40 amu), N_2^+ (28 amu), and Na^+ (23 amu).



for which the cross section as a function of collision energy has been reported by Ervin and Armentrout.¹⁸ In reaction (5), primary and secondary ions have very similar velocities, making accurate integral cross-section measurements possible with numerous methods. A cross-section measurement using the present instrument at thermal temperatures, with the cell configured for volatile target species, is shown in Fig. 7. The scaled data are compared with the measurements of Ervin and Armentrout (solid line).¹⁸ The scaling procedure yielded the best agreement between the two room tem-

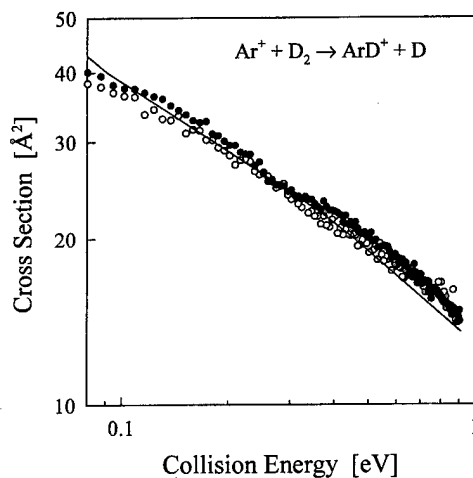


FIG. 7. Collision energy dependence of the $\text{Ar}^+ + \text{D}_2 \rightarrow \text{ArD}^+ + \text{D}$ cross section. The filled circles are the room temperature results in the present instrument, and were used to calibrate the cell by comparison to the results by Ervin and Armentrout (Ref. 18), given by the solid line. The open circles comprise the cross section measured in this work with the system operating at 619 K, after correction for thermal transpiration.

perature data sets when an effective collision cell length of 2.66 cm was used. This corresponds to 50% of the actual collision cell length.

Figure 7 also includes the cross section for reaction (5) measured at 619 K. This cross section confirms both the proper octopole operation at high temperature, and the cell temperature measurement. This conclusion follows from the fact that the density used in calculating the cross section at 619 K must be corrected for the effects of thermal transpiration that arise from the temperature difference between the cell and manometer.^{19,20} For collision cell pressures below 1 mTorr the difference in temperature at the cell and manometer, which are connected by a long tube, results in a pressure gradient. The measured pressure or density must, therefore, be corrected by

$$n_2 = n_1 \sqrt{\frac{T_1}{T_2}}, \quad (6)$$

where n_1 is the density derived from the manometer pressure reading, n_2 is the actual density in the collision cell, and T_1 and T_2 are the temperatures of the cell during calibration and during the given experiment, respectively. This assumes that any difference in manometer and cell temperature during calibration is accounted for in the calibration procedure. With this correction the cross sections measured at low and high temperature are in excellent agreement.

High-temperature measurements of nonvolatile samples are conducted with the sample plugs in place. Product ion formation is monitored while the oven cell and poles are heated. Since the pole temperature cannot be measured while the rf voltage is applied, the temperature versus power dependence of the poles was determined separately using thermocouples spot welded temporarily onto the pole surfaces. The octopole rods are always heated to a temperature that is slightly higher than that of the oven to limit condensation of the sample onto the poles. The cell operating temperature for the target of interest is chosen so that the vapor pressure falls within the range 0.020–0.200 mTorr to limit the beam–target interaction to single-collision conditions while allowing a viable signal level. The materials used in the heater construction limit the operating temperature of the system to ~1200 K.

The current instrument permits at least two independent cell vapor density measurements. The cell temperature, as measured by thermocouple or pyrometer (not presently used), may be related to the known target vapor pressure curve to derive the density. Alternately, the 90° beam bender and off-axis detector provide a line of sight through the collision cell along the ion beam that permits the use of atomic absorption spectrometry to measure the cell vapor density directly. The instrument has been equipped with a tungsten–halogen continuum light source (Ealing Electro-optics), and a 0.18 m spectrograph (Thermo Jarrell Ash) with a liquid nitrogen cooled CCD detector (Princeton Instruments). The vapor density or pressure is recovered from the curve of growth for the transition of interest, which is obtained through integration of the Voigt absorption profile.

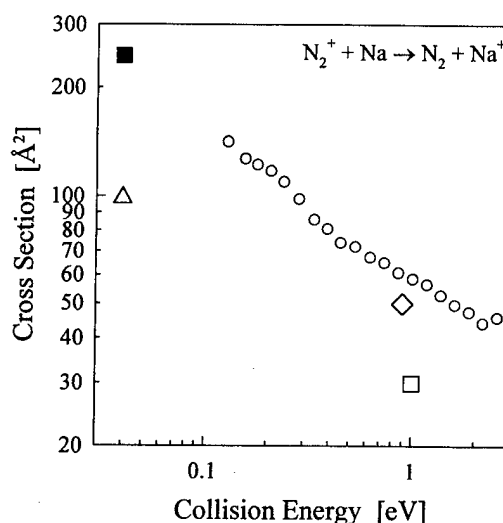
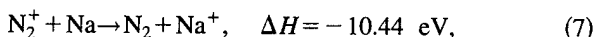


FIG. 8. Cross section for the $N_2^+ + Na \rightarrow Na^+ + N_2$ charge transfer reaction. The open circles are the present work. The other points indicate the results of other experiments, open diamond: ion trap–metal atom beam (Ref. 7); open triangle: flowing afterglow (Ref. 6); open square: crossed beam (Ref. 9). The filled square represents the extrapolation to thermal collision energy in the crossed beam work.

IV. ION–METAL ATOM EXPERIMENTS: $N_2^+ + Na \rightarrow N_2 + Na^+$

Figure 8 is the absolute cross section for the charge–transfer reaction



at collision energies of 0.1–2.25 eV. The present results were averaged from measurements at several temperatures in the range 445–462 K. The N_2^+ ions were produced in the ion source operating with an electron energy ≤ 21 eV to avoid generating metastable states. The cross section has been corrected for a large Na^+ background, usually 25%–50% of the total Na^+ current. The background is observed when no ion beam is present, and can be attributed to thermionic emission of trace sodium in the pole material or of sodium deposited onto the pole surfaces during the course of the experiments. The target density used to derive the cross section was obtained from the vapor pressure curve of sodium.²¹ The measurements were recorded at pressures between 0.031 and 0.085 mTorr ($0.66\text{--}1.78 \times 10^{12} \text{ cm}^{-3}$) for the temperatures used. Error limits on the absolute cross section are estimated to be $\pm 40\%$, however, the data averaged to give the result in Fig. 8 fell within $\pm 10\%$ despite being obtained at different temperatures and, thus, at different densities.

The density was also determined from the sodium D line absorption measurements, an example of which is shown in Fig. 9. The curve of growth calculated for this transition is shown in Fig. 10 and indicates that the densities of interest in this work occur in a region of weak absorption growth with density. Although the absorption measurements yielded densities similar to those derived from the thermocouple/vapor pressure method, the latter results gave more reproducible cross sections for sodium. It is nevertheless conceivable that absorption measurements may prove more accurate than

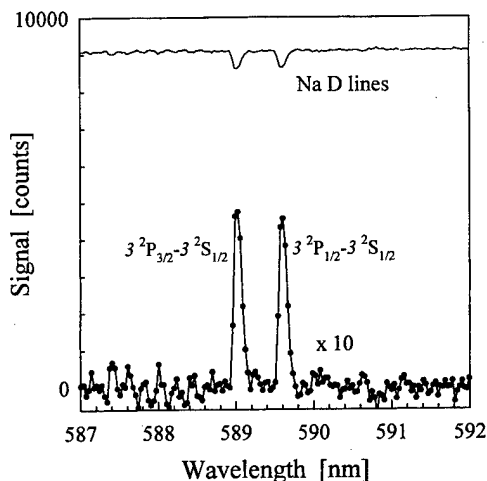


FIG. 9. Absorption spectrum of sodium in the collision cell while the thermocouple reads 462 K. The upper curve (solid line) is the sodium D line absorption spectrum with background subtracted. The lower curve (line with dots) represents the same data subtracted from the lamp intensity. The dots correspond to the CCD pixels; the light was dispersed with a 2400 groove/mm grating. When the density determined by a series of such measurements is compared to the sodium vapor pressure data, a vapor temperature of 454 ± 2.4 K is derived.

the thermocouple/vapor pressure technique for other metal targets, especially when good vapor pressure data are unavailable.

Figure 8 also depicts results of experiments from other laboratories. The best agreement with the current results was obtained in the ion trap-metal atom beam experiment,⁷ however, that technique provides no energy dependence. Agreement with the crossed beam result, shown for 1 eV but which included collision energies from ~ 0.7 to 225 eV, is less satisfactory, however, there is a qualitative similarity in energy dependence.⁹ While the present results do not extend to thermal collision energies, the high-temperature guided-ion beam experiment improves the information in the gap be-

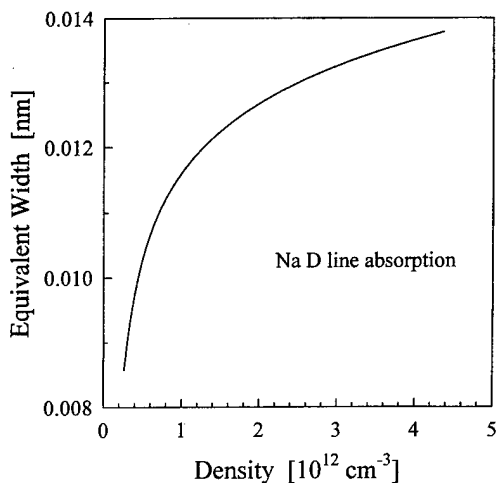


FIG. 10. Curve of growth for the sodium D absorption for range of vapor density needed in this work. The equivalent width is the width of a rectangular absorption line corresponding to complete absorption and having the same area as that of the line profile.

tween thermal and ion beam experiments, as is evident in the comparison of this work with the results of the flowing afterglow study⁶ and of the extrapolation of the crossed beam work.⁹ A more detailed study of the $\text{Na}+\text{N}_2^+$ system is in progress and will be presented later.

V. DISCUSSION

We have developed a high-temperature octopole/collision cell apparatus for studying ion-molecule reactions involving nonvolatile target species. The design features a heated collision cell and heated octopole rods, which allows for a well-characterized operating temperature necessary for absolute cross-section measurements. The system has been operated at temperatures up to ~ 620 K but is capable of operation at temperatures as high as ~ 1200 K, the limit of the heating elements used in the design. The absolute $\text{Na}+\text{N}_2^+$ charge transfer cross section has been measured for collision energies in the range 0.1–2.55 eV. This represents the first guided-ion beam measurement of an absolute ion-metal atom reaction cross section.

ACKNOWLEDGMENTS

The authors wish to thank Dr. Skip Williams for helpful discussions on thermal transpiration/effusion. Fabrication was performed at the Phillips Lab Model Shop, Hanscom AFB (SS) and at Custom Machine, Inc., Woburn, MA (tantalum and MACOR). This work was supported by AFOSR under Task Nos. 2303EP2 and ILIR5PHW018.

- ¹E. E. Ferguson, *Radio Sci.* **7**, 397 (1972).
- ²J. M. C. Plane, *Int. Rev. Phys. Chem.* **10**, 55 (1991).
- ³J. M. C. Plane and M. Helmer, *Res. Chem. Kin.* **2**, 313 (1994).
- ⁴W. J. McNeil, E. Murad, and S. T. Lai, *J. Geophys. Res.* **100**, 16847 (1995).
- ⁵W. J. McNeil, S. T. Lai, and E. Murad, *J. Geophys. Res.* **101**, 5251 (1996).
- ⁶A. L. Farragher, J. A. Peden, and W. L. Fite, *J. Chem. Phys.* **50**, 287 (1969).
- ⁷R. Loch, R. Stengler, and G. Werth, *J. Chem. Phys.* **91**, 2321 (1989).
- ⁸J. A. Rutherford, R. F. Mathis, B. R. Turner, and D. A. Vroom, *J. Chem. Phys.* **55**, 3785 (1971).
- ⁹J. A. Rutherford, R. F. Mathis, B. R. Turner, and D. A. Vroom, *J. Chem. Phys.* **56**, 4654 (1972).
- ¹⁰U.S. patent pending.
- ¹¹E. Teloy and D. Gerlich, *Chem. Phys.* **4**, 417 (1974).
- ¹²D. Gerlich, in *State-Selected and State-to-State Ion-Molecule Reaction Dynamics, Part I. Experiment*, edited by M. Baer and C. Y. Ng (Wiley, New York, 1992), pp. 1–176.
- ¹³J. M. Farrar, in *Techniques for the Study of Ion-Molecule Reactions*, edited by J. M. Farrar and W. H. Saunders, Jr. (Wiley, New York, 1988).
- ¹⁴J. F. Christian, Z. Wan, and S. L. Anderson, *J. Chem. Phys.* **99**, 3468 (1993).
- ¹⁵L. S. Sunderlin and P. B. Armentrout, *Chem. Phys. Lett.* **167**, 188 (1990).
- ¹⁶R. A. Dressler, R. H. Salter, and E. Murad, *J. Chem. Phys.* **99**, 1159 (1993).
- ¹⁷M. J. Bastian, R. A. Dressler, D. J. Levandier, E. Murad, F. Muntean, and P. B. Armentrout (in preparation).
- ¹⁸K. B. Ervin and P. B. Armentrout, *J. Chem. Phys.* **83**, 166 (1985).
- ¹⁹J. C. Maxwell, *Philos. Trans. R. Soc. London* **170**, 231 (1879).
- ²⁰K. F. Poulter, M. J. Rodgers, P. J. Nash, T. J. Thompson, and M. P. Perkin, *Vacuum* **33**, 311 (1983).
- ²¹M. W. Chase, Jr., C. A. Davies, J. R. Downey, Jr., D. J. Frurip, R. A. McDonald, and A. N. Syverud, *J. Phys. Chem. Ref. Data* **14**, Suppl. 1, 1569 (1985).

Low energy collision-induced dissociation and photodissociation studies of the $(\text{N}_2\text{O}, \text{H}_2\text{O})^+$ cluster ion

Michael J. Bastian,^{a)} Rainer A. Dressler, Dale J. Levandier,^{b)} and Edmond Murad
*Phillips Laboratory, PL/GPOC, Hanscom Air Force Base,
Massachusetts 01731-3010*

Felician Muntean and P. B. Armentrout
Department of Chemistry, University of Utah, Salt Lake City, Utah 84112

(Received 13 January 1997; accepted 10 March 1997)

Low energy collision-induced dissociation (CID) and photodissociation measurements of monohydrated nitrous oxide cluster ions are presented. The CID measurements have been conducted with ions produced in both thermal and supersonic jet sources, and with both Ne and Ar as collision gases. In all experiments, H_2O^+ , N_2O^+ , and N_2OH^+ fragments are observed, for which CID thresholds (0 K) of 1.04 ± 0.06 , 1.43 ± 0.12 and 1.32 ± 0.10 eV are determined, respectively. The thermal source experimental thresholds are consistent with all fragment ions originating from a single isomeric precursor ion, $[\text{N}_2\text{O} \cdot \text{H}_2\text{O}]^+$. Whereas both N_2O^+ and N_2OH^+ CID curves are comparable in the thermal source and supersonic jet source experiments, considerable differences are observed in the H_2O^+ CID measurements. The differences are attributed to loosely bound cluster-ion isomeric forms produced in the jet source experiment. In the photodissociation experiments, branching ratios measured with the present jet source are very similar to those observed in previously reported thermal experiments [S. T. Graul, H-S. Kim, and M. T. Bowers, *Int. J. Mass Spectrom. Ion Proc.* **117**, 507 (1992)]. All of the fragment ions can be accounted for by invoking an optical transition from ground state $[\text{N}_2\text{O} \cdot \text{H}_2\text{O}]^+$ to an excited state associated with the $\text{N}_2\text{O} + \text{H}_2\text{O}^+$ (\bar{A}) dissociation limit. The H_2O^+ and N_2O^+ branching ratios are primarily governed by predissociation of the upper state followed by charge-transfer dynamics along a repulsive dissociation coordinate. Formation of N_2OH^+ is postulated to be controlled by a competing internal conversion process that leads to a longer-lived complex that decays to proton transfer products.
© 1997 American Institute of Physics. [S0021-9606(97)00723-X]

I. INTRODUCTION

Neutral clusters possess binding energies that are typically subthermal and therefore must be investigated in cold environments such as supersonic jet expansions. Ionic clusters, however, are readily observed in thermal environments owing to the inherently attractive ion-neutral intermolecular forces. The study of cluster ions offers the possibility to compare directly the isomeric cluster structures favored in equilibrated thermal environments versus the nonequilibrium conditions of supersonic jet expansions. Such comparisons are of interest for models of nonequilibrium media such as spacecraft thruster exhaust gases and associated plasmas. In these environments, it is suspected that metastable polyatomic molecules or clusters are abundant and react more readily with other constituents, thereby releasing large amounts of energy.

Graul, Kim and Bowers¹ recently suggested that two stable isomeric forms of monohydrated nitrous oxide cluster ion, $(\text{N}_2\text{O}, \text{H}_2\text{O})^+$,² are present at thermal equilibrium conditions. In photodissociation experiments coupled with *ab initio* calculations, N_2O^+ and H_2O^+ photodissociation products were attributed to the simple generic association complex

$[\text{N}_2\text{O} \cdot \text{H}_2\text{O}]^+$. The observed N_2OH^+ photofragments were assigned to a proton transfer complex, $\text{N}_2\text{OH}^+ \cdot \text{OH}$. A phase space theory^{3,4} based analysis of the N_2OH^+ kinetic energy release distributions (KERDs) yielded a $\text{N}_2\text{OH}^+ \cdot \text{OH}$ binding energy of 1.2 eV from which a $\text{H}_2\text{O}^+ \cdot \text{N}_2\text{O}$ binding energy of 0.6–0.8 eV was inferred based on the relative *ab initio* energies of the cluster ion structures shown in Figure 1. Given a N_2O proton affinity of 6.0 ± 0.1 eV,^{5–9} the $\text{N}_2\text{OH}^+ + \text{OH}$ dissociation continuum lies approximately 0.2 eV above the $\text{H}_2\text{O}^+ + \text{N}_2\text{O}$ asymptote. Hence, the derived $\text{N}_2\text{OH}^+ \cdot \text{OH}$ binding energy suggested that N_2OH^+ originates from an isomer that is more stable than the association complex by approximately 0.5 eV.

In the present work, we combine collision-induced dissociation (CID) and photodissociation studies of $(\text{N}_2\text{O}, \text{H}_2\text{O})^+$ cluster ions prepared in a supersonic jet expansion in order to examine the effects of nonequilibrium formation conditions on the relative isomeric abundances. In addition, the present work is complemented by CID measurements of cluster ions produced under thermal conditions. Low-energy CID studies with guided-ion beams are a reliable source of dissociation energies for a large number of ions and cluster ions produced in both thermal environments and supersonic jets.^{10–14} This work can be regarded as the first study in which CID onsets of cluster ions observed in supersonic jet and thermal source experiments are compared.

While the photodissociation study of Graul *et al.*¹ was

^{a)}Current address: 128 North Street Apt. #6, Newtonville, Massachusetts 02160.

^{b)}ORION International Technologies, Inc., Albuquerque, New Mexico 87110.

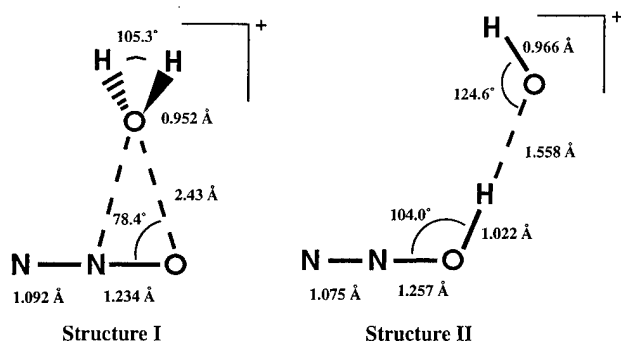


FIG. 1. Schematic representation of the two stable structures for monohydrated nitrous oxide cluster ion as located by the *ab initio* calculations of Graul *et al.* (Ref. 1).

conducted at selected visible wavelengths, the present work presents photodissociation yields from cluster ions produced in a supersonic jet source for a continuous spectral range that covers almost the entire visible spectrum from 425 to 675 nm. The observed photodissociation band shapes yield additional information on the photodissociation mechanism. As will be shown, this information coupled with the CID studies prompts a new interpretation of the experimental observations involving a single isomeric form of the cluster, the association complex, $[\text{N}_2\text{O}\cdot\text{H}_2\text{O}]^+$.

II. EXPERIMENT

A. Supersonic jet source experiments

Cold cluster ions are investigated in a modified guided-ion beam apparatus at the Geophysics Directorate of Phillips Laboratory. A schematic of the experimental apparatus is shown in Figure 2. Cluster ions are produced by association of neutrals with ions formed in a pulsed supersonic jet expansion source similar to that developed by Bieske *et al.*¹⁵

The expansion gas backing pressure is approximately 4 bar and consists of neat N_2O bubbled through distilled and out-gassed water. The gas mixture is expanded through a 0.5 mm diameter orifice in a translatable nozzle. The pulse duration is typically 240 μsec and valve pulse rates of 50 Hz and 30 Hz are used for the CID and photodissociation experiments, respectively.

The gas pulse is crossed by a 45 to 50 eV magnetically confined electron beam to generate seed ions for cluster formation. The extent of clustering is controlled by variation of the distance between nozzle orifice and electron beam, the ion extraction field, and to a lesser extent, the expansion gas backing pressure. High ion extraction fields and low source chamber pressures were found to reduce the formation of protonated cluster ions, i.e. $[\text{H}_3\text{O}\cdot\text{N}_2\text{O}]^+$, presumably because the efficiency of the $\text{H}_2\text{O}^+ + \text{H}_2\text{O} \rightarrow \text{H}_3\text{O}^+ + \text{OH}$ precursor reaction decreases dramatically as the average collision energy increases.¹⁶ Excessively high ion extraction fields, on the other hand, risk heating and dissociating the cluster ions. A 12 V/cm electric field is used to extract the ion beam through a graphite coated skimmer with a 2 mm diameter orifice into a differentially pumped chamber that contains a dc quadrupole bender and associated electrostatic ion lenses. The bender deflects the ion beam onto the axis of a guided-ion beam apparatus which has been described previously.¹⁷ The deflected ion beam is accelerated into a Wien filter assembly for mass selection. The mass-selected cluster ion beam is decelerated and injected into a system of two octopole ion-beam guides in tandem. The collision cell, which encompasses the last 3.5 cm of the first octopole, is at the same dc bias as the first octopole and contains typically 0.04 Pa (0.300 mTorr) of Ar or Ne for the CID studies. The efficient $\text{N}_2\text{O}^+ + \text{Xe}$ charge transfer reaction¹⁸ precluded the use of the common CID target gas, Xe.

The ion-neutral collision energy is varied by changing the dc bias of the octopoles and collision cell with respect to

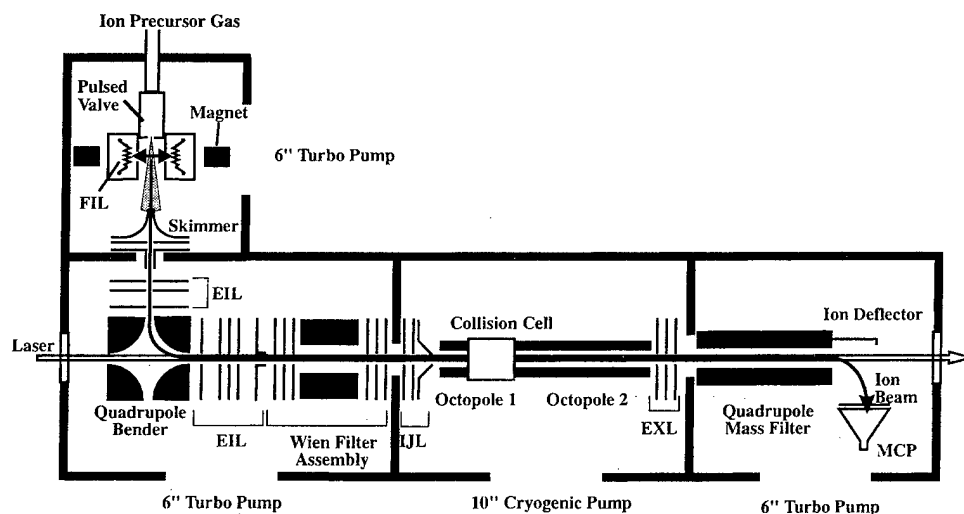


FIG. 2. Schematic of the guided-ion beam apparatus (jet source) employed for the photodissociation and CID investigation of cluster ions formed under supersonic expansion conditions. Abbreviations, FIL: thoriated iridium filament, EIL: electrostatic ion lens, IJL: injection lens, EXL: extraction lens, MCP: multi-channel plate.

the ion source potential which is held constant. Retardation scans of the octopole dc-bias potential are used to determine the axial energy distribution of the primary ion beam which is found to be nearly Gaussian with a FWHM of 0.3 eV. The dc bias potential of the second octopole is held 200 to 400 mV lower than that of the first to collect low kinetic energy product ions. The product and unreacted primary ions are extracted from the second octopole with an electrostatic lens and focused into a quadrupole mass filter. The ions that emerge from the quadrupole are deflected onto a multi-channel plate for detection.

At every collision energy investigated, a mass spectrum is obtained that normally includes both the primary and product ions. The absolute integral product ion cross section, σ_i , in the single collision regime can be determined from,

$$\sigma_i = \frac{I_{\text{prod},i}}{(I_{\text{prim}} + \sum_i I_{\text{prod},i})n\ell}, \quad (1)$$

where I_{prim} is the primary cluster ion signal, n is the number density of the target neutral, $I_{\text{prod},i}$ is the product ion signal of fragment i , and ℓ is the effective length of the primary cluster ion-neutral interaction region. The presence of single collision conditions is established by ensuring that the cross sections of each product ion are independent of n . For the present system, no dependence was observed for any of the product cross sections for target gas pressures below 0.350 mTorr. The absolute accuracy of the integral cross sections are estimated to be $\pm 30\%$. The relative error is substantially smaller.

Although the jet source cluster ions are translationally and rotationally cold, a small fraction, typically 0.1%, are formed with enough internal energy to autodissociate. The autodissociation fraction is independent of electron energy over the range of 25 to 75 eV, but strongly increases with the nozzle orifice-electron beam distance. This latter dependence suggests these fragments primarily originate from direct ionization of neutral clusters. The only autodissociation fragments observed are N_2O^+ and N_2OH^+ , typically in a ratio of 50:1.

In the photodissociation studies, the broadband output of a BBO (beta-barium borate) based Optical Parametric Oscillator (Quanta Ray MOPO 710) pumped by the third harmonic output of a 30 Hz Nd:YAG laser is propagated along the main instrument axis in order to probe mass-selected cluster ions confined by the octopoles. The MOPO output is attenuated with neutral density filters to obtain energies of approximately 0.5 mJ/pulse at a beam diameter of ~ 2.5 mm. The power dependence of photofragment yields is observed to be linear with zero intercept between 0.07 and 0.8 mJ/pulse, verifying operation in a single-photon, linear absorption regime. The valve pulse is triggered off the Nd:YAG laser Q-switch synchronous output. A delay is adjusted to maximize the cluster ion density in the octopoles during the laser shot. Photodissociation action spectra are obtained by recording primary cluster ion, secondary ion, and laser intensities while scanning the OPO wavelength. The cross section for one-photon cluster-ion photodissociation into fragment i , σ_i , is then determined from,

$$\sigma_i = \frac{I_{\text{prod},i}}{(cI_{\text{prim}} + \sum_i I_{\text{prod},i})\Phi}, \quad (2)$$

where Φ is the time integrated photon flux, I_{prim} and $I_{\text{prod},i}$ are as defined previously, and c is the fraction of the primary cluster ions in the octopole during the laser pulse. We ensure that all ions in the octopoles are in the laser field by applying sufficiently high rf amplitudes that the photodissociation yield is independent of the applied rf voltage.

At an octopole transmission energy of 1.0 eV, we determine from the time profile of the primary ion pulse that 82% of all primary ions are in the octopole during the laser pulse. Equation 2 does not account for the possibility that the irradiated cluster ions are in multiple isomeric forms that may possess significantly different photodissociation yields. Thus, the absolute photodissociation cross sections reported here represent a lower bound for a particular isomeric species.

Due to uncertainties in the photon "flux" measurements, Φ , and the ratio c , the absolute photodissociation cross sections possess substantial uncertainties of $\pm 50\%$. The relative photofragment cross sections errors, however, are significantly smaller.

B. Thermal source cluster ion experiments

Thermal cluster ions are investigated at the University of Utah using a guided-ion beam tandem mass spectrometer described in detail elsewhere,^{10,19} so only a brief description is given below. A microwave discharge ion source followed by a flow tube is used to produce the cluster ions.¹⁰ The microwave power supply is operated at 2.45 GHz and 30 W incident power. Helium is used as a flow gas, at 760 standard $\text{cm}^3 \text{min}^{-1}$ flow rate which gives a pressure of about 0.8 mTorr in the flow. The N_2O gas is introduced upstream in the flow tube, about 18 cm from the ion source. The water vapor is introduced downstream, about 70 cm from the ion source. We find that a large excess of N_2O is required to prevent the otherwise preponderant formation of water clusters. In operation, the leak valve admitting water is barely open so that the residual water vapor present in the flow tube is sufficient to form the desired clusters.

By the end of the meter long flow tube, the cluster ions undergo more than 10^4 collisions with the carrier gas, which should thermalize them. The assumption that these ions are in their ground electronic states and that their internal energy distribution is well described by a Maxwell-Boltzmann distribution at ambient temperature (300 K) is supported by the results of many previous studies.¹⁰⁻¹² Following the flow tube, the ions are sampled through a 1 mm aperture, focused through two differentially pumped chambers, and accelerated into a magnetic sector. The mass selected cluster ions are then focused into a radio frequency octopole ion guide¹⁹ which passes through a 8.26 cm long collision cell where collisions with Ar or Ne take place. The pressures of these gases are about 0.013 Pa (0.10 mTorr) in the collision cell, low enough to ensure single collision conditions. This was verified by taking data at several different pressures between 0.07 and 0.15 mTorr and observing no pressure effect on the

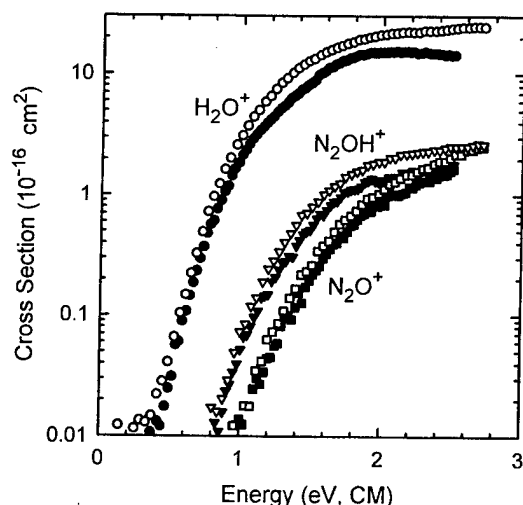


FIG. 3. Comparison between the center-of-mass collision energy dependencies of product cross sections for the $(\text{N}_2\text{O}, \text{H}_2\text{O})^+$ CID using Ar (open symbols) and Ne (black symbols) in the thermal source experiment.

resultant cross sections. Once extracted from the octopole, the product and unreacted primary ions are mass analyzed using a quadrupole mass sector and then detected with a Daly-type detector¹⁹ and standard counting electronics.

The interaction energy is controlled by varying the dc voltage on the octopole and collision cell with respect to the ion source. The actual reactant ion energy and its distribution are measured using the octopole as a retarding field analyzer.¹⁹ The cluster ion energy distributions were found to be nearly Gaussian with full width at half maximum of around 0.3 eV. The overall uncertainty in determining ion energies is estimated to be 0.05 eV lab.¹⁹ As in the supersonic CID experiments described in Section II A, lab frame energies are converted to center-of-mass (CM) energies using the stationary target approximation: $E_{\text{CM}} = E_{\text{lab}} \cdot m/(m+M)$, where m and M are the masses of the neutral and primary ion, respectively. Reaction cross sections are determined from ion intensities and pressure readings as described in Section II A. The overall uncertainties in the absolute cross sections are estimated to be $\pm 20\%$.

III. RESULTS

A. CID measurements

The same fragment ions observed in the photodissociation experiments of Graul *et al.*¹ (H_2O^+ , N_2O^+ and N_2OH^+) are detected in the present low energy CID experiments of monohydrated nitrous oxide cluster ions. The energy dependence of the thermal source cluster-ion CID cross sections with Ar and Ne are shown on a logarithmic vertical scale in Figure 3. The absolute values of the Ar CID cross sections are slightly larger than those for Ne, as anticipated given the larger size and mass of the Ar atom.

Dissociation thresholds are extracted from the CID data by convoluting an assumed functional form of the energy dependent CID cross section (3) with relative kinetic energy

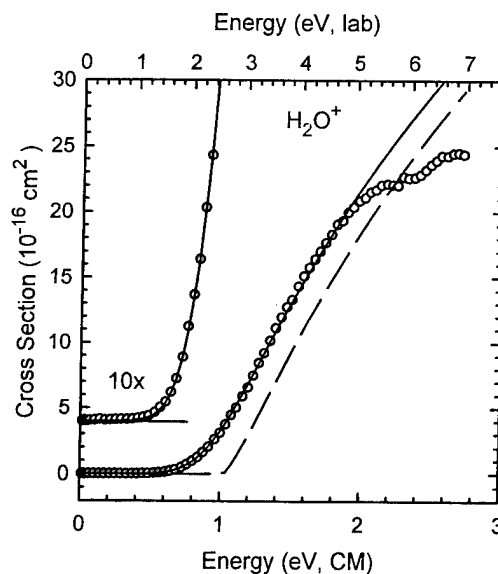


FIG. 4. Cross sections (open circles) and fit lines for the H_2O^+ product of the CID of $(\text{N}_2\text{O}, \text{H}_2\text{O})^+$ with Ar, obtained in the thermal source experiment, as a function of energy in the center-of-mass frame (lower axis) and laboratory frame (upper axis). The dashed line shows the best fit to the data using the model of Equation 3 with parameters listed in Table I, for the reactants with an internal temperature of 0 K. The solid lines show this model convoluted over the internal and kinetic energy distributions of the reactants.

distributions. The parameters of the model cross section function are then adjusted to reproduce the experimental data, as demonstrated in Figures 4 and 5. We employ the frequently used modified line-of-centers functional form,^{12,20}

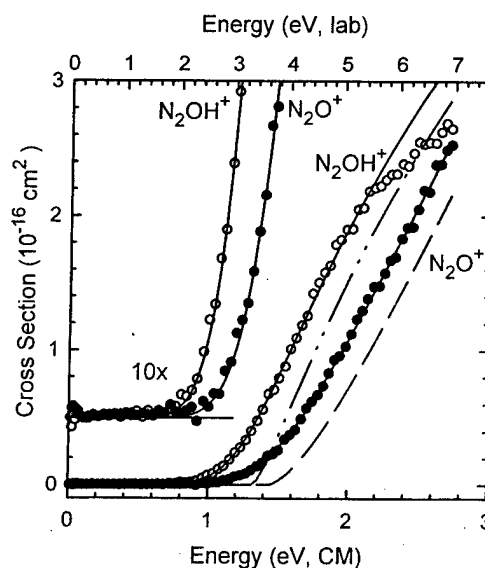


FIG. 5. Cross sections (symbols) and fit lines for the N_2O^+ and the N_2OH^+ channels of the CID of $(\text{N}_2\text{O}, \text{H}_2\text{O})^+$ with Ar, obtained in the thermal source experiment, as a function of energy in the center-of-mass frame (lower axis) and laboratory frame (upper axis). The dashed lines show the best fit to the data using the model of Equation 3 with parameters listed in Table I, for the reactants with an internal temperature of 0 K; the solid lines show this model convoluted over the internal and experimental kinetic energy distributions of the reactants.

TABLE I. Vibrational frequencies for the $[\text{N}_2\text{O} \cdot \text{H}_2\text{O}]^+$ cluster ion, used in the analysis of the CID product cross sections.

Ion	Frequencies ^a (cm^{-1})											
$[\text{N}_2\text{O} \cdot \text{H}_2\text{O}]$	111.3	177.5	237.5	420.0	424.3	443.2	524.2	1056.1	1843.3	2184.8	4031.5	4126.7

^aComputed by Graul (Ref. 21).

$$\sigma(E) = \sigma_0 \sum_i g_i \frac{(E + E_i - E_0)^n}{E}, \quad (3)$$

to model the CID cross section energy dependence, where σ_0 is a scaling parameter, E_0 is the dissociation threshold, n is a curvature parameter, and E is the relative kinetic energy available for reaction. The sum is over the rovibrational states of the reactant, with energies E_i and populations g_i .

The analysis of the CID cross sections includes the internal energy of the reactant ions in Equation 3 as described in previous papers.¹¹ Therefore, the thresholds obtained correspond to 0 K values. Vibrational frequencies for the cluster ion were computed by Graul *et al.*²¹ The values are presented in Table I after scaling by 89%, according to their suggestion. These values correspond to the $[\text{N}_2\text{O} \cdot \text{H}_2\text{O}]^+$ isomer, which is believed to represent the primary isomer present experimentally, as discussed further below. If the internal energy of the cluster ions is neglected in the analyses, the measured thresholds shift to lower energies by about 0.13 eV. This value corresponds to the computed average internal energy of the reactant ions at 300 K.

A RRKM calculation was also performed in our analysis of the thermal source cluster ion data to assess the importance of kinetic shifts.²² We assumed a tight transition state, with molecular parameters estimated simply by deleting the reaction coordinate frequency (443.2 cm^{-1}) from the vibrations of the cluster ion. This tight transition state should give the largest possible kinetic shift, an overestimate of any likely effect. The values obtained differ from our analyses without the RRKM calculation by less than 0.02 eV, which is negligible compared to other experimental uncertainties.

Table II lists the optimum fit parameters for each product channel obtained from analysis of the thermal source data. These parameters represent averages of several data sets taken over a period of several days. The uncertainties listed include the effect of changing the range of energies analyzed, the scaling factor for the frequencies (from 89% to 80% and to 100%) and the uncertainty in the energy scale

(0.05 eV lab). Considering the uncertainties in the measurements, the absolute values of the dissociation thresholds determined for Ar and Ne are in excellent agreement. The threshold values used in the discussion: 1.04 ± 0.06 , 1.43 ± 0.12 and 1.32 ± 0.10 eV for the H_2O^+ , N_2O^+ and N_2OH^+ fragments respectively, represent weighted averages of the Ar and Ne data. The weights are the inverse squares of the uncertainties for the Ar and Ne data, respectively. The reported uncertainties represent two standard deviations of the averaged thresholds.

The CID cross sections observed in the jet source experiment are shown in Figures 6, 7 and 8. The jet source N_2O^+ and N_2OH^+ CID cross sections shown in Figures 6 and 7 have been corrected for the observed autodissociation described in Section II A. The H_2O^+ cross section measurements of the jet source cluster ions (Figure 8) exhibit substantial signal below the onset observed in the respective thermal experiments. The low energy tail is independent of the nozzle orifice-electron beam distance and the electron energy over the range of 25 to 75 eV. We associate this phenomenon with higher energy cluster ions, the possible identity of which is discussed in Section IV.

The CID cross sections of the thermal source experiment (Figure 3) are significantly higher than those of the jet source experiment at higher collision energies. It is not clear whether the differences can be attributed only to systematic errors in the experiments or whether the source conditions dictate the differences. However, the product branching ratios, shown in Figure 9, are essentially the same.

The solid lines shown in Figures 7, 8 and 9 are calculated CID curves in which only σ_0 of Equation 3 was adjusted while using the parameters E_0 and n of the respective thermal source measurements (Table II), thus providing a direct comparison between the two experiments. There is an excellent agreement between the thermal and jet source experiments in the N_2O^+ and N_2OH^+ yields, except for some residual pre-threshold signal in the Ne CID data of the jet source experiments. The latter may be due to residual vibra-

TABLE II. Dissociation thresholds, E_0 , determined in the thermal source CID experiments and binding energies, E_b , determined by Graul *et al.* (Ref. 1) for fragmentation of the monohydrated nitrous oxide cluster ion.

Product	Ar CID		Ne CID		Graul <i>et al.</i>
	E_0	n	E_0	n	
H_2O^+	1.06 ± 0.04	1.34 ± 0.11	1.00 ± 0.06	1.66 ± 0.38	$0.6 \text{ to } 0.8^a$
N_2O^+	1.39 ± 0.08	1.83 ± 0.16	1.48 ± 0.09	1.70 ± 0.34	—
N_2OH^+	1.32 ± 0.07	1.33 ± 0.20	1.33 ± 0.08	1.45 ± 0.32	1.2^b

^aDetermined from the N_2OH^+ parent cluster binding energy and the relative energies of *ab initio* cluster structures I and II.^bDetermined from phase space theory simulation of N_2OH^+ kinetic energy release data. Uncertainty in the N_2OH^+ E_b value was not reported.

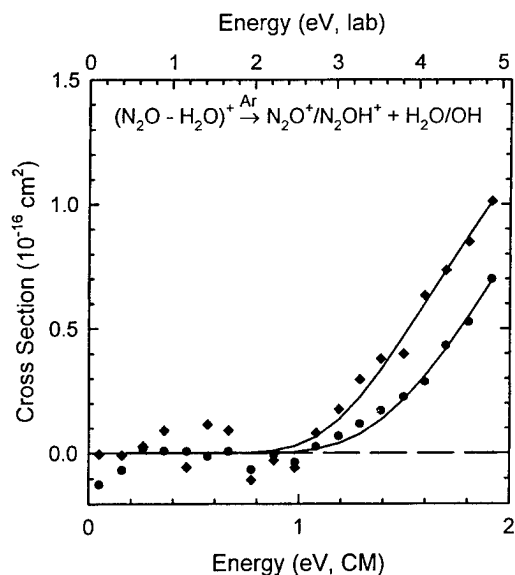


FIG. 6. Jet source CID cross sections for production of N_2O^+ (closed circles) and N_2OH^+ (closed diamonds) in collisions with Ar. Solid lines are calculated CID curves using the parameters of Equation 3 determined in the thermal experiments listed in Table I.

tional excitation energy in the expansion conditions. The thermal source fit parameters, however, clearly fail to reproduce the H_2O^+ CID cross sections of the jet source experiments. These have a substantial low-energy tail that affects the cross section curvature far above the threshold observed in the thermal source experiment. However, it is straightforward to reproduce the jet source cross sections for H_2O^+ by summing the model for the thermal source (with only the

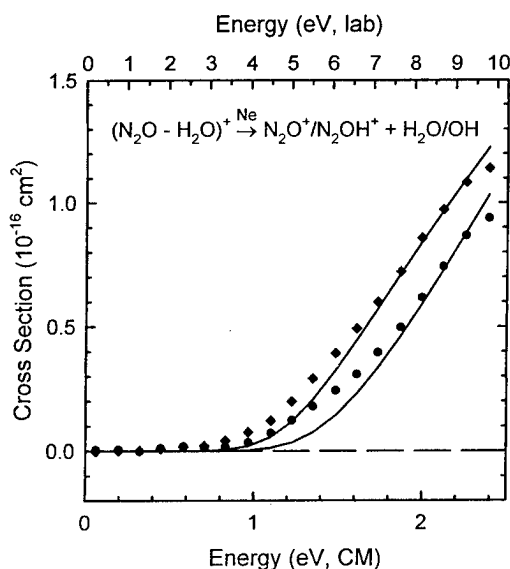


FIG. 7. Jet source CID cross sections for production of N_2O^+ (closed circles) and N_2OH^+ (closed diamonds) in collisions with Ne. Solid lines are calculated CID curves using the parameters of Equation 3 determined in the thermal experiments listed in Table I.

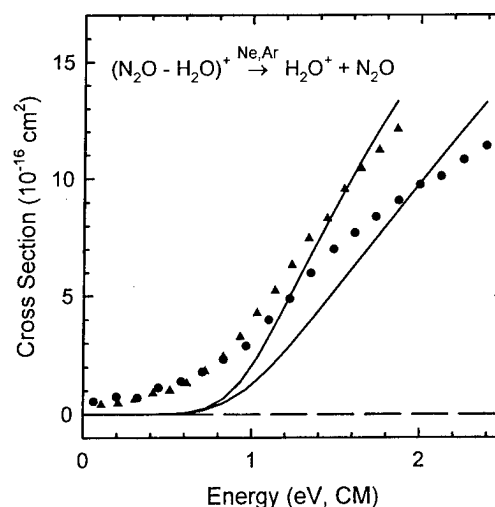


FIG. 8. Jet source CID cross sections for production of H_2O^+ in collisions with Ar (closed diamonds) and Ne (closed circles). Solid lines are calculated CID curves using the parameters of Equation 3 determined in the thermal source experiments listed in Table I.

value of σ_0 allowed to vary) with one for the low energy tail ($\sigma_0=2$, $E_0=0$ eV, $n=2$). This is shown in Figure 10 for the CID with Ne.

B. Photodissociation measurements

The photon energy dependence of photodissociation cross sections between 15 000 and 23 500 cm^{-1} (425 to 670 nm) is shown in Figure 11 for cluster ions produced in the jet source experiment. The H_2O^+ and N_2O^+ cross sections are sizable, with maxima on the order of 0.03 \AA^2 , while those of

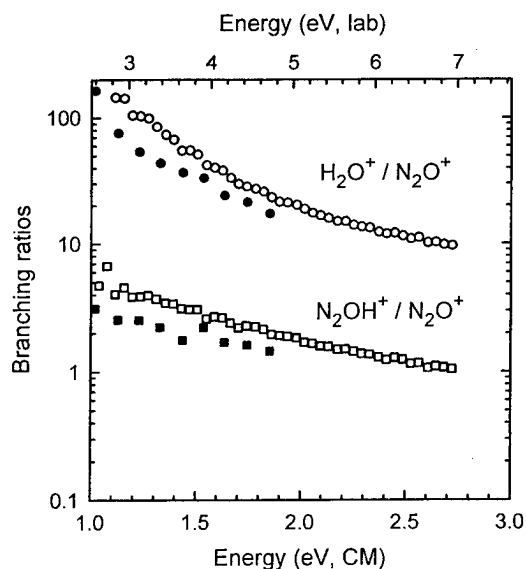


FIG. 9. Branching ratios between product cross sections of the $(\text{N}_2\text{O}, \text{H}_2\text{O})^+$ CID with Ar, as a function of the collision energy in the center-of-mass frame (lower axis) and laboratory frame (upper axis), for the thermal source (open symbols) and the supersonic jet source (closed symbols) experiments.

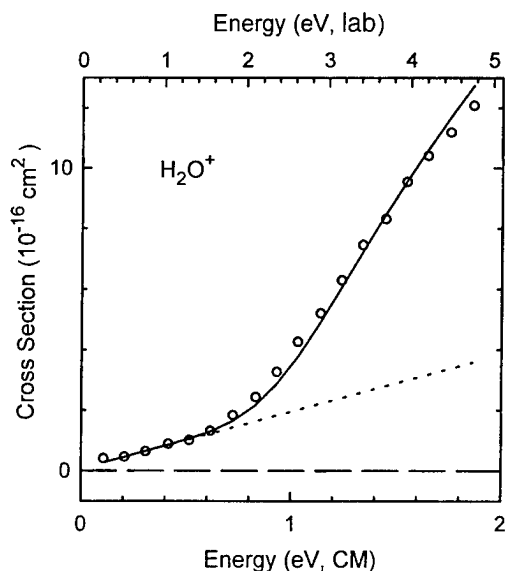


FIG. 10. Two-threshold model fit of the H_2O^+ cross sections in $(\text{N}_2\text{O}, \text{H}_2\text{O})^+$ CID with Ne using the jet source experiment. The fit is obtained using the thermal source data listed in Table I ($E_0 = 1.04$ eV, $n = 1.3$) and a low energy threshold of $E_0 = 0$ eV, $n = 2$.

the N_2OH^+ photofragment are substantially smaller. The H_2O^+ and N_2O^+ photodissociation band shapes are very similar, with the $\text{N}_2\text{O}^+:\text{H}_2\text{O}^+$ ratio increasing slightly with photon energy (approx. 1 at $15\,000\text{ cm}^{-1}$ and 1.4 at $22\,000\text{ cm}^{-1}$).

The N_2OH^+ photodissociation band is also broad but distinctly different from the H_2O^+ and N_2O^+ bands, peaking at a considerably lower photon energy of $\sim 16\,800\text{ cm}^{-1}$. The laser linewidth is such that vibrational structure in the photodissociation bands could be resolved; however, no reproducible structure is observed in any of the bands. The

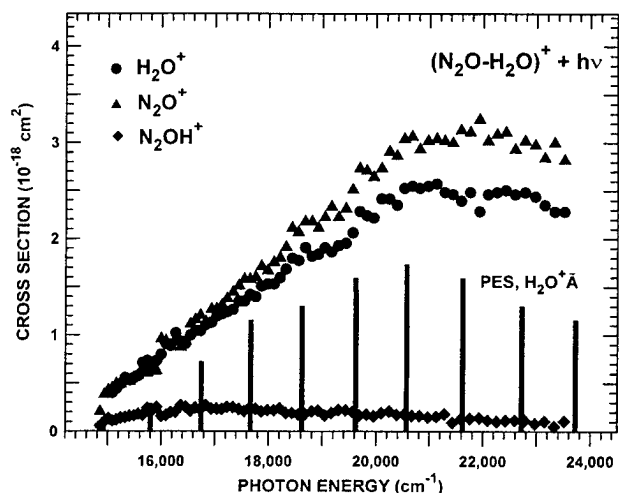


FIG. 11. Photodissociation cross sections of $(\text{N}_2\text{O}, \text{H}_2\text{O})^+$ cluster ions produced in the jet source experiment. The H_2O^+ and N_2O^+ action spectra are compared to relative bending vibrational intensities of the H_2O^+ (\tilde{A}) state photoelectron band shifted to higher energy by 2420 cm^{-1} .

present photodissociation $\text{N}_2\text{O}^+:\text{H}_2\text{O}^+:\text{N}_2\text{OH}^+$ branching ratios at $\sim 488\text{ nm}$ ($\sim 20\,490\text{ cm}^{-1}$) are 0.51:0.43:0.06. These ratios agree well with those of 0.60:0.35:0.05 found at this wavelength in the previous thermal source experiments.¹

IV. DISCUSSION

As pointed out by Graul *et al.*,¹ the $(\text{N}_2\text{O}, \text{H}_2\text{O})^+$ cluster ion exhibits peculiarities that make it an interesting candidate for structural studies. First, the $[\text{N}_2\text{O} \cdot \text{H}_2\text{O}]^+$ cluster ion is expected to exhibit considerable charge sharing because the ionization energies of N_2O and H_2O differ by only $0.27 \pm 0.01\text{ eV}$. Although H_2O^+ is more stable than N_2O , the much larger dipole moment of H_2O is likely to stabilize a $\text{N}_2\text{O}^+ \cdot \text{H}_2\text{O}$ structure. The *ab initio* calculations of Graul *et al.* indicate that the N_2O moiety retains a larger fraction of the charge. Recent density functional calculations by Stevens and Morokuma, however, suggest complete charge sharing.³⁰ Second, the relatively low proton affinity of N_2O of $6.0 \pm 0.1\text{ eV}$ (Refs. 5–9) is very similar to the OH proton affinity of $6.10 \pm 0.02\text{ eV}$.⁵ Therefore, it is reasonable that a stable proton-transfer complex, $[\text{N}_2\text{OH}^+ \cdot \text{OH}]$, could coexist with a $[\text{N}_2\text{O} \cdot \text{H}_2\text{O}]^+$ isomeric form at thermal conditions.

In their photodissociation studies of thermal source $(\text{N}_2\text{O}, \text{H}_2\text{O})^+$ cluster ions, Graul *et al.*¹ suggested that the $[\text{N}_2\text{O} \cdot \text{H}_2\text{O}]^+$ isomeric form is the origin of the observed N_2O^+ and H_2O^+ photofragments and $[\text{N}_2\text{OH}^+ \cdot \text{OH}]$ is the precursor ion of the N_2OH^+ fragment ions. Their interpretation was based on kinetic energy release measurements of the photofragment ions. The anisotropic and high kinetic energy release observed in the N_2O^+ and H_2O^+ dissociation products was attributed to photodissociation involving a common repulsive upper state surface of the $[\text{N}_2\text{O} \cdot \text{H}_2\text{O}]^+$ isomeric form which correlates with the N_2O ($\tilde{X}^1\Sigma^+$) + H_2O^+ (\tilde{X}^2B_1) dissociation limit. In order to reconcile that two ionic fragments stem from the same repulsive surface, an avoided crossing was invoked with the ground state surface that correlates with the N_2O^+ ($\tilde{X}^2\Pi$) + H_2O (\tilde{X}^1A_1) asymptotic limit. This is schematically depicted in Figure 12. Graul *et al.* attributed the low, near-statistical, kinetic energy release observed for $\text{N}_2\text{OH}^+/\text{OH}$ dissociation products to a long-lived upper bound state associated with the $[\text{N}_2\text{OH}^+ \cdot \text{OH}]$ isomeric form.

The presence of the $[\text{N}_2\text{O} \cdot \text{H}_2\text{O}]^+$ isomeric form is clearly confirmed by the present CID measurements. The difference between the extracted threshold energies for the N_2O^+ and H_2O^+ products is $0.39 \pm 0.13\text{ eV}$. This value is close to thermochemical predictions for the energy difference of the asymptotic limits, $0.27 \pm 0.01\text{ eV}$. This supports the interpretation that these two products originate from the same precursor structure. The cluster-ion binding energy of $1.04 \pm 0.06\text{ eV}$, however, is considerably higher than the $0.6\text{--}0.8\text{ eV}$ derived in the work of Graul *et al.* Part of this difference can be attributed to the internal energy of the clusters, 0.13 eV , when thermalized to 300 K , which was not explicitly accounted for in the estimate of Graul *et al.* It is also possible that the cluster ions in the previous experiment are not as thoroughly thermalized as is possible in our flow tube ion source.

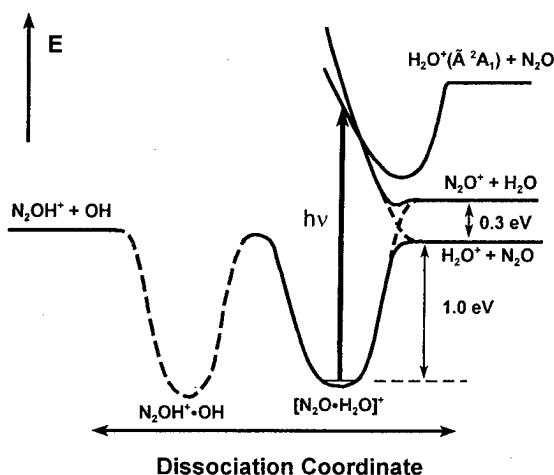


FIG. 12. Schematic potential surfaces relevant to the photodissociation of structure I. Ground electronic state species are assumed unless specified. The hypothetical potential well associated with Structure II (Figure 1) of the model suggested by Graul *et al.* (Ref. 1) is included for comparison.

The present photodissociation studies of cluster ions formed in a supersonic jet expansion provide product branching ratios that are similar to those observed by Graul *et al.* The observed photodissociation band shapes provide additional insight into the photodissociation mechanism. The almost identical photodissociation band shapes observed in the H_2O^+ and N_2O^+ action spectra further demonstrates that these products originate from the same optical transition, and are most likely the products of direct dissociation from the isomeric form, $[\text{N}_2\text{O} \cdot \text{H}_2\text{O}]^+$. In Figure 11, the H_2O^+ and N_2O^+ photodissociation bands are compared to the H_2O^+ \tilde{A} state photoelectron band,^{23–25} the structure of which is almost exclusively attributable to bending vibrational structure. The photoelectron band compares well with the observed photodissociation band shape after shifting the lines to higher photon energies by 2420 cm^{-1} (0.3 eV). The excellent comparison invokes a refined photodissociation mechanism involving a photo-induced charge-transfer transition from $[\text{N}_2\text{O} \cdot \text{H}_2\text{O}]^+$ to a temporarily bound upper state correlating with N_2O ($\tilde{X}^2\Pi$) and H_2O^+ (\tilde{A}^2A_1) dissociation fragments. The 2420 cm^{-1} shift indicates that the excited cluster ion has a shallower well depth than the ground state cluster ion. This is reasonable considering the substantially weaker ion-dipole interaction of an ion with N_2O versus that with H_2O .

If the H_2O^+ and N_2O^+ photodissociation band shapes are in fact due to a photo-induced charge-transfer transition to a $\text{N}_2\text{O}(\text{H}_2\text{O}^+, \tilde{A})$ complex, considerable bending vibrational excitation of the H_2O moiety may be assumed in the upper state of the cluster ion. This predissociation mechanism could still be consistent with the high kinetic energy release observed by Graul *et al.*, if the bending vibrational motion couples strongly to the repulsive surface, $\text{N}_2\text{O} \cdot (\text{H}_2\text{O}^+ \tilde{X})$. An upper state lifetime on the order of a vibrational period is consistent with the fact that no predissociative vibrational structure can be resolved. Evidence for

enhanced coupling of $\text{H}_2\text{O}^+ \tilde{A}$ and \tilde{X} states in the presence of a second body has been observed in ion+ H_2O charge-transfer studies,^{26–28} where efficient quenching of H_2O^+ (\tilde{A}) ions has been postulated in intimate collisions. In that work, long-range near-resonant charge-transfer transitions are observed to provide intense H_2O^+ ($\tilde{A} - \tilde{X}$) luminescence. No luminescence is detected that can be attributed to collisions that proceed through longer-lived intermediates and result in substantial energy transfer, despite clear evidence of such events in the observed scattering dynamics. The strong Renner-Teller interaction that couples $\text{H}_2\text{O}^+ \tilde{A}$ and \tilde{X} states along the bending coordinate is believed to be the rationale for the efficient quenching of $\text{H}_2\text{O}^+(\tilde{A})$.

The present model can also account for the slight increase in N_2O^+ branching ratio with photon energy. As suggested by Graul *et al.*, the dissociating cluster ion traverses a region of strong charge-transfer interaction at long range, and the $\text{N}_2\text{O}^+/\text{H}_2\text{O}^+$ branching ratios are governed by the respective charge-transfer dynamics. As the photon energy is increased, the present model predicts that the translational motion increases with respect to two nuclear coordinates, the cluster dissociation coordinate and the H_2O bending coordinate. If the charge-transfer transition is coupled by the nuclear motion with respect to the dissociation coordinate, an increase in the H_2O^+ branching ratio with photon energy would be expected, contrary to the observations. In a vibrationally coupled transition, however, a transition from the $(\text{H}_2\text{O}^+)\text{N}_2\text{O}$ to the $\text{H}_2\text{O}(\text{N}_2\text{O}^+)$ surface would be facilitated by excitation of the appropriate vibrational mode. Assuming that a significant fraction of the nascent upper-state bending vibrational motion is preserved on the repulsive surface, a vibrationally mediated charge-transfer transition can explain the increase in N_2O^+ branching ratio with photon energy. Such a mechanism is consistent with previous ion+ H_2O charge-transfer studies where it has been demonstrated that vibrational coupling is predominant at low collision energies.²⁸

The present work generally agrees with the interpretation of Graul *et al.*¹ as it pertains to the $\text{H}_2\text{O}^+/\text{N}_2\text{O}$ and $\text{H}_2\text{O}/\text{N}_2\text{O}^+$ dissociation channels. In contrast, our work does not provide corroborating evidence for their explanation of the $\text{N}_2\text{OH}^+/\text{OH}$ channel. Graul *et al.* considered two possible sources of the observed N_2OH^+ photodissociation yields: (i) photoexcitation of $[\text{N}_2\text{O} \cdot \text{H}_2\text{O}]^+$ to an excited state followed by internal energy conversion and proton transfer; and (ii) photodissociation of a second isomeric form, $[\text{N}_2\text{OH}^+ \cdot \text{OH}]$. Whereas mechanism i could account for the low kinetic energy release observed in the N_2OH^+ photodissociation yields, Graul *et al.* argued against mechanism i) because they expected a similar contribution of low energy ions in the H_2O^+ channel, given its comparable phase space. A significant low energy H_2O^+ component in the kinetic energy release distributions, however, was only observed at 657 nm, the longest wavelength investigated by these authors. Consequently, a predissociative transition involving excitation of the N_2OH^+ moiety was deemed a more plausible mechanism.

If separate isomeric forms are the predominant precursor ions of the $\text{H}_2\text{O}^+/\text{N}_2\text{O}^+$ and N_2OH^+ signals, it is likely that the thermal and supersonic jet source experiments should produce substantially different relative amounts of these two forms. However, the present CID as well as the photodissociation product intensity ratios $\text{N}_2\text{O}^+/\text{N}_2\text{OH}^+$ and $\text{H}_2\text{O}^+/\text{N}_2\text{OH}^+$ do not change beyond the experimental uncertainties when going from an equilibrated thermal to a non-equilibrium, supersonic jet expansion environment. The present CID threshold energy of 1.32 ± 0.10 eV for N_2OH^+ fragment ions (Table II) is in good agreement with the 1.2 eV derived by Graul *et al.*¹ (excellent agreement once the internal energy of 0.13 eV is considered). This threshold is only 0.28 ± 0.12 eV higher than the H_2O^+ onset, somewhat lower than the energy gap of 0.4–0.6 eV predicted by Graul *et al.*, but in agreement with the thermochemical prediction of 0.19 ± 0.20 eV, as determined from the known formation enthalpies and experimental and theoretical proton affinities.^{5,7–9} The present CID measurements, therefore, suggest that a collision-induced proton transfer reaction must account for the observed $\text{N}_2\text{OH}^+/\text{OH}$ dissociation channel.

Although the $\text{N}_2\text{O}^+/\text{H}_2\text{O}^+$ and N_2OH^+ photodissociation bands are significantly different, it is difficult to reconcile the broad N_2OH^+ band with a predissociative optical transition involving $[\text{N}_2\text{OH}^+ \cdot \text{OH}]$. Graul *et al.*¹ suggested that the electronic excitation is localized on the N_2OH^+ moiety. In order to verify whether this is a plausible mechanism, we have conducted *ab initio* calculations on N_2OH^+ and its lowest electronic states. N_2OH^+ geometries optimized using MP2/6-311++G(3df,p) and RQCISD/6-31+G(d,p) levels of computation²⁹ and the geometry of the N_2OH^+ moiety in Structure II (Figure 1) were used to determine vertical transition energies. At the CIS/6-311++G(3d,f) level, we find that the optical transition involving the first singlet excited state of N_2OH^+ is not anticipated above 200 nm. Given the closed shell nature of N_2OH^+ , the transition to the first excited triplet state is not expected to be above 250 nm. It is therefore unlikely that the presently observed N_2OH^+ photofragments at visible absorption wavelengths is associated with a transition localized on the N_2OH^+ moiety of a proton-transfer complex, $[\text{N}_2\text{OH}^+ \cdot \text{OH}]$.

The present evidence related to the N_2OH^+ photodissociation channel is more consistent with a photoinduced proton transfer mechanism involving $[\text{N}_2\text{O} \cdot \text{H}_2\text{O}]^+$ (mechanism *i* above). Upon closer inspection of the photodissociation bands, it is seen that all three cross sections simultaneously increase with photon energy at low photon energies. This similarity is an indication that the same optical transition is the source of all three fragment ions. Such a mechanism implies competition between rapid predissociation of the excited cluster ion to a repulsive surface and internal conversion to a longer-lived bound state that undergoes energy randomization. The fact that the N_2OH^+ band peaks at substantially lower photon energies before gradually declining can be interpreted as a steadily decreasing probability of forming longer-lived photo-excited cluster ions as the photon energy is increased. This interpretation is consistent with the present predissociation mechanism, which involves coupling

with respect to the bending vibrational motion of the H_2O moiety. The bending vibrational excitation in the excited state of the cluster ion is postulated to increase with excitation energy, thereby increasing the predissociating rate and decreasing the probability of forming longer-lived excited species.

The above mechanism implies that some H_2O^+ should also be produced with near statistical energy partitioning, as mentioned by Graul *et al.*¹ The low-kinetic energy band identified at 657 nm can be associated with such a process. Given the declining N_2OH^+ branching ratio with photon energy and the broad H_2O^+ kinetic energy release distributions in the experiments of Graul *et al.*, it is doubtful whether a low-kinetic energy component could be positively identified at shorter wavelengths.

Having explained the principal experimental observations on the basis of a single isomeric form, $[\text{N}_2\text{O} \cdot \text{H}_2\text{O}]^+$, the question arises as to why no evidence for the proton transfer complex $[\text{N}_2\text{OH}^+ \cdot \text{OH}]$ is observed despite its predicted stability. At this juncture we can only state that the stabilization rate of the initially formed $(\text{N}_2\text{O}, \text{H}_2\text{O})^{+*}$ adducts must be significantly faster than the isomerization rate in the thermal source and supersonic jet expansion conditions of the respective experiments. Such a situation is depicted in Figure 12, where a high barrier is postulated to exist between the isomers. Preliminary results from density functional geometry optimizations, however, cast doubt on whether the proton-transfer structure proposed by Graul *et al.* represents a local minimum at higher levels of theory, and suggest that $[\text{N}_2\text{O} \cdot \text{H}_2\text{O}]^+$ is considerably more stable. A detailed density functional and *ab initio* study on this cluster ion is currently in progress.³⁰ It is also worth noting that the global minimum of the investigated hypersurface is represented by a $\text{N}_2 \cdot \text{H}_2\text{O}_2^+$ structure. No evidence of H_2O_2^+ fragments was observed at low collision energies.

The most prominent difference between the thermal source and the jet source experiments is clearly the pre-threshold H_2O^+ signal observed in the jet source CID experiments. These ions must be associated with energetic cluster ions located near an H_2O^+ asymptote. The most obvious explanation for this phenomenon is residual vibrational excitation in the jet source experiments. If all fragment ions originate from the same precursor isomeric form, however, vibrational excitation would be expected to affect all of the fragment ion onsets in an equally dramatic way. Because substantially smaller amounts of pre-threshold signal are observed in the N_2O^+ and N_2OH^+ channels, it is conceivable that one or more additional loosely bound isomeric forms are present in the jet source experiments. A $\text{N}_2\text{O}(\text{H}_2\text{O}^+)$ complex trapped in a shallow potential well outside of the charge-transfer interaction region would account for the observed phenomenon. Calculations are currently in progress to locate such a structure.³⁰

V. CONCLUSIONS

The $(\text{N}_2\text{O}, \text{H}_2\text{O})^+$ cluster ion has been investigated under both thermal equilibrium and supersonic jet nonequilibrium

conditions using CID and photodissociation experiments. A CID binding energy of 1.04 ± 0.06 eV is determined relative to the $\text{N}_2\text{O} + \text{H}_2\text{O}^+$ asymptote. Threshold energies of 1.43 ± 0.12 eV and 1.32 ± 0.10 eV are determined for N_2O^+ and N_2OH^+ fragment ions, respectively. The observed CID thresholds in the thermal experiments are consistent with an interpretation that all fragment ions originate from the same precursor isomeric form, $[\text{N}_2\text{O} \cdot \text{H}_2\text{O}]^+$. Therefore, $\text{N}_2\text{OH}^+/\text{OH}$ CID products are the result of collision-induced isomerization. The H_2O^+ CID measurements of the jet source experiment exhibit substantial pre-threshold signal which is attributed to one or more loosely bound isomeric forms that do not decompose to $\text{N}_2\text{O}^+ + \text{H}_2\text{O}$.

The present photodissociation experiments under supersonic jet expansion conditions provide $\text{H}_2\text{O}^+:\text{N}_2\text{O}^+:\text{N}_2\text{OH}^+$ branching ratios that are similar to the thermal source experiments of Graul *et al.*¹ The observed band shapes of all fragment ions as well as the observed kinetic energy release¹ can be reconciled with a model involving a single optical transition from $[\text{N}_2\text{O} \cdot \text{H}_2\text{O}]^+$ to an excited state $\text{N}_2\text{O}(\text{H}_2\text{O}^+)$ correlated to the $\text{N}_2\text{O} + \text{H}_2\text{O}^+$ (\bar{A}) dissociation limit. The H_2O^+ and N_2O^+ photodissociation products are primarily formed via rapid predissociation to a repulsive surface correlated with $\text{N}_2\text{O} + \text{H}_2\text{O}^+$ (\bar{X}) products. The N_2OH^+ fragments are produced in a competing process involving internal conversion to a longer-lived complex, followed by proton transfer.

ACKNOWLEDGMENTS

The authors are grateful to Jon Stevens and Keiji Morokuma for communicating their theoretical results prior to publication. The authors also wish to thank M. T. Bowers for insightful comments and for permission to present the results of their *ab initio* calculations in Figure 1, and S. T. Graul for providing the frequencies of their calculations in Table I. This work was supported by NSF Grant No. CHE9530412 (PBA) and by AFOSR under Task 2303EP2. The authors thank S. Williams and Y. Chiu for helpful comments regarding the manuscript. M.J.B. is an NRC postdoctoral fellow.

¹ S. T. Graul, H-S Kim, and M. T. Bowers, *Int. J. Mass Spectrom. Ion Proc.* **117**, 507 (1992).

² We use the notation which employs parentheses, $(\text{N}_2\text{O}, \text{H}_2\text{O})^+$, when no structural information is connoted and square brackets when a cluster structure is implied.

- ³ P. Pechukas, J. C. Light, and C. Rankin, *J. Chem. Phys.* **44**, 794 (1966).
- ⁴ W. J. Chesnavich, L. Bass, T. Su, and M. T. Bowers, *J. Chem. Phys.* **74**, 2228 (1981).
- ⁵ S. G. Lias, J. E. Bartmess, J. F. Liebman, J. L. Holmes, R. D. Levine, and W. G. Mallard, *J. Phys. Chem. Ref. Data* **17** Suppl. 1 (1988).
- ⁶ J. E. Szulejko and T. B. McMahon, *J. Am. Chem. Soc.* **115**, 7839 (1993).
- ⁷ M. J. Frisch and J. E. Delbene, *Int. J. Quantum Chem. Symp.* **23**, 363 (1989).
- ⁸ J. E. Delbene and M. J. Frisch, *Int. J. Quantum Chem. Symp.* **23**, 371 (1989).
- ⁹ J. E. Delbene, E. A. Stahlberg, and I. Shavitt, *Int. J. Quantum Chem. Symp.* **24**, 455 (1989).
- ¹⁰ R. H. Schultz and P. B. Armentrout, *Int. J. Mass Spectrom. Ion Processes* **107**, 29 (1991).
- ¹¹ R. H. Schultz, K. C. Crellin, and P. B. Armentrout, *J. Am. Chem. Soc.* **113**, 8590 (1991).
- ¹² P. B. Armentrout in *Advances in Gas Phase Ion Chemistry*, edited by N. G. Adams and L. M. Babcock (JAI, Greenwich, 1992), Vol. 1, p. 83.
- ¹³ L. Hanley, S. A. Ruatta, and S. L. Anderson, *J. Chem. Phys.* **87**, 260 (1987).
- ¹⁴ D. C. Parent and S. L. Anderson, *Chem. Rev.* **92**, 1541 (1992).
- ¹⁵ E. J. Bieske, A. M. Soliva, and J. P. Maier, *J. Chem. Phys.* **94**, 4749 (1991).
- ¹⁶ C. R. Lishawa, R. A. Dressler, J. A. Gardner, R. H. Slater, and E. Murad, *J. Chem. Phys.* **93**, 3196 (1990).
- ¹⁷ R. A. Dressler, R. H. Salter, and E. Murad, *J. Chem. Phys.* **99**, 1159 (1993).
- ¹⁸ J. D. C. Jones, K. Birkinshaw, and N. D. Twiddy, *J. Phys. B* **14**, 2705 (1981).
- ¹⁹ K. M. Ervin and P. B. Armentrout, *J. Chem. Phys.* **83**, 166 (1985).
- ²⁰ R. D. Levine and R. B. Bernstein, *Molecular Reaction Dynamics and Chemical Reactivity* (Oxford University Press, New York, 1987).
- ²¹ S. T. Graul (personal communication).
- ²² F. A. Khan, D. E. Clemmer, R. H. Schultz, and P. B. Armentrout, *J. Chem. Phys.* **97**, 7978 (1993).
- ²³ R. N. Nixon, G. Duxbury, J. W. Rabalais, and L. Åsbrink, *Mol. Phys.* **31**, 423 (1976).
- ²⁴ J. E. Reutt, L. S. Wang, Y. T. Lee, and D. A. Shirley, *J. Chem. Phys.* **85**, 6928 (1986).
- ²⁵ L. Karlsson, L. Mattsson, R. Jadrny, R. G. Albridge, S. Pinchas, T. Bergmark, and K. Siegbahn, *J. Chem. Phys.* **62**, 4745 (1975).
- ²⁶ R. A. Dressler and E. Murad, *J. Chem. Phys.* **100**, 5656 (1994).
- ²⁷ S. T. Arnold, R. A. Dressler, M. J. Bastian, J. A. Gardner, and E. Murad, *J. Chem. Phys.* **102**, 6110 (1995).
- ²⁸ R. A. Dressler, S. T. Arnold, and E. Murad, *J. Chem. Phys.* **103**, 9989 (1995).
- ²⁹ GAUSSIAN 94, Revision D.1, M. J. Frisch, G. W. Trucks, H. B. Schlegel, P. M. W. Gill, B. G. Johnson, M. A. Robb, J. R. Cheeseman, T. Keith, G. A. Petersson, J. A. Montgomery, K. Raghavachari, M. A. Al-Laham, V. G. Zakrzewski, J. V. Ortiz, J. B. Foresman, J. Cioslowski, B. B. Stefanov, A. Nanayakkara, M. Challacombe, C. Y. Peng, P. Y. Ayala, W. Chen, M. W. Wong, J. L. Andres, E. S. Replogle, R. Gomperts, R. L. Martin, D. J. Fox, J. S. Binkley, D. J. Defrees, J. Baker, J. P. Stewart, M. Head-Gordon, C. Gonzalez, and J. A. Pople, Gaussian, Inc., Pittsburgh, Pennsylvania, 1995.
- ³⁰ J. Stevens and K. Morokuma (in preparation).

A high-temperature guided-ion beam study of $\text{Na} + \text{X}^+$ ($\text{X} = \text{O}_2$, NO , N_2) charge-transfer reactions

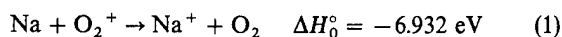
Dale J. Levandier,[†] Rainer A. Dressler,* Skip Williams[†] and Edmond Murad

Phillips Laboratory, Geophysics Directorate, Optical Effects Division, Hanscom AFB, MA 01731-3010, USA

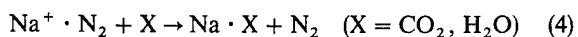
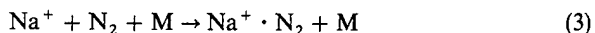
The high-temperature guided-ion beam method is used to measure absolute, integral cross-sections for charge transfer reactions of sodium with O_2^+ , NO^+ and N_2^+ in the collision energy range between *ca.* 0.2 and 10 eV (CM). At 1 eV the cross-sections are, respectively, 168, 29 and 57 Å², with errors estimated at $\pm 40\%$. These experiments, involving molecular ions present in the ionosphere at altitudes of 80–110 km, were undertaken to improve the kinetic data available to the community involved in modelling mesospheric meteoric metal layers. The cross-sections are extrapolated to thermal energy, and thermally averaged rate constants are derived. The cross-sections are discussed with respect to the effects of vibrational excitation of the reactant ions, which are produced by electron impact ionization. These results permit an improved inclusion of metal-atom reactions in the models, which are now able to account for the kinetic energy range commensurate with the meteor ablation process.

It has been known for some time that meteoric dust entering the earth's atmosphere ablates to generate a persistent layer of metal atoms.¹ Most of the ablation of this material, which exhibits velocities of 10–40 km s⁻¹, occurs at altitudes above 80 km and results in the formation of layers of the metal atoms with peak densities in the region of the mesopause at about 85–95 km, and ion layers peaked slightly above the neutrals. Because of their low ionization potentials, these metal atoms can undergo rapid charge transfer (CT) with ambient O_2^+ and NO^+ , producing the ground-state atomic ions which are very stable with respect to recombination and chemical or CT reactions.

Sodium, because of the intense D lines, is an important contributor to the nightglow, and was the first meteoric metal to be identified spectroscopically.² This metal has been the subject of renewed interest in modelling the formation and behaviour of the mesopausal metal layers.^{3–5} As suggested above, CT reactions of sodium with ambient ions are expected to be very important in the morphology of the metal:



Contrary to expectations, however, metal ion densities are lower than the neutral densities. Richter and Sechrist^{6,7} were first to point out that the facile clustering of Na^+ with N_2 , *via* three-body reactions,^{8–10} followed by ligand switching and electron-ion recombination, should constitute the primary removal mechanism for Na^+ :



Quantitative application of this essentially correct explanation has been hampered, however, by the lack of experimental data on the cross-sections of reactions (1) and (2), that is, the primary reactions that lead to the formation of the ions. In addition, the increased sophistication of metal layer modelling now permits the inclusion of hyperthermal reactions of freshly ablated material travelling at the meteoric velocity.

The rate constant for reaction (1) currently employed in atmospheric models was derived by extrapolation of crossed-beam (CB) experiments.¹¹ The accuracy of the CB cross-sections, especially at low collision energy, was compromised because of the need for an extraction field in the collision region to effect good collection efficiency. This extraction field limited the measurements to collision energies above *ca.* 4 and *ca.* 2 eV for reactions (1) and (2), respectively, requiring extrapolation over a relatively broad range to extract a thermal rate constant. The extrapolation procedure used in the CB study featured an arbitrary combination of the Langevin capture cross-section at lower collision energies with a Rapp-Francis¹²/Demkov¹³ mechanism for non-adiabatic transitions at high collision energy, the latter being a model based on atomic systems. Flowing afterglow¹⁴ (FA) and Penning ion trap¹⁵ results are available; however these techniques yielded data at single values of collision energy. It is noteworthy that the rate constant for reaction (2) currently used in atmospheric modelling was obtained from a compendium of atmospheric kinetic data,¹⁶ and appears to be derived *via* extrapolation of the CB results, however the extrapolation was not done in the original CB work.¹¹ The lack of agreement between the thermal FA measurements and the extrapolated CB results, and the interest in modelling reactions of nascent ablated material, calls for an accurate measurement of the cross-sections of interest at collision energies in the thermal through hyperthermal range.

In this work we present ion-Na CT cross-section measurements using a recently developed novel technique. We have designed a high-temperature octopole ion-guide for the determination of absolute integral cross-sections as a function of collision energy for reactions of ions with neutral vapours of non-volatile materials.^{17,18} This instrument is the first high-temperature guided-ion beam apparatus to permit accurate absolute cross-sections for ion-neutral reactions, and is based on the guided-ion beam (GIB) technique originally developed by Teloy and Gerlich¹⁹ for studies of volatile species. In a GIB experiment, single collisions of ions with the target gas occur inside the field-free trapping volume of an rf multipole, here an octopole. The confining field, which does not affect the kinetic energy of the ions and therefore enables the use of primary ion beams with kinetic energy over a broad range down to near-thermal energy, collects all scattered ions irrespective of scattering angle.²⁰ As discussed in the following sections, the key technical difficulty addressed in the high-

[†] Orion International Technologies, Inc., Albuquerque, NM 87110, USA.

temperature ion-guide design, which derives from the need to work with a high-temperature metal vapour and which is common to the methods used previously, is the accurate measurement of the target gas density.

To aid in the understanding of the behaviour seen in reactions (1) and (2) we also present data for the following reaction:



Experimental

The high-temperature octopole developed for these experiments has been described in detail elsewhere.¹⁸ The octopole assembly was incorporated into an existing tandem mass spectrometer.^{21,22} Fig. 1 is a schematic representation of the instrument. Briefly, an ion beam is generated in a continuous, electron impact source (A) and is directed onto the main instrument axis by a 90° DC quadrupole bender (B). After mass selection in a Wien velocity filter (C), the primary ion beam is decelerated to the desired energy and injected into the high-temperature octopole assembly (D). The octopole transports the ions through the target vapour in the heated oven-collision cell (E), and the resulting secondary ions as well as the transmitted primary ions are extracted into a quadrupole mass filter (F). Ions are detected with an off-axis twin-microchannel plate detector (G). The distinguishing feature of the octopole/collision cell assembly is the use of coaxial sheath heaters as octopole rods on which the ion-guide rf potential can be applied without interference from the heater circuitry. The ion beam energy and energy distribution are determined using both retarding potential and time-of-flight (TOF) measurements. The width of the distribution of ion beam energy in these experiments is typically 0.20 eV FWHM, or better, and precision of the beam energy is ± 0.05 eV.

The high-temperature system can be operated for several days between cleanings, during which time a background due to Na^+ thermionic emission and potential barriers near the cooler upstream end of the octopole become increasingly evident. The Na^+ background is easily accounted for during the experiments by measuring the sodium ion current while the primary beam is momentarily stopped. We believe the barriers, which are observed by comparison of the retarding potential and TOF energy measurements, arise from oxidation of sodium deposits on the poles. The barriers result in a lower limit of primary ion kinetic energy, but affect neither the accuracy of the energy measurement nor the distribution of ion beam energy.

The primary ions are created in their ground electronic states by operating the ion source with an electron energy less than that required to reach the first long-lived excited state of the molecular ions. For N_2^+ , the two lower excited states, $A^2\Pi_{u,1}$ and $B^2\Sigma_u^+$, have lifetimes of 17 μs and 63 ns²³

(respectively) and are expected to decay before reaching the scattering cell, permitting electron energies of ≤ 22 eV. For NO^+ and O_2^+ electron energies of < 15.5 eV and < 16 eV are used, respectively. For these energies electron impact ionization is expected to be subject to the Franck-Condon factors derived from photoelectron spectroscopy. Therefore, NO^+ and O_2^+ should have vibrational states up to $v = 4$ populated, with relative populations for $v = 0-4$ of approximately 1.0:2.2:1.9:1.1:0.5 and 1.0:2.0:2.1:1.0:0.2, respectively.²⁴ Electron impact ionization of N_2 has been estimated to yield ca. 80% of N_2^+ in $v = 0$.²⁵ Two stages of differential pumping and a 90° bend follow the source chamber, so reactions of neutral molecules from the source with sodium in the collision cell are negligible.

Cross-sections are obtained by monitoring the secondary and primary ion intensities as the ion beam energy is varied. The voltages at the extractor and deflector are computer-controlled and are adjusted for each ion as the ion beam energy is varied to correct for small differences in the collection efficiency of the primary and secondary ions. These differences in collection efficiency are due primarily to the large difference in velocity between the primary and secondary ions in exothermic CT reactions. In the single collision limit, the cross-section (σ) is obtained from:

$$\sigma = \frac{I_s}{I_T n l} \quad (1)$$

where I_s is the secondary or product ion current, I_T is the total ion current, n is the target density and l is the effective interaction length. The effective interaction length for the cross section measurements is derived from the calibration of the cell length with a volatile target.¹⁸

For the sodium experiments, the collision cell is operated at a temperature of ca. 460 K, as measured with a thermocouple on the coolest part of the cell. The octopole rods are heated to somewhat higher temperatures to reduce condensation on them. Separate Knudsen cell experiments carried out at this temperature indicate that the vapour composition is $> 99\%$ sodium with the primary impurity being potassium vapour. The presence of sodium dimer (Na_2) was not observed under our conditions, and an equilibrium vapour pressure calculation indicates that the dimer is factor of 2×10^{-3} less abundant than the monomer. A temperature of 460 K corresponds to a sodium vapour pressure (P_v) of 0.076 mTorr,²⁶ which is within the range of target pressure required to minimize multiple collisions while permitting viable signal levels.

A substantial contribution to the 25–30% error limits typically quoted for absolute cross-section measurements in GIB experiments derives from the uncertainty in the target column density, nl . This problem is compounded in the present high-temperature technique because the customary capacitance manometer cannot be used to determine the density of a

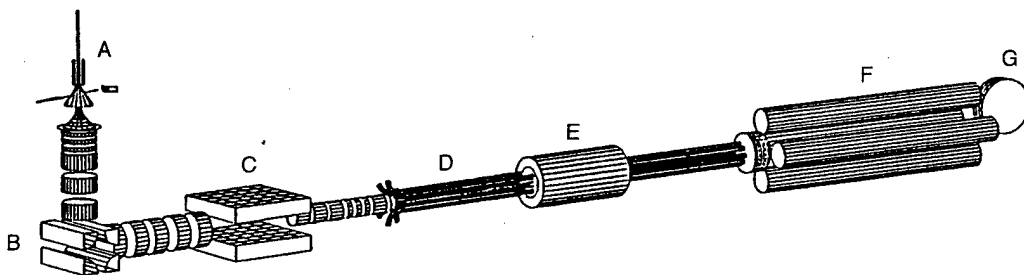


Fig. 1 Schematic of the high-temperature octopole ion-guide instrument. The labelled components are as follows: electron impact source, (A); 90° DC quadrupole bender, (B); Wien velocity filter, (C); high-temperature octopole assembly, (D); heated oven-collision cell, (E); quadrupole mass filter, (F); off-axis twin-microchannel plate detector, (G). The unlabelled elements are electrostatic ion transport lenses. The 'upstream' ends of the octopole rod heaters are curved away from the instrument centerline to accommodate the heater lead connections. The injection lens has a conical shape of dimensions that preclude the ion beam being affected by the fields in the region of the bends in the poles.

vapour that condenses at room temperature. Particular care was taken in developing the instrument used here to enable accurate measurement of the target vapour density.¹⁸ The design permits two very different methods to be used, one based on the assumption that the cell temperature can be related to the vapour pressure of the target material, and the other based on atomic absorption spectrometry.

In the temperature/ P_v pressure method, the density of the target vapour is assumed to be the vapour pressure of the target material as defined by the temperature of the coolest surface with which the vapour is in contact inside the collision cell. The cell configuration, with relatively large orifices, is only a coarse approximation of a Knudsen cell, in which vapour pressure determinations are carried out in conditions where a cell is uniformly heated and the vapour inside the cell is in equilibrium with the bulk sample, and the flux of vapour escaping through a small orifice is measured.²⁷ This is in contrast to a Langmuir configuration in which the flux of a material evaporating from a uniformly heated surface, with no flux onto the surface, is determined. The cell in the current work is not uniformly heated, owing in part to its also being heated by the octopole array, which is typically operated at slightly higher temperatures than the nominal cell temperature. Nevertheless, the success of the correction for thermal transpiration in the initial calibration of the effective cell length, performed with a volatile target gas at different operating temperatures,¹⁸ points to the validity of relating the thermocouple measurement to the target density.

The line of sight along the main instrument axis permits the use of atomic absorption spectrometry to measure the target column density directly. In this work, a tungsten-halogen continuum light source (Ealing) is used, and the transmitted light is detected with a liquid-nitrogen-cooled CCD detector (Princeton Instruments) after dispersion in a 0.18 m spectrograph (Thermo Jarrell Ash) with a 2400 groove/mm grating. The curve-of-growth for the sodium D doublet, which relates the absorption signal to the vapour density, is obtained by integration of the Voigt absorption profile, taking hyperfine structure into account.¹⁸

Comparison of the density determination techniques indicates a systematic difference, with the thermocouple/ P_v measurement giving smaller cross-sections. The difference does not exceed the typical error limits given for GIB experiments, which represents remarkably good agreement for such disparate techniques. The optical measurements exhibit greater scatter, due to low signal-to-noise arising from the low resolution of the spectrograph/CCD. This is compounded by a lack of sensitivity due to the fact that at the density necessary for the GIB experiment the sodium vapour represents an optically thick absorber, so changes in density are accompanied by relatively small changes in absorption signal. In this work, the cross-sections have been calculated using the thermocouple/ P_v measurement, largely because of the greater sensitivity and reproducibility of this method, which was manifested in good day-to-day duplication of the measurements. Error limits in the current work are estimated as $\pm 40\%$.

Results

Reactions (1), (2) and (6)

Fig. 2, 3 and 4 show the absolute cross-sections measured for reactions (1), (2) and (6), respectively, for collision energies from ca. 0.08–0.2 eV to 10 eV. Each cross-section is compared to the results of the thermal FA¹⁴ and hyperthermal CB¹¹ studies, as well as the Langevin capture cross-section for the interaction of ions with sodium. The values used in mesospheric sodium metal layer modelling are displayed in Fig. 2 and 3, and the result of the extrapolation to thermal energy of

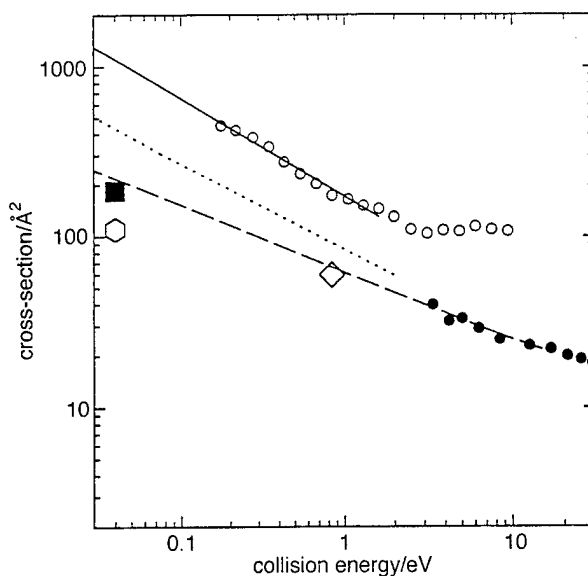


Fig. 2 Cross-section for $\text{Na} + \text{O}_2^+ \rightarrow \text{Na}^+ + \text{O}_2$, as a function of kinetic energy (small open circles). The other symbols represent: CB results¹¹ (small filled circles); thermal FA results¹⁴ (large open hexagon); Penning-trap results¹⁵ (open diamond); and the thermal value currently used in atmospheric models (large filled square). The dotted curve is the Langevin cross-section for reactions of ions with sodium, and the solid and dashed curves are exponential extrapolations of the present data and CB results, respectively, to thermal energies, as explained in the text.

the CB data is indicated in Fig. 4. The Penning-trap data¹⁵ are also shown in Fig. 2 and 4.

The three cross-sections are characterized by an exponential decrease in magnitude with increasing energy at low collision energies, and a transition to a nearly energy-independent region above ca. 2 eV. Evidence of an increase in cross-section above 5 eV can be seen for reaction (2). The cross-sections for the three reactions rank in the order $\sigma_1 > \sigma_6 > \sigma_2$, with σ_1 markedly larger than the Langevin cross-section. Although a

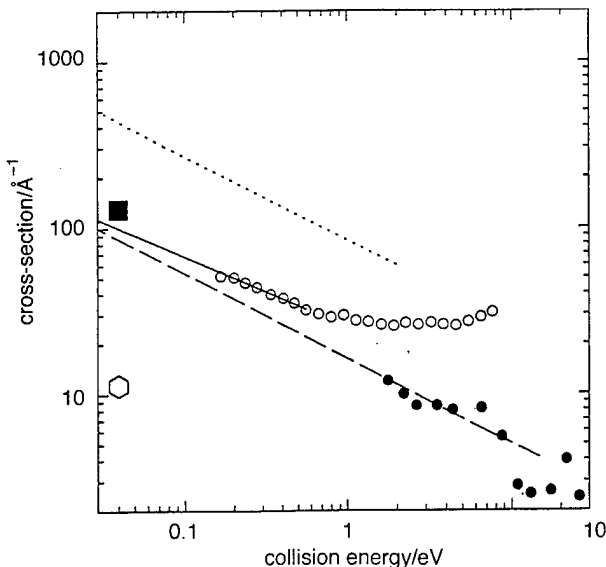


Fig. 3 Cross-section for $\text{Na} + \text{NO}^+ \rightarrow \text{Na}^+ + \text{NO}$, as a function of kinetic energy (small open circles). The other symbols represent: CB results¹¹ (small filled circles); thermal FA results¹⁴ (large open hexagon); thermal value currently used in atmospheric models (large filled square). The dotted curve is the Langevin cross-section for reactions of ions with sodium, and the solid and dashed curves are exponential extrapolations of the present data and CB results, respectively, to thermal energies, as explained in the text.

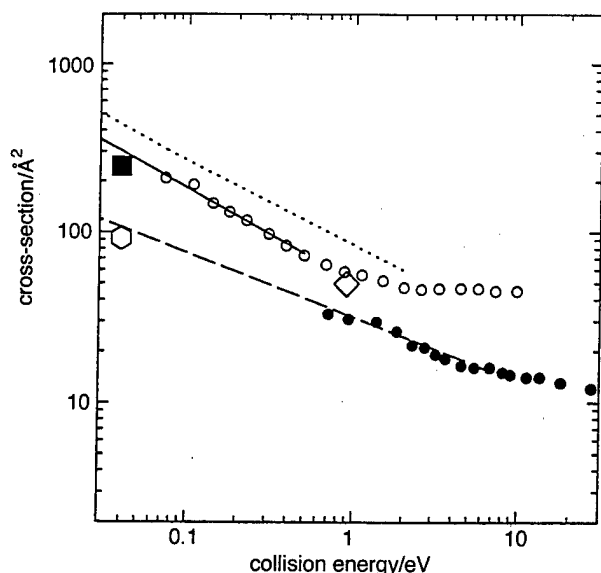


Fig. 4 Cross-section for $\text{Na} + \text{N}_2^+ \rightarrow \text{Na}^+ + \text{N}_2$, as a function of kinetic energy (small open circles). The other symbols represent: CB results¹¹ (small filled circles); thermal FA results¹⁴ (large open hexagon); Penning-trap results¹⁵ (open diamond); and the thermal value obtained by the Langevin/Rapp-Francis extrapolation in the CB work (large filled square). The dotted curve is the Langevin cross-section for reactions of ions with sodium, and the solid and dashed curves are exponential extrapolations of the present data and CB results, respectively, to thermal energies, as explained in the text.

value larger than the nominal capture cross-section has been observed for excited O_2^+ ,¹¹ participation of these species is easily precluded by keeping the ion source electron energy below 16 eV.²⁸ The present results indicate larger cross-

Table 1 Results of fitting of aE_T^{-b} to the low-energy component of the $\text{Na} + \text{XY}^+$ cross sections

XY	a	b
O_2	172.49	0.5773
NO	25.183	0.4294
N_2	51.473	0.5512

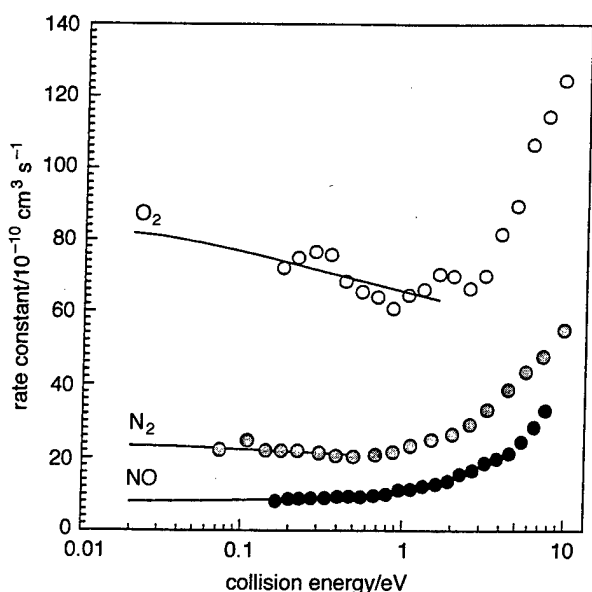


Fig. 5 Rate constants derived from present work for $\text{Na} + \text{X}^+$ charge-transfer reactions, $\text{X} = \text{O}_2$ (open), NO (filled), N_2 (shaded), as a function of kinetic energy. The data points were simply converted via $k = \sigma v$. The curves are thermal averages of the extrapolated cross-sections, as described in the text.

sections than measured previously. While the GIB cross-sections are approximately twice those obtained in the CB work, the relative magnitudes within either study compare quite well. The cross-sections for reactions (1), (2) and (6) at 1 eV are 168, 29 and 57 Å², respectively.

Compared to lower limits of ca. 2.9, 1.7 and 0.7 eV in the CB studies of reactions (1), (2) and (6), respectively, the extension of the GIB data to collision energies below 0.2 eV allows considerably more confidence in the extrapolation of these cross sections to thermal energy. The solid curves in Fig. 2, 3 and 4 are the results of extrapolation *via* fits of a simple exponential expression, $\sigma = aE_T^{-b}$ to the low energy region of the cross-sections, the results of which are given in Table 1. These results indicate a substantial difference from the quantities currently in use in atmospheric models, especially for reaction (1) for which the models employ a cross-section ca. 5 times smaller than is observed here. Note that in Fig. 2, 3 and 4 the dashed lines are extrapolations derived by the above exponential expression, rather than the formalism used in the CB study. The FA work,¹⁴ in which the authors noted particular difficulty while studying reaction (2), also reported smaller thermal rates than those indicated here. The Penning-trap cross-sections are not consistent with those from any other study, but fall within the range of the various measurements.

It is notable that the extrapolation procedure derived in the CB work,^{29,30} which employed an arbitrary combination of Langevin and Rapp-Francis¹² models, resulted in a larger thermal rate for the reaction of sodium with N_2^+ as compared to O_2^+ .¹¹ Application of this procedure on the cross-sections measured here, for comparison, was not possible since it requires data at higher kinetic energies than those employed in this study. Moreover, the publication of the CB results does not mention the temperature of the sodium beam source,¹¹ which raises the question of whether the relative collision energy for the CB configuration was derived correctly, an issue that would be most important at the low collision energies the extrapolation was intended to describe.

Fig. 5 is a plot of the present data in the form of rate constants (k), including the extrapolations. In this plot, the experimental data are simply represented as $k = \sigma v$, where v is the nominal relative velocity. The extrapolated data in Fig. 5 are derived *via* eqn. (II), in which the rate constant is obtained by averaging over the distribution of ion kinetic energy, $f(v_i)$, and thermal motion of the neutral target, $f(v_n)$, and over incident lab angle, Λ , since these effects become important at low collision energies:

$$k = \frac{\iiint dv_i dv_n \sin \Lambda d\Lambda f(v_i) f(v_n) \sigma v^2}{\iiint dv_i dv_n \sin \Lambda d\Lambda f(v_i) f(v_n) v} \quad (\text{II})$$

The ion velocity distribution is derived from a Gaussian kinetic energy distribution, and a Maxwell-Boltzmann distribution of neutral velocity is used. The denominator is a normalization factor. The simplicity of eqn. (II) results from the assumption that all primary ion velocities are parallel to the ion-guide axis, thereby reducing the problem to cylindrical symmetry.³¹

Other reactions

Other reactive channels for collisions of sodium with O_2^+ , NO^+ and N_2^+ are energetically unfavourable, and were not observed in the present work. The atomic systems:



were examined, however the extent of reaction was below the detection limits of the experiment at the hyperthermal collision energies investigated in this work.

Discussion

Exothermic charge transfer

For recent insights in the theoretical field the reader is directed to articles by Nakamura³² and by Gislason *et al.*³³ Typically, CT models describing the translational energy dependence of cross-sections derive from theories developed for atomic systems at collision energies in the range 10–1000 eV, and feature a decrease in cross-section with decreasing energy below this. The two principal scenarios are embodied in the Rapp–Francis¹² or Demkov¹³ models, that deal with nonadiabatic transitions at long range between parallel, near-resonant entrance and exit potential-energy surfaces, and the Landau–Zener model,^{34,35} which invokes surface hopping at shorter range in the vicinity of an avoided crossing. In both pictures, radial velocity enhances the negotiation of the relevant energy gap, as described by the Massey adiabaticity parameter.³⁶

In molecular systems, models of CT reactions must account for the additional vibrational degrees of freedom, since nuclear motion along vibrational coordinates can also promote charge transfer. Since the dependence of the electronic coupling along a vibrational coordinate is often negligible at high kinetic energy, the molecular CT cross-section is usually reduced to:^{33,37,38}

$$\sigma_{v \rightarrow v'} = \sigma(E_T, \Delta E_{v,v'}) \langle v | v' \rangle^2 \quad (\text{III})$$

where $\sigma_{v \rightarrow v'}$ is the vibronic state-to-state cross section, $\sigma(E_T, \Delta E_{v,v'})$ is the electronic CT cross-section dependent on the kinetic energy (E_T) and vibronic energy gap ($\Delta E_{v,v'}$), typically modelled as transitions between parallel surfaces, after Rapp–Francis/Demkov,^{12,13} and $\langle v | v' \rangle^2$ is the appropriate FCF. At the low kinetic energies of interest in the present work, and as has been observed in other studies,^{39,40} this picture is no longer suitable since the timescale of the interaction is now greater than the typical vibrational periods, and the energy dependence of the cross-section cannot usually be represented by that of atomic systems. The latter is especially so when vibrational coupling is important, in which case the long interaction times at low collision energies enhances CT, in contrast to the behaviour of atomic systems. The importance of vibrational coupling in molecular CT systems has been documented by numerous authors.^{41–45}

In the current study, the kinetic energy dependence of the cross-sections is characteristic of exothermic CT reactions in polyatomic systems. The large cross-sections indicate that reactions take place at long range, resulting in negligible momentum transfer and a concomitant disposal of exothermicity as internal energy of the products, which constitutes the energy resonance criterion for exothermic CT. The low-energy behaviour observed here can be associated with vibrationally mediated CT transitions, since the increasing interaction time of the collision partners with lower velocity increases the likelihood of the passage through the optimal electronic interaction region along the vibrational coordinate, consistent with a cross-section energy dependence of approximately $E_T^{-1/2}$.

In the present systems, the product excitation *via* near-resonant CT resides entirely in the molecular species, since the lowest Na^+ excited state is at *ca.* 32 eV. Values of D_0 for O_2 , NO and N_2 are 5.116, 6.497 and 9.76 eV,²³ respectively, and imply the availability of dissociative channels in reactions (1) and (6). Dissociative CT has been observed for reaction (6) at high kinetic energies, and was attributed to predissociation from high vibrational states of the N_2 a $^1\Pi_g$ state *via* direct spin–spin coupling to the weakly bound $\text{A}'^5\Sigma_g^+$ state.⁴⁶ In the same study, it was also pointed out that the a $^1\Pi_g$ and B $^3\Pi_g$ states are the only energetically accessible states for CT which involve a one-electron transition. The more intimate

collision events at low kinetic energies could enhance the coupling to the dissociative states accessible in reactions (1) and (6).

The vibrational state distributions of the O_2^+ and NO^+ beams require consideration of the possible vibrational effects in reactions (1) and (2). Fig. 6 shows the relevant molecular potentials for reaction (2) along the vibrational coordinate of the NO moiety, with the energy scale referenced to the zero-point energy of the entrance channel. The curves, which are drawn for infinite ion–neutral separation, are modified Morse potentials⁴⁷ derived from the appropriate molecular parameters,^{28,48} and are sufficiently accurate for the purposes of this discussion. The asymptotic region of the NO a $^4\Pi_i$ curve, in the range where the Morse potential is less satisfactory, is scaled from the ground-state potential in the same region. It can be seen that reactant ion vibrational energy should significantly promote CT, since the Franck–Condon overlap is expected to increase with reagent vibrational excitation, as the curve crossing at the repulsive part of the potential energy surfaces is approached. The poor overlap for the lowest vibrational states in NO^+ is consistent with the relatively small cross-section observed for reaction (2). The efficiency of reaction (2) should be enhanced further by the crossing of the NO a $^4\Pi_i$ and NO^+ ground states, which opens an additional CT channel for $v \approx 5$ of NO^+ . The slight increase in the CT cross-section for reaction (2) at higher collision energies may be attributable to translationally coupled transitions to NO a $^4\Pi_i$ + Na^+ products.

Another aspect of the reactions studied here arises from the substantial difference in polarizability of sodium (24 \AA^3) and the molecular products ($1.59 \leq \alpha \leq 1.74 \text{ \AA}^3$). As illustrated by the interfragment potentials for reaction (2) in Fig. 7, the resulting difference in the entrance and exit attractions leads to a large number of crossings between entrance and exit diabatic vibronic states. The exit channel ion–dipole interaction is not included because of the small NO dipole moment, and only the lower energy component of the NO ground spin-orbit state is shown.

Owing to the much stronger entrance interaction potential, the approaching reactants encounter crossings with exothermic product states. In reference to Fig. 6, this signifies that the reactant potential shifts down in energy with decreasing interfragment distance, thereby lowering the curve crossing along

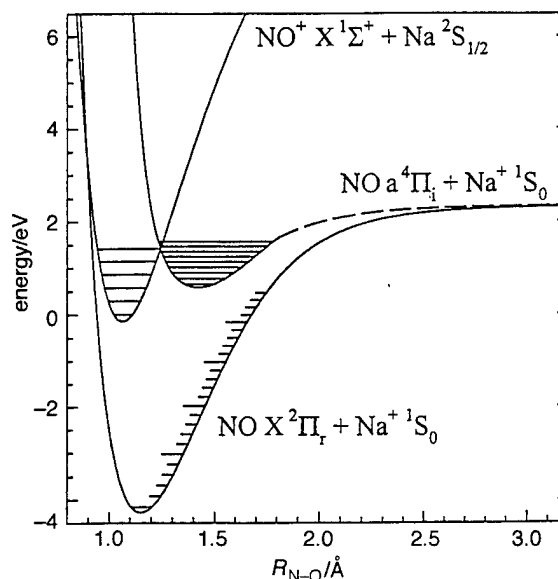


Fig. 6 Molecular potential-energy curves for reaction (2) for infinite ion–neutral separation. The energy scale is referenced to the zero-point energy of the entrance channel. The solid curves are modified Morse potentials; the dashed segment of the a $^4\Pi_i$ curve is scaled from the X $^2\Pi_i$ curve.

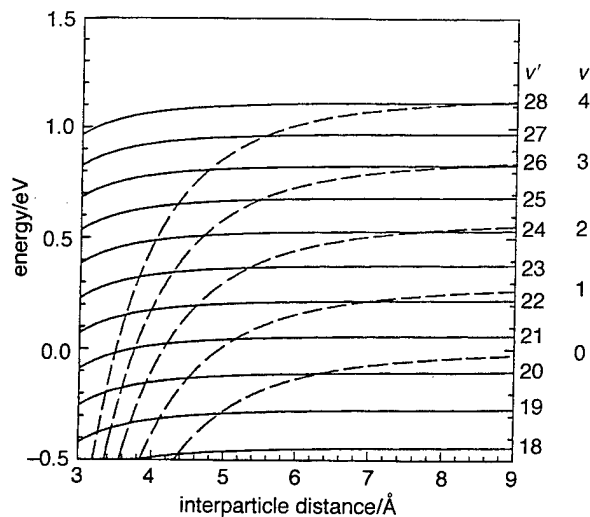


Fig. 7 Effect of the ion-atom attraction as a function of ion-neutral separation on the asymptotic entrance and exit vibronic levels for $\text{Na } ^2\text{S}_{1/2} + \text{NO}^+ \text{X}^1\Sigma^+(v=0) \rightarrow \text{Na}^+ ^1\text{S}_0 + \text{NO } \text{X}^2\Pi_r(v'=18-28)$. The relevant vibrational levels are indicated at the right side of the figure.

the repulsive part of the potential towards vibrational levels populated in the present experiments. It follows that the low-energy vibrational state-to-state cross-sections are governed by two important factors: the strength of the exchange interaction at the interfragment distance where the respective diabatic vibronic curves of Fig. 7 cross, and the Franck-Condon overlap that expresses the probability of residing in the strong interaction region along the reactant and product vibrational coordinates. Whereas little can be said on the former point in the absence of state-resolved measurements, the Franck-Condon overlap, as stated above, is clearly expected to increase with reactant vibrational energy, suggesting a strong vibrational dependence of the charge-transfer state-to-state cross-sections. Meanwhile, translational coupling *via* the Demkov mechanism may be expected to show effects already at the low energies of this work due to the small energy gaps encountered over broad interfragment distances. This would be an additional explanation of the rise in the $\text{NO}^+ + \text{Na}$ charge-transfer cross-section observed at the highest kinetic energies of this work.

Unlike reaction (2), a large number of electronic states are accessible in reactions (1) and (6). An analysis as performed in Fig. 7 is consequently not possible, because the necessary excited-state molecular polarizabilities are not known. An analysis as outlined in Fig. 6, however, shows that for reaction (1) the O_2^+ ground state potential near $v=0$ crosses the O_2 $\text{A } ^3\Sigma_u^+$, $\text{C } ^3\Delta_u$ and $\text{c } ^1\Sigma_u^-$ potentials along their repulsive walls in the respective dissociation continua. These interactions should be very efficient due to the favourable FCFs and perfect resonance conditions, as well as to the irreversibility of dissociative charge transfer, which is consistent with the very large observed cross-sections. Moreover, at infinite ion-neutral separation, the O_2^+ ground state potential crosses the $v=3$ level of the O_2 $\text{B } ^3\Sigma_u^-$ potential, suggesting that a noticeable vibrational enhancement could be observed if the electronic coupling to this state is significant.

The above deliberations on vibrational effects warrant further comparison of the present results to the earlier measurements. As seen in Fig. 2 and 4, the FA experiments gave comparable rate constants for reactions (1) and (6). Those studies were carried out in a 300 K carrier gas, so the reactions involved vibrationally cold molecular ions.¹⁴ In contrast, in both the present GIB experiments and the CB studies, where NO^+ was formed by electron impact on N_2O , the molecular ions should have vibrational distributions similar to those indicated in the experimental section, which is borne out

by the similar relative cross-sections among the three reactions for either technique. Since the GIB cross-sections benefit from more accurate neutral density measurement, improved ion collection efficiency and negligible primary *vs.* product ion discrimination, the magnitudes are expected to be more accurate than previously obtained. If the relative magnitudes of the FA rate constants are representative of cold reagents, scaling the FA results to the more accurate absolute GIB cross-sections *via* the measurements for reaction (6), which involves cold N_2^+ in both cases, would recover the absolute thermal cross-section with cold reactants for reactions (1) and (2). The cross-section for reaction (1) measured here would then indicate considerable vibrational effects, the removal of which would result in a near-Langevin cross-section for cold O_2^+ reaction. Likewise, if the present measurement of the cross-section for reaction (2) has a similar degree of vibrational enhancement, consistent with the above analyses, then reaction with cold NO^+ would result in a cross-section corresponding to the scaled FA result. These considerations point to the need for the accurate experimental determination of vibrational effects in reactions (1) and (2), especially if the goal of comparing the systems studied here to existing theories for exothermic CT is to be met.

Implications for atmospheric models

Preliminary atmospheric model calculations⁴⁹ indicate that the cross-sections measured here, at thermal energies and with no adjustment to account for possible vibrational effects, do not have a substantial influence on the Na^+ altitude profile. On the other hand, the profile of Na is significantly affected. The top edge of the neutral layer is now pushed downward until Na nearly vanishes at an altitude of *ca.* 115 km at noon, as compared to *ca.* 130 km in the previous studies, while the nighttime profile is not affected much. This results in a considerably greater diurnal variation in the neutral layer profile than was seen in previous work.

Given the sensitivity of the atmospheric model to the CT cross-sections, it will be beneficial to quantify the vibrational effects in the present measurements. Until this is achieved, we propose, for the purpose of atmospheric modelling, that the rate constants indicated in Fig. 8 for reactions (1), (2) and (6) be taken as representing reactions with vibrationally cold

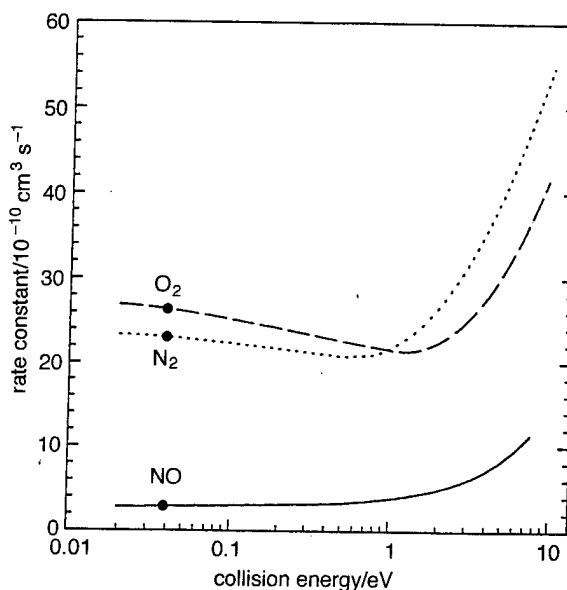


Fig. 8 Rate constants for vibrationally cold reactants ($\text{Na} + \text{X}^+$, $v=0$, $\text{X} = \text{O}_2$, N_2 or NO), derived as described in the text. The curves are comprised of the thermally averaged extrapolations at low energies, shown in Fig. 5, and polynomial fits to the present data. The dots represent the respective scaled flowing afterglow rate constants.

ions. These rate constants were obtained from the scaling derived from the comparison of the FA and present results, as discussed above. Application of these results to the atmospheric model, including hyperthermal reactions, is under way.⁴⁹

Conclusion

The $\text{Na} + \text{X}^+$ ($\text{X} = \text{O}_2$, NO , N_2) charge-transfer systems exhibit large cross-sections consistent with the long-range nature of near-resonant exothermic charge-transfer reactions. CT cross-sections for these systems at 1 eV are 168, 29 and 57 Å², respectively. The differences among the cross-sections can be explained by the access to dissociative CT for reactions with O_2^+ and N_2^+ , along with the possibility of vibrational effects owing to the internal energy distributions of the primary ions. The latter point can also be used to explain the differences in the relative cross-sections for the three reactions as observed in the present high-temperature guided-ion beam experiment and the earlier flowing afterglow work. The present experiment confirms the advantages of the high-temperature guided-ion beam technique over the others with regard to the ability to measure ion–neutral reaction cross-sections at the near-thermal to hyperthermal kinetic energies and to accuracy owing to improvements in target vapour density measurement, ion collection efficiency, and the elimination of primary *vs.* secondary ion discrimination. In preliminary calculations, the results reported here have been illustrated to have significant consequences for the modelling of the meteoric metal layers. For the purposes of refining these calculations, we have attempted to derive from the present data the CT cross-sections for reactions with vibrationally cold ions.

This work was supported by AFOSR under Task Nos. 2303EP2 and ILIR5PHW018. The authors are indebted to Mr W. J. McNeil and Dr S. T. Lai for communicating the preliminary results of the atmospheric modelling based on the present work.

References

- 1 J. W. Chamberlain and D. M. Hunton, *Theory of Planetary Atmospheres*, Academic, San Diego, 1987.
- 2 V. M. Slipher, *Publ. Astron. Soc. Pac.*, 1929, **41**, 262.
- 3 J. M. C. Plane, *Int. Rev. Phys. Chem.*, 1991, **10**, 55.
- 4 W. J. McNeil, E. Murad and S. T. Lai, *J. Geophys. Res.*, 1995, **100**, 16847.
- 5 R. M. Cox, J. M. C. Plane and J. S. A. Green, *Geophys. Res. Lett.*, 1993, **20**, 2841.
- 6 E. S. Richter and C. F. Sechrist, *Geophys. Res. Lett.*, 1979, **6**, 183.
- 7 E. S. Richter and C. F. Sechrist, *J. Atmos. Terr. Phys.*, 1979, **41**, 579.
- 8 F. E. Niles, J. M. Heimerl, G. E. Keller and L. J. Puckett, *Radio Sci.*, 1972, **7**, 117.
- 9 R. A. Perry, B. R. Rowe, A. A. Viggiano, D. L. Albritton, E. E. Ferguson and F. C. Fehsenfeld, *Geophys. Res. Lett.*, 1980, **7**, 693.
- 10 D. Smith, N. G. Adams, E. Alge and E. Herbst, *Astrophys. J.*, 1983, **272**, 365.
- 11 J. A. Rutherford, R. F. Mathis, B. R. Turner and D. A. Vroom, *J. Chem. Phys.*, 1972, **56**, 4654.
- 12 D. Rapp and W. E. Francis, *J. Chem. Phys.*, 1962, **37**, 2631.
- 13 Y. N. Demkov, *Sov. Phys. JETP*, 1964, **18**, 139.
- 14 A. L. Farragher, J. A. Peden and W. L. Fite, *J. Chem. Phys.*, 1969, **50**, 287.
- 15 R. Loch, R. Stengler and G. Werth, *J. Chem. Phys.*, 1998, **91**, 2321.
- 16 M. J. McEwan and L. F. Phillips, in *Chemistry of the Atmosphere*, Edward Arnold, London, 1975.
- 17 D. J. Levandier and R. A. Dressler, *High-Temperature Octopole Ion Guide with Coaxially Heated Rods*, US Pat. Pending, 1997.
- 18 D. J. Levandier, R. A. Dressler and E. Murad, *Rev. Sci. Instrum.*, 1997, **68**, 64.
- 19 E. Teloy and D. Gerlich, *Chem. Phys.*, 1974, **4**, 417.
- 20 D. Gerlich, *Adv. Chem. Phys. I*, 1992, **82**, 1.
- 21 R. A. Dressler, R. H. Salter and E. Murad, *J. Chem. Phys.*, 1993, **99**, 1159.
- 22 M. J. Bastian, R. A. Dressler, D. J. Levandier, E. Murad, F. Muntean and P. B. Armentrout, *J. Chem. Phys.*, 1997, in press.
- 23 A. A. Radzig and B. M. Smirnov, *Reference Data on Atoms, Molecules and Ions*, ed. J. P. Toennies, Springer-Verlag, Berlin, 1985, vol. 31.
- 24 D. W. Turner, C. Baker, A. D. Baker and C. R. Brundle, *Molecular Photoelectron Spectroscopy*, Wiley-Interscience, London, 1970.
- 25 G. Henri, M. Lavollee, O. Dutuit, J. B. Ozenne, P. M. Guyon and E. A. Gislason, *J. Chem. Phys.*, 1988, **88**, 6381.
- 26 M. W. Chase, C. A. Davies, J. R. Downey, D. J. Frurip, R. A. McDonald and A. N. Syverud, *JANAF Thermochemical Tables*, 3rd edn., Part II, *J. Phys. Chem. Ref. Data*, 1985, vol. 14.
- 27 R. C. Paule and J. L. Margrave, in *The Characterization of High Temperature Vapors*, ed. J. L. Margrave, Wiley, New York, 1967.
- 28 K. P. Huber and G. Herzberg, *Constants of Diatomic Molecules*, Van Nostrand Reinhold, New York, 1979.
- 29 F. A. Wolf and B. R. Turner, *J. Chem. Phys.*, 1968, **48**, 4226.
- 30 J. A. Rutherford, R. F. Mathis, B. R. Turner and D. A. Vroom, *J. Chem. Phys.*, 1971, **55**, 3785.
- 31 D. Gerlich, *J. Chem. Phys.*, 1988, **90**, 127.
- 32 H. Nakamura, *Adv. Chem. Phys. II*, 1992, **82**, 243.
- 33 E. A. Gislason, G. Parlant and M. Sizun, *Adv. Chem. Phys. II*, 1992, **82**, 321.
- 34 L. D. Landau, *Phys. Z. Sowjetunion*, 1932, **2**, 46.
- 35 C. Zener, *Proc. R. Soc. London, A*, 1932, **137**, 696.
- 36 M. S. Child, *Molecular Collision Theory*, Academic Press, London, 1974.
- 37 M. R. Spalburg, J. Los and E. A. Gislason, *Chem. Phys.*, 1985, **94**, 327.
- 38 E. A. Gislason and G. Parlant, *Comments At. Mol. Phys.*, 1987, **19**, 157.
- 39 I. Kusunoki and T. Ishikawa, *J. Chem. Phys.*, 1985, **82**, 4991.
- 40 Y. Shiraishi and I. Kusunoki, *J. Chem. Phys.*, 1987, **87**, 6530.
- 41 K. Yamashita, K. Morokuma, Y. Shiraishi and I. Kusunoki, *J. Chem. Phys.*, 1990, **92**, 2505.
- 42 V. Sidis, *Adv. Chem. Phys. II*, 1992, **82**, 73.
- 43 S. Chapman, *Adv. Chem. Phys. II*, 1992, **82**, 423.
- 44 R. A. Dressler, S. T. Arnold and E. Murad, *J. Chem. Phys.*, 1995, **103**, 9989.
- 45 R. A. Dressler, M. J. Bastian, D. J. Levandier and E. Murad, *Int. J. Mass Spec. Ion Processes*, 1997, **159**, 245.
- 46 A. B. van der Kamp, L. D. A. Siebbeles and W. J. van der Zande, *J. Chem. Phys.*, 1994, **101**, 9271.
- 47 G. Herzberg, *Molecular Spectra and Molecular Structure I. Spectra of Diatomic Molecules*, Van Nostrand Reinhold, New York, 1950.
- 48 K. P. Huber and M. Vervloet, *J. Mol. Spectrosc.*, 1988, **129**, 1.
- 49 W. J. McNeil, S. T. Lai and E. Murad, to be published.

Paper 7/01872J; Received 17th March, 1997

Comments Relating to Energy Resonance, Franck-Condon and Langevin Criteria in Low-Energy Charge-Transfer Collisions

Energy resonance, Franck-Condon and Langevin criteria are discussed for low-energy singly charged ion-neutral charge-transfer collisions. The suitability of these criteria are debated using the $(\text{O} + \text{Xe})^+$, $(\text{O} + \text{NO})^+$ and $(\text{N} + \text{NO})^+$ charge-transfer systems as examples.

Key Words: *charge transfer, ion-molecule, charge exchange, Franck-Condon, Langevin, low-energy collisions*

Low energy ion-molecule charge-transfer collisions often result in products with large amounts of internal energy. Unlike most other common gas-phase molecular collision events, high product excitation can occur even when the trajectory does not negotiate the chemical interaction region of the intermolecular potential. Such long-range exothermic charge-transfer reactions can be very efficient, signifying very large cross sections at both thermal and hyperthermal translational energies. Consequently, exothermic charge-transfer reactions are the predominant ion-molecule process observable above 1 eV and play an important role in plasma environments such as those encountered in the upper atmosphere,¹ interstellar space,² and in the environment of low-Earth-orbiting spacecraft.³ The analysis of optical and plasma parameters in these environments requires accurate knowledge of relevant charge-transfer cross sections or rate coefficients and product energy disposal.

In many cases, such as charge-transfer reactions between ions and atomic species like atomic oxygen or metal atoms, no accurate cross section measurements exist over the pertinent translational energy ranges.

Comments At. Mol. Phys.
1998, Vol. 34, No. 1, pp. 43-55
Reprints available directly from the publisher
Photocopying permitted by license only

© 1998 OPA (Overseas Publishers Association)
Amsterdam B.V. Published under license
under the Gordon and Breach
Science Publishers imprint
Printed in India

Due to the high complexity of rigorous theories on charge transfer reactions, calculations of heavy-atom systems are not reliable as of yet, leaving geophysicists to speculate on the approximate size of relevant charge-transfer reaction rate parameters and their respective energy dependences. The most frequently applied arguments to estimate the rate parameters of naturally occurring singly charged charge-transfer reactions are *energy resonance*, *Franck-Condon*, and *Langevin*⁴ criteria. The purpose of this Comment is to clarify the origin of these criteria and to provide guidance to the reader on the limitations of their applicability.

Integral charge-transfer cross sections at a translational energy, E_T , are given by the simple expression:

$$\sigma(E_T) = 2\pi \int_0^{b_{\max}} P(b, E_T) b \, db \quad (1)$$

where b is the collision impact parameter and $P(b, E_T)$ is the charge-transfer probability. Usually, the electron hops are confined to a narrow range of interfragment distances, R . If the most probable interfragment distance, R_{CT} , is at long range, i.e., charge-transfer occurs in a region where the ion-neutral interaction is weak, the charge-transfer collisions are well described by straight-line trajectories at hyperthermal energies, signifying $b_{\max} = R_{CT}$. Equation (1) then reduces to

$$\sigma(E_T) = P(E_T) \pi R_{CT}^2. \quad (2)$$

In terms of estimating charge-transfer cross sections at collision energies above 1 eV, Eq. (2) is a good start; however, the problem still requires a reasonable assessment of $P(E_T)$ and R_{CT} , usually not a simple endeavor.

$P(E_T)$ is governed by a combination of two-level nonadiabatic transition probabilities, p_i , which can be grouped into two types of mechanisms: one involving *near-parallel states* and the other located at an *avoided crossing*. These models are based on the principle that if a system traverses a region of strong exchange interaction at high velocities with respect to one or more nuclear coordinates, the adiabatic levels become broadened according to the uncertainty principle, allowing state mixing across energy gaps, ΔE_a . This is quantified by the well-known Massey adiabaticity criterion.⁵ Models by Demkov,⁶ Rosen-Zener⁷ and Rapp and Francis⁸ describe charge-transfer probabilities for near parallel two-level systems. (For convenience we will refer to these as *Demkov* systems). According to Demkov systems, a maximum nonadiabatic tran-

sition probability along a nuclear coordinate, Q_i , occurs at a distance, Q_D , at which the following condition applies:

$$2H_{12}(Q_D) = \Delta E_d. \quad (3)$$

ΔE_d is the energy difference between diabatic charge-transfer states, Ψ_1^d and Ψ_2^d , which describe the system with charge localized on one or the other fragment throughout the trajectory, and $H_{12}(Q)$ is the electronic coupling between the diabatic charge-transfer states. In atomic models, an exponential dependence on the only nuclear coordinate, the interfragment coordinate, R , is assumed:

$$H_{12}(R) = A \exp(-aR), \quad (4)$$

where A and a are constants, the latter taking only positive values. The Demkov two-level charge-transfer transition probability, p_D , at $R = R_D$, the interfragment distance at which Eq. (3) holds, is then given by

$$p_D = \left[1 + \exp \frac{\pi \Delta E_d}{\hbar a R} \right]^{-1}. \quad (5)$$

Equation (5) conveys that a maximum transition probability $p_D = 0.5$ is attained at high relative velocities corresponding to complete mixing of diabatic states.

Nonadiabatic transitions at avoided crossings are described by the well-known *Landau-Zener* curve-crossing model for linear diabatic states.^{9,10} At the crossing radius, R_{LZ} , the Landau-Zener nonadiabatic transition probability between adiabatic states, Ψ_1^a and Ψ_2^a , has a sharp maximum, and is given by

$$p_{LZ} = \exp \left[-2\pi \frac{H_{12}(Q_{LZ})^2}{\hbar \dot{Q}_i \Delta F} \right], \quad (6)$$

where ΔF is the difference in slopes of the diabatic potentials with respect to the nuclear coordinate, Q_i . In contrast to the Demkov models, p_{LZ} ranges from 0 to 1, corresponding to entirely adiabatic and diabatic traversals of the crossing region, respectively.

Since for most charge-transfer systems the electronic coupling is sufficient to allow charge-transfer at long range, where the ion-neutral interaction is still very weak, these reactions are inherently accompanied by small amounts of translational energy transfer, and are therefore lim-

ited to exothermic systems at near-thermal collision energies. The small degrees of energy transfer signify that the charge-transfer products have an internal excitation energy approximately equal to the exothermicity of the charge-transfer reaction. Consequently, the reactant and product energy levels will be near-resonant. Aside from these kinematic arguments for *energy resonance* between reactant and product internal states, the rapidly increasing charge-transfer probabilities with decreasing energy gaps as prescribed by the Demkov models also point toward a preponderance of near-resonant charge-transfer transitions. Demkov models predict, however, that as the collision energy is increased, product states with increasing energy gaps can experience complete mixing, provided the electronic coupling is significant. Energy resonance arguments are therefore inappropriate at keV collision energies.

Much insight into charge-transfer mechanisms can be gained by studying simple atomic transfer systems which comprise a single nuclear coordinate. Figure 1 illustrates schematically charge-transfer collision trajectories using the atomic $O^+(^4S) + Xe$ system as an example. The nearest resonant charge-transfer states are the $O(^3P) + Xe^+(^2P_{1/2})$ products with an exothermic energy gap of ~ 0.17 eV. Two types of trajectories are depicted: a large-impact parameter, straight-line trajectory and a small impact parameter trajectory that negotiates the repulsive area of the interatomic interaction potential (shaded area) which changes with charge-transfer state. The relevant diabatic charge-transfer potentials^{11,12} are also shown on the same scale of the two-dimensional figure, and indicate a curve crossing at $R \approx 3.6$ Å which could efficiently promote charge transfer.

Guided-ion-beam measurements by Bastian *et al.*¹² of the collision energy dependence of the integral charge-transfer cross section for the $O^+ + Xe$ system are shown in Fig. 2. A sharp increase in charge-transfer cross section with collision energy is observed. Because above 30 eV the total cross section exceeds the maximum possible cross section of ~ 20 Å² for a Landau-Zener mechanism located at the crossing at $R \approx 3.6$ Å, a Demkov-type mechanism must be important. This maximum cross section is determined from Eq. (2) assuming $P(E_T) = 0.5$. Even though the Landau-Zener transition probability, p_{LZ} , ranges from 0 to 1, the total transition probability ranges from 0 to 0.5 because the strong interaction regions, illustrated by circles R_{LZ} and R_D in Fig. 1, are each encountered twice. The total two-level probability for a charge-transfer transition, P_i , is then given by¹³

$$P_i = 2p_i(1 - p_i). \quad (7)$$

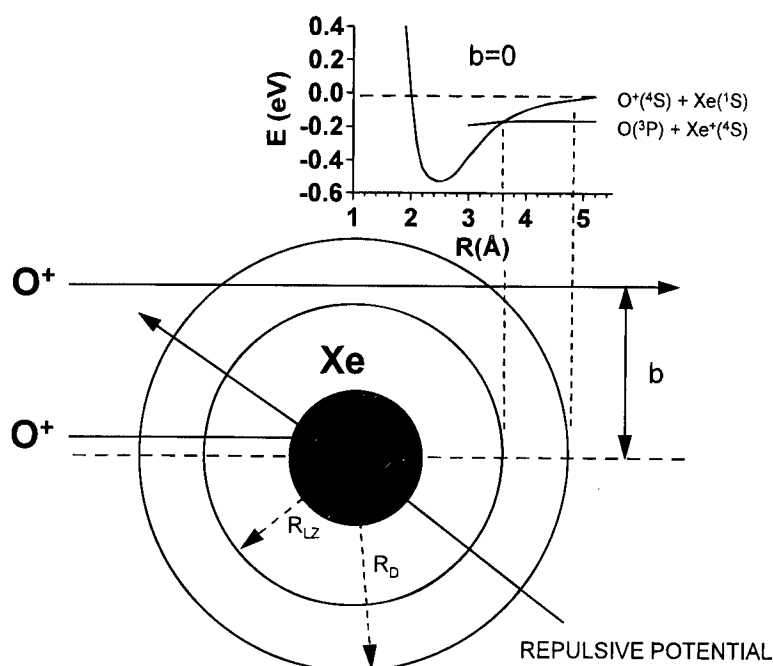


FIGURE 1 Schematic representation of $O^+ + Xe$ charge-transfer trajectories. The interfragment coordinate of the inset charge-transfer potentials (Ref. 11) is drawn on the same scale as the trajectories. Only the electrostatic long-range potential is shown for the products. R_{LZ} is the Landau-Zener and R_D is the estimated Demkov radius.

The figure compares a calculated cross section based on a Demkov model.¹⁴ The relatively large discrepancy between experiment and theory demonstrates the difficulty in determining the key quantity, $H_{12}(R)$, accurately, especially if large atoms are involved. The discrepancy may also indicate that the Landau-Zener mechanism is an important contributor to charge-transfer at low collision energies. Bastian *et al.*¹² could also discern a Xe^+ rebounding component, which could be attributed to small impact parameter collisions that sample the repulsive part of the potential. The scattering analysis demonstrated that the sample $O(^3P) + Xe(^2P_{1/2})$ products are populated as observed in the long-range collisions, implying that at small impact parameters, charge-transfer occurs primarily at R_{LZ} and short-range nonadiabatic transitions involving highly inelastic or superelastic channels are

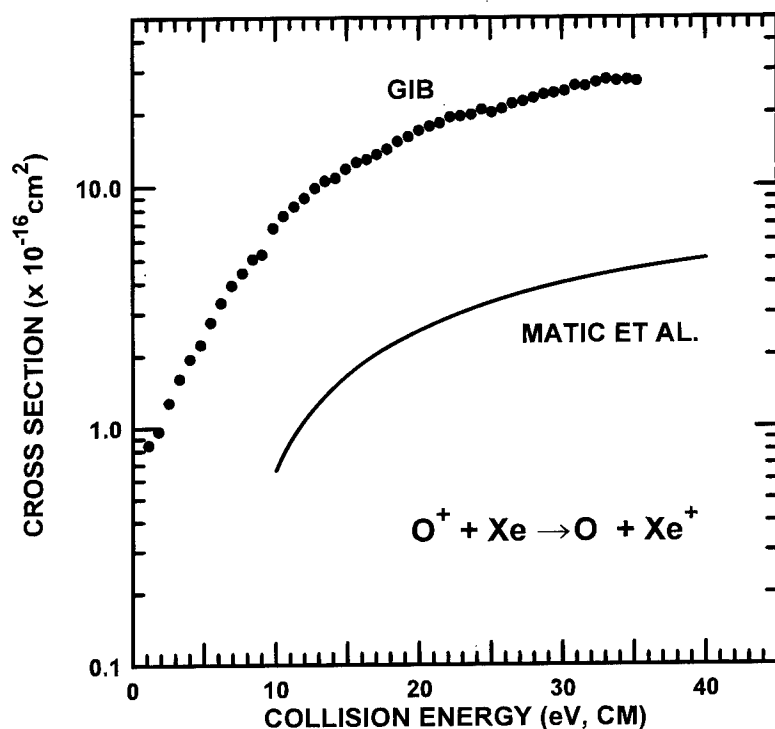


FIGURE 2 Guided-ion beam (GIB) measurements of the center-of-mass collision energy dependence of the $(\text{O} + \text{Xe})^+$ charge-transfer cross section. The solid curve is a Demkov-model calculation by Matic *et al.* (Ref. 14).

insignificant. The latter is not surprising since predominantly adiabatic behavior is expected at $R < 3 \text{ \AA}$.

In singly charged, non-symmetric atomic systems, charge-transfer energy dependences as shown in Fig. 2 are usually observed. An exception to this are accidentally resonant systems, such as the $\text{O}^+ + \text{H}$ charge-transfer system.¹⁵ It is worth noting that in multiply charged systems, curve crossings can occur at very long-range, yielding very small adiabatic energy gaps, ΔE_a , so that $p_{LZ} > 0.5$ at near thermal collision energies. The total charge-transfer probability then decreases with collision energy at low energies as p_{LZ} increases toward 1.

The situation becomes more complicated in molecular charge-transfer systems where additional nuclear degrees of freedom and anisotropy in

the electronic coupling are introduced. The coupling with respect to vibrational and angular coordinates can become significant at low energies. Usually, the vibronic coupling between vibrational charge-transfer states is described as a product between the pure electronic coupling and the *Franck–Condon* overlap, $\langle v'|v'' \rangle$, between reactant and product vibrational wavefunctions¹⁶:

$$H_{12v'v''}(R) = H_{12}(R) \langle v'|v'' \rangle. \quad (8)$$

Analytical expressions for vibrational state-to-state cross sections have been derived and usually take the form¹⁷

$$\sigma_{v' \rightarrow v''} = \sigma_0(\Delta E, E_T) \langle v'|v'' \rangle^2. \quad (9)$$

Equation (9) embodies the energy resonance and *Franck–Condon* criteria predicting large integral charge-transfer cross sections if the *Franck–Condon* factor is significant near resonance. Demkov-based atomic models for $\sigma_0(\Delta E, E_T)$ correctly predict¹⁸ that as the collision energy is raised the number of off-resonant levels with maximum electronic transition probabilities will include entire electronic bands of *Franck–Condon* active states, and the product distribution then equals a *Franck–Condon* distribution. This behavior has been demonstrated in ion + H₂O and He⁺ + N₂ luminescence studies.^{19–22}

Models given by Eq. (9) have had mixed success in explaining charge-transfer state-to-state cross sections and the energy dependence thereof at near-thermal to hyperthermal energies. Unlike atomic systems, many molecular charge-transfer systems exhibit cross sections that drop with $\sim E_T^{-0.5}$ dependence at collision energies below ~ 1 eV, similar to predictions of the *Langevin*⁴ model for ion–molecule reactions. The *Langevin* model predicts that reaction cross sections are given by an ion–molecule capture cross section. The cross section for a pure ion-induced dipole interaction is then determined to be

$$\sigma_L = \frac{\pi}{2} \sqrt{\frac{\alpha}{E_T}}, \quad (10)$$

where α is the target molecule polarizability. Although the *Langevin* model is not recommended for charge-transfer processes due to the long-range characteristics, there are many examples of molecular charge-transfer systems that exhibit near-collisional rate coefficients at thermal

energies.^{23,24} Consequently, Demkov models based on translational coupling are inappropriate to describe this large class of molecular charge-transfer reactions because they predict near-zero nonadiabatic transition probabilities at thermal energies. Demkov models also predict zero probabilities for the case of complex formation, where \dot{R} is zero.

At collision energies below 1 eV, the velocity with respect to vibrational coordinates becomes comparable to or higher than the velocity with respect to the interfragment coordinate. Vibrationally induced charge-transfer transitions can consequently play an important role and explain the high charge-transfer efficiencies observed at thermal conditions. An example of a vibrational mechanism in a charge-transfer system $(A + BC)^+$ is illustrated in Fig. 3. The charge-transfer potentials are drawn with respect to the BC vibrational coordinate, Q_{vib} . In this example, the zero-point vibrational motion encounters a crossing seam with the charge-transfer product surface. An enlargement of the crossing area is shown for two interfragment

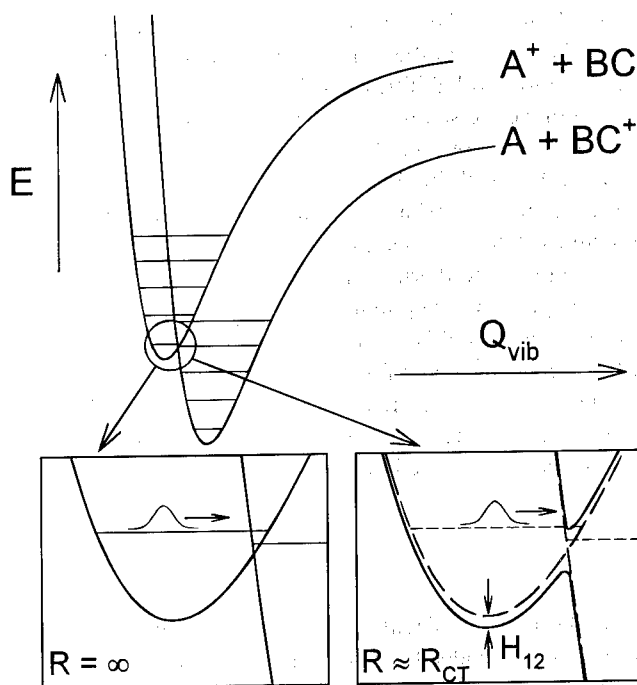
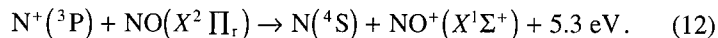
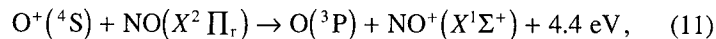


FIGURE 3 Schematic representation of a vibrationally mediated charge-transfer transition.

distances: one corresponding to asymptotic conditions and one in the region of high exchange interaction. It is seen that charge-transfer can occur adiabatically if the vibrational wave packet encounters the avoided crossing during the traversal of the strong interaction region. The charge-transfer cross section is then governed by this probability, which is expressed to some degree by the Franck–Condon overlap between the charge-transfer vibrational wavefunctions. Since the probability of encountering the crossing region is inversely proportional to the interaction time, a maximum probability occurs in the case of longer-lived intermediates. Strongly vibrationally coupled systems are therefore expected to mimic Langevin behavior at near-thermal collision energies.²⁴

In the following we discuss the caveats of using energy resonance and Franck–Condon arguments on the example of two charge-transfer reactions involving the upper-atmospheric species, NO:



While the $\text{O}^+(\text{}^4\text{S}) + \text{NO}$ reaction exhibits a very small rate coefficient of less than $8 \times 10^{-12} \text{ mol}^{-1} \text{ cm}^3 \text{ s}^{-1}$ at room-temperature thermal conditions,^{25,26} $\text{N}^+(\text{}^3\text{P}) + \text{NO}$ has a very high rate coefficient of $\sim 6 \times 10^{-10} \text{ mol}^{-1} \text{ cm}^3 \text{ s}^{-1}$ which is $\sim 60\%$ of the Langevin cross section.^{27–30} Applying energy resonance and Franck–Condon criteria, we find that the $\text{O}^+(\text{}^4\text{S}) + \text{NO}(\text{}X^2\Pi_r, v=0)$ reactants are near resonant with $\text{O}(\text{}^1\text{S}) + \text{NO}^+(\text{}X^1\Sigma^+, v=0)$ products that have substantial Franck–Condon overlap. These conditions are illustrated in Fig. 4, which depicts the asymptotic charge-transfer reactant and accessible product potentials with respect to the NO vibrational coordinate. The very low rate despite the excellent resonance and Franck–Condon conditions must be explained by poor electronic coupling, which is the result of the fact that $\text{O}(\text{}^1\text{S}) + \text{NO}^+(\text{}X^1\Sigma^+)$ products are spin-forbidden, as is the more exothermic $\text{O}(\text{}^1\text{D}) + \text{NO}^+(\text{}X^1\Sigma^+)$ channel. It is easily seen that the spin-allowed ground-state products can only be accessed through an extreme position hop, consistent with the very low observed rate coefficient.

Asymptotic potentials for the efficient $\text{N}^+(\text{}^3\text{P}) + \text{NO}$ charge-transfer system are shown in Fig. 5. This system has three open channels, all of which are spin-allowed. Franck–Condon arguments suggest very inefficient charge transfer from the ground vibronic reactant level because all accessible product channels exhibit vanishing Franck–Condon factors near res-

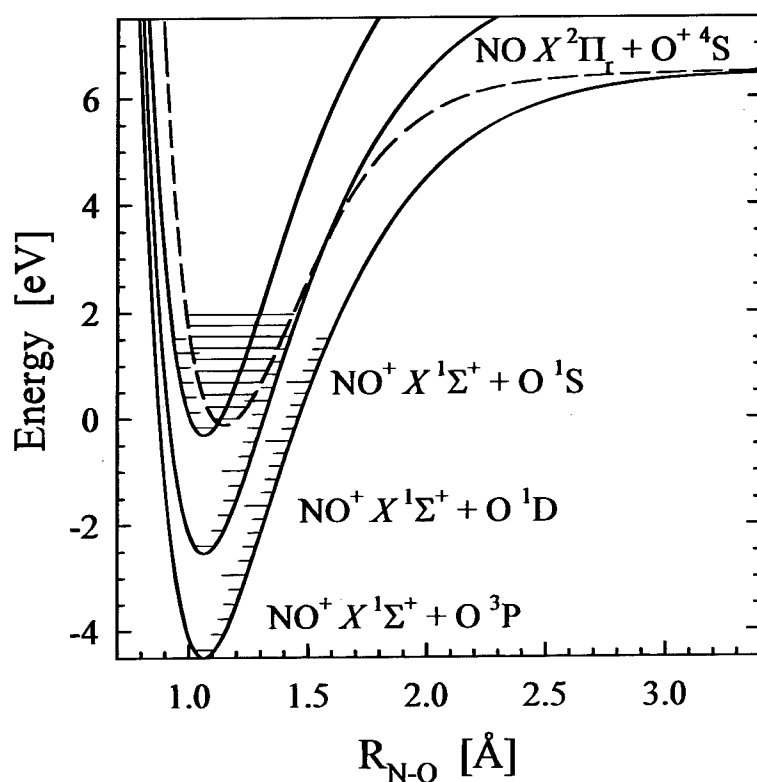


FIGURE 4 Relevant asymptotic vibrational potentials of the $(\text{O} + \text{NO})^+$ charge-transfer system.

onance. The $\text{N}(^2\text{P}) + \text{NO}^+(\text{X}^1\Sigma^+)$ product potential crosses the reactant potential at approximately $v' = 4$ and is expected to exhibit the strongest charge-transfer interaction. The crossing, however, represents a large barrier to charge-transfer along this vibrational coordinate. Nevertheless, the rate coefficient suggests that charge transfer from $v' = 0$ is very efficient. Spin-selection rules predict that a maximum of one third of reactants entering the strong interaction region, those proceeding on a doublet surface, will form $\text{N}(^2\text{P}) + \text{NO}^+(\text{X}^1\Sigma^+)$ products. The 60% Langevin efficiency may be rationalized by an electron transfer in a region where a strong exchange interaction induces an avoided crossing with a substantially lower and narrower barrier (see Fig. 3).

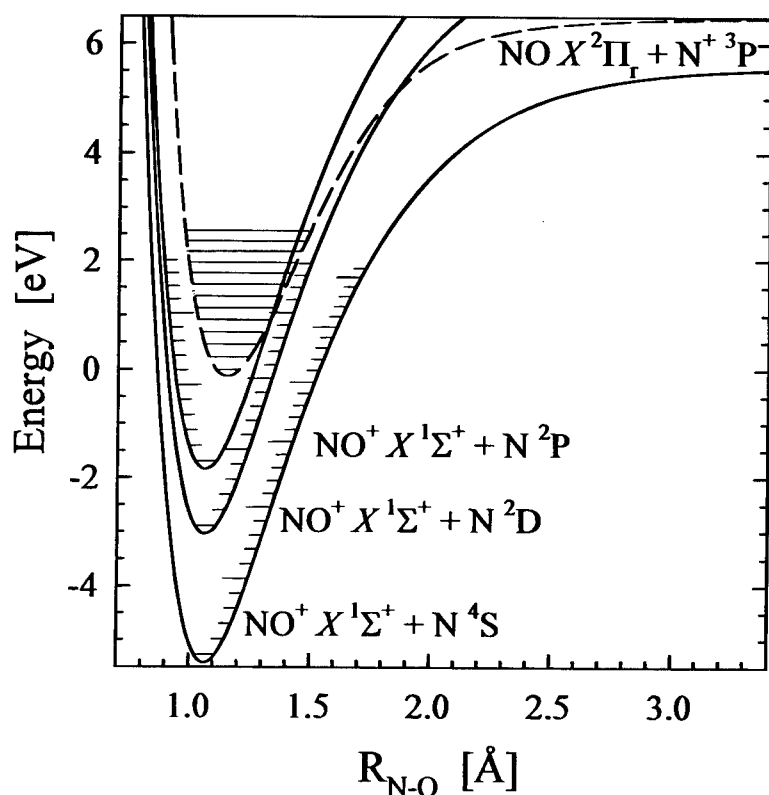


FIGURE 5 Relevant asymptotic vibrational potentials of the $(\text{N} + \text{NO})^+$ charge-transfer system.

Another possibility is a shift of the entrance potential with respect to the product potential as the reactants approach the strong chemical interaction region governed by the N_2O^+ global minimum of the potential energy surface. This shift could create resonances with the first off-resonant $\text{N}(^2\text{P}) + \text{NO}^+(\text{X}^1\Sigma^+)$ vibrational levels, $v'' = 4$ and 5, that have small but measurable Franck-Condon factors, as seen in the NO photoelectron spectrum.^{31,32} A preference for off-resonant state-to-state cross sections is observed in charge-transfer systems where entrance and exit long-range interactions are significantly different. Exothermic shifts of ~ 0.2 eV have been observed in the product vibrational distributions of ion + H_2O charge-transfer systems, where the ion-dipole interaction of the entrance potential

is dominant.^{21,33} Strong deviations from orthodox asymptotic energy gap model predictions are also expected in ion + metal atom systems, such as O^+ charge transfer to high-polarizability atoms Ba and Sr, the cross sections for which are unknown and are needed to interpret Ba and Sr space-release experiments.^{34,35} Finally, it must be mentioned that the asymptotic Franck-Condon factors can change at shorter range, providing an additional explanation for the efficient $N^+ + NO$ charge-transfer reaction.

In conclusion, singly charged atomic charge-transfer systems (except for accidental resonance cases) exhibit increasing cross sections with collision energy which are very difficult to predict. When applying resonance arguments, it must be kept in mind that $\Delta E(R_{CT})$ is the critical energy gap, not the usually referenced asymptotic value, $\Delta E(R = \infty)$. In case of weak spin-orbit coupling, spin-selection rules are very important. Charge-transfer rate coefficients of molecular systems can exhibit near-Langevin behavior at low energies if the collision trajectory encounters vibronic resonances with substantial Franck-Condon overlap. Examination of the pertinent vibronic potentials of the charge-transfer states can prove helpful in elucidating exceptions to these rules.

Acknowledgements

This work was solely funded by the Air Force Office of Scientific Research (AFOSR) under task 2303EP2 and in cooperation with DDR&E Air Plasma Ramparts MURI program.

RAINER A. DRESSLER, DALE J. LEVANDIER,*
SKIP WILLIAMS* and EDMOND MURAD

Phillips Laboratory,
PL/GPOC, Optical Effects Division,
29 Randolph Rd.,
Hanscom AFB, Massachusetts 01731-3010

References

1. J. W. Chamberlain and D. M. Hunten, *Theory of Planetary Atmospheres. An Introduction to their Physics and Chemistry*, Second Edition (Academic Press, New York).
2. D. R. Flower, *Interstellar Chemistry*, *Int. Revs. Phys. Chem.* **14**, 421 (1995).
3. R. A. Dressler and E. Murad, in *Unimolecular and Bimolecular Ion-Molecule Reaction Dynamics*, Wiley Series in Ion Chemistry and Physics, edited by C.-Y. Ng, T. Baer and I. Powis (Wiley, New York, Chichester, 1994).

* Orion International Technologies, Inc.

4. G. Gioumiosis and D. P. Stevens, *J. Chem. Phys.* **29**, 292 (1958).
5. N. F. Mott and H. S. W. Massey, *The Theory of Molecular Collisions*, 3rd ed. (Oxford, London, 1965).
6. Y. U. Demkov, *Sov. Phys. JETP* **18**, 138 (1964).
7. N. Rosen and C. Zener, *Phys. Rev.* **40**, 502 (1932).
8. D. Rapp and W. E. Francis, *J. Chem. Phys.* **37**, 2631 (1962).
9. L. D. Landau, *Phys. Z. Sowjetunion* **2**, 46 (1932).
10. C. Zener, *Proc. R. Soc. London Ser. A* **137**, 696 (1932).
11. M. F. Guest, A. Ding, J. Karlau, J. Weise and I. H. Hiller, *Mol. Phys.* **38**, 1427 (1979).
12. M. J. Bastian, R. A. Dressler and E. Murad, *J. Chem. Phys.* **103**, 144 (1995).
13. E. W. McDaniel, V. Cermak, A. Dalgarno, E. E. Ferguson and L. Friedman in *Ion Molecule Reactions* (Wiley-Interscience, New York, 1970).
14. M. Matic, V. Sidis, M. Vujovic and B. Cobic, *J. Phys. B* **13**, 3665 (1980).
15. W. L. Fite, A. C. H. Smith and R. F. Stebbings, *Proc. R. Soc. A* **268**, 527 (1963).
16. E. Bauer, E. R. Fisher and F. R. Gilmore, *J. Chem. Phys.* **51**, 4173 (1969).
17. M. R. Spalburg, J. Los and E. A. Gislason, *Chem. Phys.* **94**, 327 (1985).
18. E. A. Gislason and G. Parlant, *Comments At. Mol. Phys.* **19**, 157 (1987).
19. R. A. Dressler, J. A. Gardner, R. H. Salter and E. Murad, *J. Chem. Phys.* **96**, 1062 (1992).
20. S. T. Arnold, R. A. Dressler, M. J. Bastian, J. A. Gardner and E. Murad, *J. Chem. Phys.* **102**, 6110 (1995).
21. R. A. Dressler, S. T. Arnold and E. Murad, *J. Chem. Phys.* **103**, 9989 (1995).
22. R. F. Holland and W. B. Maier II, *J. Chem. Phys.* **55**, 1299 (1971).
23. Y. Ikezoe, S. Matsuoka, M. Takebe and A. Viggiano, *Gas Phase Ion-Molecule Reaction Rate Constants Through 1986* (Maruzen Company, Ltd., Tokyo, 1987).
24. J. B. Laudenslager, W. T. Huntress Jr. and M. T. Bowers, *J. Chem. Phys.* **61**, 4600 (1974).
25. M. McFarland, D. L. Albritton, F. C. Fehsenfeld, A. L. Schmeltekopf and E. E. Ferguson, *J. Geophys. Res.* **79**, 2005 (1974).
26. J. Glosik, A. B. Rakshit, N. D. Twiddy, N. G. Adams and D. Smith, *J. Phys. B* **11**, 3365 (1978).
27. F. C. Fehsenfeld, A. L. Schmeltekopf and E. E. Ferguson, *J. Chem. Phys.* **46**, 2019 (1967).
28. S. Matsuoka, H. Nakamura, T. Fujii and T. Tamura, *Mass Spectroscopy (Japan)* **32**, 253 (1984).
29. N. G. Adams, D. Smith and J. F. Paulson, *J. Chem. Phys.* **72**, 288 (1980).
30. D. W. Fahey, I. Dotan, F. C. Fehsenfeld, D. L. Albritton and L. A. Viehland, *J. Chem. Phys.* **74**, 3320 (1981).
31. D. W. Turner, C. Baker, A. D. Baker and C. R. Brundle, *Molecular Photoelectron Spectroscopy* (Wiley-Interscience, London, 1970).
32. O. Edqvist, E. Lindholm, L. E. Selin, H. Sjögren and L. Åsbrink, *Arkiv Fysik* **40**, 439 (1969).
33. R. A. Dressler, M. J. Bastian, D. J. Levandier and E. Murad, *Int. J. Mass Spect. Ion Proc.* **159**, 245 (1996).
34. D. E. Hunton, *Geophys. Res. Lett.* **22**, 2115 (1995).
35. K. Liou and R. B. Torbert, *J. Geophys. Res.* **100(A4)**, 5811 (1995).

Deuterium isotope effects in collision-induced dissociation and photodissociation of the $(\text{N}_2\text{O}, \text{H}_2\text{O})^+$ cluster ion

S. Williams,^{a),b)} Y.-H. Chiu, D. J. Levandier,^{b)} and R. A. Dressler^{a)}

Air Force Research Laboratory/VSBM, 29 Randolph Road, Hanscom Air Force Base, Massachusetts 01731-3010

(Received 15 December 1997; accepted 6 March 1998)

We present low energy collision-induced dissociation (CID) and visible photodissociation (PD) data of jet-cooled $(\text{N}_2\text{O}, \text{H}_2\text{O}/\text{D}_2\text{O})^+$ cluster ions. The same three fragment ions are observed in both CID and PD, namely, $\text{H}_2\text{O}^+/\text{D}_2\text{O}^+$, N_2O^+ , and $\text{N}_2\text{OH}^+/\text{N}_2\text{OD}^+$. The H_2O^+ and N_2O^+ product channels exhibit a small deuterium isotope effect in both CID (10%) and PD (15%). The N_2OH^+ product channel, on the other hand, exhibits a much larger deuterium isotope effect for CID (30%) and PD (230%). The large difference in deuterium isotope effects observed in the N_2OH^+ product channel for CID and PD suggests that this product is formed via collision-induced and photoinduced proton-transfer reactions. These results are consistent with the interpretation that a single isomeric form, namely a $(\text{N}_2\text{O} \cdot \text{H}_2\text{O})^+$ association complex, predominates. No evidence is found supporting the existence of a proton-transfer complex, i.e., $\text{N}_2\text{OH}^+ \cdot \text{OH}$. Evidence for the formation of minor amounts of a weakly bound isomeric form with the charge localized on the H_2O moiety, i.e., $\text{N}_2\text{O} \cdot \text{H}_2\text{O}^+$, is found. © 1998 American Institute of Physics. [S0021-9606(98)02622-1]

I. INTRODUCTION

Ionic clusters are present in a wide variety of environments ranging from the Earth's atmosphere to interstellar clouds,¹⁻³ and as a result, ionic clusters have been the subject of numerous investigations. Unlike their neutral counterparts, the binding energies associated with ionic clusters can be large, on the order of an electron volt. Given the large binding energies and the relatively "floppy" character of cluster ions, several isomeric forms could coexist. One such example was reported by Graul, Kim, and Bowers,⁴ who suggested that two stable isomeric forms of nitrous oxide-water cluster ion, namely $(\text{N}_2\text{O} \cdot \text{H}_2\text{O})^+$ and $\text{N}_2\text{OH}^+ \cdot \text{OH}$, are formed under thermal conditions.⁵ Their conclusion was based on photodissociation (PD) experiments and *ab initio* calculations which led the authors to suggest a binding energy for the $(\text{N}_2\text{O} \cdot \text{H}_2\text{O})^+$ association complex of 0.6–0.8 eV and a binding energy for the $\text{N}_2\text{OH}^+ \cdot \text{OH}$ proton-transfer complex that is 0.5 eV higher. In their PD experiments, H_2O^+ and N_2O^+ photoproducts were observed at visible photon energies and were attributed to photodissociation involving a common upper state surface of the $(\text{N}_2\text{O} \cdot \text{H}_2\text{O})^+$ isomeric form. A N_2OH^+ product channel was also observed and was attributed to ground state vibrational predissociation after initial excitation to a bound upper state of the $\text{N}_2\text{OH}^+ \cdot \text{OH}$ isomeric form.

In a more recent series of experiments conducted in this laboratory by Bastian *et al.*,⁶ collision-induced dissociation (CID) thresholds for the nitrous oxide-water cluster ion confirmed the existence of the $(\text{N}_2\text{O} \cdot \text{H}_2\text{O})^+$ association complex. The difference between the extracted threshold energies for the N_2O^+ and H_2O^+ products was determined, and a

value of 0.39 ± 0.13 eV was reported. This value agrees, within the experimental error, with the thermochemical predictions of 0.27 ± 0.01 eV for the energy difference of the $\text{N}_2\text{O}^+ + \text{H}_2\text{O}$ and the $\text{N}_2\text{O} + \text{H}_2\text{O}^+$ asymptotic limits. The measured CID threshold energy of 1.32 ± 0.10 eV for the N_2OH^+ product is 0.28 ± 0.12 eV higher than the H_2O^+ onset. This threshold as well is in agreement with the thermochemical prediction of 0.19 ± 0.20 eV for the energy difference of the $\text{N}_2\text{OH}^+ + \text{OH}$ and the $\text{N}_2\text{O} + \text{H}_2\text{O}^+$ asymptotic limits. Therefore, contrary to the previous PD studies,⁴ the CID thresholds can just as well be rationalized on the basis of a single isomeric form, namely, the $(\text{N}_2\text{O} \cdot \text{H}_2\text{O})^+$ association complex.

The work of Bastian *et al.* also compared measurements of cluster ions prepared in a thermal source to those prepared in a supersonic jet source. In general, the CID thresholds derived from the thermal source data agreed well with the supersonic jet source data with the exception of a weak, low energy threshold signal in the H_2O^+ channel. It was postulated that a $\text{N}_2\text{O} \cdot \text{H}_2\text{O}^+$ complex trapped in a shallow potential well outside of the charge-transfer region was responsible for the low energy signal. No differences in the product branching ratios were observed at energies above threshold between the two experiments which was interpreted as a lack of evidence for the proton-transfer complex $\text{N}_2\text{OH}^+ \cdot \text{OH}$. This conclusion was based on the reasonable assumption that since the association complex, $(\text{N}_2\text{O} \cdot \text{H}_2\text{O})^+$, and the proton-transfer complex, $\text{N}_2\text{OH}^+ \cdot \text{OH}$, have different binding energies, differences in their relative abundance, hence product branching ratios, would be expected in separate experiments where the cluster ions are produced under either thermal equilibrium or nonequilibrium conditions.

^{a)}Authors to whom correspondence should be addressed.

^{b)}Under contract to Orion International Technologies, Albuquerque, NM.

The supposition that a single isomeric form of the nitrous oxide–water cluster ion, namely $(\text{N}_2\text{O}\cdot\text{H}_2\text{O})^+$, is capable of explaining all observed fragmentation channels signifies that N_2OH^+ products are formed in collision-induced and photoinduced proton-transfer reactions. A straightforward way of confirming this interpretation is to compare the absolute cross sections and product branching ratios of the $(\text{N}_2\text{O},\text{H}_2\text{O})^+$ and $(\text{N}_2\text{O},\text{D}_2\text{O})^+$ isotopomers in both CID and PD. This statement follows from the fact that when a hydrogen or deuterium bond is broken in a rate-controlling step, the cross section for the reaction of the hydrogen compound, σ_{H} , exceeds the cross section for the same reaction of the corresponding deuterium compound, σ_{D} .⁷ Consequently, the ratio of the absolute cross sections $\sigma_{\text{H}}/\sigma_{\text{D}}$ for the two isotopomers should be greater than unity if a proton-transfer reaction is responsible for the production of N_2OH^+ , as observed in numerous proton- and hydrogen atom-transfer reactions.^{8–12} Furthermore, since CID and PD involve different potential energy surfaces, substantial differences in the deuterium isotope effect between the two methods is expected.

In the present work, CID and PD experiments are used to investigate the isomeric structure of $(\text{N}_2\text{O},\text{H}_2\text{O}/\text{D}_2\text{O})^+$ cluster ions prepared in a supersonic jet, electron-impact source. Particular attention is paid to reconciling whether the proton-transfer complex $\text{N}_2\text{OD}^+\cdot\text{OH}/\text{OD}$ and metastable $\text{N}_2\text{O}\cdot\text{H}_2\text{O}^+/\text{D}_2\text{O}^+$ complexes are formed. In Sec. II, we discuss the pertinent experimental details. In Sec. III, CID and PD data of the nitrous oxide–water cluster ion are presented. We have conducted a detailed study of discrimination effects in PD measurements in our apparatus, and the data are discussed in the context of these findings in Sec. III. The results are discussed in Sec. IV, and we present the conclusions of our findings in Sec. V.

II. EXPERIMENT

A. Supersonic jet source GIB apparatus

Cold cluster ions are produced in a pulsed, supersonic expansion source and are interrogated using a guided-ion beam apparatus described previously.^{6,13} In brief, the source gas backing pressure is approximately 4 bar, and the expansion gas consists of neat N_2O bubbled through deionized water having undergone at least three freeze–pump–thaw cycles. For the D_2O studies, the deuterium oxide- d_2 purity is 99.8% D (Kor Isotopes, Inc.), and all source components in contact with liquid H_2O are thoroughly rinsed with D_2O . The resulting gas mixture, either $\text{N}_2\text{O}/\text{H}_2\text{O}$ or $\text{N}_2\text{O}/\text{D}_2\text{O}$, is expanded through a 0.5 mm diameter orifice in a translatable nozzle (General Valve) operating at 30 Hz with a pulse duration of approximately 150 μs (FWHM). The gas pulse is crossed by a 50 eV magnetically confined electron beam to generate seed ions for cluster formation which is thought to occur early in the expansion via termolecular association reactions. The experimental conditions are carefully matched for experiments using D_2O to those of H_2O so that any differences exhibited in the CID and PD studies are unlikely to be attributable to differences in source conditions.

The ions are extracted through a 2 mm skimmer using a

10 V/cm electric field into a differentially pumped chamber containing a dc quadrupole bender and associated electrostatic ion lenses. The deflected ion beam is accelerated into a Wien velocity filter assembly for mass selection. The mass-selected cluster ion beam is decelerated and injected into a system of two octopole ion guides in tandem with lengths of 7.3 and 16.7 cm, respectively. The last 3.5 cm of the first octopole is encompassed by a collision cell which can be filled with a target gas for scattering experiments. Ions are extracted from the second octopole with a thin electrostatic lens stack and focused into a quadrupole mass filter. The filtered ions emerging from the quadrupole are deflected onto a multichannel plate, and the signal is processed using standard counting electronics.

The cluster ion beam purity and intensity depend on the distance between the nozzle orifice and the electron beam, the ion extraction field, and the N_2O backing pressure. In experiments using H_2O , less than 2% of the cluster ions are protonated, i.e., $(\text{N}_2\text{O},\text{H}_3\text{O})^+$. Less than 0.05% of the cluster ions are metastable and undergo spontaneous dissociation to produce H_2O^+ and N_2O^+ during transit between the Wien filter and the ion detector. In the case of the D_2O experiments, the cluster ion beam consists of approximately 89% $(\text{N}_2\text{O},\text{D}_2\text{O})^+$ and 10% $(\text{N}_2\text{O},\text{HOD})^+$ with the deuterated cluster ions, $(\text{N}_2\text{O},\text{D}_3\text{O})^+$ and $(\text{N}_2\text{O},\text{HOD}_2)^+$, making up the remaining 1%. Flushing the ion source supply lines and reservoir with D_2O decreased the fraction of $(\text{N}_2\text{O},\text{HOD})^+$ until the 10% level was obtained. Further D_2O rinses, however, had little effect on the fraction of $(\text{N}_2\text{O},\text{HOD})^+$ produced. The presence of a small amount of $(\text{N}_2\text{O},\text{HOD})^+$ does not preclude the accurate determination of CID and PD cross sections (see Sec. III). Less than 0.05% of the $(\text{N}_2\text{O},\text{D}_2\text{O})^+$ cluster ions undergo spontaneous dissociation.

B. Collision-induced dissociation (CID) measurements

The cluster ion kinetic energy in the collision cell is controlled by varying the dc voltage on the first octopole and collision cell with respect to the ion source. The resulting primary ion energy and energy distribution are measured using the octopole as a retarding field analyzer. The axial energy distribution of the primary ion beam is found to be nearly Gaussian with a FWHM of 0.25 eV. The dc bias potential of the second octopole is set 0.2 to 0.4 V lower than the first octopole to minimize the effect of surface potential barriers on the collection of low kinetic energy product ions. Laboratory frame kinetic energies are converted to center-of-mass (CM) kinetic energies using the stationary target approximation, $E_{\text{CM}} = E_{\text{lab}} \cdot m/(m+M)$, where m and M are the masses of the neutral target and primary ion, respectively.

A mass spectrum of the primary and product ions is obtained at each collision energy and is converted to an absolute integral reaction cross section by

$$\sigma_i = \frac{I_{\text{prod},j}}{(I_{\text{prim}} + \sum_j I_{\text{prod},j})nl}, \quad (1)$$

where I_{prim} is the primary cluster ion signal, n is the number density of the target neutral, $I_{\text{prod},j}$ is the ion signal of prod-

uct i , and l is the effective length of the collision cell. Equation (1) is valid for cross sections measured under single collision conditions. In the present experiments, no pressure dependence was observed for any of the CID cross sections for argon gas pressures below 0.35 mTorr, and typical argon gas operating pressures were 0.25 mTorr. The absolute accuracy of the integral cross sections is estimated to be $\pm 30\%$. The relative error between the $(\text{N}_2\text{O}, \text{H}_2\text{O})^+$ and $(\text{N}_2\text{O}, \text{D}_2\text{O})^+$ cluster measurements is less than $\pm 10\%$.

C. Photodissociation (PD) measurements

Excitation is provided by a Nd:YAG pumped, broadband optical parametric oscillator (OPO) laser system (Quanta Ray GCR-170 and MOPO-710) operated over the wavelength range of 450–660 nm (signal) with an average bandwidth over this range of approximately 10 cm^{-1} (1 meV) and a temporal pulse width of approximately 7 ns. The output of the OPO passes through a series of apertures and a reducing telescope to produce a beam collimated over approximately 2 m with a minimum beam waist of 1.75 mm. The laser beam and ion beam propagate collinearly down the octopole axis. The minimum beam waist of the laser beam is located at the midpoint of the first octopole. The laser energy is attenuated with neutral density filters to obtain output energies in the 0.2 to 0.7 mJ/pulse range. The photofragment yield over this energy range is observed to be linear with a zero intercept which indicates that the photofragments are produced by single-photon processes. A variable delay generator (SRS DG 535), triggered by the TTL output of the pulsed valve driver (General Dynamics IOTA one), triggers the flashlamps of the Nd:YAG laser and a symmetric pulse forming network used to gate the primary ion beam (20 μs FWHM). The Q-switch of the Nd:YAG laser is internally triggered, and the delay generator is set so that the laser pulse intercepts the gated ion beam at the midpoint of the first octopole.

Photodissociation action spectra are obtained by recording the primary cluster ion signal, the secondary ion signals, and the laser power while scanning the OPO wavelength. The cross section for one-photon dissociation into photofragment i is given by

$$\sigma_i = \frac{I_{\text{prod},i}/d_i}{(cI_{\text{prim}} + \sum_j I_{\text{prod},j}/d_j)\Phi}, \quad (2)$$

where I_{prim} and $I_{\text{prod},i}$ are as defined previously, d_i is the fractional collection efficiency of product i , and c is the fraction of the primary cluster ions exposed to the time integrated photon flux Φ . For primary beam energies from 1.5 to 4 eV, the 20 μs primary ion time profile corresponds to a spatial profile ranging from 4 to 7 cm, respectively. Under these conditions all of the primary ions are in the first octopole during the laser pulse. A fraction of the ions along the radial direction lie outside of the laser beam, however, and it is these ions for which the c factor provides a correction in Eq. (2).

The fraction of primary ions exposed to the time integrated photon flux Φ is evaluated using two-dimensional ion trajectory calculations.¹⁴ The transverse energy distribution of the primary ion beam is determined using a radio fre-

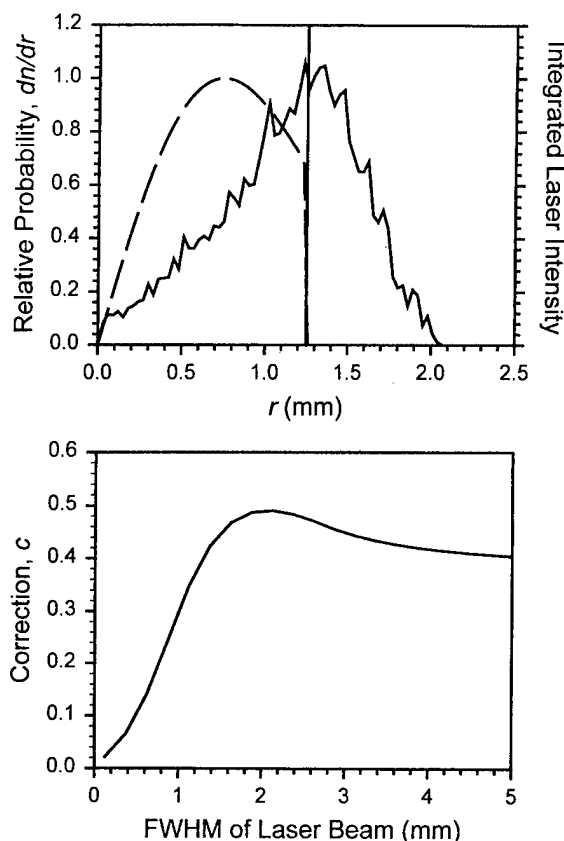


FIG. 1. (a) Average ion probability density, dn/dr , for $m/q=62$, 0.07 eV transverse kinetic energy ions as a function of radial position (solid line) and integrated Gaussian beam radial profile of 1.75 mm FWHM (dashed line). The vertical line shows the radial position of the 2.5 mm diameter injection lens aperture. (b) Cross section correction, c , versus FWHM of laser beam for the average ion probability density shown in (a) when the laser power is measured at the exit port of the chamber.

quency amplitude analysis in which the primary beam transmission is measured as a function of octopole rf voltage.¹⁵ The average transverse kinetic energy is approximately 0.07 eV, and this value is used in the calculations. The solid line of Fig. 1(a) shows the average ion probability density, dn/dr , for $m/z=62$ versus radial position.¹⁶ The vertical line shows the position of the 2.5 mm diam injection lens aperture, and the dashed line is the intensity profile for a Gaussian laser beam of 1.75 mm FWHM integrated over the area element $rdrd\theta$. If the laser power is measured at the exit port of the chamber, Fig. 1(b) shows the dependence of the laser FWHM and injection lens aperture on the correction factor c . Laser beams with FWHM larger than the injection aperture interact more strongly with a larger number of ions but are clipped extensively along the ion beam axis producing stray ions at the detector. Laser beam diameters of 1.5 to 2 mm are used in this study, because beams of this size propagate through the chamber with minimal clipping and interact with a large fraction, approximately 47%, of the primary ions. Because of the many assumptions made to calculate c , the integrated PD cross sections are associated with substantial uncertainties. The estimated error is $\pm 50\%$ for the absolute cross sections and $\pm 20\%$ for the relative measurements.

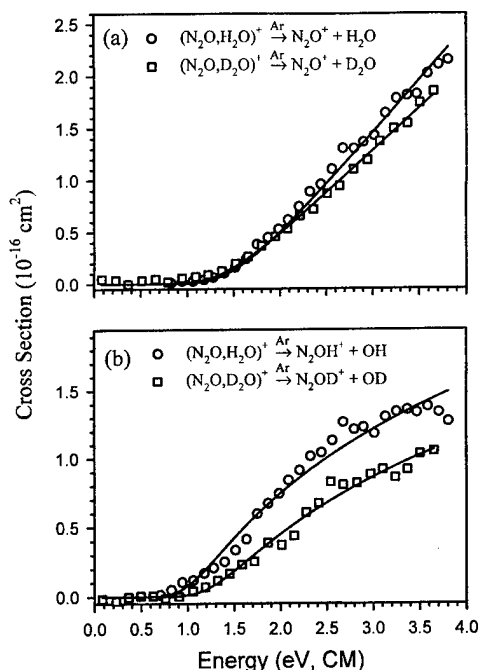


FIG. 2. (a) Center-of-mass collision energy dependence of cross sections for the production of the N_2O^+ fragments formed in the CID of $(\text{N}_2\text{O}, \text{H}_2\text{O})^+$ (circles) with Ar and $(\text{N}_2\text{O}, \text{D}_2\text{O})^+$ (squares) with Ar. The solid lines are calculated CID curves using the parameters listed in Table II, Ref. 6 ($E_0 = 1.39 \text{ eV}$, $n = 1.83$). (b) Cross sections for the production of the N_2OH^+ fragment formed in the CID of $(\text{N}_2\text{O}, \text{H}_2\text{O})^+$ (circles) and the N_2OD^+ fragment formed in the CID of $(\text{N}_2\text{O}, \text{D}_2\text{O})^+$ (squares) with Ar. The solid lines are calculated CID curves using the parameters listed in Table II, Ref. 6 ($E_0 = 1.32 \text{ eV}$, $n = 1.33$).

III. RESULTS

A. Collision-induced dissociation (CID) experiments

The fragment ions produced in low energy CID of $(\text{N}_2\text{O}, \text{H}_2\text{O})^+$ with Ar are H_2O^+ , N_2O^+ , and N_2OH^+ as pre-

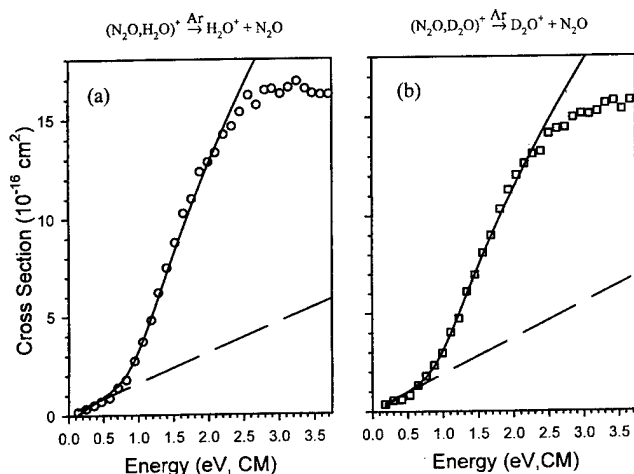


FIG. 3. (a) Center-of-mass collision energy dependence of cross sections and generated dissociation threshold curves for the H_2O^+ fragment (a) and D_2O^+ fragment (b) formed in the CID of $(\text{N}_2\text{O}, \text{H}_2\text{O})^+$ and $(\text{N}_2\text{O}, \text{D}_2\text{O})^+$ with Ar, respectively. The dissociation threshold curves in (a) and (b) are generated using the thermal source parameters listed in Table II, Ref. 6 ($E_0 = 1.06 \text{ eV}$, $n = 1.34$) and a low energy threshold of $E_0 = 0 \text{ eV}$, $n = 2$ (dashed line).

viously reported.⁶ Similarly, the fragment ions observed in the CID of $(\text{N}_2\text{O}, \text{D}_2\text{O})^+$ cluster ions with Ar are D_2O^+ , N_2O^+ , and N_2OD^+ . Figures 2 and 3 show the cross sections for the N_2O^+ , $\text{N}_2\text{OH}^+/\text{N}_2\text{OD}^+$, and $\text{H}_2\text{O}^+/\text{D}_2\text{O}^+$ fragments formed in the argon CID studies as a function of center-of-mass collision energy. The H_2O^+ and N_2O^+ fragmentation channels exhibit a small deuterium isotope effect (10%) while a significantly larger isotope effect (30%) is observed for the N_2OH^+ fragmentation channel. The data shown in Figs. 2 and 3 have been corrected for the small metastable dissociation and chamber background gas contribution to the observed cross sections by subtracting a background scan from the raw data. High resolution mass scans show that the 10% of $(\text{N}_2\text{O}, \text{HOD})^+$ present in the $(\text{N}_2\text{O}, \text{D}_2\text{O})^+$ CID experiments produces HOD^+ and N_2OH^+ with cross sections approximately equal to those for the equivalent fragmentation channels of the $(\text{N}_2\text{O}, \text{H}_2\text{O})^+$ cluster ion. Note that the cross section for the N_2OH^+ fragmentation channel for clusters with HOD is half that for clusters with H_2O as expected statistically. We are unable to determine conclusively whether N_2O^+ and N_2OD^+ are produced in the CID of $(\text{N}_2\text{O}, \text{HOD})^+$. We make the reasonable assumption, however, that the cross section for the production of N_2O^+ from $(\text{N}_2\text{O}, \text{HOD})^+$ is the same as that from $(\text{N}_2\text{O}, \text{D}_2\text{O})^+$, and that the cross section for the production of N_2OD^+ from $(\text{N}_2\text{O}, \text{HOD})^+$ is one half that from $(\text{N}_2\text{O}, \text{D}_2\text{O})^+$. These assumptions lead to approximately a 10% and a 5% reduction in the observed N_2O^+ and N_2OD^+ cross sections, respectively. The assumptions made in these corrections are rationalized by the relatively small differences in the CID cross sections of the different isotopomers.

The solid lines in Figs. 2 and 3 are calculated dissociation threshold curves obtained using the modified line-of-centers functional form¹⁷⁻¹⁹ convoluted with the experimental kinetic energy distribution.⁶ The parameters used in the modified line-of-centers model for the $(\text{N}_2\text{O}, \text{H}_2\text{O})^+$ cluster ion experiments are given in Table II of Ref. 6. Isotope shifts in the dissociation thresholds for the $(\text{N}_2\text{O}, \text{D}_2\text{O})^+$ cluster ion have been calculated to be in the 0.01 to 0.06 eV range and result primarily from the differences in the zero point energies of the reactants and products.²⁰ Energy shifts of this magnitude are difficult to distinguish in these data where a fitting accuracy of 0.15 eV determined by the signal-to-noise ratio is realized. For this reason, the threshold energy, E_0 , and curvature, n , parameters used to generate the $(\text{N}_2\text{O}, \text{D}_2\text{O})^+$ cluster ion dissociation threshold curves are the same as those used to generate the $(\text{N}_2\text{O}, \text{H}_2\text{O})^+$ cluster ion dissociation threshold curves. The scaling parameter, σ_0 , is adjusted for each data set to give the best agreement. In a previous publication,⁶ we noted that the threshold model parameters determined from completely thermalized cluster ions failed to reproduce the H_2O^+ cross sections of the jet source experiments and that a second threshold function needed to be added to properly reproduce the jet source CID curves. The results of the combined model are shown in Fig. 3 which demonstrates that the two threshold model is necessary to explain the cross sections for the D_2O^+ fragmentation channel [Fig. 3(b)] as well.

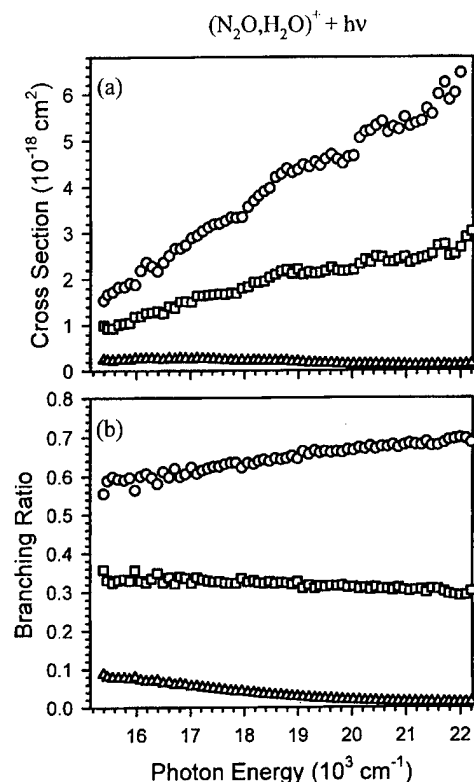


FIG. 4. (a) Photodissociation cross sections of $(\text{N}_2\text{O}, \text{H}_2\text{O})^+$ cluster ions as a function photon energy. (b) Photodissociation branching ratios as a function of photon energy. In both (a) and (b), the H_2O^+ photoproduct channel is denoted by circles, the N_2O^+ photoproduct channel is denoted by squares, and the N_2OH^+ photoproduct channel is denoted by triangles.

B. Photodissociation (PD) experiments

The photofragment ions formed when irradiating $(\text{N}_2\text{O}, \text{H}_2\text{O})^+$ and $(\text{N}_2\text{O}, \text{D}_2\text{O})^+$ cluster ions with visible light are the same as those produced in low-energy CID. Figs. 4(a) and 5(a) show the absolute PD cross sections for the formation of these products between 15 151 and 22 222 cm^{-1} (660 to 450 nm), and Figs. 4(b) and 5(b) show the same data represented as branching ratios. As in the CID experiments, the N_2O^+ and N_2OD^+ cross sections of Fig. 5(a) have been reduced by approximately 10% and 5%, respectively, to correct for the presence of $(\text{N}_2\text{O}, \text{HOD})^+$ in the $(\text{N}_2\text{O}, \text{D}_2\text{O})^+$ experiments.

The cross sections for the N_2O^+ and N_2OH^+ photoproduct channels are essentially the same as previously reported by our laboratory.⁶ However, the cross sections for the H_2O^+ photoproduct channel are two times those reported previously by our laboratory⁶ and three times those reported by Gaul *et al.*⁴ The amount of H_2O^+ collected in the experiments of Gaul *et al.* is calculated from their reported branching ratios, approximately 0.35 for H_2O^+ , with the assumption that there was no discrimination of the other photoproduct channels. By varying the extraction lens aperture sizes and voltages, we confirmed that the larger H_2O^+ cross sections, in comparison to the previous work of this laboratory, are due to an improved extraction lens assembly. The extraction losses are due to the fact that the H_2O^+ photoproduct ion can exit the second octopole with transverse veloci-

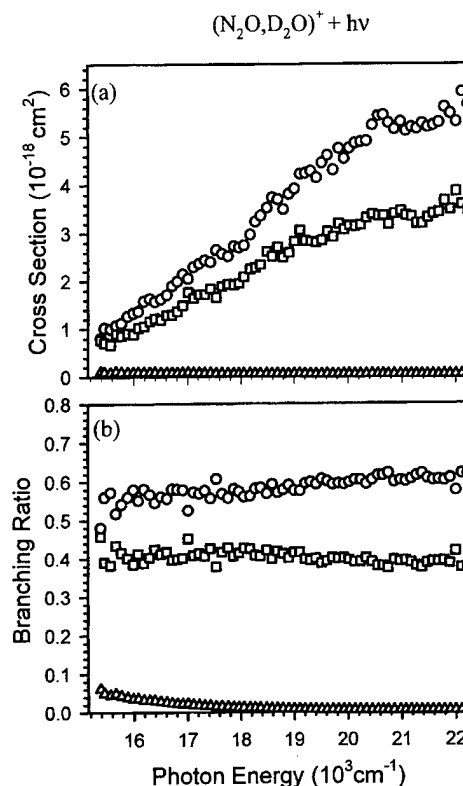


FIG. 5. (a) Photodissociation cross sections of $(\text{N}_2\text{O}, \text{D}_2\text{O})^+$ cluster ions as a function photon energy. (b) Photodissociation branching ratios as a function of energy. In both (a) and (b), the D_2O^+ photoproduct channel is denoted by circles, the N_2O^+ photoproduct channel is denoted by squares, and the N_2OD^+ photoproduct channel is denoted by triangles.

ties of several thousand meters per second. By performing radio frequency amplitude scans, it is determined that the H_2O^+ product ion is collected at 97% efficiency at 15 151 cm^{-1} (660 nm) and 74% efficiency at 22 222 cm^{-1} (450 nm) with an approximately linear decrease in collection efficiency between these two extremes.¹⁵ The N_2O^+ and N_2OH^+ products are collected with 100% efficiency over the entire energy range. The cross section and branching ratio data of Figs. 4 and 5 have been corrected for discrimination. The correction for the D_2O^+ photoproduct channel is calculated from the H_2O^+ data taking into consideration the increased mass on the instrument function and with the assumption that the kinetic energy release distribution as a function of photon energy is the same for H_2O^+ and D_2O^+ .^{4,15} The net result is that the H_2O^+ and D_2O^+ ions are now observed to be the major photoproducts contrary to previous observations.

In general, the photodissociation action spectra and branching ratios are very similar for both isotopomers. The most pronounced feature in Figs. 4 and 5 is the marked difference in the PD cross sections of the N_2OH^+ and the N_2OD^+ photoproducts. The comparison in the photodissociation action spectra is made clear in Fig. 6 where the ratio of the PD cross sections, $\sigma_{\text{H}}/\sigma_{\text{D}}$, for each photoproduct channel are shown over the energy range from 15 151 to 22 222 cm^{-1} (660 to 450 nm). Whereas the average cross sections for the water ions and nitrous oxide ions are within

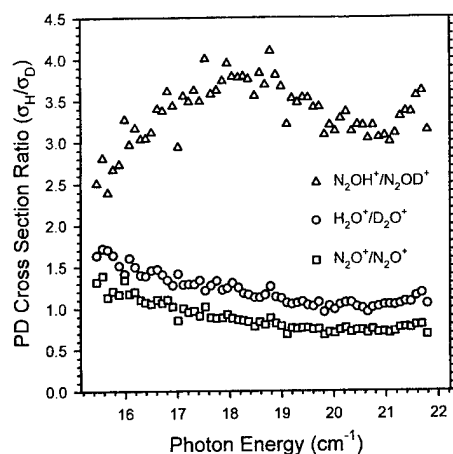


FIG. 6. Isotopic photodissociation cross section ratio, $\sigma(\text{N}_2\text{O}, \text{H}_2\text{O})^+/\sigma(\text{N}_2\text{O}, \text{D}_2\text{O})^+$, for all photodissociation fragmentation channels as a function of photon energy. In the figure, the $\text{H}_2\text{O}^+/\text{D}_2\text{O}^+$ photoproduct channel ratio (1.16 average) is denoted by open circles, the N_2O^+ photoproduct channel ratio (0.89 average) is denoted by squares, and the $\text{N}_2\text{OH}^+/\text{N}_2\text{OD}^+$ photoproduct channel ratio (3.3 average) is denoted by triangles.

16% for the two isotopomers over this range, the N_2OH^+ average cross sections are approximately 230% larger than those for the formation of N_2OD^+ . This cross section difference is clearly outside of the relative error limits of the experiment, and this isotope effect is substantially higher than that observed in CID.

IV. DISCUSSION

The H_2O^+ and N_2O^+ fragmentation channels exhibit a small isotope effect of approximately 10% in the CID studies. The N_2OH^+ fragmentation channel, on the other hand, exhibits a larger isotope effect of approximately 30% ($\sigma_{\text{H}}/\sigma_{\text{D}} = 1.3$). With regard to PD, the photodissociation action spectra of the H_2O^+ and N_2O^+ fragments are very similar in both shape and intensity for both isotopomers. The most significant isotope effect observed in this study, 230% ($\sigma_{\text{H}}/\sigma_{\text{D}} = 3.3$), is observed in the N_2OH^+ photoproduct channel. Since N_2O is coexpanded with H_2O in a supersonic jet crossed by an electron beam, the observation of a N_2OH^+ fragment must be preceded by a proton-transfer reaction in both CID and PD. This conclusion is supported by the fact that the deuterium isotope effect for this product channel is significantly greater than unity.⁷⁻¹² The proton-transfer reaction can either occur during the cluster ion formation in the source region whereby the reaction products are incorporated into a proton-transfer complex, as suggested by Graul *et al.*, or the proton transfer occurs in the octopole ion guide signifying that the reaction is either collision-induced or photoinduced, as suggested by Bastian *et al.*

In the first case, the cluster ion formation dynamics results in different isomeric production ratios of $(\text{N}_2\text{O} \cdot \text{H}_2\text{O})^+/\text{N}_2\text{OH}^+ \cdot \text{OH}$ and $(\text{N}_2\text{O} \cdot \text{D}_2\text{O})^+/\text{N}_2\text{OD}^+ \cdot \text{OD}$. This isotope effect is a combination of both primary and secondary isotope effects and merely represents the different population of two isomeric forms for each isotopomer. The isotope effect exhibited in the subsequent dissociation reac-

tions would be entirely secondary in nature. Given the small secondary isotope effects observed in the H_2O^+ and N_2O^+ product channels, this scenario suggests that very similar isotope effects would be observed in the CID and PD N_2OH^+ fragmentation channels if no isomerization occurs following a collision or the absorption of a photon. The large differences in isotope effects observed in the CID and PD studies contradict this scenario and lead to the conclusion that a large fraction of the N_2OH^+ yield cannot be attributed to collision-induced or photoinduced dissociation of a $\text{N}_2\text{OH}^+ \cdot \text{OH}$ isomeric form. Substantial differences in the primary and secondary deuterium isotope effects between the two experimental methods, on the other hand, are consistent with the second case. This statement follows from the fact that the proton-transfer dynamics in CID and PD involve different potential energy surfaces as well as different areas of common surfaces. Therefore, the observed deuterium isotope effects invoke the interpretation that N_2OH^+ products are primarily formed in collision-induced and photoinduced proton-transfer reactions. This conclusion is confirmed by recent *ab initio* calculations by Stevens and Morokuma²¹ which determine that the $\text{N}_2\text{OH}^+ \cdot \text{OH}$ isomer is significantly more energetic than the $(\text{N}_2\text{O} \cdot \text{H}_2\text{O})^+$ isomer and that the $\text{N}_2\text{OH}^+ \cdot \text{OH}$ isomer may represent a local minimum on the global potential energy surface.

The observed dissociation dynamics are thus primarily associated with a $(\text{N}_2\text{O} \cdot \text{H}_2\text{O})^+$ complex. Evidence for an additional structure is represented by the previously reported⁶ weak, low-energy threshold behavior in the H_2O^+ fragmentation channel and confirmed in this work for both isotopomers. This effect is not observed in thermal source experiments.⁶ Unrelaxed vibrational excitation in the supersonic jet source does not appear to be a plausible explanation for the low-energy signal since vibrational energy would be expected to affect the N_2O^+ and $\text{N}_2\text{OH}^+/\text{N}_2\text{OD}^+$ thresholds as well. The N_2O^+ and $\text{N}_2\text{OH}^+/\text{N}_2\text{OD}^+$ CID curves shown in Fig. 2, however, agree well with the threshold function determined in the thermal source experiment of Ref. 6. Whereas almost complete charge-sharing is determined from *ab initio* calculations by Stevens and Morokuma²¹ for the $(\text{N}_2\text{O} \cdot \text{H}_2\text{O})^+$ structure, the calculations also identify a local minimum attributable to a weakly bound, hydrogen bonded form of the cluster with the charge localized on the water moiety. Such a metastable cluster ion or one similar to it is likely to be responsible for the low energy threshold signal observed in the H_2O^+ and D_2O^+ fragmentation channels.

V. CONCLUSIONS

In the present work we demonstrate that the combination of CID and PD experiments provide an excellent means of elucidating the isomeric structure of cluster ions. Isotope effects in the low energy CID and PD of jet-cooled $(\text{N}_2\text{O} \cdot \text{H}_2\text{O}/\text{D}_2\text{O})^+$ cluster ions have been evaluated. The same three ionic products are formed in both CID and PD, namely, $\text{H}_2\text{O}^+/\text{D}_2\text{O}^+$, N_2O^+ , and $\text{N}_2\text{OH}^+/\text{N}_2\text{OD}^+$. The H_2O^+ and N_2O^+ product channels exhibit a small deuterium isotope effect in both CID (10%) and PD (15%). The N_2OH^+ product channel, on the other hand, exhibits a much larger isotope effect for CID (30%) and PD (230%). The large dif-

ference in the deuterium isotope effect observed for N_2OH^+ fragments in CID and PD suggests that these products are formed in collision-induced and photoinduced proton-transfer reactions. These results are consistent with the interpretation that a single isomeric form of the nitrous oxide-water cluster ion, namely $(\text{N}_2\text{O}\cdot\text{H}_2\text{O})^+$ and $(\text{N}_2\text{O}\cdot\text{D}_2\text{O})^+$, is primarily responsible for the observed fragment ion yields when formed in a supersonic jet expansion. As for the $(\text{N}_2\text{O},\text{H}_2\text{O})^+$ isotopomer, evidence for a weakly bound isomeric form of the $(\text{N}_2\text{O},\text{D}_2\text{O})^+$ cluster ion, namely $\text{N}_2\text{O}\cdot\text{D}_2\text{O}^+$, was observed. All the data for both isotopomers can be explained without invoking the formation of a proton-transfer complex, i.e., $\text{N}_2\text{OH}^+\cdot\text{OH}$ and $\text{N}_2\text{OD}^+\cdot\text{OD}$. Our conclusion that this isomeric form is not produced to a significant degree is supported by recent *ab initio* calculations by Stevens and Morokuma.²¹

Photodissociation cross sections presented here for the H_2O^+ photoproduct are significantly larger than those reported previously. We attribute the difference to discrimination in the previous studies.^{4,6} The amount of discrimination was determined by performing radiofrequency amplitude scans. The details of this approach as well as methods enabling the determination of photoproduct kinetic energy and angular distributions in octopole ion guides will be discussed in a future publication.¹⁵

ACKNOWLEDGMENTS

The authors are grateful to Jon Stevens and Keiji Morokuma for communicating their theoretical results prior to publication and for helpful discussions, Susan T. Gaul for suggesting the isotope study, and Edmond Murad for helpful discussions. This work was supported by AFOSR under Task 2303EP2. Y.-H. Chiu is an NRC postdoctoral fellow.

¹E. E. Ferguson, F. C. Fehsenfeld, and D. L. Albritton, in *Gas Phase Ion Chemistry*, Vol. 1, edited by M. T. Bowers (Academic, New York, 1979), pp. 45–82.

²D. Smith and N. G. Adams, *Top. Curr. Chem.* **89**, 1 (1980).

³W. W. Duley, *Astrophys. J.* **471**, L57 (1996).

⁴S. T. Gaul, H.-S. Kim, and M. T. Bowers, *Int. J. Mass Spectrom. Ion Processes* **117**, 507 (1992).

⁵In what follows, $(\text{N}_2\text{O},\text{H}_2\text{O})^+$ refers to all isomeric forms of the nitrous oxide-water cluster ion, $(\text{N}_2\text{O}\cdot\text{H}_2\text{O})^+$ refers to the nitrous oxide-water association complex, $\text{N}_2\text{OH}^+\cdot\text{OH}$ refers to the nitrous oxide-water proton-transfer complex, and $\text{N}_2\text{O}\cdot\text{H}_2\text{O}^+$ refers to a weakly bound form of the nitrous oxide-water cluster ion with the charge localized on the water moiety. The same nomenclature is applicable to the deuterated isotopomers.

⁶M. J. Bastian, R. A. Dressler, D. J. Levandier, and E. Murad, *J. Chem. Phys.* **106**, 9570 (1997).

⁷F. H. Westheimer, *Chem. Rev.* **61**, 265 (1961).

⁸W. Tumas, R. F. Foster, M. J. Pellerite, and J. I. Brauman, *J. Am. Chem. Soc.* **109**, 961 (1987).

⁹G. Laguzzi, T. H. Osterheld, and J. I. Brauman, *J. Phys. Chem.* **98**, 5931 (1994).

¹⁰D. J. Levandier, R. A. Dressler, and E. Murad, *Chem. Phys. Lett.* **251**, 174 (1996).

¹¹C. E. Johnson, K. A. Sannes, and J. I. Brauman, *J. Phys. Chem.* **100**, 8827 (1996).

¹²E. M. Snyder and A. W. Castleman, Jr., *J. Chem. Phys.* **107**, 744 (1997).

¹³R. A. Dressler, R. H. Salter, and E. Murad, *J. Chem. Phys.* **99**, 1159 (1993).

¹⁴D. A. Dahl, SIMION 6.0 ed. (Idaho National Engineering Laboratory, Idaho Falls, 1995).

¹⁵S. Williams, Y.-H. Chiu, R. A. Dressler, D. J. Levandier, and E. Murad (*in preparation*, 1998).

¹⁶The average ion probability density is calculated assuming that the ion beam radial profile is Gaussian and that the injection aperture diameter is less than the FWHM of the ion beam. In this case, the injected radial ion distribution is approximately proportional to the radial displacement from the ion beam axis. Trajectories were run for 4 initial radial positions (all less than the injection lens aperture radius) with 12 starting angles at each position, and each trajectory included a minimum of six reflections to ensure statistically significant sampling.

¹⁷R. H. Schultz, K. C. Crellin, and P. B. Armentrout, *J. Am. Chem. Soc.* **113**, 8590 (1991).

¹⁸F. A. Khan, D. E. Clemmer, R. H. Schultz, and P. B. Armentrout, *J. Phys. Chem.* **97**, 7978 (1993).

¹⁹P. B. Armentrout, in *Advances in Gas Phase Ion Chemistry*, Vol. 1, edited by N. G. Adams and L. M. Babcock (JAI, Greenwich, 1992), pp. 83.

²⁰Calculations were performed at the UB3LYP/6-31G(d) level using GAUSSIAN 94, Revision D1 by M. J. Frisch, G. W. Trucks, H. B. Schlegel, P. M. W. Gill, B. G. Johnson, M. A. Robb, J. R. Cheeseman, T. Keith, G. A. Petersson, J. A. Montgomery, K. Raghavachari, M. A. Al-Laham, V. G. Zakrzewski, J. V. Ortiz, J. B. Foresman, J. Cioslowski, B. B. Stefanov, A. Nanayakkara, M. Challacombe, C. Y. Peng, P. Y. Ayala, W. Chen, M. W. Wong, J. L. Andres, E. S. Replogle, R. Gomperts, R. L. Martin, D. J. Fox, J. S. Binkley, D. J. Defrees, J. Baker, J. P. Stewart, M. Head-Gordon, C. Gonzalez, and J. A. Pople (Gaussian, Inc., Pittsburgh PA, 1995).

²¹J. Stevens and K. J. Morokuma (personal communication, 1997).

Collision energy dependence and product recoil velocity analysis of $O^+(^4S) + C_2H_2$ charge-transfer and chemical reaction channels

Yu-hui Chiu, Rainer A. Dressler, Dale J. Levandier,^{a)} Skip Williams,^{a)} and Edmond Murad
*Air Force Research Laboratory/VSBM, 29 Randolph Road, Hanscom Air Force Base,
 Massachusetts 01731-3010*

(Received 28 April 1998; accepted 29 June 1998)

Guided-ion beam cross section and product ion time-of-flight (TOF) measurements are presented for the $O^+(^4S) + C_2H_2$ reaction over the center-of-mass collision energy range of 0.05–18 eV. Despite a large number of exothermic channels, the total reaction cross section at low energies is more than two orders of magnitude smaller than the capture cross section. A common energy onset for charge-transfer, CH^+ , and COH^+/HCO^+ products is observed at 1.70 ± 0.10 eV, above which the total cross section for these channels rapidly rises with energy, eventually exceeding 5 \AA^2 . Above 4 eV, the C_2H^+ and CO^+ products also become significant, and weaker channels producing C^+ , C_2^+ , and CH_2O^+ are also identified. The C_2H^+ fragment is interpreted as being primarily a dissociative charge transfer (CT) channel at collision energies above ~ 3.79 eV, while the threshold for forming CO^+ can be associated with a $CO^+ + H + CH$ channel. The TOF measurements demonstrate that efficient $C_2H_2^+ \tilde{A}$ state formation occurs above ~ 2.7 eV. The onset at 1.70 ± 0.10 eV is attributed to a transition state associated with an excited quartet hypersurface. © 1998 American Institute of Physics. [S0021-9606(98)02237-5]

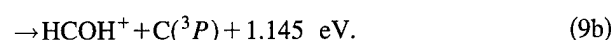
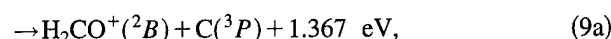
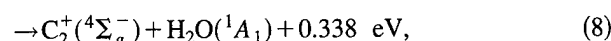
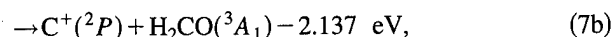
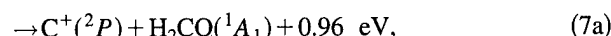
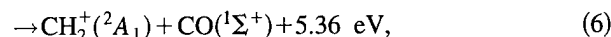
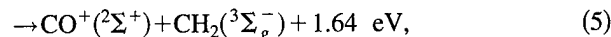
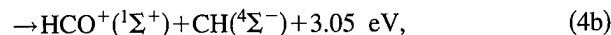
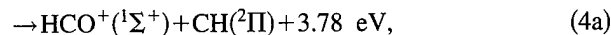
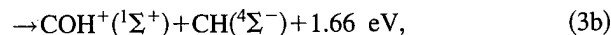
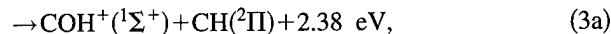
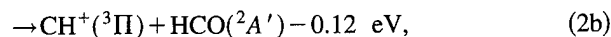
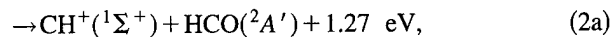
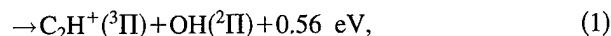
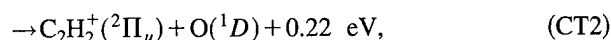
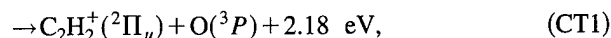
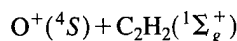
I. INTRODUCTION

The study of gas-phase ion–molecule reactivity over a wide range of collision energies has provided valuable insight into chemical reaction dynamics. In particular, the guided-ion beam (GIB) technique¹ coupled with product recoil time-of-flight (TOF) analysis² has allowed accurate assessment of the competition between direct and complex-mediated dynamics as the translational energy is varied. In recent years, the detailed dynamics of ion chemistry involving small polyatomic organic molecules has attracted considerable interest. Organic ion–molecule collision complexes usually have multiple deep potential wells associated with covalently bound organic molecular ions. In some reactions, these intermediates strongly affect the dynamics, particularly at low collision energies, in others there is no evidence that the stable intermediates have any bearing on the outcome of the reaction throughout the investigated collision energy range.

Recent experiments indicate that the degree of coupling to the charge-transfer surface may be a determining factor on the role of stable intermediates. In reaction systems such as $C_2H_2^+ + CH_4$ and $C^+ + C_2H_6$, where charge-transfer is an endothermic process, guided-ion beam or crossed-beam experiments have demonstrated that longer-lived complexes are important at low collision energies and that products associated with the dissociation of covalently bound intermediates are observed.^{3,4} In the reactions of $C_2H_2^+ + ND_3$ and $C_2H_2^+ + CH_3OH$, however, charge transfer is exothermic and only charge transfer and simple hydrogen atom, proton or hydride ion transfer products, formed primarily in direct

long-range encounters, are observed in the collision energy range (~ 0.1 –5 eV).^{5,6}

In light of these arguments, the $O^+(^4S) + C_2H_2$ reaction may represent an interesting intermediate case. This reaction has two exothermic charge-transfer channels (CT1 and CT2) and a large number of near thermoneutral and exothermic reaction channels with the following energetics (298 K):^{7–10}



^{a)}Orion International Technologies, Inc., Albuquerque, NM 87110.

Although the exothermicities suggest that the charge transfer channels (CT1) and (CT2) and the H^- transfer reaction (1) are dominant and thus could obscure dynamics attributable to short-range interactions, this is not necessarily the case because both exothermic charge-transfer surfaces are anticipated to be very poorly coupled to the reactants at long range due to negligible Franck-Condon factors in (CT1) and a spin-forbidden electronic transition in (CT2). Similar to the $O^+(^4S) + HCN$ system studied in our laboratory,¹¹ where charge-transfer is essentially thermoneutral, competition between charge transfer and the chemically reactive channels (1)–(9) may be expected.

Apart from the interesting chemical kinetic aspects of this reaction, we are also motivated by a continued effort to investigate the important hyperthermal ion-molecule reactions that occur in the spacecraft environment.^{12,13} At an altitude of ~ 300 km, where spacecraft in low-Earth orbit travel at an orbital velocity of ~ 7.8 km/s, the $O^+(^4S)$ ions are the dominant ionic species in the atmosphere. These atomic ions interact with engine exhaust molecules such as HCN and C_2H_2 ^{14,15} producing molecular ions that either undergo secondary or dissociative recombination reactions. Dissociative recombination reactions are the source of ionospheric holes and optical radiation.¹⁶

In this work, we present GIB cross section measurements for the $O^+(^4S) + C_2H_2$ reaction over the collision energy range of 0.05–18 eV. The integral cross sections of important channels are complemented with a product recoil velocity analysis using the GIB-TOF technique. The combined results provide a comprehensive picture of a reaction system that is strongly hindered on the ground-state surface of the reactants, but turns on efficiently following passage of a transition state associated with an excited-state charge-transfer surface.

II. EXPERIMENT

The guided-ion beam apparatus and data analysis methods have been described in detail previously.¹⁷ Only a brief description is given here. A beam of ground-state $O^+(^4S)$ is produced by the dissociation of CO_2 with 20.5 eV electrons in an electron impact source. This low electron energy avoids formation of the electronically excited $O^+(^2D)$ and $O^+(^2P)$ states,^{18,19} which lie ~ 3.32 and 5.02 eV above the $O^+(^4S)$ appearance potential of 19.1 eV, respectively.^{20,21} We estimate the beam to be $>98\%$ pure ground-state ion. This is confirmed by carefully checking for cross-section dependences on electron energy.

The O^+ primary ion beam has a ~ 0.2 eV full width at half maximum (FWHM) energy spread and is mass selected by a Wien velocity filter before injection into a series of two radio frequency (rf) octopole ion guides.² An rf amplitude of ~ 130 V at ~ 10 MHz is applied to the octopole rods to trap the ions and ensure 100% ion collection efficiency. The first octopole ion guide has a length of 7.4 cm, the last 3.5 cm of which is encompassed by a collision cell containing the target gas. To ensure single collision conditions, a C_2H_2 gas pressure of ~ 0.18 mTorr is employed. The C_2H_2 (Matheson, 99.6%) is passed through a cold trap to remove an acetone impurity.

Both the unreacted primary and product ions are guided into a second, 16.7 cm long, octopole which is biased ~ 0.3 – 0.4 eV lower than the first octopole. This bias accelerates slow product ions to kinetic energies sufficient to overcome local barriers resulting from the inhomogeneities of rod surface potentials. When necessary, a positive potential of ~ 30 – 50 V is applied to a cylindrical ring electrode surrounding the octopole at the entrance of the collision cell, producing a small potential barrier of ~ 60 – 100 mV that reflects laboratory backscattered ions into the forward direction. At the exit of the second octopole, all ions are extracted and focused into a quadrupole mass analyzer. The mass-selected ions are then detected by an off-axis microchannel plate (MCP) or a channel electron multiplier.

The collision energy is varied by changing the direct current (dc) bias of the collision cell and octopole assembly with respect to the ion source. The absolute integral cross section for product i , σ_i , is determined from the following equation:

$$\sigma_i = \frac{I_{\text{prod},i}}{\left(I_{\text{prim}} + \sum_i I_{\text{prod},i} \right) nl}, \quad (10)$$

where I_{prim} is the primary ion O^+ intensity, n is the number density of the neutral C_2H_2 target, $I_{\text{prod},i}$ is the ion intensity of product i , and l is the effective length of the primary ion-neutral interaction region. The effective length is determined using the following calibration reaction:²²



The uncertainty of the absolute cross section is estimated to be $\pm 30\%$.

To measure the product TOF distributions, ~ 3 to $4 \mu\text{s}$ wide primary ion pulses are generated by gating a split pair deflector electrode prior to the octopole injection. The primary and product flight times are recorded using a time-to-digital converter. To avoid background signals, the rf voltage on the octopole is briefly switched off prior to each cycle to purge slow ions formed by previous primary ion pulses. The arrival time for primary and product ions are accumulated over many TOF cycles. The resulting TOF spectra are transformed into laboratory axial velocity distributions, $f(v'_{1p})$, where v'_{1p} is the product ion laboratory velocity component parallel to the octopole ion-guide axis.¹⁷

In the current study, secondary reaction products complicate the analysis. Their existence is confirmed by comparing the cross sections measured under continuous wave (cw) and pulsed TOF conditions, and by target pressure dependences. In the pulsed conditions, very slow product ions that cause secondary reactions are not registered due to the rf-bursting technique applied in TOF mode. In the present double-octopole system, the secondary reaction products are minimized by the lower bias potential of the second octopole that accelerates slow product ions from the first octopole to a kinetic energy of ~ 0.4 eV.

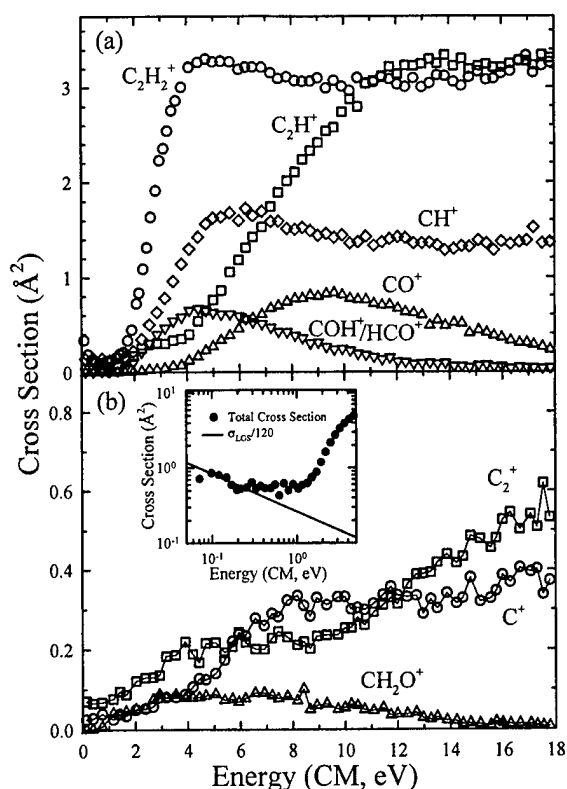
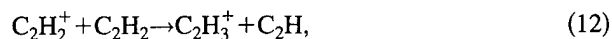


FIG. 1. (a) Energy dependence of integral cross sections for the main product ions of $O^+(^4S)+C_2H_2$ collisions, $C_2H_2^+$ (○), C_2H^+ (□), CH^+ (◇), COH^+/HCO^+ (▽), and CO^+ (△). (b) Energy dependence of integral cross sections for minor products, C_2^+ (□), C^+ (○), and CH_2O^+ (△). The insert in (b) is a logarithmic plot of the total cross section. The low-energy cross sections are compared with an $E_T^{-0.5}$ dependence (LGS/120).

III. RESULTS

A. Cross-section measurements

The energy dependent cross sections for products formed in the reaction of $O^+(^4S)+C_2H_2$ are shown in Figs. 1(a) and 1(b). Note that the $C_2H_2^+$ cross section shown in Fig. 1(a) includes the cross section of $m/z=27$ products, $C_2H_3^+$ and $^{13}CCH_2^+$, which is $\sim 10\%$ of the $C_2H_2^+$ cross section for $E_T > 1.6$ eV and $\sim 22\%$ for $E_T < 1.6$ eV. The cross section of the $m/z=26$ and 27 products exhibit a similar energy dependence, as expected in the case of isotopomers and secondary products. The isotopic $m/z=27$ contribution is $\sim 2\%$. The secondary products stem from the reaction



that has a rate constant on the order of 10^{-11} and 10^{-9} molecule $^{-1}$ cm 3 s $^{-1}$ for the ground and electronically excited $C_2H_2^+$ reactant states, respectively.^{23,24}

All channels are observed to be weak below 1.6 eV. The insert in Fig. 1(b) shows a logarithmic plot of the total cross section at low energies. The cross sections below 1 eV exhibit a $E_T^{-0.5}$ energy dependence that is more than two orders of magnitude smaller than the Langevin-Gioumousis-Stevens (LGS) capture cross section for an ion-induced dipole interaction.²⁵ Above 1.6 eV, several channels turn on abruptly, of which the CT channel predominates. CT acquires a nearly constant cross section of $\sim 3.2 \text{ \AA}^2$ at ~ 4 eV.

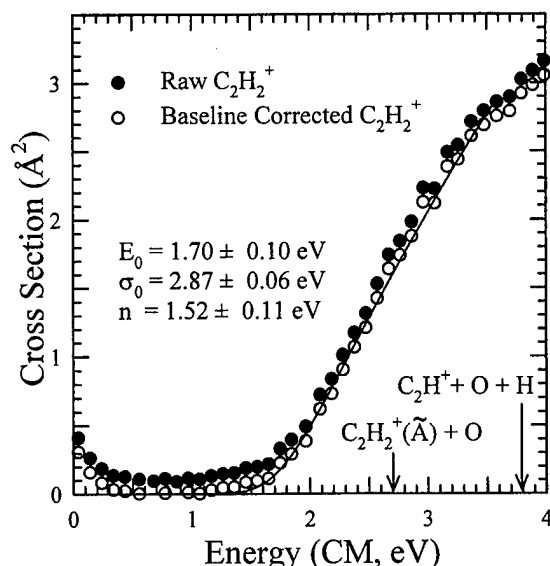


FIG. 2. Expanded view of low-energy charge-transfer cross sections. Raw (●) and baseline corrected (○) cross sections of $C_2H_2^+$ are shown. The solid line is a modified line-of-centers threshold function [Eq. (13)] corresponding to the listed fit parameters.

The second strongest C_2H^+ channel turns on weakly at a translational energy of ~ 0.5 eV, then increases more rapidly above ~ 4 eV.

The CH^+ cross section is also weak at collision energies below 1.6 eV, after which it rises to a maximum value of $\sim 1.7 \text{ \AA}^2$ at ~ 5 eV. There is no measurable reactivity to COH^+/HCO^+ and CO^+ products at low collision energies. The COH^+/HCO^+ cross section also appears to have a threshold near ~ 1.6 eV and peak at ~ 4.5 eV. The CO^+ product channel turns on around ~ 3 eV, with a maximum at ~ 9 eV. Note that the COH^+ and HCO^+ products are indistinguishable in our experiments. The cross sections of minor products C^+ , C_2^+ , and CH_2O^+ [Fig. 1(b)], although associated with exothermic channels, are all very small below 1 eV and increase with collision energy. Unlike C^+ and C_2^+ , CH_2O^+ peaks at about 4 eV after which the cross section declines with energy.

Given the thresholdlike behavior of several observed product channels, we have performed modified line-of-centers model fits of the charge-transfer, C_2H^+ , CH^+ , COH^+/HCO^+ and CO^+ yields in order to determine the onsets of the respective products. The data is fit to the model threshold function

$$\sigma(E_T) = \sigma_0 \sum_i g_i \frac{(E_T + E_i - E_0)^n}{E_T}, \quad (13)$$

where E_0 is the threshold energy, σ_0 is a scaling parameter, and n is a curvature parameter. The fits involve convoluting the experimental collision energy distribution with Eq. (13).²⁶ The sum is over internal states of the reactants, with energies E_i and populations g_i . The modeled onset at ~ 1.6 eV of the charge-transfer cross section is shown in Fig. 2. The raw charge-transfer cross section is corrected for the weak low-collision energy process prior to fitting. Given the relatively constant cross section at low energies, we believe a

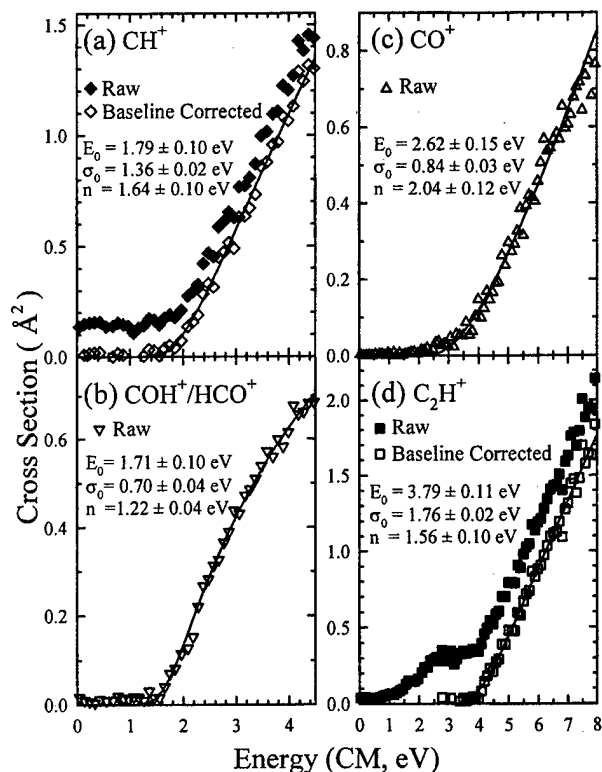
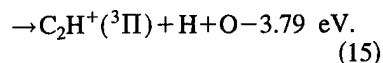
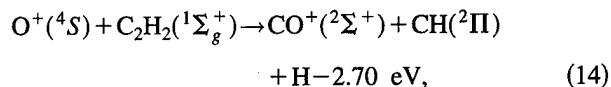


FIG. 3. Low-energy cross sections of CH^+ (a), $\text{COH}^+/\text{HCO}^+$ (b), CO^+ (c), and C_2H^+ (d) formation including the resulting fit parameters of the modified line-of-centers threshold models.

simple baseline correction is justifiable. The fit yields an onset energy (0 K) of 1.70 ± 0.10 eV for the high-energy cross section enhancement. Expanded views of the modeled CH^+ and $\text{COH}^+/\text{HCO}^+$ cross sections are shown in Figs. 3(a) and 3(b). Threshold energies of 1.79 ± 0.10 eV and 1.71 ± 0.10 eV are determined for these products, respectively. Figures 3(c) and 3(d) are the expanded views of the modeled CO^+ and C_2H^+ cross sections, yielding thresholds of 2.62 ± 0.15 eV and 3.79 ± 0.11 eV, respectively. Whereas the thresholds of ~ 1.7 eV observed for charge-transfer, CH^+ , and $\text{COH}^+/\text{HCO}^+$ cannot be associated with any particular asymptotic limit, the latter thresholds can clearly be attributed to the opening of the dissociative channels



The competitive nature of the energy dependences of the corresponding nondissociative and dissociative processes are also consistent with this interpretation.

No evidence is found for CH_2^+ formation, despite the high exothermicity leading to $\text{CH}_2^+(^2A_1) + \text{CO}(^1\Sigma^+)$ products [Reaction (6)]. Note that these products are spin-forbidden.

B. TOF measurements

Product ion velocity-transformed TOF distributions, $f(v'_{1p})$, are shown for C_2H_2^+ (CT) products at different col-

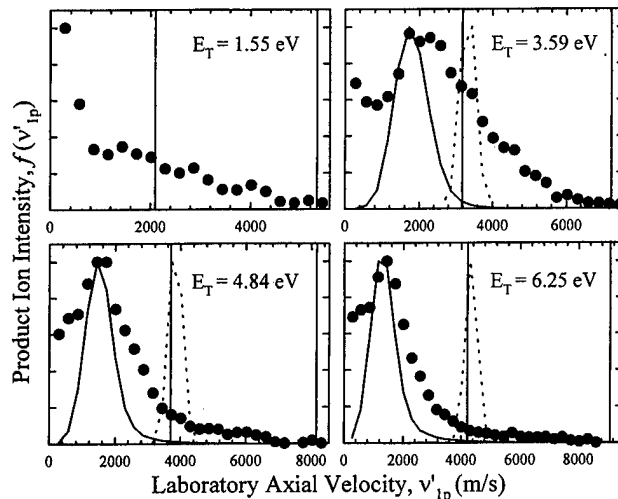
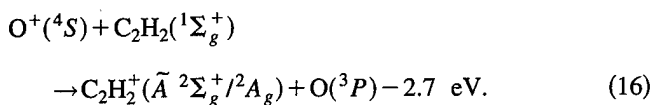


FIG. 4. Axial velocity distributions of the C_2H_2^+ product ions as a function of collision energy. The vertical lines in each collision energy frame indicate v_{cm} and v_{max} , the center-of-mass and maximum energetically allowed velocities. The solid lines are calculated osculating complex model distributions for a discrete translational-to-internal energy transfer of 2.7 eV and a very short complex lifetime. The dotted lines indicate the experimental distribution of v_{cm} .

lision energies in Fig. 4. In each frame, the vertical lines indicate the center-of-mass (CM) velocity, v_{cm} , and the maximum energetically allowed velocity, v_{max} . These velocities are calculated assuming the target gas is at rest. The dotted curves are the experimentally broadened CM velocity which are a measure of the present experimental resolution.

At 1.55 eV, it can be stated that approximately half of the products stem from the low-energy mechanism, and half are attributable to the 1.70 eV threshold process. Note that the thermally broadened collision energy FWHM at a nominal collision energy of 1.55 eV is ~ 0.45 eV. The product velocity distribution exhibits a peak intensity at near-zero laboratory velocities as well as significant intensity centered around v_{cm} . At collision energies above 1.70 eV, the peak intensity is clearly at higher laboratory velocities, indicating a process with translational to internal energy transfer. At 4.84 and 6.25 eV, the band becomes considerably narrower with a decrease in intensity near v_{cm} .

The C_2H_2^+ velocity distributions at collision energies of 3.59 eV and higher are compared with simulations (solid curves) taking all known experimental broadening kinematics into account.^{17,27} Product velocities are calculated for the case that CM backscattered $\text{C}_2\text{H}_2^+(\tilde{A})$ products are formed with no vibrational and rotational excitation. The energetics for \tilde{A} state formation are given by



Note that the equilibrium geometry of the $\text{C}_2\text{H}_2^+ \tilde{A}$ state is trans-bent.²⁸ The simulations are based on an osculating complex model,²⁹⁻³¹ assuming a discrete translational-to-internal energy transfer of 2.7 eV and a very short-lived complex. The calculated bands agree well with the maxima

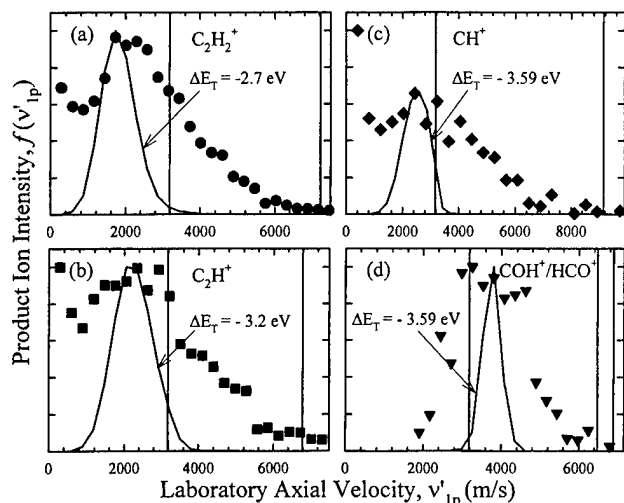


FIG. 5. Axial velocity distributions at $E_T = 3.59$ eV for product ions, $C_2H_2^+$ (a), C_2H^+ (b), CH^+ (c), and COH^+/HCO^+ (d). Note that two lines representing v_{max} for COH^+ and HCO^+ , respectively, are indicated in Fig. 5(d). Calculated velocity distributions (solid lines) for representative discrete translational energy transfer values, ΔE_T , are shown for each observed velocity distribution.

and low-velocity edges of the main TOF bands, implying that \tilde{A} state formation is efficient at higher collision energies.

While the measurement at 3.59 eV has substantial intensity in the vicinity of v_{cm} , this is no longer the case at 4.84 eV and higher energies. This is consistent with the previous suggestion that C_2H^+ is primarily a dissociative charge-transfer product. The dissociative charge-transfer threshold of 3.79 eV precludes efficient dissociation at 3.59 eV, implying that $C_2H_2^+$ can acquire all of the available kinetic energy without dissociating, while the observed C_2H^+ products are primarily associated with an OH neutral fragment [Reaction (1)]. The signal near v_{cm} in the 3.59 eV measurement is thus evidence of high internal excitation. At 4.84 and 6.25 eV, partitioning of kinetic energy exceeding 3.79 eV, results in loss of $C_2H_2^+$, which is consistent with loss of $C_2H_2^+$ signal near v_{cm} and the resulting narrower bands at these energies.

This is further corroborated through the comparison of $C_2H_2^+$ and C_2H^+ axial velocity distributions in Figs. 5–7. Simulations representative of a discrete translational energy transfer, ΔE_T , are shown for the purpose of orientation. While both product channels have very similar TOF spectra at 3.59 eV [Figs. 5(a) and 5(b)], maxima of the C_2H^+ velocity distributions are shifted substantially closer to v_{cm} at 4.84 and 6.25 eV [Figs. 6(a) and 7(a)], implying that this channel is associated with higher degrees of energy transfer. Samples of CH^+ and COH^+/HCO^+ axial velocity distributions are also shown in Figs. 5–7. While CH^+ is primarily CM back-scattered, COH^+/HCO^+ product velocity distributions are CM forward scattered. Interestingly, at the three collision energies, the peak velocities in both channels correspond to very similar energy transfers, as the sample simulations demonstrate. The CO^+ products are also primarily CM forward scattered, as seen in Figs. 6(d) and 7(d). The velocity distributions are very similar to those observed for COH^+/HCO^+ , consistent with CO^+ being a product of sequential dissociation of excited COH^+/HCO^+ products.

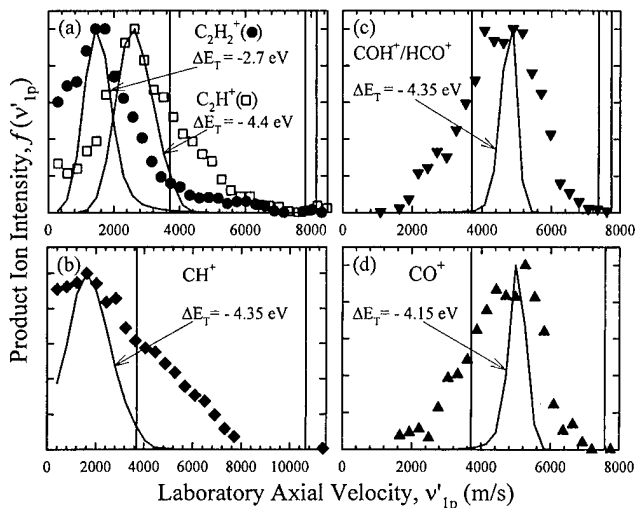


FIG. 6. Axial velocity distributions at $E_T = 4.84$ eV for product ions, $C_2H_2^+$ and C_2H^+ (a), CH^+ (b), COH^+/HCO^+ (c), and CO^+ (d). Note that two lines representing v_{max} for COH^+ and HCO^+ , respectively, are indicated in (c). Calculated velocity distributions (solid lines) for representative discrete translational energy transfer values, ΔE_T , are shown for each observed velocity distribution.

C. Density functional calculations of $(O-C_2H_2)^+$ complex ions

The small low energy cross sections and thresholdlike behavior imply that short-range interactions are important in this collision system. We have, therefore, conducted a density functional survey of the $(O-C_2H_2)^+$ quartet and doublet local minima. Geometry optimizations are carried out at the B3LYP/6-31G(d) level (GAUSSIAN 94).³² This level of theory has been demonstrated to be useful in exploring the relative energetics as well as geometries for ion–molecule reaction intermediates.³³ The determined local minima and their optimized structures are shown schematically in Fig. 8 along with the relative energies of reactants and products. Note that

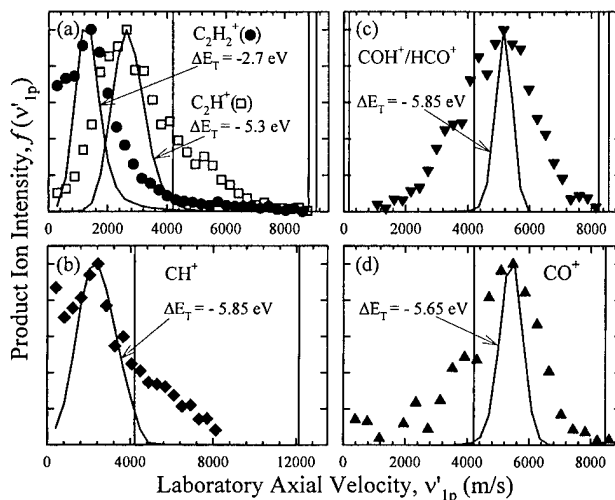


FIG. 7. Axial velocity distributions at $E_T = 6.25$ eV for product ions, $C_2H_2^+$ and C_2H^+ (a), CH^+ (b), COH^+/HCO^+ (c), and CO^+ (d). Note that two lines representing v_{max} for COH^+ and HCO^+ , respectively, are indicated in (c). Calculated velocity distributions (solid lines) for representative discrete translational energy transfer values, ΔE_T , are shown for each observed velocity distribution.

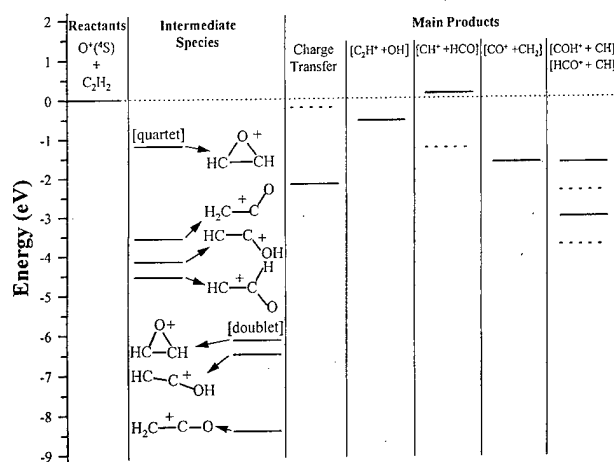


FIG. 8. Schematic potential energy diagram for the $\text{O}^+(^4\text{S})+\text{C}_2\text{H}_2$ reaction system. The intermediate species energies are those calculated in the present work for the shown optimized structures. Dashed product energy levels indicate spin-forbidden channels.

the potential energy shown here includes the thermal internal energy (300 K), determined from normal frequency calculations,³² and is plotted with respect to the reactant energy, which is indicated by a horizontal dotted line. While a HC-CHO⁺ structure is found to be the most stable quartet geometry, the ketene ion is the global minimum of the doublet hypersurface, as previously determined by Bouma *et al.*³⁴ Given the significant enhancement of reactivity with collision energy above a threshold of 1.7 eV, we have looked for a barrier on the ground-state surface of reactants. All located transition states to intermediates did not represent barriers to reaction at the present level of theory.

IV. DISCUSSION

Clearly the most remarkable feature of the present observations is the pronounced collision energy enhancement of the main CT, CH^+ , and $\text{COH}^+/\text{HCO}^+$ channels above 1.7 eV. At collision energies below 1.7 eV, all channels are very inhibited, despite considerable exothermicities. The C_2H_2 axial velocity distribution at 1.55 eV (Fig. 4) indicates that the weak charge-transfer channel at low energies is primarily attributable to a long-range mechanism with little energy transfer. Consequently, either a weakly coupled long-range mechanism or trace amounts of O^+ metastable ions associated with a large charge-transfer cross section are responsible for the low-energy yields. We are unable to distinguish between the two possibilities. A weakly coupled charge-transfer reaction, however, is consistent with energy resonance and Franck–Condon criteria that usually govern low-energy, exothermic ion–molecule CT.^{35,36} Two weakly-coupled, near-resonant transitions are possible: Franck–Condon restricted charge-transfer to ground-state products, and a spin-forbidden transition to $\text{O}(^1D) + \text{C}_2\text{H}_2^+(\tilde{X})$ products, where the Franck–Condon overlap is very favorable. It is worth noting that the present low-energy cross sections are comparable to those of the isoelectronic $\text{O}^+(^4S) + \text{N}_2$ collision system. Formation of $\text{NO}^+ + \text{N}(^4S)$ is interpreted to proceed via a spin-forbidden transition to a doublet surface at low energies.³⁷

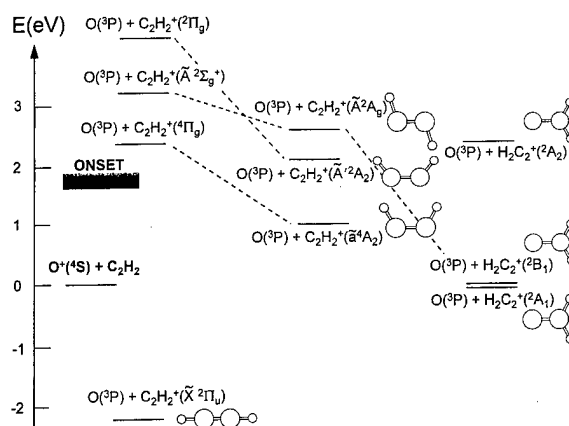


FIG. 9. Asymptotic excited state structures of the $\text{O}^+(\text{}^4\text{S})+\text{C}_2\text{H}_2$ charge-transfer system. Energies and optimized geometries are taken from Ref. 42.

The TOF measurements of CT product ions at higher energies indicate significant degrees of translational energy transfer associated with smaller impact parameter collisions. The kinematic analysis suggests that a surface associated with $\text{C}_2\text{H}_2^+ \tilde{A}$ state products plays an important role. The observed onset of 1.70 ± 0.10 eV for the high-energy feature of the charge-transfer cross section, however, lies significantly below the threshold for $\text{O}(^3P) + \text{C}_2\text{H}_2^+(\tilde{A} \ ^2A_g)$ formation. Consequently, the observations cannot be interpreted simply by invoking the opening of an additional exit channel that has a much higher degree of charge-transfer coupling. Since our density functional survey could not locate a barrier leading to one of the observed local minima of the ground-state reactant surface, we conclude that the reactions associated with the 1.70 eV threshold are proceeding on an excited-state surface. More precisely, excited charge-transfer surfaces need to be considered because they are the only spin-allowed excited-state surfaces in the energy range of interest.

Several experimental^{28,38,39} and theoretical^{40–42} studies have investigated the low-lying excited states of acetylene radical cation, the charge-transfer product. In addition to studying the structure of the \tilde{A} state, the theoretical work has identified two additional states that are not observed in the photoelectron spectrum, the $^2\Pi_g$ and $^4\Pi_g$ shake-up states. These states lie slightly above and below the \tilde{A} state, respectively, and also have bent equilibrium geometries with substantially elongated C–C bonds. There are, therefore, a number of $C_2H_2^+$ states in the energy region of interest, of which the two doublet states have been shown to be strongly vibronically coupled through the bending vibrational coordinates.⁴² Consequently, it is not surprising that calculations^{40,42} and experiments^{28,39} find the \tilde{A} state to be very short lived. A barrier-free relaxation to vinylidene ion (H_2CC^+) is found. A barrier slightly below 0.5 eV has been determined for the vinylidene isomerization to the $^2\Pi_u$ acetylene cation.^{43,44}

Figure 9 displays a schematic energy diagram of asymptotic states of the $O^+ + C_2H_2$ charge-transfer system illustrating the high density of states attributed to the trans-

and cis-bent low-lying states and their correlations to the linear and vinylidene ion. The energetics and geometries are taken from Chambaud *et al.*⁴² It is seen that the energy of the observed threshold lies in the vicinity of charge-transfer product states associated with electronically excited $C_2H_2^+$ states. The high preference for $C_2H_2^+ \tilde{A}$ state products at energies exceeding 2.7 eV suggests that the collisions pass through a $[O, C_2H_2^+(\tilde{A})]$ intermediate above 1.7 eV. At energies below 2.7 eV, this intermediate cannot decay to $O + C_2H_2^+(\tilde{A})$, and highly excited $C_2H_2^+ \tilde{X}$ state or metastable vinylidene must be formed in the observed charge-transfer channels. Given the high degree of vibronic coupling and the diverse geometries of the low-lying $C_2H_2^+$ excited states, it may be assumed that the hydrogen atoms are extremely mobile in a loosely bound $[O, C_2H_2^+(\tilde{A})]$ complex. It is, therefore, not surprising that chemical reaction channels also become efficient at energies above 1.7 eV.

Interestingly, the H^- transfer reaction (1) only experiences a minor enhancement above 1.70 eV and, having attributed the substantial C_2H^+ yields to dissociative charge transfer, is not a major factor throughout the investigated energy range. The CH^+ and COH^+/HCO^+ channels [Reactions (2) and (3) and/or (4)], however, are obviously mediated by the same excited-state surface as the charge-transfer channel. The TOF measurements indicate that energy transfer is very efficient in all of the investigated channels. This is exemplified in the C_2H^+ channel, which becomes very efficient above the thermodynamic threshold at 3.79 eV for dissociative charge-transfer leading to $C_2H^+ + O + H$ products. Assuming that the observed recoil velocities are characteristic of a sequential mechanism involving charge-transfer followed by dissociative decay, the simulations demonstrate that the C_2H^+ products are highly excited. This is further corroborated by the enhancement of C_2^+ production above the threshold of 9.1 eV for $C_2^+ + O + H + H$ formation [Fig. 1(b)].

It is worth pointing out that the presently suggested sequential mechanism involving charge transfer to vibrationally excited $C_2H_2^+(\tilde{A})$ product ions followed by efficient dissociation to $C_2H^+ + H$ fragments is consistent with the photoelectron-photoion coincidence (PEPICO) studies of excited $C_2H_2^+$ states, in which the dissociation efficiency to form C_2H^+ is found to be near unity above threshold.⁴⁵

The present experiments also point to high internal excitation of the CH^+ and HCO^+/COH^+ products. The cross sections demonstrate that these products are excited to internal energies near the dissociation limit. While the HCO^+/COH^+ cross sections appear to be in competition with CO^+ , the latter turning on at the $CO^+ + H + CH$ threshold of 2.7 eV, a similar, but more subtle situation is observed for the CH^+ and C^+ channels, where C^+ exhibits an enhancement above the $C^+ + H + HCO$ thermochemical limit of 2.8 eV. The recoil velocity distributions are observed to be very close to the CM velocity indicating high internal excitation. Some caution needs to be taken in making this conclusion because most of the kinetic energy may be carried off by an H atom formed in a simultaneous production of two neutral products. The almost identical energy transfer ob-

served in the CH^+ and HCO^+/COH^+ product channels, however, suggests that these products are produced in very similar trajectories. Since these products are charge-transfer analogs, a mechanism can be invoked in which the identity of the fragment ion is determined through a charge-transfer interaction in the outgoing trajectory at longer range. This is fully consistent with the fact that these products are scattered in opposite directions. This scenario implies intact $CH^+ + HCO$ and $HCO^+/COH^+ + CH$ moieties at long range and, therefore, a sequential mechanism if fragmentation of the initial neutral product occurs. In this case, the observed ion recoil velocity distributions of the $CH^+ + HCO$ and $HCO^+/COH^+ + CH$ products would be representative of the internal energy of fragments involving a single neutral product.

The recoil velocity measurements of the CH^+ and COH^+/HCO^+ product ions do not provide conclusive evidence on the favored approach geometry and location of the O^+ insertion into acetylene, and thus the isomeric identity of the $m/z = 29$ product. The scattering angles indicate a stripping mechanism in which the incident ion picks up a CH fragment. A study of cross sections involving deuterated acetylene may be helpful in assessing whether C/H or C-C insertion are the predominant pathways of the reactive channels.

The present cross section and TOF measurements thus convey a mechanism where translational energy transfer is necessary to access an excited-state complex that exhibits many barrier free isomerization and dissociation channels. Maybe the most intriguing question that remains is why the reactivity is so poor at energies below the observed onset of 1.70 eV, despite the large number of exothermic channels and stable intermediates. Only charge transfer and CH^+ formation are observed to have cross sections exceeding 0.1 \AA^2 below 1 eV. Note that the first spin-allowed CH^+ channel is endothermic by 0.12 eV [Reaction (2b)]. The increase in cross section with collision energy at near-thermal energies is indicative of a reaction with low threshold, implying that $CH^+(^3\Pi) + HCO(^2A')$ products are formed. While the low cross sections to form CH^+ and CT products can be explained with spin-conservation or Franck-Condon rules, there is no obvious reason why none of the remaining highly exothermic spin-allowed reaction channels are produced efficiently in the collision energy regime below 1 eV where complex formation and statistical energy partitioning can predominate the dynamics.

A possible reason for the low reactivity of this collision system may be found in poor correlation of electronic orbital motion. This would be the case if the favored intermediate has considerable symmetry. An obvious complex that could be formed with a relatively large range of impact parameters would be a T-shaped intermediate with C_{2v} symmetry. Such a complex would have 4A_2 symmetry. The T-shaped local minimum (the oxirene ion) determined by the present density functional survey of the quartet hypersurface, however, has 4B_2 symmetry. It is thus conceivable that production of the lowest oxirene ion 4A_2 excited state is endothermic to a degree that the crossing leading to the 4B_2 surface represents a substantial barrier. The other quartet hypersurface minima

are asymmetric, but involve bond insertion or major hydrogen atom migration. The formation of such complexes is likely to be limited to a smaller range of impact parameters. A detailed theoretical treatment of the excited states of the quartet hypersurface would go a long way in providing answers regarding both the efficient dynamics at high collision energies as well as the poor reactivity at low collision energies.

V. CONCLUSIONS

The $O^+(^4S) + C_2H_2$ collision system has a reaction cross section that is more than two orders of magnitude smaller than the Langevin–Gioumousis–Stevens capture cross section at low collision energies, despite the large number of exothermic channels and several stable intermediates. Above a collision energy of 1.7 eV, charge-transfer, CH^+ and COH^+/HCO^+ channels turn on abruptly. Above 2.7 eV, CT is found to lead to $O(^3P) + C_2H_2^+(\tilde{A})$ products, indicating that the reaction preferentially proceeds via an excited-state surface. The high density of $C_2H_2^+$ states in this energy regime, and their instability with respect to H-atom migration, provide an explanation for the sudden high reactivity once sufficient translational energy has been transferred into internal energy of the collision complex. Product recoil velocity distributions demonstrate that translational energy transfer is extremely efficient for all of the main product channels, leading to sequential dissociation at higher collision energies. The C_2H^+ , CO^+ , and C^+ channels are primarily attributed to sequential dissociation events.

The small charge-transfer cross sections below 1 eV can be attributed to poor Franck–Condon factors associated with ground-state products, and a spin-forbidden transition with near-resonant $O(^1D) + C_2H_2^+(\tilde{X})$ products. The low reaction cross sections despite several stable intermediates may be attributed to poor orbital correlations with an oxirene ion intermediate. We thus find that, contrary to common observations of other small organic ion–molecule reaction systems, the $O^+(^4S) + C_2H_2$ reaction is neither governed by facile charge-transfer and/or hydrogen atom transfer reactions, nor by products associated with the dissociation of stable intermediates, but by an excited charge-transfer surface that promotes both CT and reaction channels.

ACKNOWLEDGMENTS

This work is supported by AFOSR under Task 2303EP2. Y.-H. Chiu is an NRC postdoctoral fellow. We thank Professor Keiji Morokuma and Dr. Charles Kolb for valuable comments regarding this work.

¹E. Teloy and D. Gerlich, Chem. Phys. **4**, 417 (1974).

²D. Gerlich, in *State-Selected and State-to-State Ion-Molecule Reaction Dynamics: Experiment, Part I*, Adv. Chem. Phys. Vol. 82, edited by C. Y. Ng and M. Baer (Wiley, New York, 1992), p. 1.

³Y. Chiu, H. Fu, J. Huang, and S. L. Anderson, J. Chem. Phys. **102**, 1199 (1995).

⁴R. A. Curtis and J. M. Farrar, J. Chem. Phys. **90**, 862 (1989).

⁵J. Qian, H. Fu, and S. L. Anderson, J. Phys. Chem. **101**, 6504 (1997).

⁶J. Qian, R. J. Green, and S. L. Anderson, J. Chem. Phys. **108**, 7173 (1998).

⁷S. G. Lias, J. E. Bartmess, J. F. Liebman, J. L. Holmes, R. D. Levin, and

W. G. Mallard, Gas-Phase Ion and Neutral Thermochemistry, J. Phys. Chem. Ref. Data **17**, Suppl 1 (1988).

⁸A. A. Radzig and B. M. Smirnov, *Reference Data on Atoms, Molecules, and Ions* (Springer-Verlag, Berlin, 1985).

⁹K. P. Huber and G. Herzberg, *Molecular Spectra and Molecular Structure IV. Constants of Diatomic Molecules* (Van Nostrand Reinhold, New York, 1979).

¹⁰G. Herzberg, *Molecular Spectra and Molecular Structure III. Electronic Spectra and Electronic Structure of Polyatomic Molecules* (Van Nostrand Reinhold, New York, 1966).

¹¹M. J. Bastian, R. A. Dressler, E. Murad, S. T. Arnold, and A. A. Viggiano, J. Chem. Soc., Faraday Trans. **92**, 2659 (1996).

¹²R. A. Dressler and E. Murad, in *Unimolecular and Bimolecular Ion-Molecule Reaction Dynamics*, edited by C. Y. Ng, T. Baer, and I. Powis (Wiley, New York, 1994), p. 87.

¹³E. Murad, J. Spacecr. Rockets **33**, 131 (1996).

¹⁴O. J. Orient, A. Chutjian, and K. E. Martus, Phys. Rev. A **48**, 427 (1993).

¹⁵O. J. Orient, A. Chutjian, and E. Murad, Phys. Rev. A **51**, 2094 (1995).

¹⁶M. Mendillo, J. Baumgartner, P. D. Allen, J. Foster, J. Holt, G. R. A. Ellis, A. Klekociuk, and G. Reber, Science **238**, 1260 (1987).

¹⁷R. A. Dressler, R. H. Salter, and E. Murad, J. Chem. Phys. **99**, 1159 (1993).

¹⁸C. E. Moore, Natl. Bur. Stand., Circ. **467**, Vol. I, p. 47 (1949).

¹⁹T. O. Tiernan and B. M. Hughes, J. Chem. Phys. **55**, 3419 (1971).

²⁰J. A. Appell, J. Durup, and F. Heitz, Adv. Mass Spectrom. **3**, 457 (1969).

²¹J. L. Franklin, J. G. Dillard, H. M. Rosenstock, J. T. Herron, K. Draxl, and F. H. Field, Ionization Potentials, Appearance Potentials, and Heats of Formation of Gaseous Positive Ions, Nat. Stand. Ref. Data Ser. **26**, (1969).

²²K. M. Ervin and P. B. Armentrout, J. Chem. Phys. **83**, 166 (1985).

²³Y. Ikezoe, S. Matsuoka, M. Takabe, and A. A. Viggiano, *Gas Phase Ion-Molecule Reaction Rate Constants Through 1986* (Maruzen Co., Tokyo, 1987).

²⁴P. J. Derrick and I. Szabo, Int. J. Mass Spectrom. Ion Phys. **7**, 55 (1971).

²⁵G. Gioumousis and D. P. Stevenson, J. Chem. Phys. **29**, 294 (1958).

²⁶M. J. Bastian, R. A. Dressler, D. J. Levandier, E. Murad, F. Muntean, and P. B. Armentrout, J. Chem. Phys. **106**, 9570 (1997).

²⁷D. Gerlich, J. Chem. Phys. **90**, 127 (1989).

²⁸J. E. Reutt, L. S. Wang, J. E. Pollard, D. J. Trevor, Y. T. Lee, and D. A. Shirley, J. Chem. Phys. **84**, 3022 (1986).

²⁹G. A. Fisk, J. D. McDonald, and D. R. Herschbach, Discuss. Faraday Soc. **44**, 228 (1967).

³⁰M. K. Bullitt, C. H. Fisher, and J. L. Kinsey, J. Chem. Phys. **60**, 478 (1974).

³¹D. M. Sonnerfroh, R. A. Curtis, and J. M. Farrar, J. Chem. Phys. **83**, 3958 (1985).

³²GAUSSIAN 94, Revision D.1, M. J. Frisch, G. W. Trucks, H. B. Schlegel, P. M. W. Gill, B. G. Johnson, M. A. Robb, T. K. J. R. Cheeseman, G. A. Petersson, J. A. Montgomery, K. Raghavachari, V. G. Z. M. A. Al-Laham, J. V. Ortiz, J. B. Foresman, J. Cioslowski, A. N. B. B. Stefanov, M. Challacombe, C. Y. Peng, P. Y. Ayala, W. Chen, J. L. A. M. W. Wong, E. S. Replogle, R. Gomperts, R. L. Martin, D. J. Fox, D. J. D. J. S. Binkley, J. Baker, J. P. Stewart, M. Head-Gordon, C. Gonzalez, and J. A. Pople (Gaussian, Inc., Pittsburgh PA, 1995).

³³A. Luna, A. M. Mebel, and K. Morokuma, J. Chem. Phys. **105**, 3187 (1996).

³⁴W. J. Bouma, P. M. W. Gill, and L. Radom, Org. Mass Spectrom. **19**, 610 (1984).

³⁵E. A. Gislason, G. Parlant, and M. Sizun, in *State-Selected and State-to-State Ion-Molecule Reaction Dynamics, Part II*, Adv. Chem. Phys., Vol. 82, edited by C. Y. Ng and M. Baer (Wiley, New York, 1992), p. 321.

³⁶H. Nakamura, in *State-Selected and State-to-State Ion-Molecule Reaction Dynamics, Part II*, Adv. Chem. Phys. Vol. 82, edited by C. Y. Ng and M. Baer (Wiley, New York, 1992), p. 243.

³⁷J. D. Burley, K. M. Ervin, and P. B. Armentrout, J. Chem. Phys. **86**, 1944 (1986).

³⁸C. Servais and R. Loch, Chem. Phys. Lett. **236**, 96 (1995).

³⁹C. Cha, R. Weinkauff, and U. Boesl, J. Chem. Phys. **103**, 5224 (1995).

⁴⁰P. Rosmus, P. Botschwina, and J. P. Maier, Chem. Phys. Lett. **84**, 71 (1981).

⁴¹W. P. Kraemer and W. Koch, Chem. Phys. Lett. **212**, 631 (1993).

⁴²G. Chabaud, R. Van den Boom, and P. Rosmus, Chem. Phys. Lett. **247**, 79 (1995).

⁴³T. C. Hamilton and H. F. Schaefer, III, J. Phys. Chem. **93**, 7560 (1989).

⁴⁴J. Baker, Chem. Phys. Lett. **159**, 447 (1989).

⁴⁵K. Norwood and C. Y. Ng, J. Chem. Phys. **91**, 2898 (1989).

Determination of photofragment ion translational energy and angular distributions in an octopole ion guide: A case study of the Ar_2^+ and $(\text{N}_2\text{O}\cdot\text{H}_2\text{O})^+$ cluster ions

S. Williams,^{a)} Y.-H. Chiu, D. J. Levandier,^{a)} and R. A. Dressler

Air Force Research Laboratory/VSBM, 29 Randolph Road, Hanscom Air Force Base, Massachusetts 01731-3010

(Received 4 May 1998; accepted 28 July 1998)

The first measurement of ion photodissociation product recoil velocity and angular anisotropy in an octopole ion guide are presented. The experimental and numerical procedures required to obtain photofragment ion translational energy and angular distributions are discussed. Cluster ions are photodissociated in an octopole ion guide, and photofragment ion velocity distributions are measured using time-of-flight (TOF). The instrumental discrimination function is determined using guiding field variation (VAR). A validation study using the $^2\Sigma_g^+ \leftarrow ^2\Sigma_u^+$ transition of Ar_2^+ probed at 300 nm and a photodissociation dynamics study of $(\text{N}_2\text{O}\cdot\text{H}_2\text{O})^+$ to form $\text{N}_2\text{OH}^+ + \text{OH}$, $\text{N}_2\text{O}^+ + \text{H}_2\text{O}$, and $\text{H}_2\text{O}^+ + \text{N}_2\text{O}$ in the 458–657 nm range are presented. The H_2O^+ and N_2O^+ photofragment translational energy and angular distributions are derived, and new information regarding the photodissociation of the $(\text{N}_2\text{O}\cdot\text{H}_2\text{O})^+$ cluster ion is obtained. © 1998 American Institute of Physics. [S0021-9606(98)00541-8]

I. INTRODUCTION

The observation of the fragments produced in gas-phase photodissociation experiments provides important information regarding the structure and energetics of the species being studied. Several experimental techniques have been developed to probe the asymptotic properties of photodissociation events.¹ These include photofragment translational spectroscopy,^{2–8} state-resolved photofragment detection,^{9,10} Doppler spectroscopy,^{11,12} photofragment imaging,^{13–16} and position-sensitive detection/coincidence methods.^{17–20} In this paper a novel approach to studying photodissociation events of molecular ions is outlined. To date, the majority of detailed measurements of the photodissociation dynamics of ionic species have been carried out in reverse-geometry sector mass spectrometers.⁸ In the present guided ion-beam (GIB) experiment,²¹ the exceptional transmission properties of the effective potential generated in a radiofrequency (rf) octopole ion guide are exploited to measure photofragment ion translational energy and angular distributions with high sensitivity.

In gas-phase ion chemistry, the GIB technique is well established for measuring reliable absolute integral cross sections of ion-molecule reactions over a wide range of collision energies. In these applications, the rf octopole ion guide is utilized predominately to ensure 100% collection efficiency of the primary and secondary ionic products regardless of their kinetic energy or scattering angle. Because ion velocity distributions are unaffected by the rf voltage in octopole ion guides operated under certain conditions, the GIB method is readily applied to measure velocity and angular distributions of product ions, whereby the axial component is determined

by using the time-of-flight method (GIB-TOF) and the transverse component by guiding field variation (GIB-VAR).^{22,23} In a GIB experiment, the overall symmetry is defined by the primary ion beam guided along the octopole axis, and the cylindrical symmetry of the effective guiding potential leads automatically to an integration over the azimuthal angle. For this geometry, the axial and transverse velocity components can be determined independently, and hence, the GIB method is capable of providing the same doubly differential information as photofragment imaging^{13–16} and position-sensitive detection/coincidence methods.^{17–20}

In recent years, an increasing number of research groups^{24–27} have exploited the versatility of rf ion guides in photodissociation experiments. While these experiments have yielded photofragment ion action spectra, no direct measurements probing the details of the photodissociation dynamics have been reported. In this paper, the determination of center-of-mass kinetic energy release and angular distributions with high accuracy is added to the list of GIB capabilities. A diatomic validation study using the $^2\Sigma_g^+ \leftarrow ^2\Sigma_u^+$ transition of Ar_2^+ probed at 300 nm and a photodissociation dynamics study of the positive cluster ion of N_2O and H_2O , namely $(\text{N}_2\text{O}\cdot\text{H}_2\text{O})^+$, in the 458–657 nm range are presented.

II. EXPERIMENT

A. Photodissociation measurements

Cold cluster ions are produced in a pulsed supersonic expansion source and are interrogated using a guided ion-beam apparatus previously described.^{28–30} Excitation is provided by a Nd:YAG pumped, broadband optical parametric oscillator (OPO) laser system (Quanta Ray GCR-170 and MOPC-710) operated over the wavelength range of 450–660

^{a)}Also at: Orion International Technologies, Albuquerque, NM.

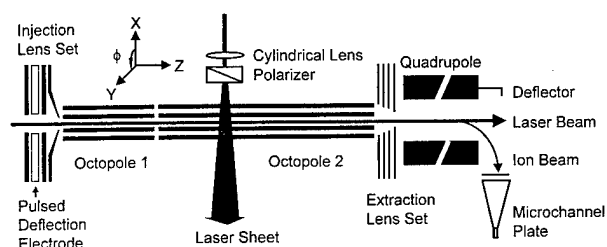


FIG. 1. Schematic representation of the interaction region of the guided ion-beam experiment for the measurement of photofragment translational energy and angular distributions.

nm (signal) with an average bandwidth over this range of approximately 10 cm^{-1} (1 meV) and a temporal pulse width of approximately 7 ns. In the Ar_2^+ study, the laser output at 600 nm was frequency doubled in BBO. A reducing telescope is used in conjunction with a 30 cm focal length cylindrical lens to produce a weakly focused sheet of laser light that propagates through the rods of the second octopole (Fig. 1). The laser sheet is approximately $1 \text{ mm} \times 5 \text{ mm}$, and the longer dimension is parallel to the octopole axis. The laser energy is attenuated with neutral density filters to obtain per pulse energy densities in the $5\text{--}90 \text{ mJ/cm}^2$ range. The photofragment yield over this energy density range is observed to be linear with a zero intercept which indicates that the photofragments are produced by single-photon processes. A variable delay generator (SRS DG 535), triggered by the TTL output of the pulsed valve driver (General Dynamics IOTA one), triggers the flashlamps of the Nd:YAG laser and a symmetric pulse forming network used to gate the primary ion beam ($20 \mu\text{s}$ FWHM). The Q-switch of the Nd:YAG laser is triggered internally. A high octopole guiding field sufficient to collect all transverse velocity components of the primary cluster ions and product ions is used. A TOF spectrum consisting of ion counts versus arrival time is recorded for each mass using a multi-channel scaler (SRS SR 430).

Figure 2(a) shows a $(\text{N}_2\text{O} \cdot \text{H}_2\text{O})^+$ primary ion TOF spectrum at an energy of 4.4 eV. The dip in the spectrum corresponds to a hole burned into the cluster ion arrival time distribution by the laser pulse. This narrow dip provides a well defined measure of the starting time of the experiment. The visible photodissociation of $(\text{N}_2\text{O} \cdot \text{H}_2\text{O})^+$ cluster ions produces H_2O^+ , N_2O^+ , and N_2OH^+ photofragments.^{29–31} TOF spectra obtained with the quadrupole mass analyzer set to m/z equal to 44–45 and 18 are shown in Fig. 2(b) and 2(c), respectively. The signal level at a mass resolution sufficient to discern $m/z=44$ (N_2O^+) from $m/z=45$ (N_2OH^+) is very low, and as a result, both ions are collected simultaneously. The laser polarization is parallel to the octopole axis, and a background scan with the laser off has been subtracted from the data shown in Fig. 2(b) and 2(c). A calculated primary ion velocity distribution including experimental broadening is shown in Fig. 2(d). This velocity distribution is essentially the experimentally broadened velocity transform of the dip in the data shown in Fig. 2(a) and represents a photofragment ion spectrum for zero kinetic energy release. Figure 2(e) and 2(f) shows the data of 2(b) and 2(c) transformed into laboratory velocity space using a bin-

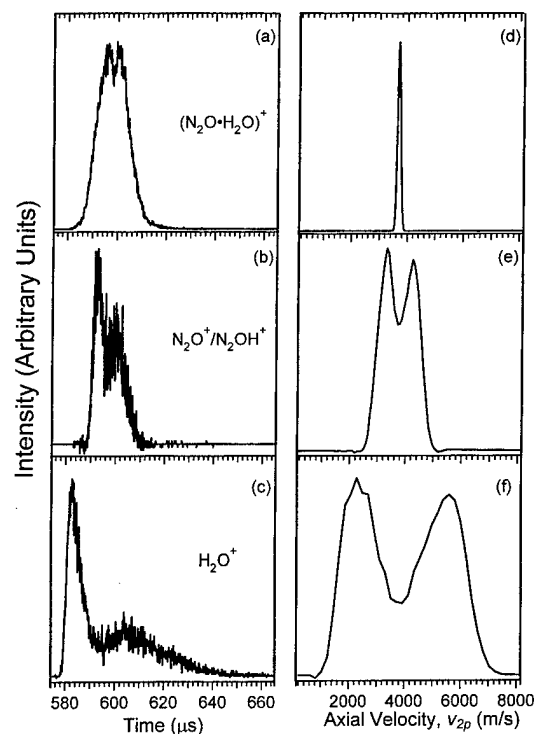


FIG. 2. TOF spectra of $(\text{N}_2\text{O} \cdot \text{H}_2\text{O})^+$ primary ion, (a), $\text{N}_2\text{O}^+/\text{N}_2\text{OH}^+$ photoproducts, (b), and H_2O^+ photoproduct, (c) recorded at 514 nm with the laser polarization parallel to the octopole axis, $\chi=0^\circ$. Monte Carlo simulation of the spatially broadened velocity distribution of the primary ions irradiated by the laser, (d). Velocity transformed TOF spectra of $\text{N}_2\text{O}^+/\text{N}_2\text{OH}^+$, (e), and H_2O^+ , (f), photofragments.

ning technique previously applied in this laboratory.^{32–37} The bin width is on the order of the velocity resolution of the experiment.

The velocity distribution of Fig. 2(d) is narrow compared to the observed photofragment distributions and is indicative of the high resolution of the TOF experiment. The experimental resolution is determined by the center velocity and the velocity width of the primary ion beam, the photolysis length, and the flight distance. The primary ion velocity and width are measured using the octopole as a retarding field analyzer. The broadening due to the photolysis length is accounted for by calculating distributions for several representative origins within the photolysis region and averaging, and the flight distance of 10.9 cm is fixed by the experimental geometry.

B. Instrument discrimination function

Photodissociation of molecular ions can produce fragment ions with velocity components transverse to the octopole axis that are much larger than those encountered in typical GIB scattering experiments. These large transverse velocity components are subject to losses particularly in the octopole extraction stages. Information regarding the instrumental discrimination function can be obtained from GIB-VAR measurements of a well characterized, high kinetic energy release system such as Ar_2^+ . The principle behind the GIB-VAR experiment has been discussed in detail by Gerlich²² and Mark and Gerlich.²³ The method is based on the fact that the maximum transmitted transverse energy is

proportional to the square of the variable rf voltage that governs the guiding field. Hence, the octopole acts as a low-pass transverse energy analyzer. Gerlich²² and Mark and Gerlich²³ have shown that by applying a dc potential, V_{dc} , to the rods a transverse energy component of qV_{dc} is imparted to the ions. The transverse energy confinement potential is calibrated by measuring the transmitted ion current as a function of rf voltage. For a given V_{dc} , the inflection point of the curve (ca. 50% transmission) is assigned to the guiding field strength producing the effective potential equal to $\frac{1}{2}m\nu_t^2$ where ν_t is the transverse velocity component of the ions. Calibrations were performed for m/z ratios of 18, 40, 44, 62, 64, and 80.

In the GIB-VAR photolysis experiments, the laser beam and ion beam propagate collinearly down the octopole axis. In this geometry, the laser polarization is always perpendicular to the octopole axis (Fig. 1). The reducing telescope is adjusted so that the laser beam waist is approximately 1 mm in the octopole. The Q-switch of the laser is fired when the 20 μ s cluster ion pulse is centered in the first octopole, and the ~ 7 ns laser pulse passes through the ion pulse. Approximately 0.5 μ s after the Q-switch is fired, the applied rf voltage is ramped down to a new variable level with a decay time constant of less than 1.5 μ s. It is this new level that constitutes the discriminating rf voltage of the VAR measurement. These conditions assure that the injected primary ion-beam spatial density and energy profiles are constant for different applied rf voltages, and hence, that reductions in secondary ion counts can be attributed solely to a loss of secondary ions with transverse kinetic energies in excess of the ion guide effective potential. The GIB-VAR method is an integral technique whereby the number of ion counts at a specific rf voltage represents all ions with transverse kinetic energies less than or equal to the effective potential. Therefore the derivative of the transmission curve is related to the radial speed distribution, as shown in the Appendix.

III. ANALYSIS

A. Velocity diagrams and expressions

The vector diagrams appropriate for photodissociation studies in an octopole ion guide are depicted in Fig. 3, and Table I provides a compiled reference for the symbols used in the figure and the discussion below. The figure identifies the origin of the laboratory (LAB) and center-of-mass (CM) coordinate frames. The LAB and CM coordinate systems have axis labels (X, Y, Z) and (x', y', z'), respectively. The ion-beam axis defines the location of the Z axis, and the laser polarization unit vector \hat{e} defines the location of the z' axis. We follow the notation where unprimed symbols are referenced to the LAB frame origin, primed symbols are referenced to the CM frame origin, the subscripts 1, 2, and 3 refer to the primary ion, ionic photoproduct, and neutral photoproduct, respectively, and bold face symbols refer to vectors while the same italicized, normal face symbols represent their scalar magnitudes.

The photofragment ion parallel velocity, ν_{2p} , measured by GIB-TOF is the projection of \mathbf{v}_2 on the octopole axis (Z axis), and the transverse velocity, \mathbf{v}_{2t} , measured by GIB-

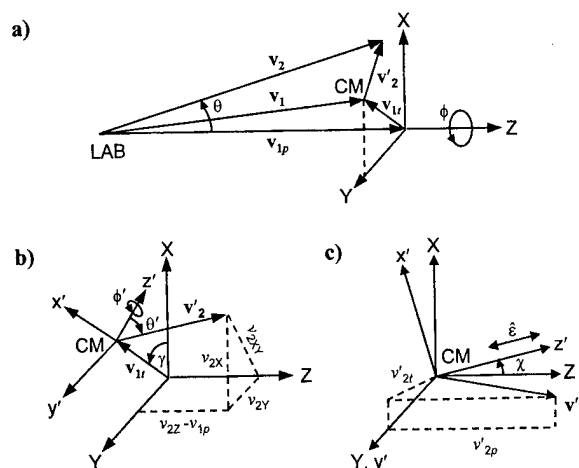


FIG. 3. Vector diagrams for photodissociation studies. The symbols used in the figure are defined in Table I. The origins of the laboratory and center-of-mass coordinate frames are labeled LAB and CM, respectively. The LAB frame XYZ coordinate system is defined with respect to the octopole axis (Z axis), and the CM frame $x'y'z'$ is defined with respect to the laser polarization unit vector, \hat{e} (z' axis).

VAR is the projection of \mathbf{v}_2 on the octopole cross sectional plane (the XY plane). The laser polarization unit vector \hat{e} is allowed to rotate in the XZ plane as shown in Fig. 3(c). Considering Fig. 3, the X , Y , and Z components of \mathbf{v}_2 , namely ν_{2X} , ν_{2Y} , and ν_{2Z} , are

$$\nu_{2X} = \nu'_2 \cos(\theta') \sin(\chi) + \nu'_2 \sin(\theta') \cos(\phi') \cos(\chi) + \nu_{1t} \cos(\gamma), \quad (1a)$$

$$\nu_{2Y} = \nu'_2 \sin(\theta') \sin(\phi') + \nu_{1t} \sin(\gamma), \quad (1b)$$

TABLE I. Nomenclature for the photodissociation scattering dynamics. The subscripts 1, 2, and 3 refer to the primary ion, ionic photoproduct, and neutral photoproduct, respectively. The unprimed symbols are referenced to the laboratory (LAB) frame origin, and the primed symbols are referenced to the center-of-mass (CM) frame origin.

m_1	total mass (primary ion)
m_2, m_3	photoproduct mass (ion, neutral)
$\mu = m_2 m_3 / m_1$	reduced mass
$\mathbf{v}_1, \mathbf{v}_2$	velocity in the LAB frame
$\mathbf{v}_{1p}, \mathbf{v}_{1t}$	primary LAB velocity (axial, transverse)
$\mathbf{v}_{2p}, \mathbf{v}_{2t}$	ionic photoproduct LAB velocity (axial, transverse)
$\mathbf{v}'_2, \mathbf{v}'_3$	velocity in the CM frame
$\mathbf{v}'_{2p} = \mathbf{v}_{2p} - \mathbf{v}_{1p}$	ionic photoproduct CM axial velocity
$\mathbf{v}'_{2t} = \mathbf{v}_{2t} - \mathbf{v}_{1t}$	ionic photoproduct CM transverse velocity
$\mathbf{v}_{rel} = \mathbf{v}_3 - \mathbf{v}_2 = \mathbf{v}'_3 - \mathbf{v}'_2$	relative velocity
$E_T = \frac{1}{2} \mu \mathbf{v}_{rel} ^2$	kinetic energy release
\hat{e}	laser polarization unit vector (defines z' axis)
χ	laser polarization angle ($0 \leq \chi \leq \pi/2$)
θ'	CM frame photodissociation scattering angle ($0 \leq \theta' \leq \pi$)
ϕ'	CM frame photodissociation scattering azimuthal angle ($0 \leq \phi' \leq 2\pi$)
θ	LAB frame photodissociation scattering angle ($0 \leq \theta \leq \pi$)
ϕ	LAB frame photodissociation scattering azimuthal angle ($0 \leq \phi \leq 2\pi$)
γ	angle between \mathbf{v}_{1t} and X axis ($0 \leq \gamma \leq 2\pi$)

$$\nu_{2Z} = \nu'_2 \cos(\theta') \cos(\chi) - \nu'_2 \sin(\theta') \cos(\phi') \sin(\chi) + \nu_{1p}, \quad (1c)$$

and the magnitude of the CM velocity vector, \mathbf{v}'_2 , is given by

$$\nu'_2 = \frac{(m_1 - m_2)}{m_1} |\mathbf{v}_{\text{rel}}| = \frac{(m_1 - m_2)}{m_1} \sqrt{\frac{2E_T}{\mu}}, \quad (2)$$

where m_1 is the total mass, m_2 is the ionic photoproduct mass, μ is the photoproduct reduced mass, \mathbf{v}_{rel} is the photofragment relative velocity, and E_T is the kinetic energy release of the fragments. By definition, the magnitude of \mathbf{v}_{2p} is

$$\nu_{2p} = |\nu_{2Z}|, \quad (3)$$

and the magnitude of \mathbf{v}_{2t} is

$$\nu_{2t} = \sqrt{\nu_{2X}^2 + \nu_{2Y}^2} = |\nu_{2XY}|, \quad (4)$$

where $|\nu_{2i}|$ is the absolute value of the velocity component ν_{2i} . Equations (1)–(4) are used to derive the translational energy and angular distributions of the photodissociation event from the experimentally observed quantities.

We note that the primary ions have oscillatory trajectories and that the majority of these ions are photolyzed off the octopole axis.³⁰ The transverse velocity component, ν_{1t} , depends on the radial position, \hat{r} , of the primary ion and is given by²²

$$\nu_{1t} = \sqrt{\frac{2(E_{1t} - U^*)}{m_1}}, \quad (5)$$

where E_{1t} is the total transverse energy of the primary ion, and U^* is the effective potential²² calculated for the primary ion mass, m_1 , at a radial distance of r at the rf voltage of the experiment.

The above treatment also assumes that the vector additions are independent of r because ions originating at $r=0$ always result in \mathbf{v}_{2t} being normal to the tangent. An ion photolyzed off the octopole axis, however, experiences a reduced transverse velocity, because \mathbf{v}_{2t} no longer intersects the octopole boundaries normal to the tangent. This effect causes some of the photofragment velocity to become angular velocity. Following trigonometric relations, the magnitude of the corrected transverse component normal to the tangent, ν_{2tc} , is given by

$$\nu_{2tc} = \nu_{2t} \cos[\arcsin(r \cos \eta)], \quad (6a)$$

where

$$\eta = \arctan(\nu_{2\hat{r}} / \nu_{2\hat{r}_\perp}), \quad (6b)$$

$\nu_{2\hat{r}}$ is the velocity component parallel to the radial displacement direction, and $\nu_{2\hat{r}_\perp}$ is the velocity component perpendicular to the radial displacement direction. The correction of Eq. (6) depends on the overlap geometry between the ion-beam and laser intensity profiles and in most cases is small. For example, the average correction using the present TOF and VAR photolysis conditions is approximately 1% and 5%, respectively.

The velocity expressions presented in this section are incorporated into two distinct methods of analysis. The first is a forward convolution analysis based on numerical evalua-

tion, and the second is a direct inversion analysis based on analytic expressions. The details of both methods are discussed below.

B. Forward convolution analysis

In the forward convolution analysis method, Monte Carlo simulations including all known experimental broadening mechanisms are compared to GIB-TOF and GIB-VAR measurements. The masses of the primary ion and the photoproducts, the rf voltage before and after the laser pulse, and the angle χ are set to the values used in the experiment to be simulated. The program chooses r , ν_{1p} , ν_{1t} , and all the remaining angles randomly from normalized probability tables and computes ν_{2p} and ν_{2tc} . The probability function for the initial radial position is a "top hat" function representing our best estimate of the convolution of laser intensity profile and the simulated ion probability density profile over the overlap region.³⁰ The probability functions for ν_{1p} and ν_{1t} of the primary ion beam are determined from retardation scans using the octopole as a retarding field analyzer²¹ and from VAR measurements,²³ respectively. The angles ϕ' and γ are determined trivially from uniform probability distribution functions, and θ' is determined using the expression

$$P(\theta') = \frac{1}{4\pi} [1 + \beta P_2(\cos \theta')], \quad (7)$$

where β is the anisotropy parameter ranging from -1 to 2 with 0 representing an isotropic distribution, and $P_2(\cos \theta')$ is the second order Legendre polynomial in $\cos \theta'$.^{3,38–41} The Monte Carlo forward convolution program simulates anywhere from 10 000 to 100 000 photofragment trajectories to generate TOF and VAR spectra for specific values for β , χ , and E_T . These calculated TOF and VAR basis functions are then fit to experimental data using a linear least squares fitting routine based on a singular value decomposition (SVD) algorithm.

C. Direct inversion analysis

Application of the Monte Carlo forward convolution technique to a polyatomic system can be a formidable task if the number of product channels available is quite large. The task of deriving a β parameter is particularly arduous, because it is typically obtained by trial and error. If the experimental broadening mechanisms are small, as in the present experiments, then direct inversion of the experimental data is possible. Direct inversion methods for transforming raw data of other experiments have been discussed by Continetti *et al.*¹⁷ and Jarrold *et al.*^{42–44}

For a distribution of kinetic energy releases, the probability that the products have a resultant velocity along the ion-beam axis with a magnitude between ν'_{2p} and $\nu'_{2p} + d\nu'_{2p}$ over the axial range $\nu'_{2p} \leq \nu'_2$ for a single kinetic energy release, E_T is given by

$$I(\nu'_{2p}) = \int_{\nu'_{2p}}^{\infty} \frac{P(\nu'_2)}{\nu'_2} \left[1 + \frac{\beta(\nu'_2)}{2} \times \left(3 \frac{\nu'^2_{2p}}{\nu'^2_2} - 1 \right) P_2(\cos \chi) \right] d\nu'_2, \quad (8)$$

where $P(\nu'_2)$ is the product CM velocity distribution, and $\beta(\nu'_2)$ is the asymmetry parameter as a function of product CM velocity. At magic angle, $\chi=54.7^\circ$, $P_2(\cos \chi)$ is equal to zero, and the derivative of the distribution described by Eq. (8) yields the useful result

$$\frac{dI(\nu'_{2p})}{d\nu'_{2p}} = - \frac{P(\nu'_2 = \nu'_{2p})}{\nu'_{2p}}, \quad (9)$$

which states that the product center of mass velocity distribution can be obtained directly from the derivative of the velocity transformed TOF spectrum taken at magic angle. The derivation of Eq. (8) and other applicable velocity expressions is outlined in the Appendix.

IV. RESULTS

A. Instrument evaluation

The photodissociation of the Ar_2^+ cluster ion provides an excellent means by which to evaluate the instrument response. The $\text{Ar}^+ + \text{Ar}$ photofragments do not acquire internal energy apart from spin-orbit excitation, and with vibrationally cold cluster ions, $P(\nu'_2)$ is essentially a delta function. The spectroscopy of the Ar_2^+ cluster ion is also favorable.⁴⁵⁻⁵¹ The ultraviolet absorption bands of Ar_2^+ involve the parallel $^2\Sigma_g^+ \leftarrow ^2\Sigma_u^+$ transition which has an absorption maximum at 317 nm.⁵² The dissociation energy of Ar_2^+ is 1.38 ± 0.05 eV,⁵³ and the excited $^2\Sigma_g^+$ correlates with the formation of Ar^+ in the excited $^2P_{1/2}$ spin-orbit component which in turn lies 0.18 eV above the ground state. At 300 nm (4.13 eV), the dissociation occurs almost exclusively on the purely repulsive $^2\Sigma_g^+$ surface, and the photon energy is 2.57 eV above the dissociation threshold. Thus direct dissociation is an excellent assumption.

Figure 4 shows the LAB axial velocity component distributions of Ar^+ following the photoexcitation of Ar_2^+ at 300 nm with the laser polarization set to magic angle ($\chi=54.7^\circ$). The initial primary ion velocity, ν_{1p} , is 3850 m/s. At magic angle, $I(\nu_{2p})$ is independent of β , and a rectangular distribution centered at ν_{1p} is expected. Substantial loss of the ion signal is observed near ν_{1p} where ν_{2t} is large indicating that the majority of the discrimination is occurring in the transverse direction. The solid curve in Fig. 4 is the result of a fit by a linear combination of Monte Carlo forward convolution simulations incorporating a discrimination step function defined with respect to a transverse velocity of 2500 m/s. The fit of Fig. 4 yields an average CM kinetic energy release of 2.51 ± 0.09 eV, suggesting that the Ar_2^+ ions possess an average internal energy of approximately 0.06 eV consistent with previous studies conducted in this cluster ion source.²⁹ As can be seen in Fig. 4, the simple discrimination function captures the major spectral features but does not reproduce the small asymmetry. The small asymmetry in the spectrum is indicative of axial discrimina-

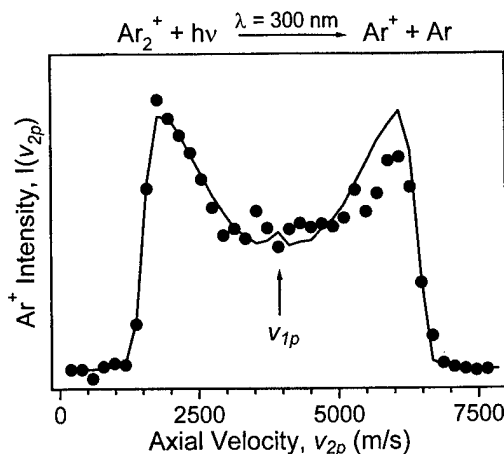


FIG. 4. LAB axial velocity distribution of Ar^+ following the photoexcitation of Ar_2^+ at 300 nm with the laser polarization at $\chi=54.7^\circ$ (magic angle). The solid symbols are the velocity transformed TOF experimental data; the solid curve is the fitted velocity distribution including discrimination in the Monte Carlo forward convolution simulations.

tion and arises because the optimal extraction lens and deflector plate voltages vary slightly over the extensive velocity range exhibited between the slow backward-scattered (ca. 1200 m/s) and the fast forward-scattered (ca. 6600 m/s) ions. For smaller kinetic energy releases, such as for the $(\text{N}_2\text{O} \cdot \text{H}_2\text{O})^+$ cluster ion shown in Fig. 2, the asymmetry is much reduced and the axial discrimination is ignored.

In cases where the kinetic energy release is not predictable, the variations in the TOF spectrum could be caused by discrimination and/or the presence of multiple kinetic energy release channels. Therefore, another analysis method is necessary, and we find the GIB-VAR method to be useful in this case. Figure 5(a) shows the VAR spectrum of the H_2O^+ photofragment produced by the photolysis of $(\text{N}_2\text{O} \cdot \text{H}_2\text{O})^+$

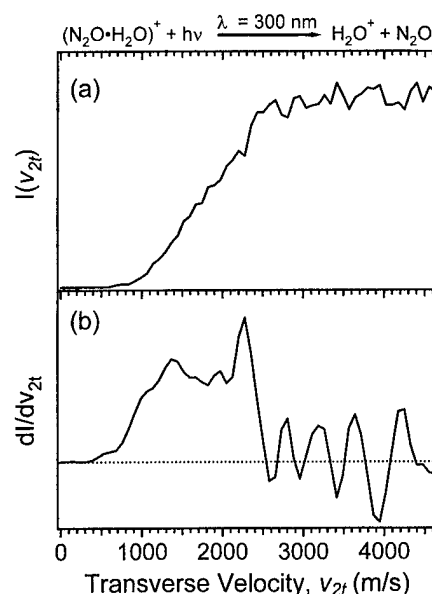


FIG. 5. (a) VAR spectrum of H_2O^+ photofragments produced by the 300 nm photolysis of $(\text{N}_2\text{O} \cdot \text{H}_2\text{O})^+$ cluster ions with a beam velocity of 3600 m/s. The laser polarization is perpendicular to the octopole axis. (b) Derivative of (a).

cluster at a wavelength of 300 nm and a primary beam velocity of 3600 m/s, and Fig. 5(b) shows the derivative of the same data. The derivative of the VAR spectrum represents the probability distribution function for ν_{2t} [Eq. (A5) of the Appendix]. The H_2O^+ transverse velocity distribution of Fig. 5(b) cuts off sharply at 2500 m/s consistent with the discrimination function used for Ar^+ in the Ar_2^+ study.

The transverse discrimination function was investigated by varying the photolysis wavelength (photofragment velocity), the extraction lens aperture diameters, and the primary ion velocity. The results of these studies suggest that the discrimination is most likely to occur in the octopole extraction optics. Experiments performed with both Ar_2^+ and $(\text{N}_2\text{O}\cdot\text{H}_2\text{O})^+$ cluster ions consistently exhibited cutoff velocities of approximately 2500 m/s for the primary ion velocity range of 3600 m/s to 3900 m/s used in this study. The primary beam velocity used represents a compromise between resolution, collection of backward-scattered ions, and discrimination. The velocity range chosen provides sufficient resolution (Fig. 2), collection of all backward-scattered ions, and minimal discrimination effects. Specifically, using a combined TOF and VAR analysis, it is determined that the H_2O^+ product ion is collected at 96% efficiency at 657 nm and 77% efficiency at 458 nm with an approximately linear decrease in collection efficiency between these two extremes. The N_2O^+ and N_2OH^+ products are collected with 100% efficiency over the entire wavelength range.

B. Photodissociation dynamics of $(\text{N}_2\text{O}\cdot\text{H}_2\text{O})^+$

Product recoil velocity distributions of the $\text{N}_2\text{O}^+/\text{N}_2\text{OH}^+ + \text{H}_2\text{O}/\text{OH}$ and $\text{H}_2\text{O}^+ + \text{N}_2\text{O}$ photodissociation channels in the 657–458 nm range have been measured using TOF. The squares shown in Fig. 6(a)–6(c) are the LAB axial velocity distributions, $I(\nu_{2p})$, for $\text{N}_2\text{O}^+/\text{N}_2\text{OH}^+$ ionic photoproducts from the photodissociation of $(\text{N}_2\text{O}\cdot\text{H}_2\text{O})^+$ at 458 nm for laser polarization angles, χ , of 54.7°, 0°, and 90°, respectively. Figure 6(d) and 6(e) are the CM transformed distribution, $I(\nu'_{2p})$, of Fig. 6(a) and 6(b), respectively. Note that after the transformation $\nu'_{2p} = |\nu_{2p} - \nu_{1p}|$, the two symmetric portions of the velocity distribution are averaged. The data of Fig. 6(f) are the difference distribution resulting from the normalized subtraction of 6(d) from 6(e).

Kinetic energy release distributions are determined from magic angle measurements. The solid curve in Fig. 6(a) is the SVD fit of the Monte Carlo forward convolution basis functions for discrete values of E_T to the experimental magic angle data. Kinetic energy release distributions determined at 590 nm, 514 nm, 488 nm, and 458 nm using forward convolution analysis (curves) are shown in Fig. 7 and are compared to distributions determined using direct inversion analysis (squares) of the same data. The arrows in Fig. 7 indicate the maximum available energy possible for formation of N_2O^+ which is the difference between the excitation photon energy and the collision-induced dissociation (CID) threshold for the production of $\text{N}_2\text{O}^+ + \text{H}_2\text{O}$ products of 1.43 ± 0.12 eV.²⁹ The internal energy of the $(\text{N}_2\text{O}\cdot\text{H}_2\text{O})^+$ cluster ion, estimated at 0.13 eV,²⁹ is not considered in the calculation which partially accounts for the probability distributions

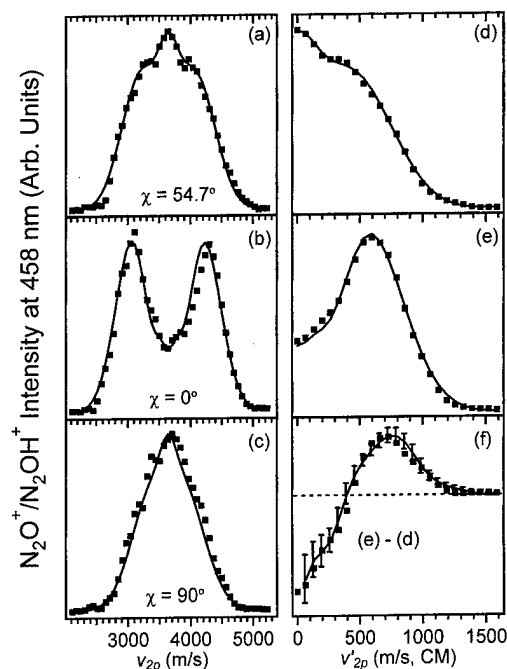


FIG. 6. (a) Velocity transformed TOF measurements of $\text{N}_2\text{O}^+/\text{N}_2\text{OH}^+$ from the photodissociation of $(\text{N}_2\text{O}\cdot\text{H}_2\text{O})^+$ at 458 nm for $\chi = 54.7^\circ$. (b) $\chi = 0^\circ$. (c) $\chi = 90^\circ$. (d) and (e) are the CM transforms of (a) and (b), respectively. (f) Difference distribution, (d) minus (e). The solid line in (a) is a SVD fit of the Monte Carlo forward convolution basis functions to the data. The solid curves in (b)–(e) are Monte Carlo forward convolution simulations including discrimination. The dashed line in (f) marks zero probability, and the solid curve is a $\langle\beta\rangle$ fit of Eq. (8) to the data assuming the kinetic energy release distribution obtained from (d).

extending past the maximum available energy.

The kinetic energy release distributions for the $\text{N}_2\text{O}^+/\text{N}_2\text{OH}^+ + \text{H}_2\text{O}/\text{OH}$ product channels shown in Fig. 7 are bimodal with a narrow, low-energy feature peaking below 0.2 eV and a much broader feature peaking at higher energy. Graul *et al.*³¹ measured the visible photodissociation dynamics of this cluster ion in a reverse-geometry sector mass spectrometer experiment and resolved the two product channels. These authors observed that the kinetic energy re-

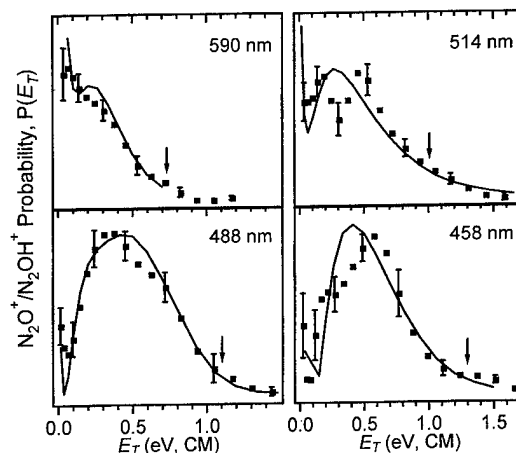


FIG. 7. CM kinetic energy release distributions for $\text{N}_2\text{O}^+/\text{N}_2\text{OH}^+ + \text{H}_2\text{O}/\text{OH}$ produced from the photodissociation of $(\text{N}_2\text{O}\cdot\text{H}_2\text{O})^+$ at 590 nm, 514 nm, 488 nm, and 458 nm. The arrows in the figure indicate the maximum available energy possible for formation of $\text{N}_2\text{O}^+ + \text{H}_2\text{O}$.

TABLE II. Average asymmetry parameter, $\langle\beta\rangle$, and average kinetic energy release, $\langle E_T \rangle$, for $(\text{N}_2\text{O} \cdot \text{H}_2\text{O})^+ + h\nu \rightarrow \text{N}_2\text{O}^+/\text{N}_2\text{OH}^+ + \text{H}_2\text{O}/\text{OH}$.

λ	Forward convolution			Direct inversion			Graul <i>et al.</i> ^c	
	$\langle\beta\rangle^a$	$\langle E_T \rangle$	$\langle E_T \rangle^b$	$\langle\beta\rangle$	$\langle E_T \rangle$	$\langle E_T \rangle^b$	$\langle\beta\rangle$	$\langle E_T \rangle$
590 nm	1.1	0.26	0.27	0.74 ± 0.12	0.29 ± 0.04	0.31 ± 0.05	1.0	0.35
514 nm	1.3	0.50	0.52	1.09 ± 0.05	0.49 ± 0.05	0.51 ± 0.05	1.1	0.50
488 nm	1.2	0.53	0.54	1.14 ± 0.05	0.55 ± 0.05	0.56 ± 0.06	1.2	0.58
458 nm	1.5	0.57	0.59	1.30 ± 0.04	0.59 ± 0.06	0.61 ± 0.07	1.3	0.65

^aError for all values is ± 0.2 .^bCorrected for $\text{N}_2\text{OH}^+ + \text{OH}$ contribution.^cReference 31, error not reported.

lease distributions for $\text{N}_2\text{OH}^+ + \text{OH}$ products peak near zero energy and drop off approximately exponentially with energy and that the kinetic energy release distribution for $\text{N}_2\text{O}^+ + \text{H}_2\text{O}$ products is roughly triangular and peaked far from zero kinetic energy release. Fitting the two features of the bimodal distributions of Fig. 7 to a linear combination of an exponential and Gaussian function, respectively, yields relative probabilities of the two features as a function of wavelength closely approximating the relative photodissociation cross sections for the production of N_2OH^+ and N_2O^+ reported by Williams *et al.*³⁰ Therefore, we attribute the low-energy feature to the production of $\text{N}_2\text{OH}^+ + \text{OH}$ photoproducts and the high-energy feature to the production of $\text{N}_2\text{O}^+ + \text{H}_2\text{O}$ photoproducts. Table II lists the results for $\text{N}_2\text{O}^+/\text{N}_2\text{OH}^+ + \text{H}_2\text{O}/\text{OH}$ products obtained by the Monte Carlo forward convolution and direct inversion analysis methods and compares them with the results measured by Graul *et al.*³¹ The average kinetic energy releases measured for $\text{N}_2\text{O}^+ + \text{H}_2\text{O}$ products are corrected for the contribution of $\text{N}_2\text{OH}^+ + \text{OH}$ products using the relative photodissociation branching ratios measured by Williams *et al.*³⁰ and the average kinetic energy releases for the production of $\text{N}_2\text{OH}^+ + \text{OH}$ products measured by Graul *et al.*³¹

The asymmetry parameter averaged over E_T , i.e., $\langle\beta\rangle$, is obtained by modeling data taken at $\chi=0^\circ$ and $\chi=90^\circ$. The solid lines of Fig. 6(b) and 6(c) are Monte Carlo simulations using the kinetic energy release distribution obtained from the data of 6(a) and an optimized value for $\langle\beta\rangle$ of 1.5. In the direct inversion analysis method, velocity distributions taken at $\chi=0^\circ$ and $\chi=54.7^\circ$ are modeled with Eq. (8) to obtain $\langle\beta\rangle$. Note that the first term in Eq. (8) represents the velocity distribution taken at magic angle, and it is convenient to subtract this contribution to yield a function that is proportional to $\langle\beta\rangle$. The solid curve in Fig. 6(f) shows the results of the fit to the difference distribution. The fitted curve has error bars which correspond to the propagated error associated with the kinetic energy release coefficients derived from the direct inversion analysis of the data shown in 6(c). The values of $\langle\beta\rangle$ obtained by both analysis methods for $\text{N}_2\text{O}^+/\text{N}_2\text{OH}^+ + \text{H}_2\text{O}/\text{OH}$ products and those for the $\text{N}_2\text{O}^+ + \text{H}_2\text{O}$ products reported by Graul *et al.*³¹ for data taken at excitation wavelengths of 590 nm, 514 nm, 488 nm, and 458 nm are recorded in Table II. The contribution of the $\text{N}_2\text{OH}^+ + \text{OH}$ channel to $\langle\beta\rangle$ is small compared to the contribution of the $\text{N}_2\text{O}^+ + \text{H}_2\text{O}$ channel as evidenced by the close

agreement between our values with those of Graul *et al.*³¹ in Table II.

LAB axial velocity distributions, $I(\nu_{2p})$, for H_2O^+ produced in $(\text{N}_2\text{O} \cdot \text{H}_2\text{O})^+$ photodissociation at 488 nm are shown as solid circles in Fig. 8(a)–8(c) for laser polarization angles of 54.7° , 0° , and 90° , respectively. Figure 8(c) and 8(e) are the CM transformed distributions, $I(\nu'_{2p})$, of Fig. 8(a) and 8(b), respectively. The data of Fig. 8(f) is the difference distribution resulting from the subtraction of 8(d) from 8(e). The analysis methods for the H_2O^+ photofragment are the same as those applied to the $\text{N}_2\text{O}^+/\text{N}_2\text{OH}^+$ photofragment with the exception that prior to applying the direct inversion method, the raw data taken at magic angle is corrected for discrimination. This correction is based on the

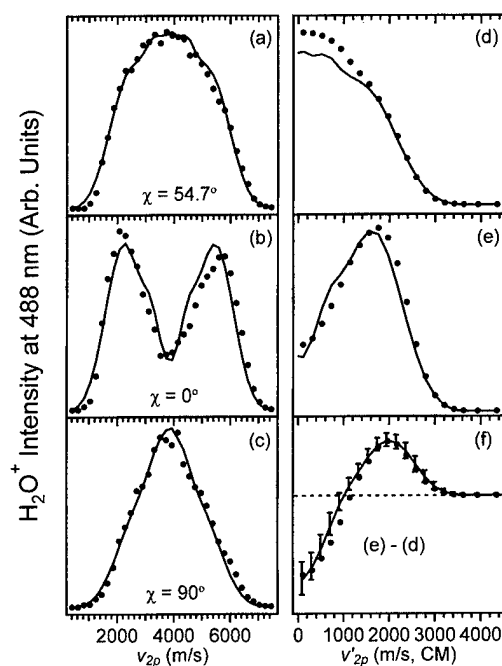


FIG. 8. (a) Velocity transformed TOF measurements of H_2O^+ from the photodissociation of $(\text{N}_2\text{O} \cdot \text{H}_2\text{O})^+$ at 488 nm for $\chi=54.7^\circ$. (b) $\chi=0^\circ$. (c) $\chi=90^\circ$. (d) is the CM transform of (a) corrected for discrimination. (e) is the CM transform of (b). (f) Difference distribution, (d) minus (e). The solid line in (a) is a SVD fit of the Monte Carlo forward convolution basis functions to the data. The solid curves in (b)–(e) are Monte Carlo forward convolution simulations including discrimination. The dashed line in (f) marks zero probability, and the solid curve is a $\langle\beta\rangle$ fit of Eq. (8) to the data assuming the kinetic energy release distribution obtained from (d).

TABLE III. Average asymmetry parameter, $\langle\beta\rangle$, and average kinetic energy release, $\langle E_T \rangle$, for $(\text{N}_2\text{O} \cdot \text{H}_2\text{O})^+ + h\nu \rightarrow \text{H}_2\text{O}^+ + \text{N}_2\text{O}$.

λ	Forward convolution		Direct inversion		Graul <i>et al.</i> ^b	
	$\langle\beta\rangle^a$	$\langle E_T \rangle$	$\langle\beta\rangle$	$\langle E_T \rangle$	$\langle\beta\rangle$	$\langle E_T \rangle$
657 nm	0.9	0.30	0.88 ± 0.08	0.35 ± 0.05		0.30
590 nm	1.1	0.39	1.04 ± 0.09	0.44 ± 0.07		0.38
514 nm	1.4	0.58	1.41 ± 0.07	0.62 ± 0.09	1.1	0.51
488 nm	1.4	0.62	1.38 ± 0.06	0.65 ± 0.10	1.1	0.57
458 nm	1.5	0.68	1.52 ± 0.13	0.71 ± 0.13		0.66

^aError for all values is ± 0.2 .^bReference 31, error not reported.

signal intensity expressions of Eqs. (8) and (9) which show that the signal intensity for the i th axial velocity component, $I(\nu'_{2p(i)})$, contributes equally at CM velocities $\nu'_{2p(j)} \leq \nu'_{2p(i)}$. Assuming that the transverse velocity discrimination function is a step function occurring at $\nu_{2t} = \nu_c$, where ν_c is the cutoff velocity, the signal intensity for axial velocity components less than $\sqrt{\nu_{2p(i)}^2 - \nu_c^2}$ will be diminished by an amount $I(\nu'_{2p(i)})$. The correction is applied starting at $\nu'_{2p(\infty)} = \nu'_{\max}$ and stopping at $\nu'_{2p(i)} = \nu_c$. The magnitude of the correction is relatively small as shown by the difference between the corrected data and the simulation including discrimination shown in Fig. 8(d). The raw data taken at $\chi = 0^\circ$ cannot be corrected for discrimination without using a specific value of $\langle\beta\rangle$. Fortunately, the correction is negligible at this angle, because the majority of the photoproducts are either forward or backward scattered ($\langle\beta\rangle \sim 1.4$), i.e., the photoproducts have small transverse velocity components and few are lost. The opposite is true for the data taken at $\chi = 90^\circ$.

The results for the average asymmetry parameter and average kinetic energy release for the H_2O^+ photofragment using the Monte Carlo forward convolution and direct inversion analysis methods are shown in Table III along with the results obtained by Graul *et al.*³¹ The kinetic energy release distributions obtained at 657 nm, 590 nm, 514 nm, 488 nm, and 458 nm are shown in Fig. 9. The arrows in Fig. 9 indicate the maximum available energy possible for formation of $\text{H}_2\text{O}^+(\tilde{X}^2B_1)$ which is the difference between the excitation photon energy and the previously reported CID threshold for the production of $\text{H}_2\text{O}^+ + \text{N}_2\text{O}$ products of 1.04 ± 0.06 eV.²⁹ The probability distributions are consistent with the maximum available energy, particularly if the internal energy of the cluster ion is considered. The arrows marked with an asterisk indicate the maximum available energy possible for formation of $\text{H}_2\text{O}^+(\tilde{A}^2A_1)$ which becomes energetically feasible at 548 nm.

The determination of $\beta(E_T)$ requires doubly differential measurements such as the combined TOF and VAR approach outlined in the Appendix. In the absence of doubly differential measurements, Jarrold, Illies, and Bowers⁴⁴ have pointed out that trends in β as a function of E_T can be obtained by allowing the function $\beta(\nu'_2)$ of Eq. (8) to be approximated by a polynomial expansion. The error associated with $\beta(\nu'_2)$ using this approximation, however, increases rapidly with increasing order of the polynomial, because ν'_{2p} and χ are not independent variables. When $\beta(\nu'_2)$ is approxi-

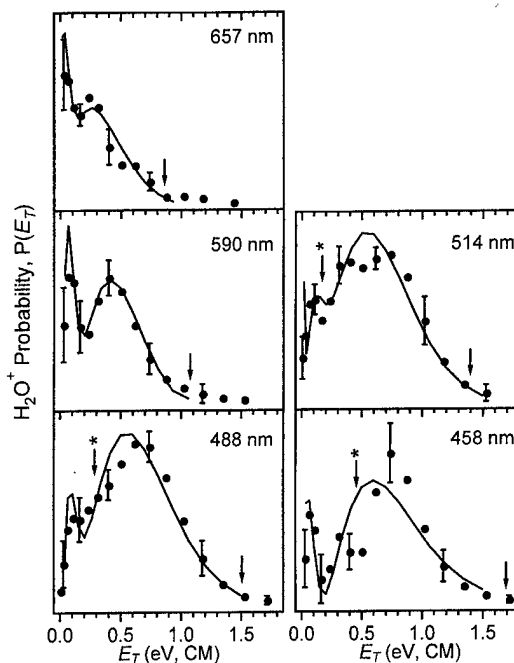


FIG. 9. CM kinetic energy release distributions for $\text{H}_2\text{O}^+ + \text{N}_2\text{O}$ produced from the photodissociation of $(\text{N}_2\text{O} \cdot \text{H}_2\text{O})^+$ at 657 nm, 590 nm, 514 nm, 488 nm, and 458 nm. The arrows in the figure indicate the maximum available energy possible for formation of $\text{H}_2\text{O}^+(\tilde{X}^2B_1) + \text{N}_2\text{O}$, and the arrows marked with an asterisk indicate the maximum available energy possible for formation of $\text{H}_2\text{O}^+(\tilde{A}^2A_1) + \text{N}_2\text{O}$.

mated by a first order polynomial (line), the error is small enough to discuss general trends in β as a function of E_T . The results presented below are obtained by assuming a linear dependence for $\beta(\nu'_2)$ in Eq. (8), and the resulting expression is used to analyze difference velocity distributions such as those shown in Figs. 6(f) and 8(f).

The asymmetry parameter for the $\text{N}_2\text{O}^+/\text{N}_2\text{OH}^+$ kinetic energy release distributions increases from low to high energy for all excitation wavelengths studied. This result is consistent with the previous studies by Graul *et al.*³¹ where the $\text{N}_2\text{OH}^+ + \text{OH}$ products were observed to form via a dissociation involving a long-lived intermediate (low anisotropy), and the $\text{N}_2\text{O}^+ + \text{H}_2\text{O}$ products exhibited characteristics of a direct dissociation (high anisotropy). Since the low-energy feature is attributed to the production of $\text{N}_2\text{OH}^+ + \text{OH}$ and the high-energy feature to the production of $\text{N}_2\text{O}^+ + \text{H}_2\text{O}$ in this study, an increase in β as a function of energy is expected. Figure 10 shows the plot of $\beta(E_T)$ associated with the production of $\text{H}_2\text{O}^+ + \text{N}_2\text{O}$ products for excitation wavelengths of 657 nm, 514 nm, and 458 nm. The results of Fig. 10 are obtained by allowing β to vary linearly with velocity, hence, the curvature in Fig. 10 arises from plotting the results as a function of energy. The asymmetry parameter at 657 nm has values of 0.5 at low kinetic energy release, 1.2 at high kinetic energy release, and 0.9 on average. This sharp increase in β is contrasted by the lack of energy dependence of the data taken at 458 nm which does not deviate significantly from the average value of 1.5. Data taken at wavelengths between 657 nm and 458 nm are intermediate to these two extremes as exemplified by the 514 nm data also shown in Fig. 10.

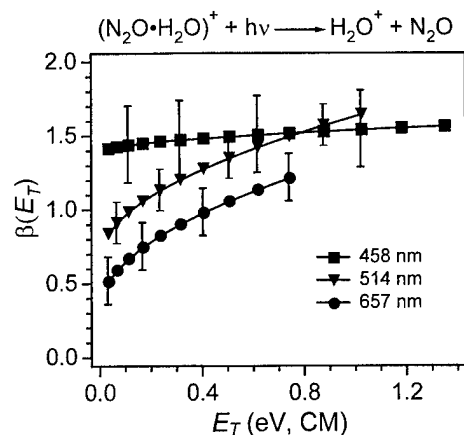


FIG. 10. Asymmetry parameter $\beta(E_T)$ associated with the production of $\text{H}_2\text{O}^+ + \text{N}_2\text{O}$ products for excitation wavelengths of 458 nm, 514 nm, and 657 nm.

V. DISCUSSION

We have demonstrated that the GIB-TOF technique is suitable for determining photodissociation product recoil velocity and angular distributions. The present results for $(\text{N}_2\text{O} \cdot \text{H}_2\text{O})^+$ photolysis obtained in a GIB apparatus compare favorably to the measurements conducted by Graul *et al.*³¹ in a reverse-geometry sector mass spectrometer. The majority of the H_2O^+ and N_2O^+ fragments are produced with large recoil velocities and high degrees of anisotropy. Product recoil velocity distributions with these characteristics are consistent with excitation to a repulsive surface followed by rapid dissociation. One possibility, as suggested by Graul *et al.*,³¹ is that the excited repulsive surface correlates with $\text{H}_2\text{O}^+(\tilde{X}^2B_1) + \text{N}_2\text{O}$ products and crosses a bound surface correlating with the $\text{N}_2\text{O}^+ + \text{H}_2\text{O}$ products. In this scenario, the N_2O^+ moiety is the charge carrier in the ground state, and the photoexcitation initiates a charge transfer reaction where H_2O^+ becomes the charge carrier. As the system enters the crossing region, a second charge transfer may occur to produce $\text{N}_2\text{O}^+ + \text{H}_2\text{O}$, or the system may continue on the repulsive surface to produce $\text{H}_2\text{O}^+(\tilde{X}^2B_1) + \text{N}_2\text{O}$. This mechanism explains the similarity in the photodissociation dynamics observed in these two product channels and the relatively energy-independent branching ratios.^{29,30}

The most significant differences between this study and that of Graul *et al.*³¹ are found in the results observed for the $\text{H}_2\text{O}^+ + \text{N}_2\text{O}$ product channel where the determined values for $\langle\beta\rangle$ and $\langle E_T\rangle$ are higher. Furthermore, a bimodal distribution is observed at all wavelengths in this study for the formation of $\text{H}_2\text{O}^+ + \text{N}_2\text{O}$ products, whereas Graul *et al.*³¹ only observed a bimodal kinetic energy release distribution at 657 nm. As noted in our previous publication,³⁰ we observe H_2O^+ to be the most abundant ion produced in the visible photodissociation of the $(\text{N}_2\text{O} \cdot \text{H}_2\text{O})^+$ cluster ion contrary to Graul *et al.*³¹ who report that N_2O^+ is the most abundant ionic photoproduct. Both experiments measure an essentially wavelength independent branching ratio, however, our measurements indicate an average H_2O^+ branching ratio of 64% which is approximately twice the 35% value reported by Graul *et al.*³¹ Excessive transverse discrimina-

tion, possibly occurring at the entrance slit of the electrostatic energy analyzer, could reduce the detection sensitivity in their experiments. These authors state that the Monte Carlo forward convolution method used to analyze their data included effects of discrimination, and indeed, the average kinetic energy release obtained by these authors is in general agreement with our results shown in Table III. This finding suggests that the correction used by Graul *et al.*³¹ partially accounts for the discrimination in their experiments but is not sufficient to recover the low-energy feature which appears in the region of their energy spectra that would suffer the most from transverse discrimination. The observation of a low-energy feature at all wavelengths in this study changes the previous interpretation of the photodissociation dynamics.

The bimodality suggests that other dissociation pathways exists for the production of H_2O^+ fragments. Graul *et al.*³¹ observed that the production of $\text{N}_2\text{OH}^+ + \text{OH}$ products is associated with a small asymmetry parameter and that the internal energy of the dissociated species is statistically distributed. Furthermore, deuterium isotope studies conducted in this laboratory indicate that the N_2OH^+ moiety is formed from photoinduced proton transfer reactions.³⁰ One scenario put forward by Graul *et al.*³¹ is that the $\text{N}_2\text{OH}^+ + \text{OH}$ products arise from excitation to a bound upper state followed by internal conversion to the ground state surface to form a vibrationally excited cluster ion. This vibrationally excited ion can then either undergo proton transfer to produce $\text{N}_2\text{OH}^+ + \text{OH}$ products or predissociate to produce $\text{H}_2\text{O}^+ + \text{N}_2\text{O}$ products. If vibrational predissociation is occurring on the ground state surface, a contribution of a low energy, statistically partitioned $\text{H}_2\text{O}^+ + \text{N}_2\text{O}$ products at excitation wavelengths paralleling the persistent formation of the $\text{N}_2\text{OH}^+ + \text{OH}$ products is expected. This scenario was discounted by Graul *et al.*³¹ since the low-energy feature was not observed. A predissociation mechanism, however, is consistent with the small asymmetry at low kinetic energy releases shown in Fig. 10 at long wavelengths where the branching ratio for the formation of $\text{N}_2\text{OH}^+ + \text{OH}$ products is largest.³⁰

At 458 nm, the β parameter of both the high- and the low-energy features is large. In this case, the low-energy feature can be attributed to highly excited, rapidly dissociating products. Given the short time allowed for rovibrational redistribution, it is likely that one or both of the products are electronically excited. The only energetically accessible product electronic state is $\text{H}_2\text{O}^+(\tilde{A}^2A_1)$. Therefore, we suggest that at the wavelengths below 548 nm, excitation to a minimum of two repulsive surfaces, one correlating to $\text{H}_2\text{O}^+(\tilde{X}^2B_1) + \text{N}_2\text{O}$ and another to $\text{H}_2\text{O}^+(\tilde{A}^2A_1) + \text{N}_2\text{O}$, is observed. Consequently, we attribute the low-energy feature primarily to formation of $\text{H}_2\text{O}^+(\tilde{X}^2B_1) + \text{N}_2\text{O}$ via a statistical dissociation (low anisotropy) at long wavelengths and of $\text{H}_2\text{O}^+(\tilde{A}^2A_1) + \text{N}_2\text{O}$ via a direct dissociation (high anisotropy) at short wavelengths.

The observation of $\text{N}_2\text{O}^+ + \text{H}_2\text{O}$ and $\text{H}_2\text{O}^+ + \text{N}_2\text{O}$ products with large kinetic energy releases and high degrees of asymmetry implies an impulsive mechanism. We assume a pseudodiatomic impulsive model^{3,41} for a polyatomic ion

AB^+ where the average kinetic energy released to the fragments, $\langle E_T \rangle$, is related to the available energy, E_{avail} , by

$$\langle E_T \rangle = (\mu_a / \mu_f) E_{\text{avail}}, \quad (10)$$

where μ_a is the reduced mass of the atoms through which AB^+ is associated and μ_f is the reduced mass of the fragments A and B^+ . The available energy is expressed as

$$E_{\text{avail}} = h\nu + E_{\text{int}} - E_0, \quad (11)$$

where $h\nu$ is the photon energy, E_{int} is the internal energy of the AB^+ polyatomic ion before photolysis, and E_0 is the dissociation threshold at zero Kelvin. Based on a previous study,²⁹ the $(\text{N}_2\text{O} \cdot \text{H}_2\text{O})^+$ cluster ions produced in our source have an internal energy of approximately 0.13 eV.

A plot of the average kinetic energy releases for the $\text{N}_2\text{O}^+ + \text{H}_2\text{O}$ and $\text{H}_2\text{O}^+ + \text{N}_2\text{O}$ fragments as a function of excitation photon energy yields a linear relationship confirming that the dynamics are described by an impulsive mechanism. A linear regression analysis of the $\text{N}_2\text{O}^+ + \text{H}_2\text{O}$ product channel yields a reduced mass ratio, μ_a / μ_f , of 0.52 ± 0.07 and a value of 1.36 ± 0.36 eV for E_0 . Likewise, a linear regression analysis of the $\text{H}_2\text{O}^+ + \text{N}_2\text{O}$ product channel yields a reduced mass ratio, μ_a / μ_f , of 0.47 ± 0.03 and a value of 1.02 ± 0.15 eV for E_0 . The slopes of the two lines corresponding to a reduced mass ratio of 0.5 indicate that approximately half of the available energy is partitioned into translation and that the dissociation occurs between two heavy atoms since $\mu_a / \mu_f \approx 0.6$ for an O–O or an O–N dissociation. This result is consistent with recent *ab initio* structure calculations.⁵⁴ Note that a much smaller fraction of the available energy would be partitioned into translation if the dissociation occurred between an O–H or a N–H coordinate because $\mu_a / \mu_f \approx 0.07$. The dissociation thresholds at zero Kelvin for $\text{N}_2\text{O}^+ + \text{H}_2\text{O}$ products and $\text{H}_2\text{O}^+ + \text{N}_2\text{O}$ products obtained here agree well with the previously reported thresholds of 1.43 ± 0.12 eV and 1.04 ± 0.06 eV obtained from low-energy CID studies.²⁹ We note that there are two spin-orbit components of the N_2O^+ ion separated by 0.016 eV⁵⁵ associated with the two lowest dissociation limits of $\text{N}_2\text{O}^+ + \text{H}_2\text{O}$. This energy difference is less than our experimental resolution, and hence, only one threshold is reported.

VI. CONCLUSIONS

The information obtained using the GIB technique includes reaction cross sections, complex lifetimes, isotopic scrambling, distinct reaction pathways, reaction barriers, photodissociation cross sections, and reaction mechanisms. The present work adds photofragment recoil analysis to the extensive list of GIB capabilities, further improving the versatility of this technique. The present recoil velocity measurements of Ar_2^+ and $(\text{N}_2\text{O} \cdot \text{H}_2\text{O})^+$ photolysis demonstrate that octopole ion guides are readily amenable to photodissociation dynamics studies. Two techniques have been proposed to characterize the photofragment ion recoil velocity distribution in this experimental setup that benefits from cylindrical symmetry: the GIB-TOF technique to determine $P(\nu_{2p})$ and the GIB-VAR technique to measure $P(\nu_{2t})$.

In the present GIB-TOF measurements, the laser is propagated transverse to the ion-beam axis, and conse-

quently the observed $P(\nu_{2p})$ depends on the laser polarization angle. High resolution kinetic energy release distributions are obtained from magic angle measurements. The laser polarization angle dependence allows the average asymmetry parameter, $\langle \beta \rangle$, describing the angular distribution to be obtained. The axial velocity component and the laser polarization angle are not independent variables and hence cannot be used to determine $\beta(E_T)$. However, general trends in $\beta(E_T)$ can be obtained as shown in Fig. 10. A truly doubly differential measurement providing the kinetic energy release dependence of the asymmetry parameter, $\beta(E_T)$, requires the additional determination of $P(\nu_{2t})$. In principle, $P(\nu_{2t})$ can be provided by the GIB-VAR technique. The GIB-VAR technique is subject to high degrees of kinematic averaging in the present study and is very sensitive to discrimination with respect to high ν_{2t} components. Therefore, GIB-VAR is used here to determine the transverse velocity discrimination function for each photofragment ion at the conditions of a GIB-TOF experiment.

The results for the $(\text{N}_2\text{O} \cdot \text{H}_2\text{O})^+$ photofragment analysis obtained using this new methodology compare favorably to measurements conducted in a reverse-geometry sector mass spectrometer,³¹ and additional, previously undetected features could be discerned in the $\text{H}_2\text{O}^+ + \text{N}_2\text{O}$ product channel. Specifically, the translational energy distributions of the $\text{H}_2\text{O}^+ + \text{N}_2\text{O}$ photoproducts are bimodal at all wavelengths studied, contrary to previous observations. From the observed photofragment ion translational energy and angular distributions, we deduce a minimum of three separate mechanisms for the formation H_2O^+ fragments. First, rapid dissociation on a repulsive surface correlating to $\text{H}_2\text{O}^+(\tilde{X}^2B_1) + \text{N}_2\text{O}$. Second, predissociation of a long lived intermediate resulting in the formation of $\text{H}_2\text{O}^+(\tilde{X}^2B_1) + \text{N}_2\text{O}$ products. Third, rapid dissociation leading to the production of electronically excited $\text{H}_2\text{O}^+(\tilde{A}^2A_1)$ and N_2O .

ACKNOWLEDGMENTS

We are grateful to Jon Stevens and Keiji Morokuma for communicating their theoretical results prior to publication and for helpful comments. This work was supported by AFOSR under Task 2303EP2. Y.-H. Chiu is an NRC postdoctoral fellow.

APPENDIX

Equations enabling the direct transformation of LAB frame GIB-TOF and GIB-VAR experimental data to parameters that describe the photodissociation event in the CM frame are derived. The equations apply to experiments where the primary ion-beam axial and transverse velocity widths are negligible, the primary ions are photolyzed near the octopole axis so the corrections expressed by Eqs. (5) and (6) are small, and no dc potential difference is applied to the rods (rf-only) so that \mathbf{v}_{1t} is equal to zero in the absence of

potential distortions. The derivation is simplified by translating the LAB frame origin along the Z axis and setting \mathbf{v}_{1p} equal to zero. In this case, $v_2 = v'_2$.

Referring to Fig. 3, the following transformations are obtained:

$$v_{2Z} = v'_2 \cos \theta, \quad v_{2XY} = v'_2 \sin \theta, \quad (\text{A1})$$

and

$$\cos \theta' = \cos \theta \cos \chi - \sin \theta \cos \phi \sin \chi. \quad (\text{A2})$$

Substituting Eq. (A2) into Eq. (7), and integrating the resulting expression over ϕ yields the familiar expression^{43,56-58}

$$P(\theta) \sin \theta d\theta = (1/2) [1 + \beta P_2(\cos \theta) P_2(\cos \chi)] \times \sin \theta d\theta. \quad (\text{A3})$$

Note that for $\chi=0$, the LAB and CM frames are identical, and Eq. (A3) reduces to the expression of Eq. (7) integrated over ϕ' as expected.

Equation (A1) is used to relate Eq. (A3) to the LAB frame TOF observable, and the resulting expression describing differential TOF measurements is

$$P(v_{2Z}) dv_{2Z} = \frac{dv_{2Z}}{2v'_2} \left[1 + \frac{\beta}{2} \left(3 \frac{v_{2Z}^2}{v'^2_2} - 1 \right) P_2(\cos \chi) \right], \quad (\text{A4})$$

which expresses the probability that the products have a resultant velocity along the ion-beam axis with a magnitude between v_{2Z} and $v_{2Z} + dv_{2Z}$ over the axial range $-v'_2 \leq v_{2Z} \leq v'_2$ for a single kinetic energy release, E_T . For a distribution of kinetic energy releases, the probability expression of Eq. (A4) becomes Eq. (8)

$$I(v'_{2t}) = \begin{cases} \left[1 - \frac{\sqrt{v'^2_2 - v'^2_{2t}}}{v'_2} \right] + \frac{\beta}{2} P_2(\cos \chi) \frac{\sqrt{v'^2_2 - v'^2_{2t}}}{v'_2} \left[1 - \frac{(v'^2_2 - v'^2_{2t})}{v'^2_2} \right], & v'_{2t} \leq v'_2 \\ 1, & v'_{2t} > v'_2 \end{cases} \quad (\text{A6})$$

For a distribution of discrete kinetic energy releases, the expression of Eq. (A6) becomes

$$I(v_{2t}) = \int_0^{v'_{2t}} P(v'_2) dv'_2 + \int_{v'_{2t}}^{v'_2} \left[1 - \frac{\sqrt{v'^2_2 - v'^2_{2t}}}{v'_2} \right] P(v'_2) dv'_2 + \int_{v'_{2t}}^{v'_2} \frac{\beta(v'_2)}{2} P_2(\cos \chi) \frac{\sqrt{v'^2_2 - v'^2_{2t}}}{v'_2} \times \left[1 - \frac{(v'^2_2 - v'^2_{2t})}{v'^2_2} \right] P(v'_2) dv'_2. \quad (\text{A7})$$

Doubly differential measurements are obtained by taking a VAR spectrum at each TOF interval corresponding to a parallel velocity component, v'_{2p} . The derivative of Eq. (A7) evaluated at a constant value of v'_{2p} is

$$I(v'_{2p}) = \int_{v'_{2p}}^{\infty} \frac{P(v'_2)}{v'_2} \left[1 + \frac{\beta(v'_2)}{2} \times \left(3 \frac{v'^2_{2p}}{v'^2_2} - 1 \right) P_2(\cos \chi) \right] dv'_2, \quad (\text{8})$$

where the substitution $v'_{2p} = |v_{2Z}|$ has been made based on symmetry arguments.

Similarly, Eq. (A1) is used to relate Eq. (A3) to the LAB frame VAR observable yielding the following expression for differential VAR measurements

$$P(v'_{2t}) dv'_{2t} = \frac{dv'_{2t}}{v'_2} \frac{v'_{2t}}{\sqrt{v'^2_2 - v'^2_{2t}}} \times \left\{ 1 + \frac{\beta}{2} \left[3 \frac{(v'^2_2 - v'^2_{2t})}{v'^2_2} - 1 \right] P_2(\cos \chi) \right\}, \quad (\text{A5})$$

where the substitutions $v'_{2t} = |v_{2XY}|$ and $v'_{2p} = \sqrt{v'^2_2 - v'^2_{2t}}$ have been made. In Eq. (A5), $P(v'_{2t}) dv'_{2t}$ is the probability that the products have a resultant velocity perpendicular to the ion-beam axis with a magnitude between v'_{2t} and $v'_{2t} + dv'_{2t}$ over the transverse velocity range $v'_{2t} \leq v'_2$. As discussed in Sec. II B of the text, VAR experiments measure the integral of the probability distribution function defined in Eq. (A5) over v'_{2t} . Performing the integration yields the following expression for the VAR signal intensity for a single kinetic energy release

$$\frac{dI(v'_{2t})}{dv'_{2t}} \bigg|_{v'_{2p}} = P(v'_2) \frac{v'_{2t}}{v'_2} \left\{ \left[1 - \frac{v'_{2p}}{v'_2} \right] + \frac{\beta(v'_2)}{2} P_2(\cos \chi) \frac{v'_{2p}}{v'_2} \left[1 - \frac{v'^2_{2p}}{v'^2_2} \right] \right\}, \quad (\text{A8})$$

where $v'_2 = \sqrt{v'^2_{2t} + v'^2_{2p}}$. Note the limits of integration in deriving Eq. (A8) from Eq. (A7) are from ∞ to $\sqrt{v'^2_{2t} + v'^2_{2p}}$ since v'_{2p} is constant. Equation (A8) shows that a doubly differential VAR measurement contains information regarding the CM kinetic energy release distribution (both terms) and the angular distribution as a function of E_T (second term). Several doubly differential VAR measurements taken over the desired range of v'_{2p} are necessary to fully characterize the angular anisotropy of the photolysis event as a function of E_T .

The expressions presented above are used to validate the Monte Carlo forward convolution programs discussed in the text.

- ¹M. N. R. Ashfold, I. R. Lambert, D. H. Mordaunt, G. P. Morley, and C. M. Western, *J. Phys. Chem.* **96**, 2938 (1992).
- ²G. E. Busch, J. F. Cornelius, R. T. Mahoney, R. I. Morse, D. W. Schlosser, and K. R. Wilson, *Rev. Sci. Instrum.* **41**, 1066 (1970).
- ³G. E. Busch and K. R. Wilson, *J. Chem. Phys.* **56**, 3626 (1972).
- ⁴A. M. Wodtke and Y. T. Lee, in *Molecular Photodissociation Dynamics*, edited by M. N. R. Ashfold and J. E. Baggot (Royal Society of Chemistry, London, 1987), p. 31.
- ⁵H. J. Krautwald, L. Schneider, K. H. Welge, and M. N. R. Ashfold, *Faraday Discuss. Chem. Soc.* **82**, 99 (1986).
- ⁶L. Schneider, W. Meir, K. H. Welge, M. N. R. Ashfold, and C. M. Western, *J. Chem. Phys.* **92**, 7027 (1990).
- ⁷J. Segall, Y. Wen, R. Lavi, R. Singer, and C. Wittig, *J. Phys. Chem.* **95**, 8078 (1991).
- ⁸M. T. Bowers, in *Ion and Cluster Ion Spectroscopy and Structure*, edited by J. P. Maier (Elsevier, Amsterdam, 1989), p. 241.
- ⁹P. Andresen and R. Schinke, in *Molecular Photodissociation Dynamics*, edited by M. N. R. Ashfold and J. E. Baggot (Royal Society of Chemistry, London, 1987), p. 61.
- ¹⁰H. Reisler, M. Noble, and C. Wittig, in *Molecular Photodissociation Dynamics*, edited by M. N. R. Ashfold and J. E. Baggot (Royal Society of Chemistry, London, 1987), p. 139.
- ¹¹J. P. Simons, *J. Phys. Chem.* **91**, 5378 (1987).
- ¹²G. E. Hall and P. L. Houston, *Annu. Rev. Phys. Chem.* **40**, 375 (1989).
- ¹³D. W. Chandler and P. L. Houston, *J. Chem. Phys.* **87**, 1445 (1987).
- ¹⁴M. H. M. Janssen, D. H. Parker, G. O. Sitz, S. Stolte, and D. W. Chandler, *J. Phys. Chem.* **95**, 8007 (1991).
- ¹⁵T. Suzuki, V. P. Hradil, S. A. Hewitt, P. L. Houston, and B. J. Whitaker, *Chem. Phys. Lett.* **187**, 257 (1991).
- ¹⁶A. J. R. Heck and D. W. Chandler, *Annu. Rev. Phys. Chem.* **46**, (1995).
- ¹⁷R. E. Continetti, D. R. Cyr, D. L. Osborn, D. J. Leahy, and D. M. Neumark, *J. Chem. Phys.* **99**, 2616 (1993).
- ¹⁸D. P. de Bruijn and J. Los, *Rev. Sci. Instrum.* **53**, 1020 (1982).
- ¹⁹J. C. Brenot and M. Durup-Ferguson, in *State-Selected and State-to-State Ion-Molecule Reaction Dynamics, Part I: Experiment*, edited by C. Y. Ng and M. Baer (Wiley, New York, 1992), p. 309.
- ²⁰J. C. Brenot and M. D. Ferguson, *Adv. Chem. Phys.* **82**, 309 (1992).
- ²¹E. Teloy and D. Gerlich, *Chem. Phys.* **4**, 417 (1974).
- ²²D. Gerlich, in *State-Selected and State-to-State Ion-Molecule Reaction Dynamics*, edited by C.-Y. Ng and M. Baer (Wiley, New York, 1992), Vol. LXXXII, p. 1.
- ²³S. Mark and D. Gerlich, *Chem. Phys.* **209**, 235 (1996).
- ²⁴L. I. Yeh, M. Okumura, J. D. Myers, J. M. Price, and Y. T. Lee, *J. Chem. Phys.* **91**, 7319 (1989).
- ²⁵E. J. Bieske, A. M. Soliva, A. Friedmann, and J. P. Maier, *J. Chem. Phys.* **96**, 28 (1991).
- ²⁶E. J. Bieske, *J. Chem. Phys.* **99**, 8672 (1993).
- ²⁷T. G. Spence, T. D. Burns, G. B. Guckenberger, V., and L. A. Posey, *J. Phys. Chem. A* **101**, 1081 (1997).
- ²⁸R. A. Dressler, R. H. Salter, and E. Murad, *J. Chem. Phys.* **99**, 1159 (1993).
- ²⁹M. J. Bastian, R. A. Dressler, D. J. Levandier, E. Murad, F. Muntean, and P. B. Armentrout, *J. Chem. Phys.* **106**, 9570 (1997).
- ³⁰S. Williams, Y.-H. Chiu, D. J. Levandier, and R. A. Dressler, *J. Chem. Phys.* **108**, 9383 (1998).
- ³¹S. T. Graul, H.-S. Kim, and M. T. Bowers, *Int. J. Mass Spectrom. Ion Processes* **117**, 507 (1992).
- ³²R. A. Dressler, R. H. Salter, and E. Murad, *J. Chem. Phys.* **99**, 1159 (1993).
- ³³R. A. Dressler, R. H. Salter, and E. Murad, *Chem. Phys. Lett.* **204**, 111 (1993).
- ³⁴R. A. Dressler and E. Murad, *J. Chem. Phys.* **100**, 5656 (1994).
- ³⁵S. T. Graul, S. Williams, R. A. Dressler, R. H. Salter, and E. Murad, *J. Chem. Phys.* **100**, 7348 (1994).
- ³⁶S. T. Arnold, R. A. Dressler, M. J. Bastian, J. A. Gardner, and E. Murad, *J. Chem. Phys.* **102**, 6110 (1995).
- ³⁷M. J. Bastian, R. A. Dressler, E. Murad, S. T. Arnold, and A. A. Viggiano, *J. Chem. Soc., Faraday Trans.* **92**, 2659 (1996).
- ³⁸R. N. Zare, *Mol. Photochem.* **4**, 1 (1972).
- ³⁹S.-c. Yang and R. Bersohn, *J. Chem. Phys.* **61**, 4400 (1974).
- ⁴⁰M. Dzvonik, S.-c. Yang, and R. Bersohn, *J. Chem. Phys.* **61**, 4408 (1974).
- ⁴¹K. A. Trentelman, S. H. Kable, D. B. Moss, and P. L. Houston, *J. Chem. Phys.* **91**, 7498 (1989).
- ⁴²M. F. Jarrold, A. J. Illies, N. J. Kirchner, W. Wagner-Redaker, M. T. Bowers, M. L. Mandich, and J. L. Beauchamp, *J. Phys. Chem.* **87**, 2213 (1983).
- ⁴³M. F. Jarrold, A. J. Illies, and M. T. Bowers, *J. Chem. Phys.* **81**, 214 (1984).
- ⁴⁴M. F. Jarrold, A. J. Illies, and M. T. Bowers, *J. Chem. Phys.* **82**, 1832 (1985).
- ⁴⁵W. J. Stevens, M. Gardner, A. Karo, and P. Julienne, *J. Chem. Phys.* **67**, 2860 (1977).
- ⁴⁶J. T. Moseley, R. P. Saxon, B. A. Huber, P. C. Cosby, R. Abouaf, and M. Tadjeddine, *J. Chem. Phys.* **67**, 1659 (1977).
- ⁴⁷L. C. Lee, G. P. Smith, T. M. Miller, and P. C. Cosby, *Phys. Rev. A* **17**, 2005 (1978).
- ⁴⁸L. C. Lee and G. P. Smith, *Phys. Rev. A* **19**, 2329 (1979).
- ⁴⁹W. R. Wadt, *J. Chem. Phys.* **73**, 3915 (1980).
- ⁵⁰C. A. Woodward, B. J. Whitaker, and A. J. Stace, *J. Chem. Soc., Faraday Trans.* **86**, 2069 (1990).
- ⁵¹B. J. Whitaker, C. A. Woodward, P. J. Knowles, and A. J. Stace, *J. Chem. Phys.* **93**, 376 (1990).
- ⁵²T. F. Magnera, *Chem. Phys. Lett.* **192**, 99 (1992).
- ⁵³E. C. M. Chen, J. G. Dojahn, and W. E. Wentworth, *J. Phys. Chem. A* **101**, 3088 (1997).
- ⁵⁴J. Stevens and K. J. Morokuma (personal communication).
- ⁵⁵E. J. Bieske, A. M. Soliva, A. Friedmann, and J. P. Maier, *J. Chem. Phys.* **96**, 7535 (1992).
- ⁵⁶R. N. Zare and D. R. Herschbach, *Proc. IEEE* **51**, 173 (1963).
- ⁵⁷R. Schmiedl, H. Dugan, W. Meier, and K. H. Welge, *Z. Phys. A* **304**, 137 (1982).
- ⁵⁸P. L. Houston, *J. Phys. Chem.* **91**, 5388 (1987).

Guided-ion beam study of the $O_2^+ + C_2H_2$ charge-transfer and chemical reaction channels

Yu-hui Chiu,^{a)} Rainer A. Dressler, Dale J. Levandier,^{b)} Skip Williams,^{b)}
and Edmond Murad

Air Force Research Laboratory, Space Vehicles Directorate, 29 Randolph Road, Hanscom Air Force Base,
Massachusetts 01731-3010

(Received 13 October 1998; accepted 23 November 1998)

Guided-ion beam cross section and product ion time-of-flight (TOF) measurements are presented for the $O_2^+(^2\Pi_g) + C_2H_2$ reaction over the center-of-mass collision energy range of 0.05–12 eV. The reaction exhibits a strong charge-transfer (CT) channel and several weak chemical reaction channels leading to the following product ions: $C_2H_2O^+$, CH_2^+ , COH^+/HCO^+ , CO^+ , CH^+ , and C^+ . The magnitude of the charge-transfer cross section is comparable to the capture cross section at low collision energies. The charge-transfer products are characterized predominantly by a direct, long-range mechanism that is accompanied by smaller impact parameter collisions involving longer-lived complexes, whose lifetimes are several times shorter than the complex rotational period. The TOF analysis indicates that the complexes also decay to chemical reaction products at higher energies. A density functional survey of intermediates is conducted. The chemical reaction products are postulated to be formed via an endothermic transition state associated with a $H_2CCO_2^+$ intermediate. © 1999 American Institute of Physics. [S0021-9606(99)00309-8]

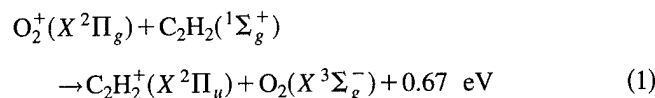
I. INTRODUCTION

There has been a renewed interest in elucidating the detailed dynamics of ion collisions with small organic molecules. This has been partly fueled by new insights obtained in recent studies^{1–8} using the guided-ion beam (GIB) technique.⁹ The number of organic ion-molecule reaction studies has been limited because of the large number of open reaction channels, the ionic products of which frequently undergo rapid secondary reactions with the neutral reactant. Secondary reactions can be problematic in conventional flowing afterglow¹⁰ or single octopole GIB experiments if product branching ratios are of interest. In a GIB experiment this problem is overcome through the use of a second octopole that is situated immediately after the collision cell and that is floated at a dc bias potential different from that of the first octopole. Consequently, slow product ions [e.g., charge-transfer (CT) product ions] can be accelerated to higher kinetic energies as they exit the collision cell and enter the second octopole, thereby substantially reducing the secondary ion residence times and reaction rates. Furthermore, the addition of a second octopole allows the measurement of product ion time-of-flight spectra, thus providing a means for investigating the energy transfer in the respective channels. Such a versatile guided-ion beam experiment is, therefore, an ideal technique for studying the dynamics of individual and competing reaction channels of organic ion-molecule systems at near-thermal to hyperthermal collision energies.

In this work, we present GIB cross section and TOF measurements for the $O_2^+(X^2\Pi_g) + C_2H_2$ reaction over the

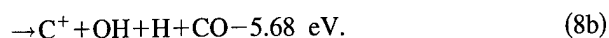
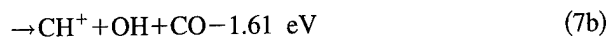
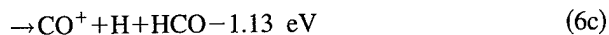
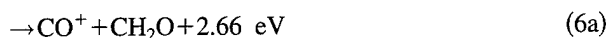
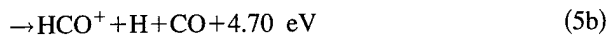
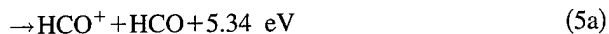
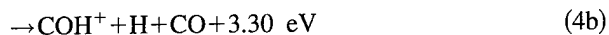
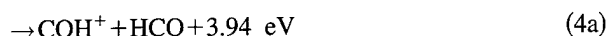
collision energy range of 0.05–12 eV. This work is a continuation of a series of studies on reactions between atmospheric ions and spacecraft engine exhaust molecules, such as HCN and C_2H_2 .^{6,11} The induction of polyatomic species in space can have profound consequences on the spacecraft environment.¹² In a recent study of the $O^+(^4S) + C_2H_2$ collision system,⁶ we found that even though nine product ion mass channels are open at thermal collision energies, the total near-thermal reactivity is more than two orders of magnitude lower than the collisional rate, and that both charge transfer and the observed chemical reactions proceeded preferentially via an excited quartet surface, despite numerous stable intermediates. It is, therefore, interesting to investigate whether other ion-acetylene reactions also exhibit such highly nonstatistical behavior.

Contrary to the $O^+(^4S) + C_2H_2$ reaction, the $O_2^+ + C_2H_2$ reaction system includes a charge-transfer channel with favorable Franck-Condon factors. This usually leads to an efficient long-range charge-transfer mechanism producing slow product ions that are subject to secondary reactions. Meanwhile, as in the $O^+(^4S) + C_2H_2$ collision system, a number of chemical reaction channels are accessible at low collision energies with the following energetics (298 K):^{13–16}



^{a)}Electronic mail: YH_CHIU@hotmail.com

^{b)}Orion International Technologies, Inc., 2201 Buena Vista Dr. SE, Suite 211, Albuquerque, NM 87106.



Given the substantially higher exothermicities of channels (2) through (6) compared with the CT channel [reaction (1)], competition may be expected between charge transfer and chemical reaction at low collision energies. Except for an early study of the endothermic $\text{O}_2^+ + \text{C}_2\text{D}_2$ deuterium atom transfer reaction by Chiang *et al.*,¹⁷ no hyperthermal studies are known to us on the $\text{O}_2^+ + \text{C}_2\text{H}_2$ reaction. While the $\text{O}^+({}^4\text{S}) + \text{C}_2\text{H}_2$ collision system is dominated by short-range dynamics, the present study involves a reaction where both long- and short-range interactions play an important role.

II. EXPERIMENT

The guided-ion beam apparatus and data analysis methods used in this study have been described elsewhere.⁷ Only a brief description will be given here. The primary O_2^+ beam is produced in the ground state by electron impact ionization of O_2 with an electron energy < 15 eV. The O_2^+ beam thereby produced is vibrationally excited with relative populations for $v = 0-4$ of approximately 0.16:0.32:0.33:0.16:0.03, derived from the ionization Franck-Condon factors taken from the O_2 photoelectron spectrum.¹⁸ The kinetic energy spread of the primary beam is ~ 0.2 eV full width at half maximum (FWHM). After mass selection in a Wien velocity filter, the ion beam is injected into a two-segment radio frequency (rf) octopole ion guide. The first octopole passes through a 3.5 cm long collision cell, in which the C_2H_2 target gas is maintained at a pressure of ~ 0.2 mTorr to ensure single collision conditions. Prior to entering the cell, the C_2H_2 (Matheson, 99.6%) is passed through a cold trap to remove an acetone impurity. The unreacted primary and product ions are guided into the second 16.7 cm long octopole, which is biased $\sim 0.3-0.4$ eV lower than the first octopole. This bias accelerates slow product ions to kinetic energies sufficient to overcome local barriers resulting from inhomogeneities of octopole rod surface potentials. When necessary, a positive potential of $\sim 30-50$ V is applied to a cylindrical ring electrode surrounding the octopole at the entrance of the collision cell, producing a small potential barrier of $\sim 60-100$ mV along the axis of the octopole that reflects laboratory

backscattered ions into the forward direction. At the exit of the second octopole, all ions are extracted and focused into a quadrupole mass analyzer and then detected by a channel electron multiplier.

The collision energy is varied by changing the dc bias of the collision cell and first octopole with respect to the ion source. The absolute integral cross section for product i , σ_i , is determined from the following equation:

$$\sigma_i = \frac{I_{\text{prod},i}}{\left(I_{\text{prim}} + \sum_i I_{\text{prod},i} \right) nl} \quad (9)$$

where I_{prim} is the primary ion O_2^+ intensity, n is the number density of the neutral C_2H_2 target, $I_{\text{prod},i}$ is the intensity of product ion i , and l is the effective length of the primary ion-neutral interaction region. The effective length is determined as described elsewhere.^{7,19} The uncertainty of the absolute cross section is estimated to be $\pm 30\%$.

To measure product ion TOF spectra, $\sim 3-4$ μs wide primary ion pulses are generated by pulsing a split pair deflector electrode in front of the octopole injection lens, and the ion flight times are recorded using a time-to-digital converter. To avoid background signals, the rf voltage on the octopole is briefly switched off prior to each cycle to purge slow ions formed by previous primary ion pulses. The fraction of those slow ions that have not been recorded is obtained by determining the difference between the cross section measured in the continuous wave (CW) mode and that measured in the pulsed TOF mode. The accumulated product TOF spectra are transformed into laboratory axial velocity distributions, $f(\nu'_{1p})$, where ν'_{1p} is the product ion laboratory velocity component parallel to the octopole ion-guide axis.⁷

Despite the double octopole arrangement in the present study, products attributable to secondary reactions are observed. They are confirmed by comparing the cross sections measured under CW and pulsed TOF conditions, and by examining the target pressure dependence. We find that essentially all the observed secondary products are attributable to slow charge transfer product ions, C_2H_2^+ , that react with the target gas



The rate constants for reactions (10a)–(11b) are on the order of 10^{-9} , 10^{-9} , 10^{-11} , 10^{-11} , 10^{-10} molecule $^{-1}$ cm 3 s $^{-1}$, respectively.²⁰ Since the secondary reaction products cannot be eliminated at practical C_2H_2 gas pressures, we measure the cross sections of each secondary product and present the total charge-transfer cross section as the sum of cross sections of the above secondary reaction products [i.e., reactions (10a)–(11b)].

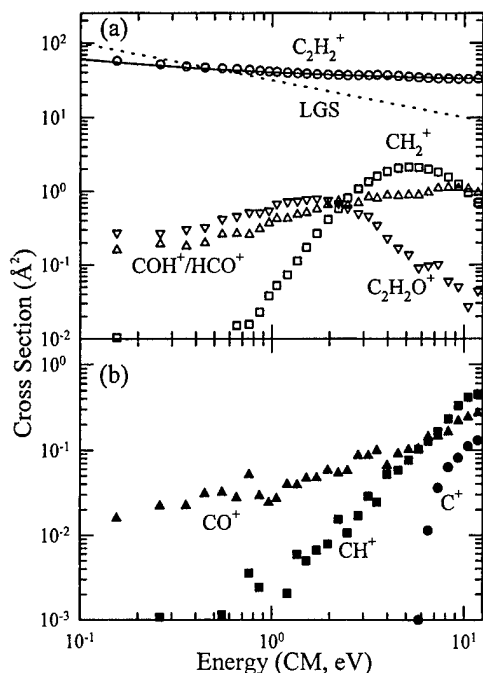


FIG. 1. (a) Energy dependence of integral cross sections for the main product ions of the $\text{O}_2^+ + \text{C}_2\text{H}_2$ collisions, $\text{C}_2\text{H}_2^+(\text{O})$, $\text{C}_2\text{H}_2\text{O}^+(\nabla)$, $\text{CH}_2^+(\square)$, and $\text{COH}^+/\text{HCO}^+(\triangle)$. The solid line is a fit of Eq. (12) to the CT cross section. The capture cross section (LGS) is also indicated by a dotted line. (b) Energy dependence of integral cross sections for minor products, $\text{CO}^+(\blacktriangle)$, $\text{CH}^+(\blacksquare)$, and $\text{C}^+(\bullet)$.

III. RESULTS

A. Cross section measurements

The collision energy dependence of the integral cross sections for the products formed in the reaction of $\text{O}_2^+ + \text{C}_2\text{H}_2$ are shown in Figs. 1(a) and 1(b). Note that the C_2H_2^+ cross section shown in the figure includes the contributions of secondary products mentioned above. This is justified by the fact that the cross section of C_2H_2^+ and secondary products exhibit near-identical energy dependences. The secondary products C_4H_2^+ and C_4H_3^+ comprise $\sim 25\%$, and C_6H_3^+ and $\text{C}_6\text{H}_4^+ \sim 3\%$ of the C_2H_2^+ cross section. The cross section of $m/z=27$ products, C_2H_3^+ and $^{13}\text{CCH}_2^+$, is $\sim 2\%$ of the C_2H_2^+ cross section. This is close to the $m/z=27$ natural isotopic abundance of acetylene. Therefore the contribution from reaction (10c) is negligible as expected from the small rate coefficient.

Also indicated in Fig. 1(a) is the Langevin-Gioumousis-Stevens (LGS) capture cross section (dotted line) for an ion-induced dipole interaction,²¹ which is comparable to the total cross section at low collision energies. The CT cross section can be modeled by a combination of a constant cross section and an $E_T^{-0.5}$ energy dependence (energy in eV)

$$\sigma_{\text{CT}} = a + bE_T^{-0.5}. \quad (12)$$

The solid line represents a fit to the experimental cross sections, where $a = 30.3 \text{ Å}^2$ and $b = 10 \text{ Å}^2 \text{ eV}^{0.5}$. In the LGS model ($a=0$), b is $31.5 \text{ Å}^2 \text{ eV}^{0.5}$ for ion + C_2H_2 capture collisions.

All reaction product channels are observed to have cross sections less or equal to 2 Å^2 in the collision energy

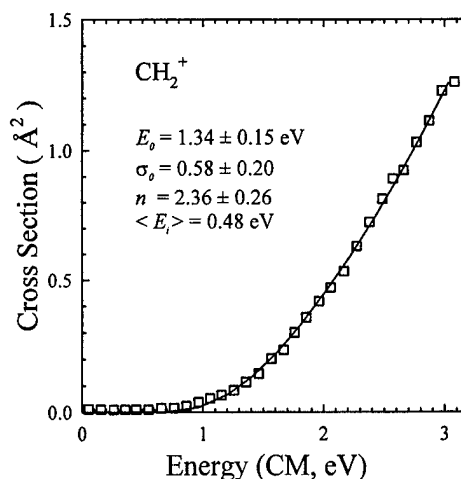


FIG. 2. Expanded view of low-energy CH_2^+ cross section. The solid line is a modified line-of-centers threshold function corresponding to the listed fit parameters. The average internal energy of O_2^+ is $\sim 0.48 \text{ eV}$ and has been taken into account in the indicated threshold.

range investigated. Although exothermic, CH_2^+ , $\text{C}_2\text{H}_2\text{O}^+$ and $\text{COH}^+/\text{HCO}^+$ channels exhibit increases in cross section with collision energy at low energies. The CH_2^+ cross section appears to have a threshold near $\sim 1 \text{ eV}$, then peaks at $\sim 5 \text{ eV}$, before declining with collision energy. The $\text{C}_2\text{H}_2\text{O}^+$ cross section is approximately 0.3 Å^2 below 0.5 eV , above which it increases to 0.8 Å^2 at $\sim 1.8 \text{ eV}$ before rapidly decreasing with energy. The $\text{COH}^+/\text{HCO}^+$ cross section is also small at low energies, and increases gradually to a near constant value of $\sim 1 \text{ Å}^2$ at higher energies. The cross sections of minor products CO^+ , C^+ , and CH^+ shown in Fig. 1(b) are considerably smaller at low energies. Unlike C^+ and CH^+ , which have onsets of ~ 6 and $\sim 0.9 \text{ eV}$, respectively, CO^+ is produced at near-thermal energies and increases gradually with collision energy, reaching $\sim 0.25 \text{ Å}^2$ at $\sim 12 \text{ eV}$.

The modified line-of-centers model is employed to determine the energy onsets of reaction products. The data are fitted by the model threshold function

$$\sigma(E_T) = \sigma_0 \sum_i g_i \frac{(E_T + E_i - E_0)^n}{E_T}, \quad (13)$$

where E_0 is the threshold energy, σ_0 is a scaling parameter, and n is a curvature parameter. The sum is over reactant internal states with energies E_i and populations g_i . The fitting routine includes convoluting the experimental collision energy distribution with Eq. (13).²² An expanded view of the modeled CH_2^+ cross section is shown in Fig. 2. Threshold energies (0 K) of 1.34 ± 0.15 , 1.5 ± 0.9 , and $6.4 \pm 0.7 \text{ eV}$ are determined for the CH_2^+ , CH^+ and C^+ products, respectively. The energy threshold of CH_2^+ is close to that of reaction (3b), while that of CH^+ is consistent with reaction (7b). The derived C^+ threshold is slightly above that of reactions (8a) and (8b). Note that the average internal energy of O_2^+ is $\sim 0.48 \text{ eV}$ and has been taken into account in the present thresholds.

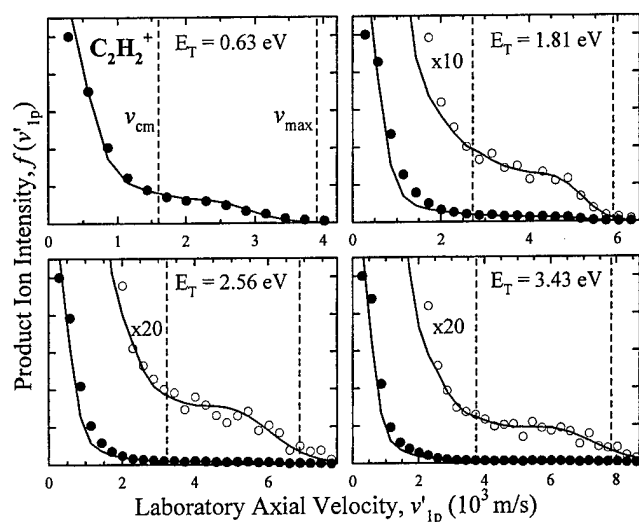


FIG. 3. Axial velocity distributions of the $C_2H_2^+$ product ions as a function of collision energy. The vertical dashed lines in each collision energy frame indicate v_{cm} and v_{max} , the center-of-mass and maximum energetically allowed velocities. The solid lines are linear least square fits of basis functions calculated using the osculating complex model.

B. TOF measurements and analysis

Product ion velocity-transformed TOF distributions, $f(v'_p)$, are shown for different collision energies in Figs. 3, 5 and 6. In each frame, the vertical dashed lines indicate the center-of-mass velocity, v_{cm} , and the maximum and minimum energetically allowed velocities, v_{max} and v_{min} . These velocities are calculated for a target gas at rest. Figure 3 shows the axial velocity distributions of the $C_2H_2^+$ CT products. At all collision energies, the velocity distribution exhibits an intense band at near zero laboratory (LAB) velocity. These ions are produced primarily in near resonant charge-transfer collisions involving little or no momentum transfer. A second broad band of forward scattered ions including velocities exceeding v_{cm} is also observed. The relative intensity of this band drops rapidly with increasing collision energy. This band is attributed to smaller-impact parameter collisions involving longer-lived intermediates.

In the past, we have demonstrated that TOF distributions, for which the scattering is primarily induced by an attractive interaction, can be modeled with the osculating complex model^{23–25} to infer product excitation.^{11,12,26} In the osculating complex model, every collision process is assumed to proceed via a rotating complex that decays with an exponential random-lifetime distribution. The solid lines in Fig. 3 are linear least square fits of basis functions calculated using the osculating complex model. Basis functions are calculated for discrete translational exoergicities, ΔE_T , and a specified complex rotational period to complex lifetime ratio, τ_r/τ_c , and intensity peaking angle, θ . The functions include all experimental broadening mechanisms.¹² The normalized fit coefficients, c_i , yield the translational energy transfer distribution for the products at collision energy, E_T . Note that $\Delta E_T > 0$ corresponds to internal-to-translational energy transfer and $\Delta E_T < 0$ corresponds to translational-to-internal energy transfer.

Figure 4 is the graphic representation of the translational

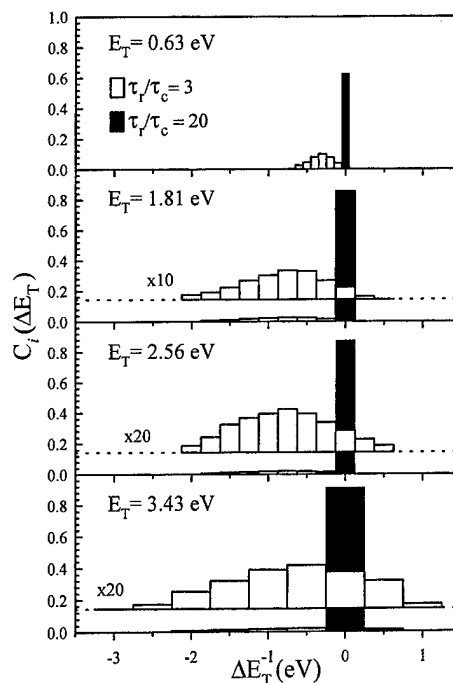


FIG. 4. Graphic representation of the translational energy transfer distributions of the CT products obtained from the normalized simulation coefficients yielding the best fits to TOF spectra shown in Fig. 3.

energy transfer distribution of the CT products deduced from the simulation. The widths of the bars reflect the resolution of the simulation. At all collision energies, two complex rotational period to lifetime ratios, $\tau_r/\tau_c = 3$ and $\tau_r/\tau_c = 20$, are needed to provide an adequate fit to the data. The short lifetime component with $\tau_r/\tau_c = 20$ (filled bars) represents the long-range direct process. At all energies, a single basis function calculated for $\Delta E_T = 0$ adequately reproduces the near-thermal energy band of the TOF distributions. The longer-lived complexes corresponding to $\tau_r/\tau_c = 3$ (open bars) account for those events producing forward-scattered ions and result in broad product internal energy distributions with an approximate 50% average translational energy conversion. The translational energy transfer distributions of the $\tau_r/\tau_c = 3$ component are peaked towards complete translational-to-internal energy transfer at 0.63 eV, signifying a near-statistical partitioning of complex energy. At higher collision energies, the peak of the distributions shifts towards a lower fraction of translational-to-internal energy transfer. The data in Fig. 3 do not include the time window of the experiment. These slow ions, the intensity of which is determined from the difference between pulsed TOF mode and CW cross sections, are assumed to be primarily produced in a long-range direct process. They are accounted for in the weight of the $\tau_r/\tau_c = 20$ component shown in Fig. 4. The osculating complex model results are validated by comparing the direct scattering fraction to those predicted by modeling the cross sections with Eq. (12). At 0.63 eV, for example, Eq. (12) indicates that 70% of the cross section is attributable to the constant, direct process. The TOF analysis in Fig. 4 attributes 64% to direct scattering. Meanwhile, at 1.81 eV, Eq. (12) predicts that 80% of the cross section is due to a

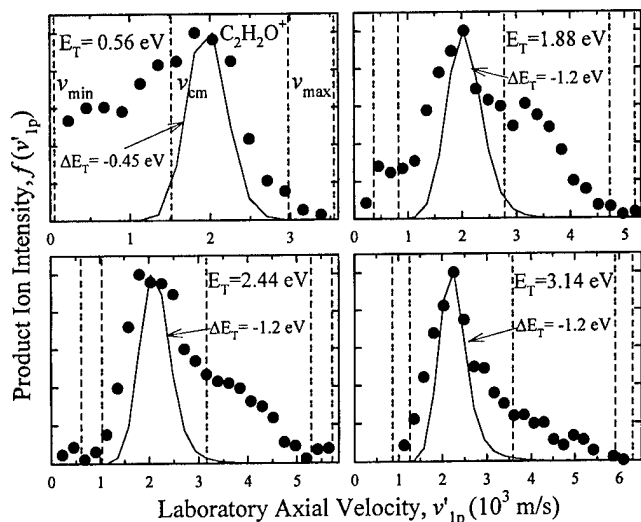


FIG. 5. Axial velocity distributions of the $C_2H_2O^+$ product ions as a function of collision energy. The solid lines are calculated osculating complex model distributions for representative discrete translational energy transfer values and direct scattering. The velocities v_{\max} and v_{\min} are indicated for both $HCCOH^+$ and CH_2CO^+ .

direct mechanism, while the TOF analysis produces 86%. The observed agreement is well within experimental and modeling uncertainties, the latter being primarily governed by the determination of the average complex lifetime of the longer-lived component.

The axial velocity distributions for production of $C_2H_2O^+$ at different collision energies are shown in Fig. 5, along with sample simulations (solid curves), for a discrete translational energy transfer and a short-lived intermediate. Note that for this product channel, two values of v_{\max} and v_{\min} are indicated for the two isomers, $HCCOH^+$ and CH_2CO^+ . The $C_2H_2O^+$ velocity distribution extends to v_{\max} and v_{\min} at all energies. At 0.56 eV, the distribution is slightly forward scattered with a large fraction of translational-to-internal energy transfer, as indicated by the comparison to a sample direct scattering simulation calculated for a discrete energy transfer of 0.45 eV. The primary beam defines the forward direction of the scattering. At energies at and above 1.88 eV, the velocity distribution is preferably backscattered with decreasing forward-scattered intensity. The distributions also exhibit a sharp drop in intensity as the velocity approaches v_{cm} . The simulations show that this drop corresponds to a loss in signal for collisions with a translational-to-internal energy transfer exceeding approximately 1.2 eV.

Figure 6 shows the CH_2^+ and the COH^+/HCO^+ axial velocity distributions at 1.88 and 3.14 eV. A narrow distribution symmetric with respect to v_{cm} is observed for CH_2^+ at both collision energies, signifying high product internal excitation. This is consistent with the interpretation that CH_2^+ can be associated with a $CH_2^+ + CO + O$ channel, as determined from the observed onset. Very similar velocity distributions shown in Fig. 6 are also observed for the COH^+/HCO^+ products. The signal centered at v_{cm} implies that the $m/z = 29$ products are either highly internally excited or two neutral products, $H + CO$, are formed, in which case

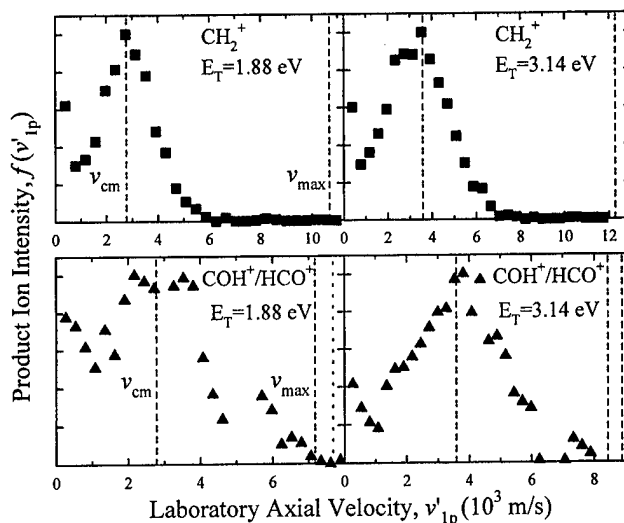


FIG. 6. Axial velocity distributions of the CH_2^+ and COH^+/HCO^+ product ions at $E_T = 1.88$ and 3.14 eV. The velocity v_{\max} is indicated for both COH^+ and HCO^+ .

the H atom would carry off most of the translational energy. The gaps in the velocity distributions in the 5000–6000 m/s region are artifacts resulting from imperfect subtraction of primary ion mass/contaminant signal.

Product velocity distributions centered near v_{cm} can have two possible origins: the formation of longer-lived intermediates or very-small impact parameter collisions involving high translational-to-internal energy transfer. In the past we have demonstrated that the energy dependence of the differential cross section for forming c.m. forward-scattered products in cases where a direct process is backscattered is well suited in identifying the source of the forward scattering.^{12,27} If longer-lived intermediates governed by the attractive interaction potential are responsible for the forward scattering, an $E_T^{-0.5}$ dependence is expected for an ion-induced dipole interaction, while an energy independent or increasing cross section with collision energy is expected in the case of hard-sphere-type scattering involving a repulsive potential. The fraction of product ion signal, $I(v'_{ip} > v_{\text{cm}})$, multiplied by the cross section obtained in the pulsed TOF mode yields the forward-scattered cross section $\sigma(v'_{ip} > v_{\text{cm}})$ shown in Fig. 7 as a function of collision energy for the charge-transfer channel. A power law fit to the charge-transfer cross sections yields an $E_T^{-1.1}$ dependence, implying that the forward-scattered signal is primarily attributable to long-range forces. The sharper drop off compared to induced-dipole predictions could possibly be attributed to competition with the chemical reaction channels. A plot including the sum of the forward-scattered cross sections of $C_2H_2^+$, CH_2^+ , COH^+/HCO^+ , and $C_2H_2O^+$ is also shown in Fig. 7. This plot yields a power law of $E_T^{-0.8}$, which is closer to our predictions. The sum of forward-scattered cross sections, however, exhibits a trend of leveling off above 2 eV. This is an indicator that the forward-scattered cross sections of CH_2^+ , COH^+/HCO^+ , and $C_2H_2O^+$ may have important small-impact parameter, hard-sphere scattering components. It is, therefore, concluded that the $\sim E_T^{-1.1}$ dependence cannot be interpreted as evidence for

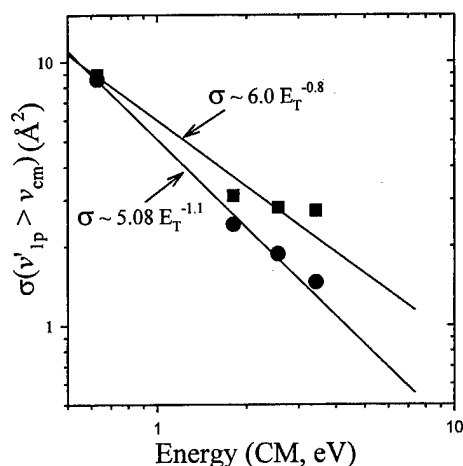


FIG. 7. Energy dependence of the forward-scattered cross section of charge-transfer product ions (●) as well as the sum of the forward-scattered cross sections of $C_2H_2^+$, CH_2^+ , COH^+/HCO^+ , and $C_2H_2O^+$ product channels (■). The solid lines are power law fits.

competition between charge-transfer and chemical reaction channels in the complex channel.

C. Density functional calculation of $(O_2-C_2H_2)^+$ intermediate ions

We have conducted a density functional survey of the $(C_2H_2O_2)^+$ doublet hypersurface to provide a qualitative picture of the relative energetics for relevant intermediate ion structures. Geometry optimizations are carried out at the B3LYP/6-31G(d), B3LYP/6-31G(d,p), and B3PW91/6-31G(d,p) levels (GAUSSIAN 94).²⁸ These methods were chosen since they were successfully applied in a previous study of the $CH_4+C_2H_2^+$ system. The methods provided different results for H-atom bridged structures, in which case the B3PW91 model was found to be more accurate.²⁹ Figure 8 displays the optimized structures for local minima (I)–(V) obtained at the B3LYP/6-31G(d) level. Only minor differences are found in optimized structures calculated at the B3LYP/6-31G(d,p) and B3PW91/6-31G(d,p) levels. The energetics of the determined local minima are listed in Table I,

TABLE I. Relative energies (eV) of local minima (I)–(V), in reference to the reactant energies calculated at the same level of theory.

Intermediate structure	B3LYP/6-31G(d)	B3LYP/6-31G(d,p)	B3PW91/6-31G(d,p)
I	−4.672	−4.659	−4.618
II	−1.684	−1.675	−1.741
III	−1.437	−1.418	−1.474
IV	−0.93	−0.935	−1.113
V	−0.751	−0.833	−0.781

in reference to the reactant energies that are calculated at the same level of theory. The B3LYP/6-31G(d) energetics are shown schematically in Fig. 9. The potential energy shown here includes the zero-point energy and thermal energy (300 K), determined from normal frequency calculations,²⁸ and is plotted with respect to the reactant energy, which is indicated by a horizontal dotted line. The most stable structures are the glyoxal ion conformations (I) and (II), while structure (IV) resembles most closely an association complex. In the case of adjacent oxygen atoms, the separation is indicated to allow comparison with O_2 and O_2^+ equilibrium bond distances of 1.2 and 1.1 Å, respectively. It is worth noting that glyoxal ions have been previously examined theoretically using restricted Hartree-Fock (RHF), complete active space self-consistent field (CASSCF), and valence bond self-consistent field (SCF) methods.^{30,31} The remaining structures involve a vinylidene association complex (III) and the CH-insertion structure (V). The relative energetics of these intermediate species calculated at the B3LYP/6-31G(d,p) and B3PW91/6-31G(d,p) levels are very similar to those calculated at the B3LYP/6-31G(d) level.

IV. DISCUSSION

The present measurements of cross sections and product recoil velocities for the $O_2^++C_2H_2$ collision system exhibit a number of collision mechanisms. Although a large number of exothermic channels exist, only charge transfer is important at near-thermal collision energies, implying that important constraints exist for the open chemical reaction chan-

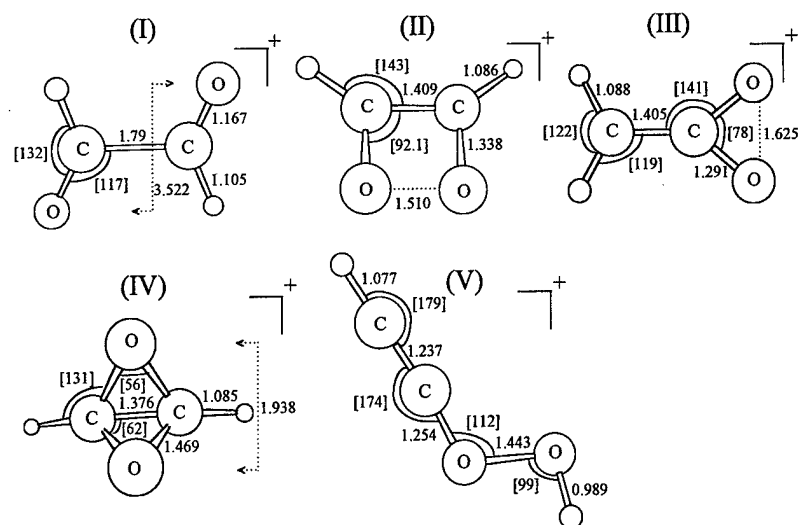


FIG. 8. The optimized structures of the determined local minima of the $C_2H_2O_2^+$ doublet hypersurface. Bond lengths are in Å and angles, denoted by brackets, are in degrees. Note that the hydrogen atom symbol is not shown.

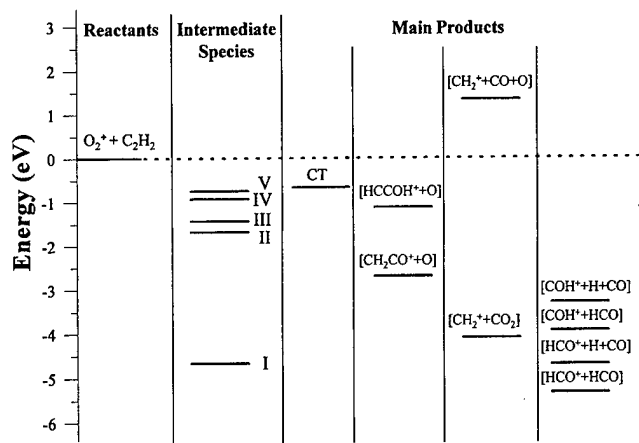


FIG. 9. Potential energy levels for the $O_2^+ + C_2H_2$ reaction system. The energies for intermediate structures are those calculated in the present work and listed in Table I.

nels. The near-collisional efficiency of charge transfer is not surprising when considering the favorable Franck-Condon factors at resonance between low vibrational levels of O_2 and C_2H_2 and their respective ions. Relevant asymptotic energy levels are shown in Fig. 10, where it is seen that due to the considerable O_2^+ vibrational populations up to $v=4$, excited charge-transfer surfaces associated with $O_2(a^1\Delta_g)$ and $O_2(b^1\Sigma_g)$ products may be accessed. It is consequently possible that the CT cross section exhibits a substantial O_2^+ vibrational energy dependence. The translational energy dependence of the charge-transfer cross section demonstrates two long-range mechanisms: one involving momentary capture, and the other a direct mechanism given by a constant charge-transfer radius and a probability that does not change significantly with collision energy. The $\sim 30 \text{ \AA}^2$ direct cross section signifies a charge-transfer radius exceeding 4.4 \AA , assuming a charge-transfer probability, $P \leq 0.5$.

These findings are fully consistent with the present TOF measurements. Contributions from direct and complex-mediated scattering can be clearly distinguished in the velocity-transformed spectra. The presently applied osculating complex model (Fig. 4) provides ratios between direct and complex scattering that agree well with those obtained

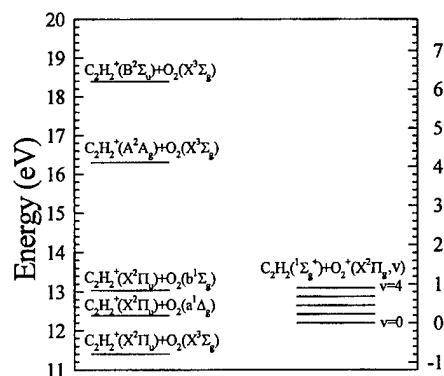


FIG. 10. Asymptotic energy levels of the $(O_2 + C_2H_2)^+$ charge-transfer system. The vertical scale at the left is referenced with respect to thermal reactant neutrals. The vertical scale at the right is the relative energy with respect to the thermal ion-molecule reactant pair.

when modeling the CT cross sections with Eq. (12). The long-range nature of the direct scattering is expressed in the negligible translational energy transfer, while broad energy transfer distributions are observed in collisions involving longer-lived intermediates.

The forward-scattered charge-transfer cross section associated with complex formation has a steeper decline than $E_T^{-0.5}$, the ion-induced dipole capture cross section dependence. This may be attributed to an increased competition with chemical reaction channels as the total energy of the collision complex increases. The main chemical reaction products at near-thermal collision energies are $C_2H_2O^+$ and COH^+/HCO^+ . These ion fragments may be associated with intermediates (III), and (I) or (II), respectively, of Fig. 9. The slowly increasing cross sections with energy at low energies point towards one or more endothermic transition states that connect to intermediates (III), and (I) or (II). A reaction proceeding via intermediate (III) would be consistent with a CH_2CO^+ isomeric product (reaction 2b) versus $HCCOH^+$ (reaction 2a). The decreasing $C_2H_2O^+$ cross section with energy above 1 eV, and the simultaneously increasing CH_2^+ cross section suggest that CH_2^+ is a dissociative decay product of CH_2CO^+ , further corroborating this isomeric form. This is also consistent with the determined CH_2^+ threshold, that is in good agreement with the $CH_2^+ + CO + O$ thermodynamic limit of 1.33 eV, and the substantial translational energy transfer observed in the TOF spectra (Fig. 6). Meanwhile, the $C_2H_2O^+$ recoil velocity distributions (Fig. 5) demonstrate a marked intensity loss in the backscattered component at translational-to-internal energy transfers exceeding $\sim 1.2 \text{ eV}$, above which CH_2CO^+ is subject to dissociative decay. Interestingly, a corresponding feature is not observed in the forward-scattered component, where the signal is preferably close to v_{cm} . This is indicative of different scattering dynamics in the forward and backscattered trajectories. One possibility is that the forward-scattered signal involves high transverse velocity components, thereby obscuring the sharp loss of signal attributable to dissociation. Another possibility is that the energy transfer is substantially higher in the case of forward scattering, and that dissociation does not occur because an $HCCOH^+$ isomeric form is involved.

The transition from primarily forward to backscattered $C_2H_2O^+$ distributions as the collision energy is raised can be explained by the change in minimum impact parameter required to transfer sufficient energy to access the transition state at low collision energies. At low energies, very small impact parameters are necessary leading to rebounding trajectories at 0.56 eV, which are observed as forward scattering. At higher energies, larger impact parameter "glancing" collisions can provide the necessary internal excitation of the collision complex, resulting in predominantly backscattered distributions. This interpretation, however, is more symptomatic of a direct mechanism. Clearly, given the short complex lifetimes determined from the osculating complex analysis of the CT recoil velocity distributions, the distinction between complex formation and direct scattering is ambiguous. It may, therefore, be assumed that both direct, "repulsive wall" scattering and scattering attributable to an

attractive interaction leading to longer-lived intermediates play a role in the observed laboratory forward-scattered chemical reaction products.

$\text{COH}^+/\text{HCO}^+$ product cross sections do not appear to be in direct competition with any other products. The similar energy dependence to that of $\text{C}_2\text{H}_2\text{O}^+$ at low energies may be an indicator that these products are accessed through the same transition state and then follow a different path to structures (I) and (II) prior to decaying dissociatively. Geometries (I) and (II) suggest that $m/z=29$ products are primarily formyl ion, HCO^+ .

The energy dependence of the CO^+ cross section is also comparable to $\text{C}_2\text{H}_2\text{O}^+$ and $\text{COH}^+/\text{HCO}^+$ products at low energies, where CO^+ cannot be associated with secondary decay products of $\text{COH}^+/\text{HCO}^+$ and CH_2CO^+ because the associated channels (6c) and (6d) are closed at low energies. Interestingly, CO^+ must, therefore, be formed in conjunction with CH_2O or $\text{CO}+\text{H}_2$ [reactions (6a) and (6b)], respectively, and is, consequently, not associated with simple dissociation of one of the calculated intermediates. The fact that the low-energy cross sections are an order of magnitude smaller than those observed for $\text{CH}_2\text{CO}^+ + \text{O}$ and $\text{COH}^+/\text{HCO}^+ + \text{HCO}$ products, for which a corresponding intermediate can be identified, is evidence that the presently calculated intermediates at least partly control short-range dynamics of this collision system.

In previous studies of state-selected $\text{C}_2\text{H}_2^+ + \text{ND}_3$ and $\text{C}_2\text{H}_2^+ + \text{CH}_3\text{OH}$ reactions, Anderson and co-workers observe only reactions involving simple hydrogen bond fission or charge transfer,^{3,32} even though several stable covalently bound intermediates exist that have dissociation paths leading to other reaction products. In the present reaction system, charge transfer is the predominant reaction product at all energies, and no hydrogen atom or hydride ion transfer reactions are observed. There is clear evidence that covalently bound intermediates that decay to chemical reaction products play a role at small impact parameters, as evidenced by the CH_2CO^+ and $\text{COH}^+/\text{HCO}^+$ product channels. However, the cross sections for these reactions are less than 1 \AA^2 at collision energies below 2 eV. This indicates that the competition from facile proton and hydride transfer reactions in the state-selected C_2H_2^+ studies reduces the probability of passing through the transition states to stable intermediates to an extent that the sensitivity of the respective experiments is insufficient to observe associated reaction products, as suggested by Anderson and co-workers.^{3,32}

Similar to the $\text{O}^+ + \text{C}_2\text{H}_2$ collision system,⁶ a number of highly exothermic chemical reaction channels exist, all of which are inefficient at low collision energies. In the $\text{O}^+ + \text{C}_2\text{H}_2$ case, the reactions are interpreted as proceeding through an excited charge-transfer surface, and the possibility of a poor orbital correlation between reactants and the critical reaction intermediate is suggested. The poor efficiency of the chemical reaction channels of the $\text{O}_2^+ + \text{C}_2\text{H}_2$ system could be explained by a reaction coordinate that passes through a weakly endothermic transition state/or intermediate. This is consistent with the similar low-energy cross section energy dependences of the three most important reaction products, $\text{C}_2\text{H}_2\text{O}^+$, $\text{COH}^+/\text{HCO}^+$ and CO^+ .

The presently applied density functional methods are not considered suitable to make a reliable search of this transition state.

V. CONCLUSIONS

The presently investigated $\text{O}_2^+ + \text{C}_2\text{H}_2$ collision system can be categorized by the following mechanisms: At large impact parameters, charge transfer is the prevailing product channel at all investigated collision energies. Near-resonant product state-to-state transitions are preferred, typical of a long-range mechanism leading to cross sections comparable with the Langevin cross section at near-thermal collision energies. Complex formation becomes an important mechanism at smaller impact parameters. The complexes have very short lifetimes that are on average approximately one third the complex rotational period. At 0.63 eV, the absolute complex lifetime is sufficient to observe near-statistical energy partitioning in the CT products. At higher collision energies, new complex decay channels become possible, leading to highly excited chemical reaction products. An endothermic transition state associated with a vinylidene association complex (III) and a glyoxal ion intermediate (I or II) could explain the low chemical reactivity at low energies despite the high respective exothermicities. These intermediates lead to the main chemical reaction products, HCO^+ and CH_2CO^+ , through simple one-step dissociation. CH_2^+ is identified as a sequential decay product of CH_2CO^+ . A more complicated reaction path leads to CO^+ , which has a cross section that is an order of magnitude smaller than that of the $\text{C}_2\text{H}_2\text{O}^+$ and $\text{COH}^+/\text{HCO}^+$ products at low collision energies. Very small impact parameter (ballistic) collisions can lead to small ion fragments such as CH^+ and C^+ that have cross sections that rapidly increase with collision energy above threshold.

ACKNOWLEDGMENTS

This work is supported by AFOSR under Task 2303EP2. Y. Chiu is a NRC postdoctoral fellow. We thank Professor Scott Anderson and Professor Keiji Morokuma for valuable comments.

- ¹ Y. Chiu, H. Fu, J. Huang, and S. L. Anderson, *J. Chem. Phys.* **101**, 5410 (1994).
- ² Y. Chiu, H. Fu, J. Huang, and S. L. Anderson, *J. Chem. Phys.* **102**, 1199 (1995).
- ³ J. Qian, H. Fu, and S. L. Anderson, *J. Phys. Chem.* **101**, 6504 (1997).
- ⁴ Y. Chiu, H. Fu, J. Huang, and S. L. Anderson, *J. Chem. Phys.* **105**, 3089 (1996).
- ⁵ C. Metayer-Zeitoun, C. Alcaez, S. L. Anderson, H. Palm, and O. Dutuit, *J. Phys. Chem.* **99**, 15523 (1995).
- ⁶ Y. Chiu, R. A. Dressler, D. J. Levandier, S. Williams, and E. Murad, *J. Chem. Phys.* **109**, 5300 (1998).
- ⁷ R. A. Dressler, R. H. Salter, and E. Murad, *J. Chem. Phys.* **99**, 1159 (1993).
- ⁸ S. Mark and D. Gerlich, *Chem. Phys.* **209**, 235 (1996).
- ⁹ D. Gerlich, in *State-Selected and State-to-State Ion-Molecule Reaction Dynamics: Experiment, Part I. Adv. Chem. Phys. Vol. 82*, edited by C. Y. Ng and M. Baer (Wiley, New York, 1992), p. 1.
- ¹⁰ N. G. Adams and D. Smith, in *Techniques for the Study of Ion-Molecule Reactions*, edited by J. M. Farrar and W. H. Saunders (Wiley, New York, 1988), p. 165.
- ¹¹ M. J. Bastian, R. A. Dressler, E. Murad, S. T. Arnold, and A. A. Viggiano, *J. Chem. Soc., Faraday Trans.* **92**, 2659 (1996).
- ¹² R. A. Dressler and E. Murad, in *Unimolecular and Biomolecular Ion-*

- Molecule Reaction Dynamics*, edited by C. Y. Ng, T. Baer, and I. Powis (Wiley, New York, 1994), p. 87.
- ¹³S. G. Lias, J. E. Bartmess, J. F. Liebman, J. L. Holmes, R. D. Levin, and W. G. Mallard, *J. Phys. Chem. Ref. Data* **17**, Suppl. 1 (1988).
- ¹⁴A. A. Radzig and B. M. Smirnov, *Reference Data on Atoms, Molecules, and Ions* (Springer, Berlin, 1985).
- ¹⁵K. P. Huber and G. Herzberg, *Molecular Spectra and Molecular Structure IV. Constants of Diatomic Molecules* (Van Nostrand Reinhold, New York, 1979).
- ¹⁶G. Herzberg, *Molecular Spectra and Molecular Structure III. Electronic Spectra and Electronic Structure of Polyatomic Molecules* (Van Nostrand Reinhold, New York, 1966).
- ¹⁷M. M. Chiang, B. H. Mahan, and C. Maltz, *J. Chem. Phys.* **57**, 5114 (1972).
- ¹⁸D. W. Turner, C. Baker, A. D. Baker, and C. R. Brundle, *Molecular Photoelectron Spectroscopy* (Wiley, London, 1970).
- ¹⁹K. M. Ervin and P. B. Armentrout, *J. Chem. Phys.* **83**, 166 (1985).
- ²⁰Y. Ikezoe, S. Matsuoka, M. Takabe, and A. A. Viggiano, *Gas Phase Ion-Molecule Reaction Rate Constants Through 1986* (Maruzen, Tokyo, 1987).
- ²¹G. Gioumoussis and D. P. Stevenson, *J. Chem. Phys.* **29**, 294 (1958).
- ²²M. J. Bastian, R. A. Dressler, D. J. Levandier, E. Murad, F. Muntean, and P. B. Armentrout, *J. Chem. Phys.* **106**, 9570 (1997).
- ²³G. A. Fisk, J. D. McDonald, and D. R. Herschbach, *Discuss. Faraday Soc.* **44**, 228 (1967).
- ²⁴M. K. Bullitt, C. H. Fisher, and J. L. Kinsey, *J. Chem. Phys.* **60**, 478 (1974).
- ²⁵D. M. Sonnernfroh, R. A. Curtis, and J. M. Farrar, *J. Chem. Phys.* **83**, 3958 (1985).
- ²⁶R. A. Dressler, R. H. Salter, and E. Murad, *Chem. Phys. Lett.* **204**, 111 (1993).
- ²⁷R. A. Dressler, R. H. Salter, and E. Murad, *Planet. Space Sci.* **40**, 1695 (1992).
- ²⁸GAUSSIAN 94, Revision D.1, edited by M. J. Frisch, G. W. Trucks, H. B. Schlegel, P. M. W. Gill, B. G. Johnson, M. A. Robb, J. R. Cheeseman, T. Keith, G. A. Petersson, J. A. Montgomery, K. Raghavachari, M. A. Al-Laham, V. G. Zakrzewski, J. V. Ortiz, J. B. Foresman, J. Cioslowski, B. B. Stefanov, A. Nanayakkara, M. Challacombe, C. Y. Peng, P. Y. Ayala, W. Chen, M. W. Wong, J. L. Andres, E. S. Replogle, R. Gomperts, R. L. Martin, D. J. Fox, J. S. Binkley, D. J. Defrees, J. Baker, J. P. Stewart, M. Head-Gordon, C. Gonzalez, and J. A. Pople, Gaussian, Pittsburgh, PA, 1995.
- ²⁹Q. Cui, Z. Liu, and K. Morokuma, *J. Chem. Phys.* **109**, 56 (1998).
- ³⁰J. H. Langenberg and P. J. A. Ruttink, *Theor. Chim. Acta* **85**, 285 (1993).
- ³¹T. Slee and R. F. W. Bader, *J. Mol. Struct.* **255**, 173 (1992).
- ³²J. Qian, R. J. Green, and S. L. Anderson, *J. Chem. Phys.* **108**, 7173 (1998).

The reaction of $O^+(^4S)$ and $N_2(X^1\Sigma_g^+)$ revisited: Recoil velocity analysis of the NO^+ product

D. J. Levandier[†], R. A. Dressler, Y.-H. Chiu[‡] and E. Murad

Air Force Research Laboratory/VSBS, 29 Randolph Road, Hanscom Air Force Base, MA 01731-3010

Abstract

The guided-ion beam method has been used to measure time-of-flight (TOF) spectra of the NO^+ produced in the reaction of $O^+(^4S)$ and $N_2(X^1\Sigma_g^+)$. Particular care was taken to minimize the participation of the $O^+(^2D, ^2P)$ metastables in the reactions, the success of which is validated by measuring the absolute cross section for the reaction as a function of collision energy in the near-thermal to 1.5 eV range. In this range, the cross section exhibits a region of low reactivity at near-thermal energies, which can be obscured by reactions of metastables and other effects, and a region of sharply increasing reactivity above a threshold of collision energy ≈ 0.3 eV.

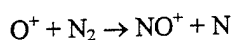
The velocity-transformed TOF spectra, at collision energies of 0.51 eV, 0.80 eV, 3.2 eV and 6.3 eV, indicate two reaction mechanisms: in the first, product ions are scattered backward with inefficient translational to internal energy conversion; in the second, product ions arise from intermediate collision complexes with efficient translational energy conversion. The first mechanism is associated with the passage through the spin-forbidden doublet ground state N_2O^+ intermediate, while the second involves passage through an endothermic quartet intermediate.

[†] Orion International Technologies, Albuquerque, NM 87110

[‡] Boston College, Institute for Scientific Research, Newton, MA 02159

Introduction

The reaction



$$\Delta H = -1.09 \text{ eV} \quad (1)$$

which involves the most abundant ion and neutral in the ionosphere *F*-region, has been studied extensively. All of the standard experimental techniques have been applied to the study of this reaction through the energy range from thermal to a few eV¹⁻¹⁴ and there have been some endeavors in theory.¹⁵⁻²¹ The cross section for reaction (1) at low collision energies is bimodal, exhibiting a threshold at ~0.3 eV,¹⁰ corresponding to a rapid increase in reaction efficiency to a maximum of ~4 Å² at ~10 eV, where NO⁺ dissociation then becomes accessible. In the pre-threshold region, the cross section is of the order of 0.1-0.3 Å². The form of the cross section in this low energy region has been attributed to the details of the N₂O⁺ potential,¹⁵⁻¹⁹ which indicates a mechanism that involves spin-forbidden surface hops to and from the N₂O⁺ doublet ground state at pre-threshold collision energies. The threshold is consistent with the availability of a quartet reaction pathway, via the N₂O⁺(1⁴A⁻) state which forms an effective barrier of ~0.2-0.3 eV.^{10,17-19}

Despite the attention given to reaction (1), there are open questions regarding the dynamics involved, particularly with respect to the energy disposal. Knowledge of the disposition of energy in the products, whether through translational to internal energy conversion or due to the exothermicity, which is sufficient to produce NO⁺ with three quanta of vibrational excitation, will allow further insight into the reaction mechanism. Moreover, this information would be required if efforts in modeling the ionosphere and air plasmas at lower altitudes are to include the effects of internal energy.

Previous investigations into the dynamics of reaction (1) have met with limited success. The results of merged beam experiments,⁵ which featured measurement of the component of product kinetic energy along the beam axis, were affected by the presence of O⁺ and N₂ excited states. A recent state-selected, GIB study of the reactions of O⁺ and N₂ illustrates the importance of avoiding the O⁺(²D, ²P) metastables when ground state species are of interest.¹³ This is particularly true for O⁺(²P), which has a larger cross section below ~0.5 eV that increases with decreasing collision energy. The thermal rate of reaction (1) has also been shown to increase dramatically for N₂(*v* ≥ 2).^{1,2,12} In a crossed beam study,⁷ limited to collision energies of ≥1.50 eV, doubly differential cross sections were obtained that were in poor agreement with the merged beam results. A beam-cell study, limited to energies above ~1.8 eV, may also have been subject to contamination by O⁺ metastables.³

Although lower in resolution than crossed beam studies, the cylindrical symmetry and 100% product ion collection efficiency of GIB time-of-flight (TOF) measurements provide many advantages when determining recoil velocity distributions of ions.²² In the study presented here, a GIB instrument is used to measure product TOF spectra from which the product velocity distributions are obtained. Care was taken to minimize the participation of O⁺ excited states, the success of which is confirmed by comparison of the measured cross section to that from other studies.

Experimental

The apparatus used in this study has been explained in detail previously,²³ so only a brief description is given here. The instrument is a tandem mass spectrometer equipped with a rf octopole ion guide located between the mass filters. The octopole has two stages, the first of which is 7.4 cm in length and passes through a 3.5 cm long collision cell. The second octopole stage begins at the exit of the collision cell and is 16.7 cm long. Lens systems exist for injecting ions into the first octopole stage and for extracting ions from the second stage prior to analysis.

Primary O⁺ ions are produced in an electron impact ion source using CO₂ as a precursor gas for dissociative ionization. By working with an electron energy of ~20 eV, 0.9 eV above and 2.3 eV below the appearance potentials for O⁺(⁴S) and O⁺(²D), respectively, it is possible to form O⁺ almost exclusively (≥99%) in its ground state. In the present study, this is easily checked by measuring the O⁺ + N₂ charge transfer cross section, which is negligible below the 1.97 eV thermochemical threshold for charge transfer onto O⁺(⁴S). For 1 eV collision energy, the charge transfer cross sections for O⁺(²D) and O⁺(²P) are ~20 Å² and 30 Å²,¹³ respectively, so even a 1% population of metastables in the primary ion beam is discernable. The ion beam is turned through 90° in a dc quadrupole bender, mass selected in a Wien filter, and then injected into the first octopole at the desired

kinetic energy. Unreacted primary ions and ions resulting from reactions in the collision cell pass into the second octopole, which is typically biased 0.3–0.4 V below the first octopole to aid in the extraction of thermal product ions from the cell. To minimize the occurrence of secondary reactions in the collision cell, the N_2 target gas is maintained at a pressure of ~ 0.25 mTorr. The ion beam energy is known to better than ± 0.1 eV, with beam spreads typically of 0.22–0.25 eV fwhm, as measured by the retarding potential method and by time-of-flight.

Absolute cross sections are determined by integrating the mass spectrometer signal intensities for the product and transmitted primary ions, monitoring the pressure of the target gas, and using the low density limit of the Lambert–Beer expression, as has been described before.²³

To avoid the effect of very slow primary ions trapped within the octopole, the cross section measurements are carried out using a pulsed mode in which the ion beam and octopole rf are turned off briefly. The trapping of low energy primary ions, which may result from surface potential barriers, has the result of increasing the apparent cross section since the ions can simply reside within the ion guide until they undergo a reactive collision.²⁴ In the present study, a 5 ms pulsing cycle is used, with the octopole rf turned off for the last 25 μ s of the period to allow the slow ions to escape from the ion guide. The ion beam is turned on 5 μ s after the rf potential is restored, and remains on for 4.5 ms, the remainder of the period being used to collect the product ions derived from the latter part of the ion beam pulse. The pulsing scheme is illustrated in figure 1a. Also shown in figure 1b are the results of an experiment in which the cross section for reaction (1), at 0.19 eV collision energy, is measured for different pulsing cycle periods, with the rf and ion beam off-time unvaried. The cross sections measured with this pulsing scheme are compared to continuous mode data.

TOF spectra are measured by pulsing the primary ion beam, using a 3 μ s ion beam pulse width, and measuring the flight time of product ions arriving at the detector. Very slow ions, which would otherwise result in a background signal in subsequent pulse cycles, are eliminated at the end of each cycle by briefly turning off the octopole rf potential.

Results and Analysis

Figure 2a shows the absolute cross section measured in the present study for production of NO^+ from collisions of $O^+(^4S)$ and $N_2(X^1\Sigma_g^+)$ at kinetic energies in the range of near-thermal to ~ 1.6 eV. The data have been corrected for the primary ion residence time effect using standard deconvolution procedures.^{22,25} The data exhibit a threshold at ~ 0.3 eV, below which the cross section is a nearly constant 0.05 – 0.06 \AA^2 . The cross section rises steeply from the threshold through the remainder of the studied range; at 1 eV the cross section is 1.0 \AA^2 .

The same results are plotted in figure 2b in the form of an energy dependent rate constant. The rate constant, $k(\langle E_T \rangle)$, is obtained from the cross section, $\sigma(E_T)$, by the expression $k(\langle E_T \rangle) = v \cdot \sigma(E_T)$, where $\langle E_T \rangle$ is the average relative translational energy and v is the relative velocity. Also illustrated on this plot is the agreement between the present data and the results of drift tube⁹ and high temperature flowing afterglow experiments.¹² The high temperature flowing afterglow data were converted from temperature (T) to kinetic energy (KE) using the usual $KE = 1.5k_B T$, where k_B is the Boltzmann constant. The only noteworthy differences are the slight rise of the flowing afterglow data at ~ 0.2 eV, due to vibrational enhancement,¹² and the lack of a clear minimum in the present data, due largely to the width of the distribution of collision energies in this work.

As indicated above, monitoring of the charge transfer reaction $O^+ + N_2 \rightarrow N_2^+ + O$, which is negligible for $O^+(^4S)$ at energies below 2 eV, indicates that the ion beam used in this study should include less than 1% of the $O^+(^2D, ^2P)$ metastables. The cross section presented here compares well with the first GIB studies of reaction (1) by Burley, et al.,¹⁰ in which the primary ion beam was purged of metastable O^+ by passing the beam through an N_2 charge transfer cell prior to reaction. The agreement between the present work and the drift tube rate constant, illustrated in figure 2a, is similarly good. The same reaction was also recently studied using state-selected GIB experiments,¹³ and agreement between those results and the present data are reasonable. Moreover, the state-selected data, which include the cross sections for reaction with the O^+ metastables, further confirm that the present study is not significantly affected by reactions of these species. Specifically, the $O^+(^2P)$ cross section is appreciable at near thermal collision energy and decreases with increasing energy, typical of exothermic ion–molecule reactions. At 1 eV the cross sections for $O^+(^4S)$ and $O^+(^2P)$ are of similar magnitude, and below this energy the latter cross section is much larger, suggesting that the presence of $O^+(^2P)$ in our ion beam would severely affect our cross section in the near-thermal region.

Figure 3 presents the results of NO^+ TOF experiments at collision energies of 0.51 eV, 0.80 eV, 3.2 eV and 6.3 eV. The raw TOF data have been transformed to the velocity domain, as described previously,²⁶ and are

plotted as a function of v'_{ip} , the component of product ion laboratory velocity parallel to the ion beam axis. Also shown in each case is the corresponding velocity distribution for the primary ion beam, confirming the narrow ion beam energy spread. On each plot are indicated the velocity of the center of mass and the energetic limit of forward and backward (in one case) laboratory velocities. In this work, the forward direction is defined as the ion beam direction, and corresponds to velocities greater than the velocity of the center of mass (v_{CM}). The lowest energy TOF data, at $E_T = 0.51$ eV, represents a practical limit in sensitivity, because of the small cross section, and was attempted as a means of providing information on the pre-threshold mechanism.

The TOF data suggest two mechanisms for reaction (1) in the included energy range. In the lower energy TOF spectra, there is a strongly back-scattered component that dominates at $E_T = 0.51$ eV and which decreases with increasing energy, relative to the second component. The second component appears as a shoulder in the velocity distributions at $E_T = 0.51$ eV and 0.80 eV, and includes products which are scattered in both the forward and backward directions. In both these spectra, the forward-scattered intensity decreases monotonically, with very little intensity at velocities approaching the thermochemical maximum.

The shoulder, which appears to be located near v_{CM} in the lower energy TOF data, grows in relation to the strongly back-scattered component until it dominates the product velocity distribution at $E_T = 3.2$ eV. At this collision energy, this component exhibits similar intensities in the forward and backward directions, with a discernible peak in the forward direction at $v'_{ip} \approx 4000$ m/s. In the velocity spectrum at $E_T = 6.3$ eV, the forward-backward component, now the only mechanism, is asymmetric with respect to v_{CM} and peaks in the forward direction at $v'_{ip} \approx 5500$ m/s with a broad tail to lower velocities.

The component with forward and backward scattering is reminiscent of a complex-mediated reaction. At the lowest collision energies the details are difficult to discern due to the back-scattered component and low velocity 'pile-up' from the time-to-velocity transform. At $E_T = 3.2$ eV, however, these product velocities are nearly symmetric about v_{CM} , indicating a complex with lifetime comparable to the rotational period of the complex. The TOF spectrum also indicates a significant degree of internal energy in the products, as evidenced by the peaking well below the thermochemical limit. The velocity distribution for $E_T = 6.3$ eV is consistent with a complex whose lifetime is somewhat shorter than its rotational period, which is expected for complexes formed at higher collision energies. At still higher energies such a reaction mechanism typically evolves to direct dynamics. Indeed, the peak in this velocity distribution is near the spectator stripping limit,²⁷ as indicated by the arrow in figure 3, which is consistent with similar observations in other studies for collision energies of this magnitude.^{3,5,7}

The present TOF results agree well with the merged beam⁵ and crossed beam⁷ studies only at higher collision energies, where reaction (1) appears to proceed via a direct mechanism to yield forward-scattered NO^+ . At lower collision energies, the results of the three experiments differ significantly. The merged beam study spans the energy range examined here, and includes product kinetic energy scans at $E_T = 0.5$ eV, 0.8 eV and 3.0 eV, nearly coinciding with the lower energies for which the present TOF data were obtained. At the two lower energies, the merged beam experiments indicate nearly symmetric forward and backward scattering, with significant NO^+ product intensity at the thermochemical limits. This clearly does not correspond with the present TOF data at $E_T = 0.51$ eV and 0.80 eV, in which the forward scattered product intensity diminishes at velocities well below the thermochemical limit, and in which the scattering is dominated by a strong backward component. The difference between the two experiments may be attributed to contributions from excited states of the reactant ion and molecule in the merged beam study. Similarly, the 3.0 eV merged beam results feature more forward-scattered intensity than in the present study.

In the crossed beam work, the product ions for the lowest collision energy studied, 1.5 eV, are primarily forward scattered, with a peak well beyond the spectator stripping value and with considerable intensity near the thermochemical limit for reaction (1). Due mostly to the absence of back-scattered product, this is in clear contrast to the present results, and to the results of the merged beam study in which data are also available for $E_T = 1.5$ eV. The lack of back-scattered NO^+ in the crossed beam experiment may relate to the combination of the kinematics for this system and the restricted range of laboratory angles for detection.²⁸ The former constraint dictates that back-scattered ions have very low laboratory velocities in that study, making them very susceptible to stray fields, and the latter limits the experiment to viewing only a fraction of back-scattered ions.

To quantify the TOF results with regard to reaction energy disposal, which we consider in terms of the translational to internal energy transfer, ΔE_T , we have modeled the TOF velocity distributions for the experiments at $E_T = 3.2$ eV and 6.3 eV using the osculating complex model.²⁹ The simulations are compared with the experimental distributions in figures 4a and 5a. We have detailed our implementation of this model in previous work,^{26,30} however an outline is given here. In this model, a reaction is regarded as proceeding via a weakly

bound, orbiting complex with an exponential decay time proportional to $\exp(-t/\tau_c)$, where τ_c is the complex lifetime. The product recoil energy, given by ΔE_T , is assumed to be independent of scattering angle, and is governed by the ratio τ/τ_c , where τ is the complex rotational period. Under these conditions, for an experiment at a given collision energy, a basis set of laboratory axial velocity distributions, $S_i(v'_{1p}; \Delta E_T, \tau_i)$, may be constructed in which the adjustable parameters are $\tau = \tau/\tau_c$ and ΔE_T , and which account for the experimental broadening mechanisms. The simulations are linear combinations of the basis functions derived by a least squares fit to the experimentally observed distributions:

$$f(v'_{1p}) = \sum_i c_i S_i(v'_{1p}; \Delta E_T, \tau_i), \quad (4)$$

where the fit coefficients, c_i , are equivalent to the probability of a particular value of translational exoergicity, $P(\Delta E_T)$. The plots of $P(\Delta E_T)$, in figures 4b and 5b, represent the distributions of translational to internal energy transfer for the reactions at $E_T = 3.2$ eV and 6.3 eV, respectively.

In figure 4a, the osculating complex model (solid curve) recovers the $E_T = 3.2$ eV TOF data (solid circles) reasonably well, especially at higher velocity where there is contribution from only one of the reaction mechanisms. This fit was achieved with a single value of $\tau = 1$, indicating a complex with average lifetime similar to its rotational period. Although the present model may also be used to simulate direct dynamics, by using very large values of τ , the near thermal products were not modeled in this case. The energy transfer distribution for reaction at $E_T = 3.2$ eV, figure 4b (solid curve), is very broad and peaks at approximately $\Delta E_T = -2.2$ eV. The distribution indicates a substantial degree of energy transfer, with typically only 1 eV of energy retained in translation.

To confirm the collision complex mechanism, a TOF experiment was carried out at $E_T = 3.2$ eV in which the octopole rf trapping potential is reduced. When interpreting the TOF data, it must be remembered that the velocity distributions consist of projections of the product ion recoil velocity vector onto the octopole axis. As a result, complicated, wide-angle scattering could hinder the extraction of information on energy partitioning from the TOF data. In the present experiment, large transverse velocity components can be discriminated by reducing the radial trapping potential. The result of this experiment is included in figure 4a (open circles). The distinguishing feature of the low rf velocity distribution is the diminished intensity at v_{CM} , which is the behavior expected for the decay of a weakly bound complex. Product ions derived from an orbiting complex would be scattered isotropically (with respect to v_{CM}), with a velocity distribution independent of scattering angle. In this case, product ions with parallel laboratory velocity near v_{CM} may have a large transverse velocity component and would escape the ion guide when the lower trapping potential is used, as is observed in this experiment. The greater loss of back-scattered ions, compared to forward-scattered ions, can be attributed to losses of low energy ions due to octopole rod surface potential barriers, which are of greater consequence at low rf amplitudes where the ion trajectories pass closer to the rod surfaces.

To substantiate the validity of the osculating complex model, the low rf data at $E_T = 3.2$ eV was also modeled. Purely osculating dynamics would result in the same energy transfer distribution as seen in the high rf experiment. A basis set of velocity distributions was used that has the same value of τ and which also accounts for the loss of product ions above a calibrated transverse velocity.^{31,32} The fit is, again, satisfactory at higher velocities, as illustrated in figure 4a (dashed curve). The energy transfer distribution derived directly from the fit to the low rf data, in figure 4b (dashed curve), is in good agreement with the distribution determined in the high rf experiment, further confirming the complex-mediated mechanism. The low rf data also compare well with a simulation (dotted curve) derived by using the basis functions for the low rf configuration and the energy transfer distribution for the high rf experiment.

Figure 5a-5b depicts the results of the osculating complex modeling of the $E_T = 6.3$ eV TOF experiment. At this collision energy, the channel that dominates the low energy reaction, giving rise to the strongly back-scattered products, is no longer prominent, so the simulation reproduces the experimental data over essentially the whole range of product laboratory velocity. The resulting energy transfer distribution, for a set of basis functions constructed with a single value of $\tau = 4$, is similar in form to the translationally exoergic distribution derived from the lower energy experiment. The distribution is broad and peaked at large values of kinetic to internal energy transfer, again about 1 eV remaining as translational energy.

The energy disposal in the strongly back-scattered component, at the lower collision energies, is more difficult to discern and only an upper limit of product internal excitation can be provided. At these low collision

energies, because reaction (1) is exothermic, back-scattered product ions with velocities approaching the thermochemical limit travel backward in the laboratory frame, and cannot be directly measured in the TOF experiment. Although it is possible, in the present experiment, to recover the signal intensity due to such product ions by imposing a potential barrier that reflects these species into the forward direction, the velocity information is not preserved. The peaks at $v'_{ip} = 0$ in the TOF spectra at the lower collision energies, $E_T = 0.51$ eV and 0.80 eV, are narrower than the experimental resolution, indicated by the ion beam widths. This suggests that the back-scattered component may feature larger center-of-mass velocities than are indicated in the TOF spectra. The measured zero-velocity signal can therefore be taken to represent an upper (lower) limit of internal (translational) product energy for the relevant collision energy. For the $E_T = 0.51$ eV and 0.80 eV experiments, the upper limit on product internal energy amount to ~ 0.9 eV. TOF measurements of the NO^+ fragment in threshold photoion-photoelectron spectroscopy studies, with excitation into the $\text{N}_2\text{O}^+ X^2\Pi$ state at energies just above the O^+ appearance energy, indicate somewhat lower fragment internal energy³³ and, therefore, are consistent with the present evaluation.

Discussion

Based on their relative behavior with respect to collision energy, we assign the strongly back-scattered component to the pre-threshold reaction and the forward-backward component to the mechanism associated with the threshold. The osculating complex model simulations and the comparisons of high and low rf TOF experiments at $E_T = 3.2$ eV strongly support the suggestion that, as reaction (1) gains access to the $\text{N}_2\text{O}^+(1^4A^-)$ surface, the reaction proceeds primarily via a collision complex. Both the broad energy transfer distributions, with peaking nearer high values of translational to internal energy transfer, and the values of $\tau = 1$ and 4, derived from the fits of the data at $E_T = 3.2$ eV and 6.3 eV, respectively, are consistent with this picture. Moreover, the increase of τ with collision energy, implying decreased lifetime, is typical for a reaction via an intermediate complex.

The ability to fit the data for $E_T = 6.3$ eV with a single value of $\tau = 4$, a value consistent with a short-lived, osculating complex, indicates that the dynamics at this collision energy cannot be accounted for exclusively by the direct, forward scattering implied by the spectator stripping mechanism mentioned above. The spectator stripping model has been discounted previously, based on the fact that the maximum, at ~ 10 eV, and decline at higher energies of the cross section for reaction (1) is attributed to the loss of NO^+ via dissociation; the spectator stripping model dictates a threshold for dissociation of 13.3 eV.¹⁰ The present results suggest that the true threshold for dissociation may be obscured by the usual decline of cross sections with collision energy in reactions proceeding via complexes.

Attributing the strongly back-scattered channel to the pre-threshold reaction calls into question the actual mechanism that gives rise to the near thermal species. Earlier flowing afterglow⁸ and flow-drift⁶ studies indicate the participation of a weakly bound complex in the thermal to near-thermal energy regime, an interpretation based largely on the decrease of the rate constant with temperature or collision energy. The TOF data presented here indicate that the mechanism giving rise to these strongly back-scattered products comprises a reversal of direction of the oxygen moiety, which indicates a mechanism that involves either low-impact parameter, rebounding collisions or a collision complex formed via large impact parameters. Either mechanism should, however, yield a broader v'_{ip} distribution than indicated here, encompassing the broad angular scattering and energy release distribution expected in each case.

The unusual product velocity distribution associated with the pre-threshold channel for reaction (1) implies very constrained dynamics. The large kinetic energy release may be explained, for either the rebounding or complex-mediated mechanism, by an exit channel barrier, possibly due to a phase space bottleneck associated with the exit channel doublet to quartet surface hop. This picture is in keeping with the fact that the exit channel to which the $\text{N}_2\text{O}^+ 1^4A^-$ surface correlates adiabatically is repulsive.¹⁷ Such a bottleneck could also dictate that only very specific trajectories successfully negotiate both passages across the $\text{N}_2\text{O}^+ X^2\Pi(1^2A', 1^2A^-) - 1^4A^-(1^4\Pi)$ crossing seam and sample the chemical exchange region of the potential energy surface. In a complex-mediated mechanism, this spatial constraint could manifest itself in the very particular range of impact parameters that give rise to the sharply backward angular behavior observed. For a rebounding mechanism, the lack of broad angular scattering indicates a narrow range of small impact parameters, corresponding to those capable of overcoming this bottleneck. The behavior of the cross section at thermal energies, decreasing with increasing collision energy, can also be explained on the basis of this limitation on reactive trajectories. For reactions occurring at fixed impact parameters, in either mechanism, the efficiency of the quartet to doublet transition while

passing through the surface crossing region diminishes with increasing velocity, as has been pointed out previously.^{10,15} Without the constraint on impact parameters, however, there would exist a preference for large impact parameter collisions, during which the radial velocity is very small and would enhance the reaction efficiency.

Previous theoretical efforts have focussed on the mechanism for reaction (1) at higher collision energies, above the observed threshold, and have mostly treated the pre-threshold reaction qualitatively,¹⁵⁻¹⁹ suggesting either a long-lived complex mechanism¹⁵ or a three-body mechanism,¹⁷ the latter of which has been disproved as the principal pre-threshold mechanism.¹⁰ Theoretical studies aimed at explaining photoionization and fragmentation of N_2O^+ were not concerned with also explaining the behavior observed in the reaction studies.^{20,34} A better understanding of the thermal mechanism will require a renewed effort in theory, with the accurate ground and excited N_2O^+ surfaces needed to account for the effects on the dynamics of both the chemistry, and the surface hopping transitions, including the type of motion involved in the coupling, radial or rotational.

The present results, combined with those from other studies, permit some broad suggestions regarding product state distributions for reaction (1). The energy transfer distributions derived with the osculating complex model for the TOF experiments at $E_T = 3.2$ eV and 6.3 eV indicate a high degree of product internal excitation. The energy transfer distributions are very broad and peak approximately 1 eV below the maximum available energy. This is reminiscent of a process that is nearly statistical, in keeping with a complex-mediated reaction in which the complex survives long enough for extensive energy randomization to occur. It may be expected that at lower collision energies, still above threshold, the complex lifetimes are sufficiently large to allow a statistical energy distribution in the products.

Statistical considerations would suggest that in the intermediate energy range, represented here by the experiments at $E_T = 3.2$ eV and 6.3 eV, the dominant complex-mediated mechanism should result in the product internal energy residing primarily on the diatomic product. Moreover, for reactions proceeding on the $N_2O^+(1^4A^-)$ surface, production of atomic nitrogen in its lower excited states of ($^2D, ^2P$) involves a spin-forbidden transition. The importance of this last point is supported by the observation of stripping-like behavior at the higher collision energies,^{3,5,7} the modeling of which assumes a ground state atomic product. At still larger collision energies, where dissociation of the diatomic product is energetically possible and results in the eventual decline in cross section,^{10,13} the NO^+ that does survive should have high internal excitation.

Conclusion

The absolute cross section of the reaction $O^+(^4S) + N_2(X^1\Sigma_g^+) \rightarrow NO^+ + N$ has been remeasured in a guided-ion beam experiment, in the threshold region between near-thermal energy and 1.5 eV. This measurement agrees well with previous guided-ion beam measurements, in which particular care was taken to avoid reactions with O^+ metastables,^{10,13} and with the results of drift tube⁹ and high temperature flowing afterglow¹² studies. Time-of-flight spectra of the NO^+ product were obtained at four collision energies, 0.51 eV, 0.80 eV, 3.2 eV and 6.3 eV. The TOF data indicate two distinct mechanisms in the energy range studied. At thermal to near-thermal energies, reaction proceeds by a mechanism that may feature highly constrained dynamics yielding products with large backward velocities (in the center of mass frame) and, consequently, with little internal energy. At energies above the cross section threshold, analysis using the osculating complex model shows that reaction occurs via a weakly bound collision complex, which generates products with substantial internal excitation. These findings are of considerable importance in the context of modeling of ionospheric processes involving NO^+ , in both the thermal and hyperthermal energy ranges.

Acknowledgements

This work was solely funded by the Air Force Office of Scientific Research (AFOSR) under task 2303EP2 and in cooperation with DDR&E Air Plasma Ramparts MURI program. During this study, Y.-H. Chiu held an NRC postdoctoral fellowship.

Figure Captions

1.
 - a) Pulsing scheme used to eliminate effects of trapped primary ions. A 5 ms period is used, during which time the octopole rf potential is on for all but the last 25 μ s, the interval required for trapped ions to escape the octopole volume. The ion beam is turned on 5 μ s after the rf potential is restored, and it remains on for 4.5 ms.
 - b) Effect of the period length on the apparent cross section measured at $E_T = 0.19$ eV. The dashed line indicates the measured cross section when the normal experiment configuration is used, with a continuous octopole rf field and ion beam. The points are cross sections measured at different period lengths, while keeping the rf and ion beam off intervals constant.
2.
 - a) Absolute reaction cross section for $O^+(^4S) + N_2(\tilde{X}^1\Sigma_g^+) \rightarrow NO^+ + N$ as a function of collision energy.
 - b) The same data have been converted to a rate constant (solid circles), a function of average kinetic energy, as outlined in the text. The data are compared to data from drift tube (open triangles; ref. 9) and high temperature flowing afterglow (open squares; ref. 12) experiments.
3. Time of flight data for the NO^+ product ion from reaction (1) for the indicated collision energies (solid circles). The data have been transformed to the laboratory velocity reference frame. The velocity spectra represent the distributions of the product velocity component parallel to the primary ion beam direction. The solid curves are the ion beam velocity distributions. The horizontal lines indicate: short dash – velocity of the center of mass v_{CM} ; long dash – minimum (in one case) and maximum possible product laboratory velocities. In the plot for $E_T = 6.3$ eV, the arrow indicates the most probably product velocity for the Spectator Stripping mechanism.
4. Results of analysis of TOF data for $E_T = 3.2$ eV using the osculating complex model.
 - a) The solid and dashed curves are the osculating model simulations for the laboratory velocity distributions obtained with normal and low rf amplitudes, respectively (solid and open circles). The dotted curve represents the laboratory velocity distribution calculated using the low rf basis functions and the energy transfer distribution derived for the normal rf experiment. The dashed vertical line is v_{CM} .
 - b) The solid and dashed curves are the translational energy transfer distributions derived from the fits shown in (a) for the normal and low rf experiments, respectively.
5. Results of analysis of TOF data for $E_T = 6.3$ eV using the osculating complex model.
 - a) The osculating model simulation of the laboratory velocity distribution (solid circles). The dashed vertical line is v_{CM} .
 - b) The translational energy transfer distribution derived from the fit shown in (a).

References

- 1 A. L. Schmeltekopf, G. I. Gilman, F. C. Fehsenfeld, and E. E. Ferguson, *Planet. Space Sci.* **15**, 401 (1967).
- 2 A. L. Schmeltekopf, E. E. Ferguson, and F. C. Fehsenfeld, *J. Chem. Phys.* **48**, 2966 (1968).
- 3 J. J. Leventhal, *J. Chem. Phys.* **54**, 5102 (1971).
- 4 J. A. Rutherford and D. A. Vroom, *J. Chem. Phys.* **55**, 5622 (1971).
- 5 R. H. Neynaber and G. D. Magnuson, *J. Chem. Phys.* **58**, 4586 (1973).
- 6 M. McFarland, D. L. Albritton, F. C. Fehsenfeld, E. E. Ferguson, and A. L. Schmeltekopf, *J. Chem. Phys.* **59**, 6620 (1973).
- 7 G. P. K. Smith and R. J. Cross Jr., *J. Chem. Phys.* **60**, 2125 (1974).
- 8 W. Lindinger, F. C. Fehsenfeld, A. L. Schmeltekopf, and E. E. Ferguson, *J. Geophys. Res.* **79**, 4753 (1974).
- 9 D. L. Albritton, I. Dotan, W. Lindinger, M. McFarland, J. Tellinghuisen, and F. C. Fehsenfeld, *J. Chem. Phys.* **66**, 410 (1977).
- 10 J. D. Burley, K. M. Ervin, and P. B. Armentrout, *J. Chem. Phys.* **86**, 1944 (1987).
- 11 G. D. Flesch and C. Y. Ng, *J. Chem. Phys.* **92**, 3235 (1990).
- 12 P. M. Hierl, I. Dotan, P. V. Seeley, J. M. Van Doren, R. A. Morris, and A. A. Viggiano, *J. Chem. Phys.* **106**, 3540 (1997).
- 13 X. Li, Y. L. Huang, G. D. Flesch, and C. Y. Ng, *J. Chem. Phys.* **106**, 1373 (1997).
- 14 Y. Kaneko and N. Kobayashi, *J. Phys. Soc. Japan* **36**, 1649 (1974).
- 15 J. J. Kaufman and W. S. Koski, *J. Chem. Phys.* **50**, 1942 (1969).
- 16 A. Pipano and J. J. Kaufman, *J. Chem. Phys.* **56**, 5258 (1972).
- 17 D. G. Hopper, *J. Am. Chem. Soc.* **100**, 1019 (1978).
- 18 D. G. Hopper, *J. Chem. Phys.* **77**, 314 (1982).
- 19 D. G. Hopper, *J. Chem. Phys.* **76**, 1068 (1982).
- 20 N. Komuha, *J. Mol. Structure* **306**, 313 (1994).
- 21 H. H. Michels, (Air Force Geophysics Laboratory, United States Air Force, Hanscom AFB, 1981), pp. 1.
- 22 E. Teloy and D. Gerlich, *Chem. Phys.* **4**, 417 (1974).
- 23 R. A. Dressler, R. H. Salter, and E. Murad, *J. Chem. Phys.* **99**, 1159 (1993).
- 24 V. F. DeTuri, P. A. Hintz, and K. M. Ervin, *J. Phys. Chem. A* **101**, 5969 (1997).
- 25 K. M. Ervin, Ph.D. Thesis, University of California, Berkeley, 1986.
- 26 R. A. Dressler and E. Murad, in *Unimolecular and Bimolecular Reaction Dynamics*, Chap. 2, edited by C. Y. Ng, T. Baer, and I. Powis (Wiley & Sons, 1994).
- 27 A. Henglein, in *Ion - Molecule Reactions in the Gas Phase*, Vol. 58 (1966), pp. 63.
- 28 Z. Herman, J. D. Kerstetter, T. L. Rose, and R. Wolfgang, *Rev. Sci. Instrum.* **40**, 538 (1969).
- 29 M. K. Bullit, C. H. Fisher, and J. L. Kinsey, *J. Chem. Phys.* **60**, 478 (1974).
- 30 M. J. Bastian, R. A. Dressler, E. Murad, S. T. Arnold, and A. A. Viggiano, *J. Chem. Soc. Faraday Trans.* **92**, 2659 (1996).
- 31 S. Märk and D. Gerlich, *Chem. Phys.* **209**, 235 (1996).
- 32 S. Williams, Y.-H. Chiu, D. J. Levandier, and R. A. Dressler, *J. Chem. Phys.* **109**, 7450 (1998).
- 33 I. Nenner, P.-M. Guyon, T. Baer, and T. R. Govers, *J. Chem. Phys.* **72**, 6587 (1980).
- 34 J. A. Beswick and M. Horani, *Chem. Phys. Lett.* **78**, 4 (1981).

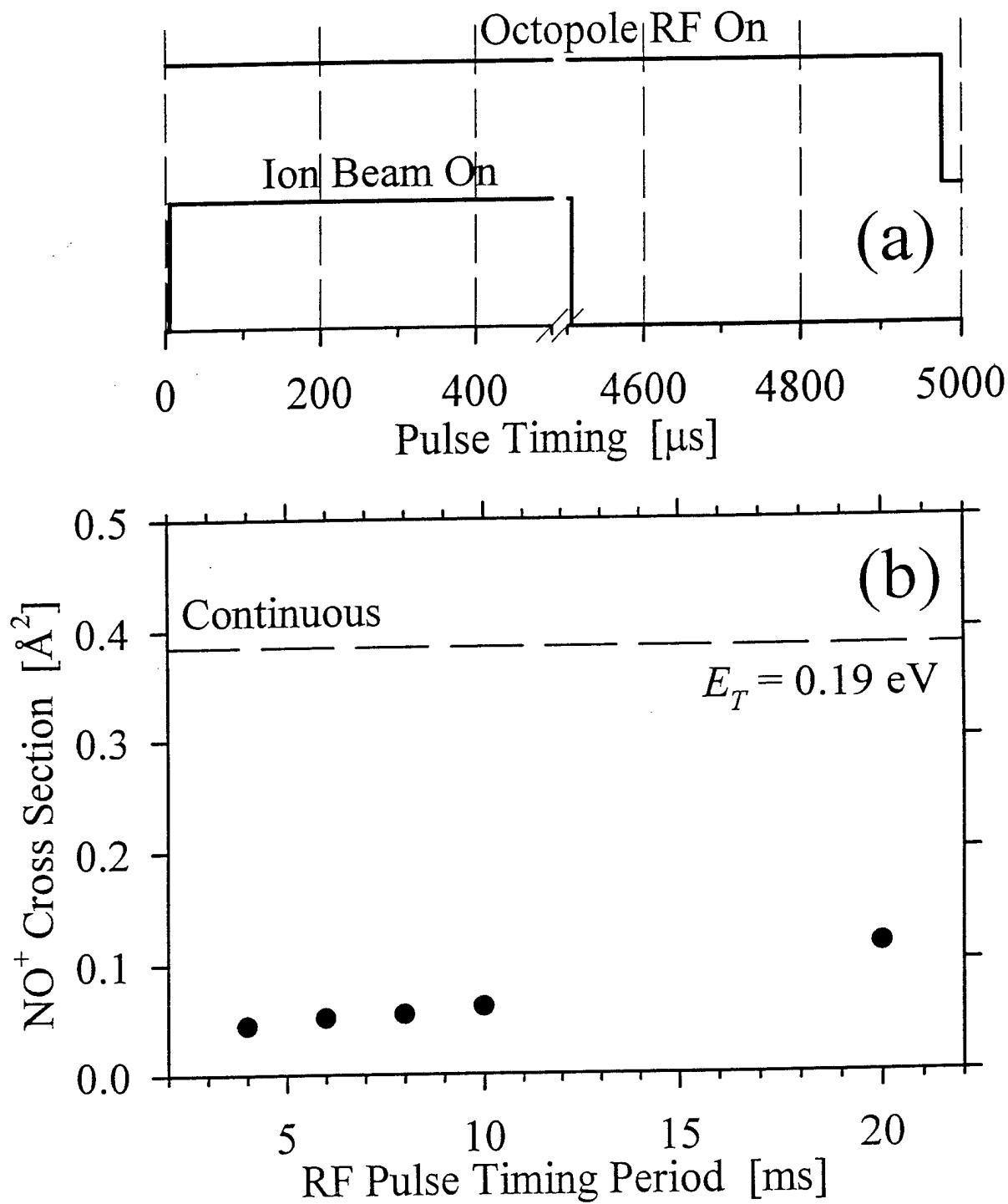


figure 1
J. Chem. Phys.
Dale J. Levandier

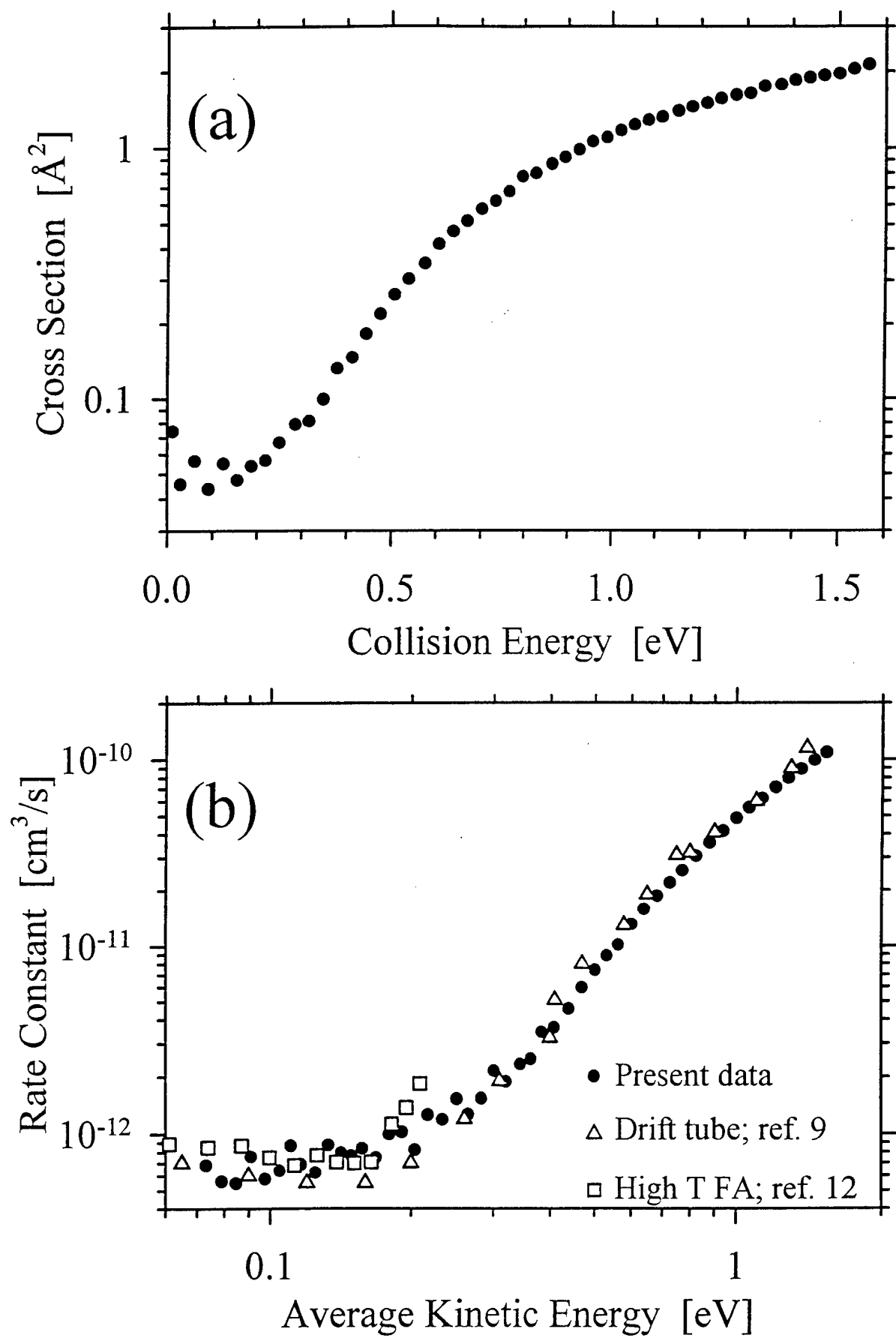


figure 2
J. Chem. Phys.
Dale J. Levandier

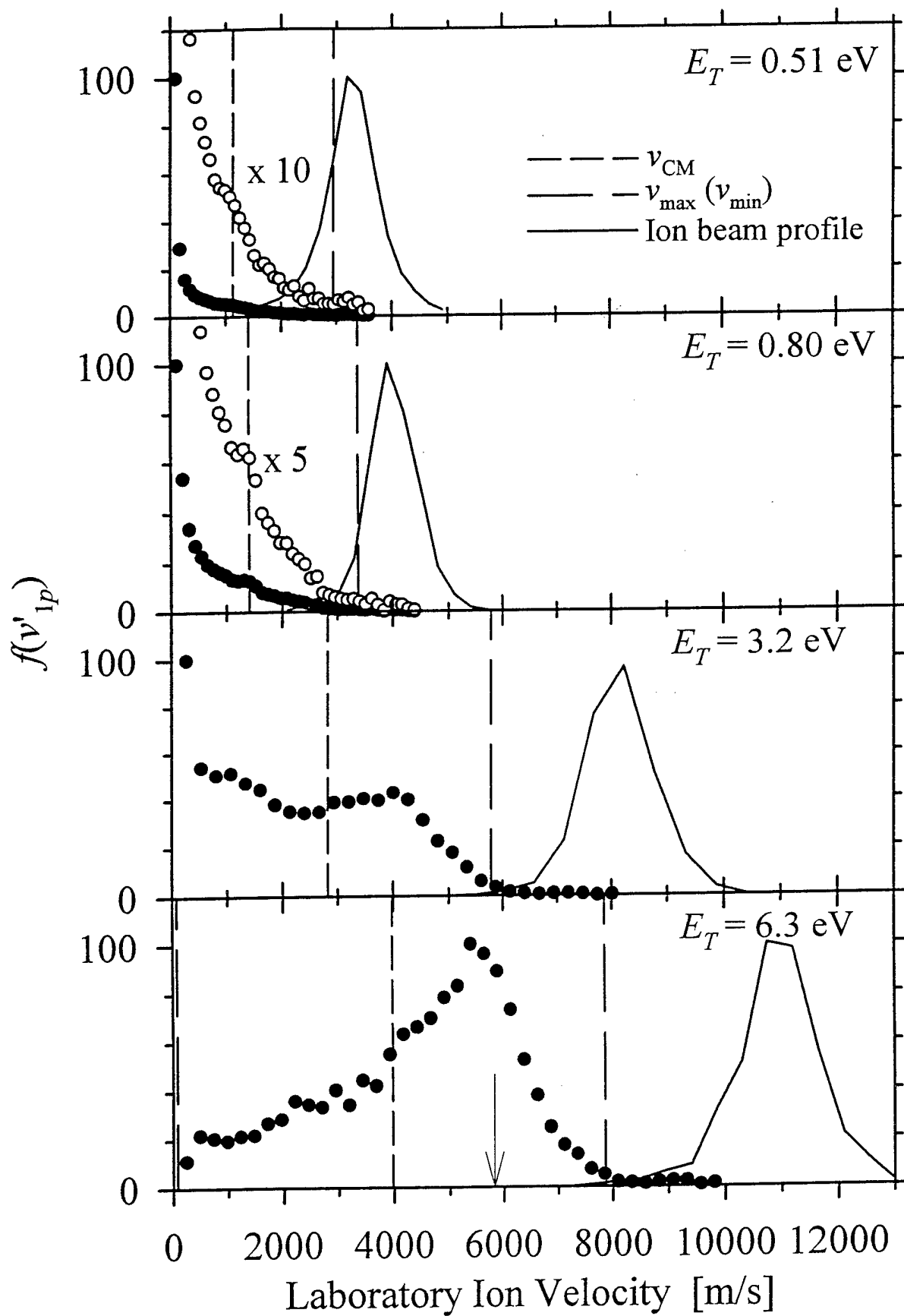


figure 3
J. Chem. Phys.
Dale J. Levandier

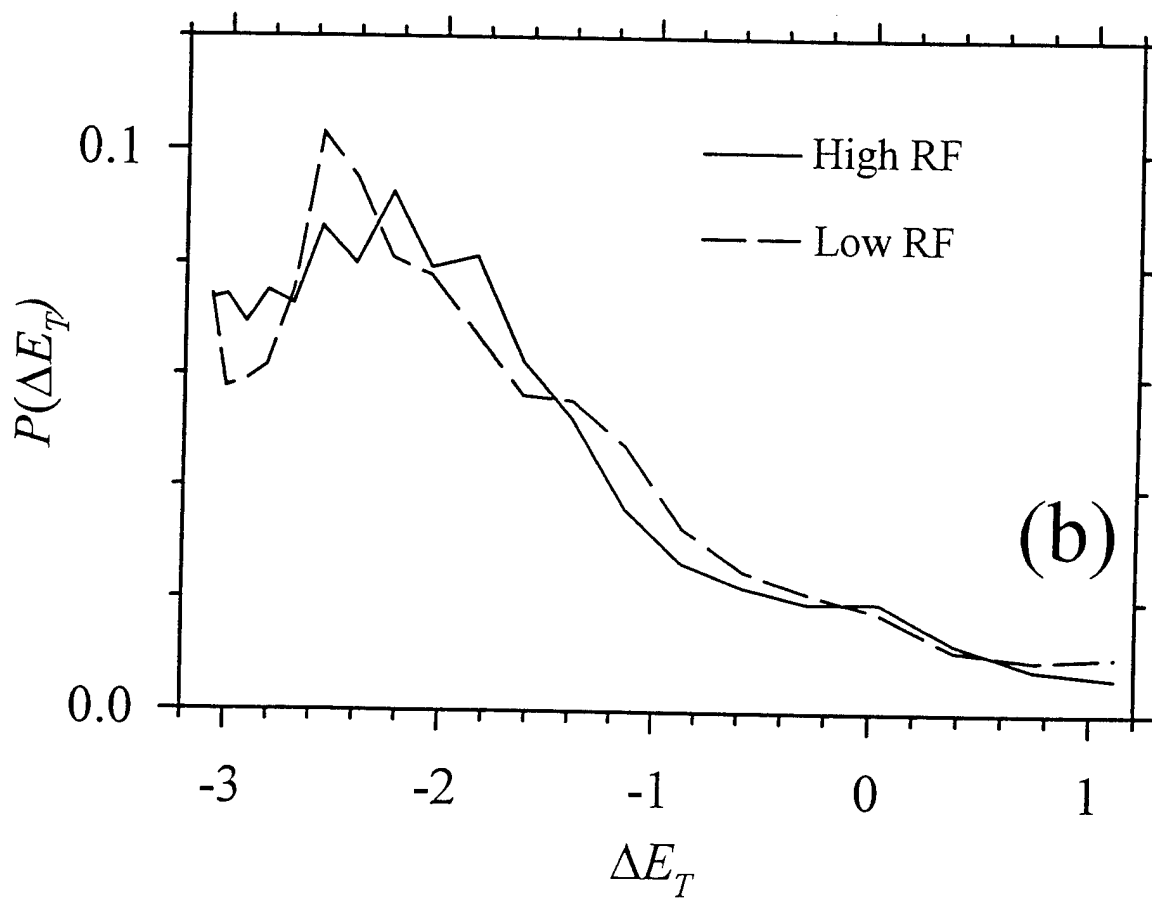
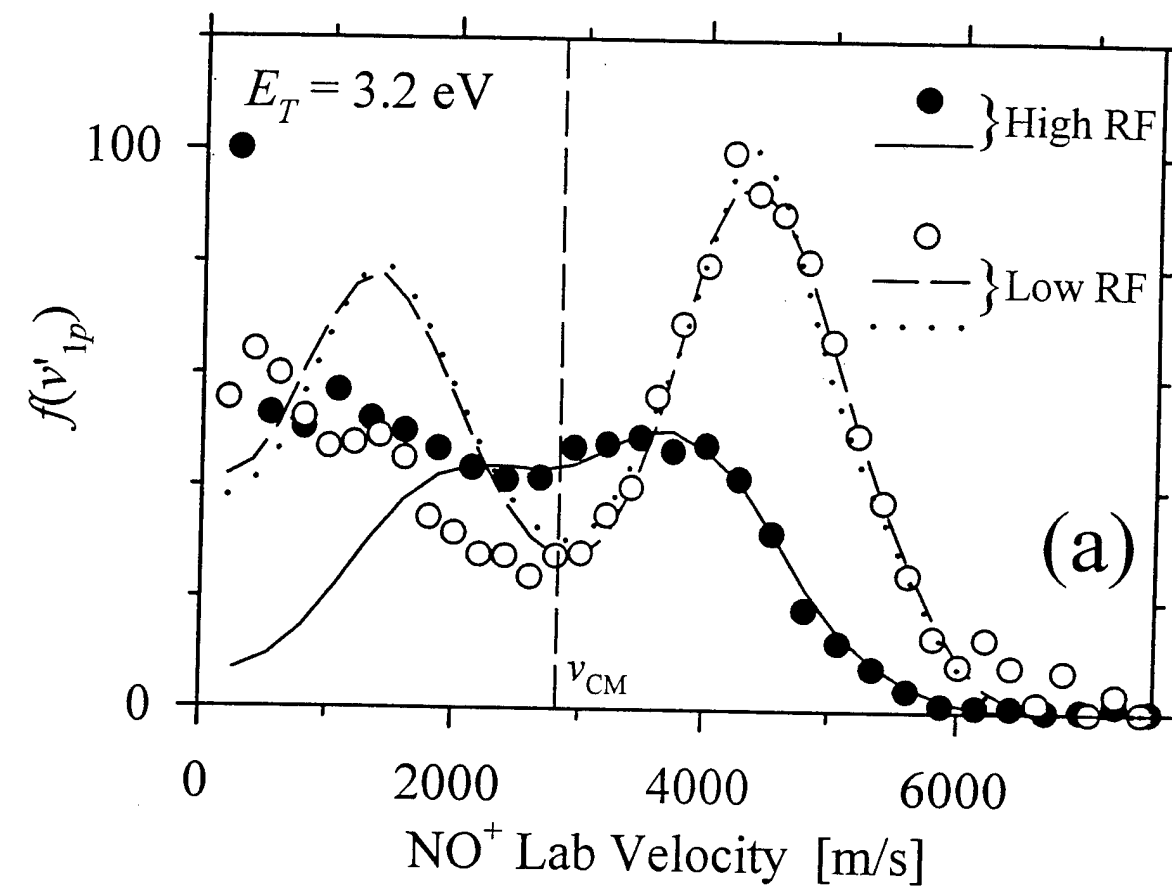


figure 4
J. Chem. Phys.
Dale J. Levandier

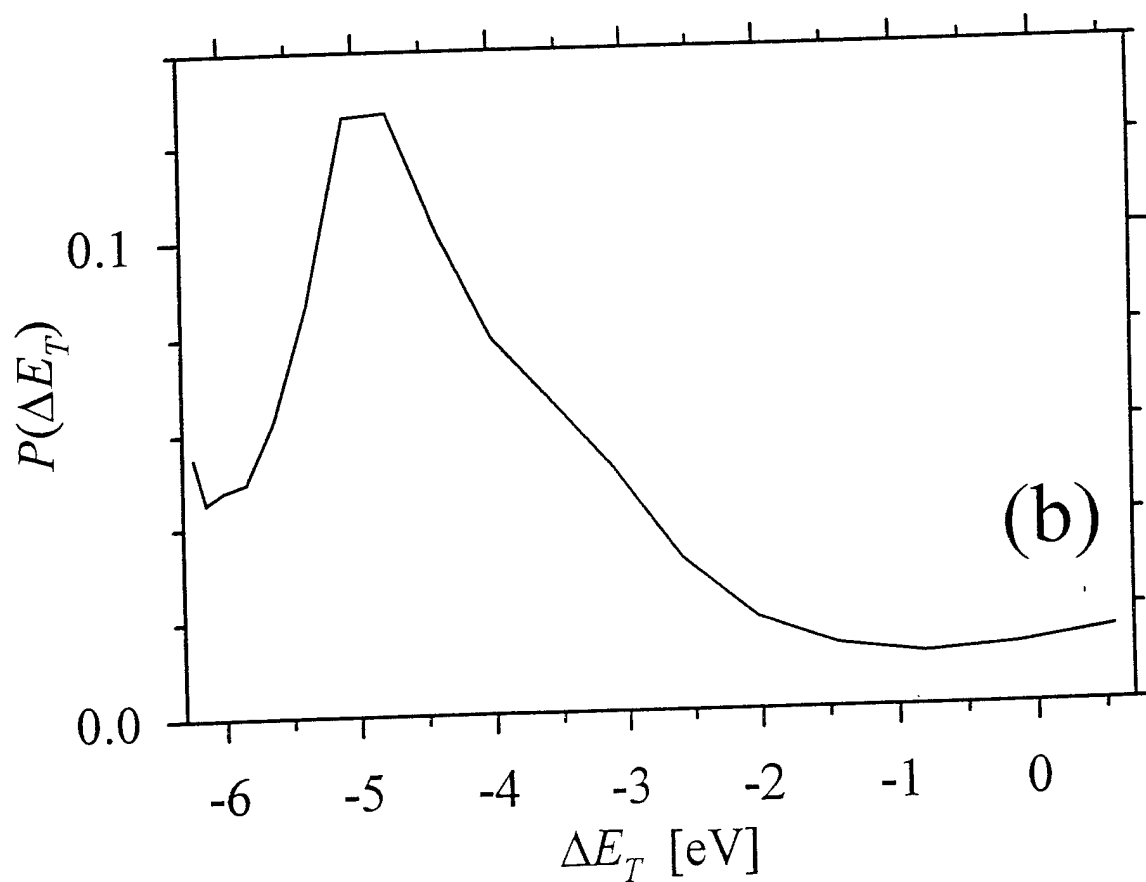
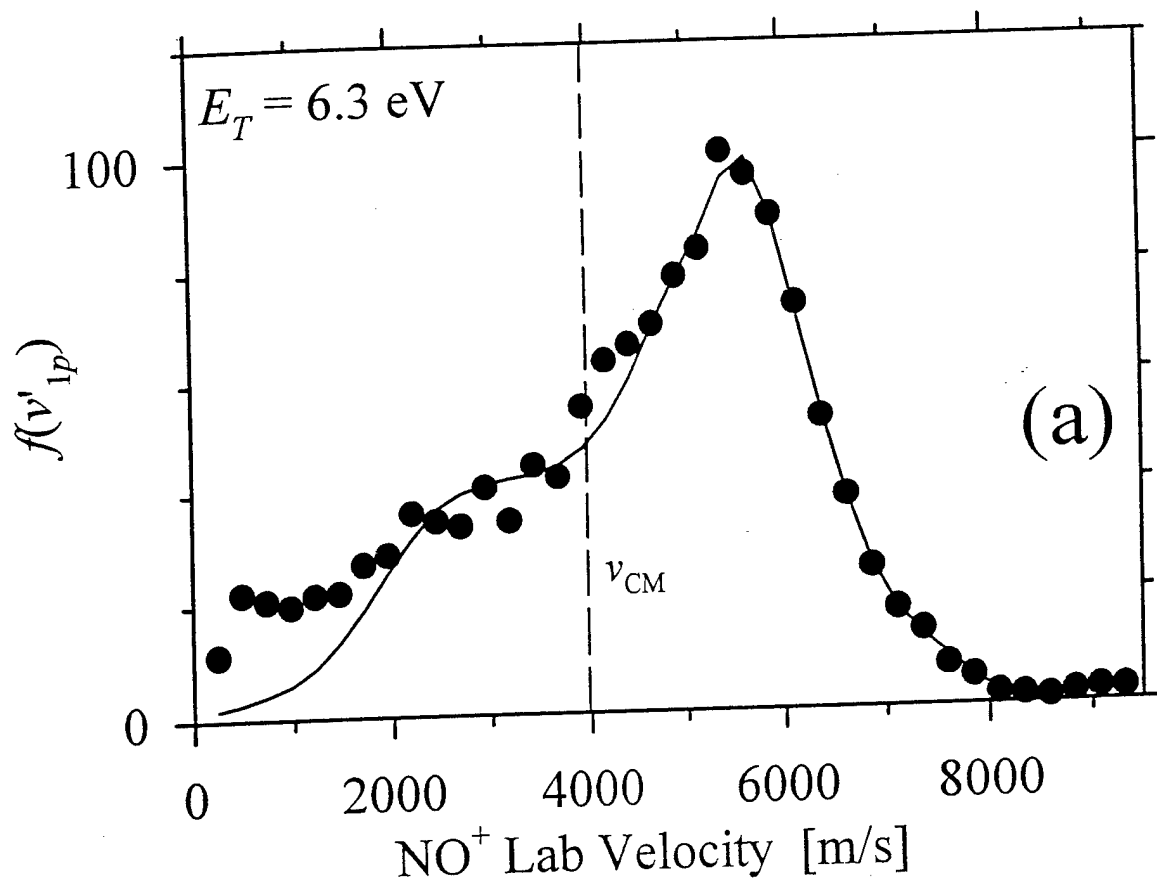


figure 5
J. Chem. Phys.
Dale J. Levandier